

**A NEW GENERATION OF HIGH STIFFNESS
ROTATIONAL MOULDING MATERIALS**

HASHIM BHABHA

A thesis submitted in partial fulfilment of the
requirements of the Manchester
Metropolitan University for the degree of
Doctor of Philosophy

**School of Healthcare Science
The Manchester Metropolitan University in
Collaboration with Rotomotive Ltd.**

February 2015

Confidentiality Clause

This PhD thesis contains confidential data belonging to Rotomotive Ltd and Manchester Metropolitan University (MMU). It should only be made available to the supervisory team, examiners and authorised members of the Graduate School at MMU. Any publication or duplication of this thesis, in partial or complete form, is prohibited. In order for patent applications to be made relating to inventions that may arise from the work in this thesis, a two year embargo period has been granted by the Research Degrees Committee at MMU. Therefore, any inspection of this thesis by third parties requires the expressed permission of Hashim Bhabha, Rotomotive Ltd. and MMU.

Abstract

Polyethylene (PE), particularly linear medium density PE (LMDPE), is the most widely used thermoplastic in the rotational moulding (RM or rotomoulding) industry, possessing a balance between melt flow characteristics and mechanical properties best suited to the RM process relative to alternative thermoplastics. Reliance of the RM industry on LMDPE limits the application envelope for manufacturers due to the inherently low modulus of the material; manufacturers overcome this low modulus by increasing the wall thicknesses of their products which is costly and energy intensive. The addition of filler particles to PE as a method of modulus enhancement was considered a feasible alternative to increasing the wall thickness. The resulting composite material could down gauge part thickness and potentially expand the application envelope of RM. Phase 1 of this study observed the behaviour of RM grade PE's with the introduction of filler particles in order to double the modulus (namely garnet, sand, cenospheres or fly-ash and the latter two combined). The PE/filler composites were mixed by dry blending or melt compounding, moulded and mechanically tested in tensile, flexural and Charpy impact mode. The aim of doubling the tensile modulus of rotomoulding grade PE was achieved by the melt compounded, rotomoulded PE/fly-ash composites. The introduction of maleic anhydride grafted linear low density polyethylene (MA-g-LLDPE) coupling agent also increased the modulus and tensile yield stress of LMDPE with the addition of fly-ash. However, the beneficial melt flow rate and impact toughness of PE decreased significantly with the addition of fly-ash. The latter was especially true for rotomoulded samples.

As the RM industry typically uses finite element analysis (FEA) to numerically approximate the stress or deflection of load-bearing parts, phase 2 of this study focused upon developing numerical material properties for FEA of the new PE/fly-ash composites. Physical measurements from compression tests on rotomoulded PE/fly-ash safety steps were close to FEA approximations (confirming the practical value of the numerical materials data), except in the case of the unfilled and highest filled PE samples. The significant differences observed between physical measurements and FEA were probably due to complex factors such as the non-linear behaviour of PE and the variation in wall thickness of rotomoulded parts, highlighting the importance of properly understanding the finite element method (FEM) for RM.

Associated Publications

1. Bhabha, H. *Using Finite Element Analysis as a Design Tool for Rotomoulded Parts*, Manchester Metropolitan University, Manchester, UK, British Plastics Federation Rotamoulding Tooling Seminar Presentation, April 2013.
2. Bhabha, H. *Using Finite Element Analysis for the Analysis of Rotomoulded Parts*, Affiliation of Rotational Moulding Organisations Newsletter, December 2013.
3. Bhabha, H. Liauw, C.M. Henwood, N.G. Taylor, H. Condliffe, J. *Critical Factors Affecting the Use of Finite Element Analysis For Rotomoulded Parts*, Manchester Metropolitan University, Manchester, UK, Rotomotive Ltd., Northampton, UK, Society of Plastics Engineers ANTEC (Annual Technical) Conference Proceedings, April 2014.

Acknowledgements

First and foremost I would like to express my utmost thanks to my supervisory team, namely my director of studies Dr. Chris Liauw, academic supervisor Dr. Howard Taylor and industrial supervisor Dr. Nick Henwood. Without the guidance of my supervisory team, this PhD study would not have been possible.

Furthermore, I am grateful to Mike Green of the polymer processing workshop at Manchester Metropolitan University (MMU) and my industrial mentor Peter Luxford of Rotomotive Ltd for training on various machinery such as the twin screw extruder, tensometer and water jet cutter.

I would also like to thank Gary Miller and Elaine Howarth of the analytical sciences department at MMU who conducted scanning electron microscopy (SEM), energy dispersive x-ray (EDX) and differential scanning calorimetry (DSC) on my behalf.

Moreover, I am thankful to the following people for assistance during the course of my studies:

- Steve Davies of Crossfield Excalibur Ltd. for providing computer aided design (CAD) files of the rotomoulded safety step.
- David White of Excelsior Ltd. for providing the rotomoulded safety steps and access to rotomoulding machinery.
- Mark and Karen Drinkwater of JSC Rotational Ltd. for introducing me to numerous members of the rotomoulding industry, including members of the British Plastics Federation (BPF).

All of the technical staff members in the Faculty of Science and Engineering also deserve great recognition for their help.

Finally, I would like to express the most heart-felt appreciation to my family and friends for providing their moral support.

Declaration

I, Hashim Bhabha, hereby confirm that this work has not been and will not be submitted for any other award apart from the award of Doctor of Philosophy from the Manchester Metropolitan University. I also confirm that where other sources of information have been included, they have been acknowledged correctly.

Signed:

H. Bhabha

Dated:

“Bismillah ir-rahman ir-rahim”

In the name of God, the most beneficent, the most merciful.

To Umi Jaan (Mother), Abba Jaan (Father) and all my family, with love.

Nomenclature

Abbreviation	Description	Units (where applicable)
PE	Polyethylene	-
LMDPE	Linear medium density polyethylene	-
HDPE	High density polyethylene	-
XLPE	Cross-linked polyethylene	-
PP	Polypropylene	-
PA	Polyamide	-
PC	Polycarbonate	-
MA-g-LLDPE	Maleic anhydride grafted linear low density polyethylene	-
TSE	Twin screw extruder/twin screw extrusion	-
SEM	Scanning electron microscopy/ Scanning electron microscope	-
RM	Rotational moulding	-
EDX	Energy dispersive x-ray	-
DSC	Differential scanning calorimetry	-
MFR	Melt flow rate	dg min ⁻¹
MPF	Maximum packing fraction	Value between 0-1
PSD	Particle size distribution	-
FE	Finite element	-
FEA	Finite element analysis	-
FEM	Finite element method	-
CAD	Computer aided design	-
CAE	Computer aided engineering	-
CNC	Computer numerical control	-

Contents

1. Introduction and Problem Statement	1
1.1 Aims and Objectives of the Study	2
2. Thesis Overview	4
3. Literature Review	6
3.1 The Rotational Moulding Process	6
3.2 Polymers Used for Rotational Moulding	8
3.2.1 <i>Polyethylene</i>	8
3.2.1.1 <i>Polymerisation of ethylene</i>	9
3.2.1.2 <i>Development of chain branches in polyethylene</i>	11
3.3 Particulate-Filled Polymers Used for Rotational Moulding	13
3.3.1 <i>Particulate-filled polymer composite theory</i>	14
3.3.1.1 Modulus of particulate-filled polymer composites	15
3.3.1.2 Yield stress of particulate-filled polymer composites	16
3.3.2 <i>Origins of the filler particles</i>	16
3.3.2.1 <i>Silica sand</i>	16
3.3.2.2 <i>Almandine garnet</i>	17
3.3.2.3 <i>Fly-ash and cenospheres</i>	17
3.3.3 <i>Effects of filler reinforcements on polymer properties</i>	17
3.3.4 <i>Filler-matrix interaction (interfacial regions)</i>	19
3.3.5 <i>Filler-matrix coupling agents and filler particle surface treatments</i>	19
3.4 Introduction to Finite Element Analysis	21
3.4.1 <i>Partial differential equations</i>	22
3.4.2 <i>History of the finite element method</i>	23
3.4.3 <i>Theory and Requirements of the Finite Element Method</i>	24
3.4.4 <i>Finite element model development</i>	25
3.4.4.1 <i>Static linear-elastic analyses</i>	26
3.4.4.2 <i>Non-linear analyses</i>	27
3.4.5 <i>Finite element model refinement</i>	28
3.5 Finite Element Analysis of Rotomoulded Parts	30
3.6 Summary of Literature Review	31
4. Experimental	35
4.1 Polyethylene Grades and Coupling Agent	35
4.1.1 <i>Maleic anhydride grafted polyethylene (MA-g-LLDPE)</i>	35
4.1.2 <i>High density polyethylene (HDPE)</i>	35
4.2 Candidate Filler Particles	36
4.3 Polyethylene and Filler Particle Characterisation	36
4.3.1 <i>Determination of melt flow rate (MFR)</i>	36
4.3.2 <i>Estimation of filler particle maximum packing fraction (MPF)</i>	37
4.3.3 <i>Determination of filler particle densities</i>	38
4.3.3.1 <i>Sand, garnet and fly-ash</i>	38
4.3.3.2 <i>Cenospheres</i>	38

4.3.4 Verification of filler particle size distribution	39
4.3.5 Determination of PE/filler composite densities	39
4.3.5.1 <i>Densometer method</i>	39
4.3.5.2 <i>Ashing method</i>	40
4.4 Blending of Filler Particles and Polyethylene to Form Composite Materials	41
4.4.1 Dry blended formulations	41
4.4.2 Two roll milled formulations	41
4.4.3 Twin screw extrusion compounded formulations	42
4.5 Moulding of PE/Filler Composites	43
4.5.1 Composite plaques prepared at Manchester Metropolitan University	43
4.5.2 Composite plaques prepared at Rotomotive Ltd.	44
4.5.3 Injection moulding of PE/fly-ash flexural test specimens	45
4.5.4 Bench-scale rotational moulding of PE/fly-ash rectangular test boxes	45
4.5.5 Commercial-scale rotational moulding of unfilled PE and PE/fly-ash safety steps	47
4.5.5.1 <i>Unfilled PE safety steps</i>	49
4.5.5.2 <i>PE/fly-ash safety steps</i>	50
4.6 Measurement of Mechanical Responses	50
4.6.1 Tensile Testing	50
4.6.1.1 <i>Determination of tensile parameters from the raw data</i>	50
4.6.2 Flexural testing	51
4.6.2.1 <i>Determination of flexural parameters from the raw data</i>	51
4.6.3 High temperature flexural testing of PE/fly-ash composites	53
4.6.3.1 <i>Determination of flexural parameters from the raw data</i>	54
4.6.4 Poisson's ratio testing of PE/fly-ash composites	54
4.6.4.1 <i>Determination of Poisson's ratio from the raw data</i>	54
4.6.5 Charpy impact testing of PE/fly-ash composites	56
4.6.6 Compression testing of rotomoulded safety steps	57
4.6.7 Tensile testing of safety step materials	58
4.6.8 Compression testing of safety step materials	59
4.6.8.1 <i>Removal of machine compliance error</i>	61
4.7 Surface Image Analysis of Rotomoulded PE/Fly-Ash Rectangular Box Test Mouldings	63
4.8 Scanning Electron Microscopy and Energy Dispersive X-Ray Analysis	65
4.8.1 Sample preparation	65
4.8.2 Scanning electron microscope and energy dispersive x-ray operating conditions	66
4.9 Differential Scanning Calorimetry	66
4.10 Finite Element Analysis of the Rotomoulded Safety Steps Sidewall Deflection	68
4.10.1 Finite element model development	69
4.10.2 Finite element model simplification and refinement	72
4.10.3 Finite element model analysis	75
5. Results and Discussion	77
5.1 Summary of Work	77
5.2 Characterisation of Materials for Composite Development	79
5.2.1 Effect of polymer structure	79
5.2.2 Dual polyethylene blends	79
5.2.2.1 <i>Dry blended formulations</i>	79
5.2.2.2 <i>Twin screw extrusion compounded formulations</i>	82
5.2.3 Key findings from the characterisation of materials for composite development	85
5.3 Analyses of Selected Candidate Fillers	85
5.3.1 Imaging of the candidate filler materials	86

5.3.1.1 <i>Sieve analysis for construction of particle size distribution</i>	88
5.3.2 <i>Energy dispersive x-ray analysis</i>	90
5.3.3 <i>Density of the candidate filler materials</i>	92
5.3.4 <i>Determination of maximum packing fraction</i>	92
5.3.4.1 <i>Single filler systems</i>	92
5.3.4.2 <i>Dual filler systems</i>	93
5.3.5 <i>Key findings from analysis of the filler particles</i>	95
5.4 Comparison of Composite Formation Processes for Large Particle Composites (Dry Blending of Pre-Mix versus Two Roll Mill Melt Blending and Moulding)	97
5.4.1 <i>Estimation of tensile modulus and yield stress for filled polyethylene composites</i>	102
5.4.2 <i>Key findings from the comparison of composite formation processes</i>	108
5.5 Use of Two Roll Mill Blending for Mixed Large/Small Particle Composites	109
5.5.1 <i>Key findings from using the two roll mill to blend large/small particle composites</i>	113
5.6 Evaluation of Twin Screw Extrusion Compounding for Production of Small Particle Composites	114
5.6.1 <i>Key findings from using the twin screw extruder to blend small particle composites</i>	118
5.7 Verification of Maleic Anhydride Coupling Agent Effect on Small Particle Composites Produced by Twin Screw Extrusion Compounding	119
5.7.1 <i>Key findings from verifying the effect of Maleic Anhydride on PE/fly-ash composites</i>	123
5.8 Comparison of Maleic Anhydride Coupling Agent Effect on HDPE and LMDPE Small Particle Composites Produced by Twin Screw Extrusion Compounding	123
5.8.1 <i>Key findings from the comparison of Maleic Anhydride effects on HDPE and LMDPE fly-ash composites</i>	128
5.9 Analysis of Rotationally Moulded Small Particle Composites	129
5.9.1 <i>Rotomoulded rectangular box test mouldings</i>	129
5.9.2 <i>Rotomoulded safety steps</i>	133
5.9.3 <i>Key findings from the analysis of rotationally moulded small particle composites</i>	141
5.10 High Temperature Flexural Testing of Injection Moulded PE/Fly-ash Composites	143
5.11 Cost Benefit Analysis of the Small Particle Composites for Rotational Moulding	144
5.12 Finite Element Analysis of Small Particle Composite Safety Step Sidewall Deflection	146
5.12.1 <i>Specification of material properties for FE model development</i>	146
5.12.1.1 <i>Tensile properties and Poisson's ratio</i>	147
5.12.2 <i>Further compression testing of small particle composite safety steps</i>	149
5.12.3 <i>Comparison of small particle composite safety step sidewall deflection with FEA</i>	151
5.12.4 <i>Formation of tensile-compression curve</i>	156
5.12.5 <i>Key findings from the finite element analysis of PE/fly-ash safety steps</i>	158
5.12.6 <i>Key considerations for the finite element analysis of rotomoulded parts</i>	159
6. Conclusions	160
6.1 Mechanical Properties	160
6.2 Filler-Matrix Blending Technique	161
6.3 Polyethylene, Filler and Coupling Agent	161
6.4 Fillers - Effect of Bimodal Particle Size Distribution	162
6.5 Small Particle Composites – Properties in the Context of Rotational Moulding	162
6.6 Finite Element Analysis of Rotomoulded Small Particle Composites	163
6.7 Overall Recommendations	164
7. Further Work	166

8. References

168

Appendix 1 - 6

192

1. Introduction and Problem Statement

Rotational Moulding (RM) or rotomoulding is an effective method for the production of large hollow components such as liquid storage tanks, kayaks and boats ^[1]. For the current repertoire of applications, polyethylene (PE) is by far the most popular polymer used for RM. PE has the mechanical properties, long-term melt stability and melt flow characteristics best suited to the RM process, relative to alternative thermoplastics ^[2]. Furthermore, despite its low glass transition temperature (T_g) PE can be easily converted into the powdered feedstock required for RM as it can be produced by grinding at ambient temperature, without recourse to cryogenic grinding. Arguably the most attractive factor favouring use of PE is its relatively low cost; PE is definitively the cheapest polymer in the context of RM. However, the modulus of PE is inherently low. Therefore, the wall thicknesses of rotomoulded products are increased to compensate for this low modulus. Increasing the wall thickness is a common tactic for larger load-bearing articles such as liquid storage tanks and silos, where manufacturers often over-thicken the walls to be confident in part strength. Although practically justified, increasing the wall thickness of RM products uses more material, slows production cycles and increases costs.

The latter limitations exemplified the requirement for “rotomouldable” materials with a higher modulus. It was recognised that filler particles could provide the required modulus enhancement to PE at relatively low expense in terms of toughness, processability and cost. Introducing particulate fillers to reinforce polymers is a common technique amongst more popular plastics manufacturing platforms such as injection or blow moulding. On the other hand, it is appreciated that the number of studies regarding fillers for rotomoulding applications is relatively small ^[3-13]; rotomoulding is a relatively low pressure process which complicates the feasibility of using particulate-filled polymers due to the reduction of melt flow properties (particularly at filler levels where the reinforcement is most effective). Consequently, little research and development in particulate-filled PE composite materials for RM has left a particularly large gap in knowledge. Thus far, Arnaud ^[14], Hanna et al. ^[15], Kanokoriboon et al. ^[16] and Chang et al. ^[17] have conducted the most noteworthy work on RM composites. However, this work was confined to using just one filler material where large decreases in impact properties and melt flow rate (MFR) were observed with relatively small increases in modulus and yield stress. Despite the latter, the option of modifying the impact properties and melt flow rate (MFR) remained unexplored by Arnaud et al ^[14-17]. Furthermore, studies by Ward et al. ^[18], Butora et al. ^[19], Lopez-Banuelos et al. ^[20], Yan et al. ^[21] and Mhike ^[22] gave little consideration to important factors such as:

- Using multiple fillers particles of various size and shape.
- Varying the level of coupling agent.
- Assessing different PE/filler blending techniques.
- Blending various grades of PE for filler addition.

Furthermore, the RM industry typically uses finite element analysis (FEA) to approximate the structural behaviour of load-bearing parts due to their geometry, material properties and load scenario. The current body of research in FEA for rotomoulded parts is particularly small with only one available reference from the Society of Plastics Engineers Annual Technical Conference proceedings [23]. Therefore, a strong academic and industrial requirement exists to investigate FEA for rotomoulded parts; the latter is especially true for load-bearing rotomoulded parts that are to be produced using the proposed new particulate-filled PE composite. The combination of polymer composite development and FEA is a novel venture in the field of rotomoulding.

1.1 Aims and Objectives of the Study

In order to address the knowledge gaps regarding the development of PE/filler composites for RM and the FEA of rotomoulded parts, the aims and objectives of this PhD study are to:

1. **Evaluate a selection of particulate fillers as reinforcement to RM grade PE in order to double its tensile modulus** – using Rotomotive’s powder blender and the compression moulders at both Rotomotive Ltd. and MMU. MMU’s tensometer facility will be used for mechanical testing.
2. **Optimise the chosen composite system for performance and processability** – using the twin screw extrusion compounder and melt flow indexer (MFI) at MMU and the RM machine at Excelsior Ltd. PE-filler interfacial modification will be controlled using chemical coupling agents. The effect of the filler and coupling agent on the PE matrix will be assessed using the SEM, DSC and EDX facilities at MMU.
3. **Validate the numerical material property data of the new particulate-filled PE composite materials using FEA** – using SOLIDWORKS Simulation 2013 to compare FEA with physical test results. Rotomoulded safety steps will be used as test subjects for the proposed PE/filler composite materials and a computer aided design (CAD) file of the safety steps 3D geometry will be used for FEA.

The primary goal of this study is to develop a particulate-filled PE composite material with at least twice the modulus of PE. Therefore, the ultimate focus for phase 1 of this study is to investigate a range of filler materials for addition to PE. Four fillers (sand, garnet, fly-ash, cenospheres and the latter two combined) will be investigated in a matrix that comprises of maleanised 25 % wt. LLDPE with 75 % wt. LMDPE (the former acts as a filler-matrix coupling agent). The filler content will be varied using dry blending or melt compounding methods. The MA-g-LLDPE content will also be varied using TSE melt blending. The possible benefits and limitations that the initial candidate fillers, PE and coupling agent have to offer with regards to mechanical properties, rheological effects and morphology will be explored during this phase. However, the earliest stages of phase 1 will be dedicated to the development of material test protocols.

The secondary goal of this study is to investigate the critical factors affecting the use of FEA for rotomoulded parts made using the new particulate-filled PE composite materials. Therefore, phase 2 of this study will focus upon developing a numerical database of material properties for the new particulate-filled PE materials. Critical research questions that will be asked include, what is FEA? How does it work? Moreover, are the mechanical properties of non-linear materials truly representative? Rotomoulded safety steps made using PE/fly-ash composite PE materials will be compression tested for sidewall deflection determination and compared with static linear-elastic and non-linear FEA simulations (applying a force or displacement). Tensile tests will be conducted to determine the mechanical properties required for FEA.

2. Thesis Overview

This study investigates the development of particulate-filled PE (PE/filler) composites to overcome the low modulus of PE (the most common material used in the RM industry). The development of numerical material property data to approximate the mechanical response of the PE/filler composite materials using FEA software will also be explored. The latter software is commonly applied to load-bearing RM parts to validate their mechanical performance before production.

Section 3 forms the literature review and is split into two sub-sections; PE/filler composite material development and FEA. The first section introduces RM and the fundamentals of its process. Furthermore, the rationale behind using PE for the vast majority of rotomoulded products is also introduced; the relative popularity, manufacturing methods and property-structure relationship of PE, in both the context of RM and the wider perspective, is discussed. However, the low modulus of PE is a serious limitation to RM. Therefore, the use of particulate-fillers to enhance the modulus of PE is discussed; fundamental polymer composite design theory such as the effect of fillers on the matrix, the contribution of matrix-filler interaction and the influence of filler particle surface treatments are explained. The second sub-section of the literature review explores the history, mathematical theory and model development techniques of the finite element method (FEM) for stress analysis, in order to provide a good understanding of FEA software.

Section 4 details the experimental methods used for both the development of PE/filler composite materials and FEA of rotomoulded PE/fly-ash safety steps. The novel image analysis technique used for the determination of pinhole count and size distribution on the surfaces of rotomoulded PE/fly-ash rectangular box test mouldings is also detailed within this section.

Section 5 presents and discusses the results obtained. The main findings of each investigation are briefly summarised in the following paragraphs:

Twin screw extrusion (TSE) melt blended composites based on a mix of LMDPE, LLDPE grafted with maleic anhydride coupling agent (MA-g-LLDPE or “maleanised” PE) and the finer filler particles (i.e. fly-ash) produced compression mouldings with the best mechanical properties. However, the improvements in tensile properties were accompanied by reduced impact toughness at higher fly-ash loadings where the modulus enhancement was more prominent. Equivalent composites based on a non-maleanised (analogue) LLDPE blended with LMDPE and fly-

ash had inferior mechanical properties. The highly-filled (70 % wt.) fly-ash LMDPE composites displayed improvements in modulus with every increase MA-g-LLDPE investigated. The same was true for equivalent HDPE composites however at lower MA-g-LLDPE loadings. Therefore, better compatibility was observed between fly-ash particles and the LMDPE/MA-g-LLDPE blends. The latter observations verify the claimed coupling activity of the MA-g-LLDPE with the finer fly-ash particles. However, the addition of fly-ash severely decreased the melt flow rate (MFR) of the resulting composites. Maximum packing fraction (MPF) tests confirmed that combinations of fly-ash and cenospheres could boost filler volume fraction in PE. Conversely, the mechanical response of the resulting composites was poor. During these trials it was concluded that the fly-ash particles offered the best modulus enhancement. Rotomoulded maleanised PE/fly-ash composites offered moduli comparable to that of higher density rotomoulding PE grades; however this was observed at higher fly-ash loadings relative to compression moulded equivalents. Furthermore, the part surface quality of rotomoulded PE decreased with the addition of fly-ash. On the other hand, the variation in wall thickness of the rotomoulded PE safety steps decreased considerably with the addition of fly-ash.

The numerical material parameters required for FEA of the PE/fly-ash composite materials were the tensile modulus, stress at yield, Poisson's ratio and full tensile stress-strain curves (for non-linear analyses). Measured values of sidewall deflection for the rotomoulded PE/fly-ah safety steps coincided reasonably well with most FEA approximations, confirming the practical value of the material data from physical testing. Static linear-elastic FE models had considerably shorter solution times in comparison to more complex non-linear FE models and yet were relatively accurate. However, in some instances the significant differences between FEA and the actual safety steps were probably due to the effect of various complex factors such as the non-linear behaviour of PE and the variation in wall thickness of rotomoulded parts, exemplifying the importance of properly understanding the FEM for rotomoulded parts.

Section 6 summarises the results of this study into a series of conclusions which are briefly discussed in the previous paragraphs.

Section 7 identifies future work for this study; investigations exploring the creep response, zero-shear MFR and processability of the PE/fly-ash composite materials are suggested.

3. Literature Review

3.1 The Rotational Moulding Process

RM involves the slow movement of powdered thermoplastic material within a heated metal mould that is bi-axially rotated in an oven. The polymer powder first in contact with the mould wall melts and sticks to the wall, sintering in to a continuous layer of polymer melt. Any residual polymer powder in the mould then sticks to the initial sintered layer, increasing it in thickness until all the powder has been consumed, leaving a coat of melt polymer around the interior wall of the mould. The moulding is then cooled down whilst slow rotation of the mould continues. Once cooled completely, the mould is opened and the moulding removed.

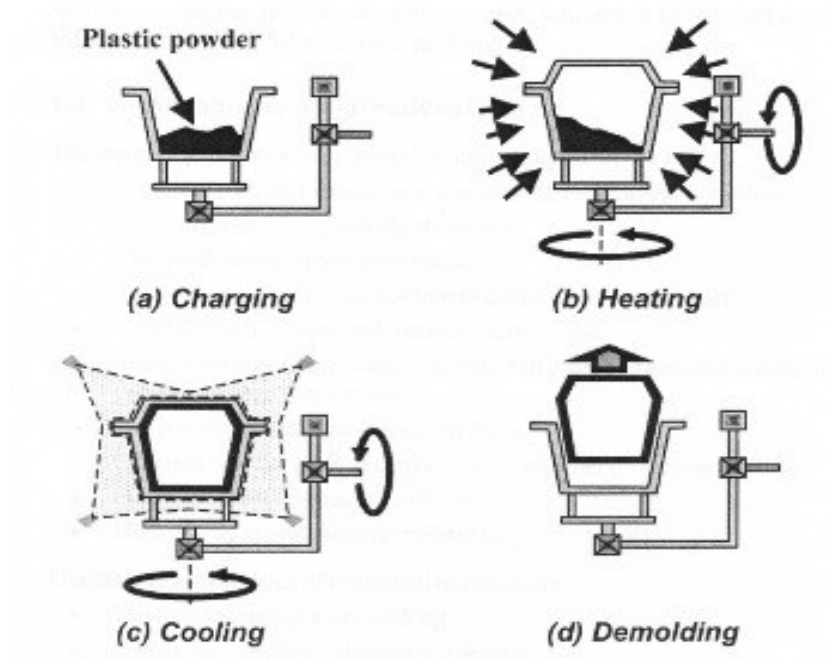


Figure 1. RM process principles ^[24]

The rotomoulding production process consists of four main stages which are represented in (Figure 1):

1. **Charging** - a predetermined mass (shot charge) of polymer (usually in powder form) is carefully poured into a metal mould of the desired part. The average wall thickness of the finished moulding is related to the mass of the charge. Currently, engineers use computer aided design (CAD) software packages to calculate the desired part wall thickness.

2. Heating and Rotation - after charging the mould with the desired shot weight, the mould is sealed and bi-axial rotation is initiated. The mould is then heated in an oven and the consequent spreading of the powder ensures an even dispersion of the sintering powder around the internals of the mould. After some time the polymer powder would have fully melted and formed a homogenous layer effectively stuck to the internal mould surfaces.
3. Cooling - once all the polymer powder has amalgamated, the mould is cooled (whilst still rotating) in an area containing air or water jets (or a combination of both). The reduction in temperature from cooling solidifies the melt polymer; this cooling stage is kept as gradual as possible as failure to do so can result in significant shrinkage or warpage of the moulding.
4. De-moulding - When the moulding has cooled sufficiently, rotation stops and the moulding is carefully removed from the mould. Consequently, the mould is then ready for the next shot charge and repeat of the process.

It is clear that rotomoulding is a unique polymer processing method in which there is no pressure-induced flow of the polymer melt. The polymer powder melts when in contact with the surface of the hot mould and sticks to it, forming a layer of polymer melt which then thickens as more powder is melt-deposited on top of the initial layer. The particles of polymer powder in the melt state have some elastic properties and are highly viscous in relation to a low molar mass liquid such as water. Inter-diffusion of polymer between particles (resulting in sintering) is therefore time dependent as the process is taking place under effectively zero-shear rate conditions. The ability of the polymer chains to inter-diffuse under zero shear places unique demands on the polymer. This factor together with the necessarily long cycle times (sometimes as long as 8 hours for exceptionally large products such as liquid storage silos), which demand unusually high levels of melt stability, places a limit on the range of materials suitable for rotomoulding.

The principles of RM have been implemented as far back as the Egyptian era, where it was used for casting hollow ceramic objects ^[25]. However, the RM process was first applied to plastic products during the 1950's, mainly using polyvinylchloride (PVC) plastisols ^[26]. Having progressed from a relatively simple method, RM is now a precisely controlled technique highly regarded by designers of hollow load bearing structures ^[27]. Research and development in RM during the latter half of the 20th century up to the present has led to notable improvements in component design ^[28], process control ^[29], moulding techniques ^[30, 31] and materials. Linear medium density polyethylene (LMDPE) is arguably the most popular thermoplastic for RM, with its use in most applications. However, an industrial requirement for stiffer rotomoulded components led to the

development of HDPE and cross-linked polyethylene (XLPE) for RM applications. Specialist applications in which the properties of PE do not suffice have led to the development of nylons (PA), polycarbonates (PC) polypropylenes (PP) and even polylactides (PLA) for RM [32]. However, the use of such thermoplastics is far from straightforward and requires tedious trial and error to produce good quality mouldings with the desired profile of properties. The added expense and processing difficulty of alternative polymers to PE for RM has led to limited developments of such materials. To summarise, the benefits and limitations of rotomoulding are:

Advantages of rotomoulding

- Good surface details and finishes.
- Inexpensive prototype moulds.
- Multi-layer laminate structures can be achieved.
- Production moulds are considerably less expensive relative to blow moulding or injection moulding.
- Capable of moulding complex geometries.
- Different sections of one product can be moulded within one tool.
- Plastic or metal inserts can be integrated.

Disadvantages of rotomoulding

- Material costs can be more expensive if pellets need to be ground into powder before moulding.
- Production times are longer in comparison to high pressure processes such as injection or blow moulding.
- Complicated or large parts can make the process labour intensive.
- Polymers with high molar mass are unsuitable for rotomoulding.
- Strengthening structures such as ribs are not easy to achieve.
- Sudden changes in geometry are not easily achievable.
- Consistency in terms of wall thickness is rarely achievable; mouldings are thicker in corners.

3.2 Polymers Used for Rotational Moulding

3.2.1 Polyethylene

PE is arguably the most popular thermoplastic in the world, with applications in shopping bags, bottles, children's toys and even bullet proof vests [33, 34, 35]. PE represents the world's number one high volume thermoplastic in the modern age [36] mainly due to its low cost and versatility. For

example, in 2008 the annual global production of PE was approximately 80 million tonnes [37]. In essence, PE has a simple structure composed of long monomer chains [38]. The monomer is ethylene, a gaseous hydrocarbon with the formula C_2H_4 which can be viewed in Figure 2 as a pair of methylene groups (CH_2) connected by a double bond [39]. The International Union of Pure and Applied Chemistry (IUPAC) name for ethylene is ethene [40]. However, the name ethylene is still used in industrial circles. Ethylene is the simplest member of the alkene family [41]. PE production accounts for about half of the world's demand for ethylene [42]. Ethylene is usually derived by steam cracking ethane or naphtha gas (and other petroleum based feedstock) or by catalytically cracking crude oil directly [43]. Essentially, under the correct temperature, pressure and catalysis, the double bond of the ethylene monomers open, permitting them to link together and form long macromolecular chains of poly(ethylene); this process is called polymerisation [44]. Polymerisation is defined as a method of linking monomers together via a chemical reaction to form polymer chains [45, 46, 47].

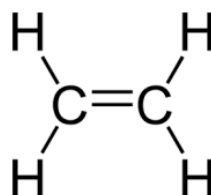


Figure 2. The ethylene (ethene) molecule [48]

3.2.1.1 *Polymerisation of ethylene*

Despite the simple structure of ethylene, the field of ethylene polymerisation is complex; there are various methods that categorise the polymerisation of ethylene, offering the opportunity to tailor a versatile range of PE grades [49]. The carbon-carbon double bond of ethylene consists of one sigma bond and one pi bond [50]. The polymerisation of ethylene is achieved via breakage of the pi bond using high or low-pressure processes. The high pressure process is usually acknowledged for producing conventional LDPE grades via free radical polymerisation [51] while the low pressure process typically produces HDPE and LLDPE via coordination polymerisation [52]. Both free radical and coordination polymerisation are chain-growth methods of polymerisation [53]; they are forms of addition polymerisation [54] where monomers are added to a growing macromolecular chain.

Free radical polymerisation involves the formation of chains via the addition of monomers to a free radical building block [55]. Free radicals are highly reactive atoms or molecules due to their unpaired electrons [56]. Free radical initiation works very well on the carbon-carbon double bond of vinyl monomers (such as ethylene) and the carbon-oxygen double bond in aldehydes and ketones [57]. Free radicals can be formed via several mechanisms typically

involving separate molecules to initiate the free radicals, these are called initiator molecules ^[58]. The latter molecules are a common initiation mechanism. However, there are several mechanisms through which free radical polymerisation can be initiated. Depending on the initiation mechanism, the active centre (centre of chain growth) will take a different form ^[59]. Free radical polymerisation may be divided into three stages: chain initiation, chain propagation, and chain termination ^[60]. Chain initiation is in two stages; during stage 1, one or two free radicals are created using initiator molecules. During stage 2, the free radicals are transferred from the initiator molecules to the monomers. For example, during the free radical polymerisation of ethylene, the introduction of a free radical breaks the pi bond of ethylene and two unpaired electrons rearrange to create a new active centre (similar to the initial free radical) ^[61]. Following its generation, the initiating free radical adds non-radical ethylene monomers to form chains (chain propagation). The free radical polymerisation of ethylene is possible only at high temperatures and pressures (approximately 80-300 °C and 1500-3000 bar) ^[62]. However, the polymerisation of vinyl chloride (for example) using the free radical method to produce polyvinylchloride (PVC) does not require such extreme temperatures and pressures to succeed ^[63].

PE was first produced using a high-pressure free-radical polymerisation process by R. Gibson and E. Fawcett at Imperial Chemical Industries (ICI) in 1933 ^[64]; it was discovered that ethylene (in its natural gaseous form) could be converted into a white solid at high pressures and temperatures in the presence of small levels of oxygen. The resulting polymerisation was a random uncontrolled process producing a wide range of ethylene molecule sizes. However, it was possible to influence the average molecule size (molecular weight) and the distribution of molecule size (molecular weight distribution) around this average via control of the reaction conditions ^[65]. The PE chains were highly branched (Section 3.2.1.2) at intervals of typically 20-50 carbon atoms using this high pressure free radical polymerisation method. ICI named this new polymer "Polythene" and were able to produce it at densities between approximately 0.91 - 0.93 g cm⁻³. It is known today as LDPE and has its single biggest usage in blown film ^[66].

Coordination polymerisation involves the addition of monomers to a growing macromolecular chain (Figure 3) through an organometallic active centre (usually metal chlorides or metal oxides); the latter serves as a catalyst and is the central point of chain growth propagation ^[67, 68]. Catalysts for the coordination polymerisation of ethylene were first developed in the early 1950's; in 1951 ^[69] the Philips Petroleum Company developed catalysts prepared by depositing chromium trioxide on silica ^[70] (Philips catalysts). Furthermore, in 1953 K. Ziegler and G. Natta ^[71] developed catalysts based on titanium tetrachloride and an aluminium co-catalyst such as methylaluminumoxane ^[65] (Ziegler-Natta catalysts). The Philips and Ziegler-Natta (ZN) catalysts

permitted the polymerisation of ethylene (via coordination polymerisation) at much lower pressures than the free radical polymerisation process developed by ICI; the PE produced had a higher modulus than any previously developed PE grade, with a density range of about 0.940 - 0.970 g cm⁻³. The increased modulus and density were due to a significantly lower level of chain branching; the microstructure consisted of straight (linear) ethylene chains with a narrow molecular weight distribution and a high average chain length. The latter was classed as HDPE. Metallocene catalysts first developed by Sinn and Kaminsky in 1980 [72] gave even better control over the microstructure of PE than Philips or ZN catalysts [73]. Generally speaking, the polymerisation method forms the distinction between LDPE, MDPE or HDPE.

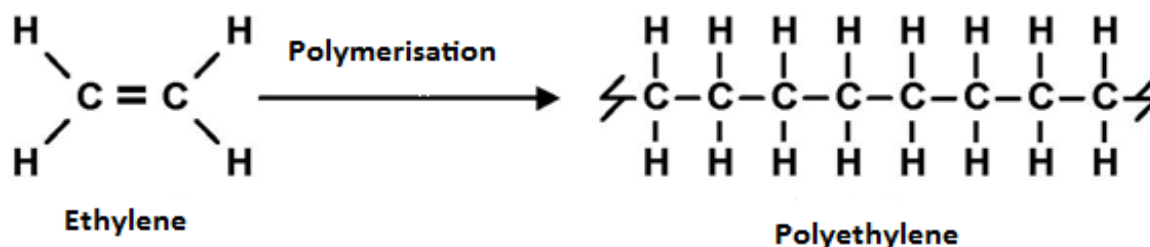


Figure 3. Polymerisation of ethylene to produce PE [74].

3.2.1.2 Development of chain branches in polyethylene

PE is semi-crystalline polymer; it has ordered monomer chains forming its crystalline regions and unordered chains forming its amorphous (non-crystalline) regions. The amorphous regions of PE are responsible for toughness and ductility [75] and the crystalline regions are responsible for rigidity [76]. PE is graded in terms of its density, which increases with crystallinity content [77]. In a PE crystal lattice, the chains in a planar zig-zag conformation [78] (Figure 5) are packed together in orthorhombic arrays [79]; these chains fold into lamellar structures forming ribbons that originate from a central nucleation site [80], resembling spherical structures called spherulites [81]. The maximum thickness of the lamellae is controlled by thermodynamic factors [82], giving a maximum melting temperature of 135 °C for linear PE [83]. Depending upon the polymerisation method used to produce PE, the carbon atoms may have alkyl side chains attached to them; this is called chain branching [84]. Examples of chain branching in PE are shown in Figure 4. The crystalline content and therefore modulus of PE decreases with the level of chain branching; chain branching prevents uniform packing of the chains as they cannot be permitted into the crystal lattice. Furthermore, chain branching causes PE chains to leave one lamellar and enter another if sufficiently few chain branches are present, giving interlammellar tying [85]. A critical level of chain branching also reduces the maximum lamellar thickness of PE and thus the melting point. This increases the amorphous (non-crystalline) content of PE and thus improves toughness.

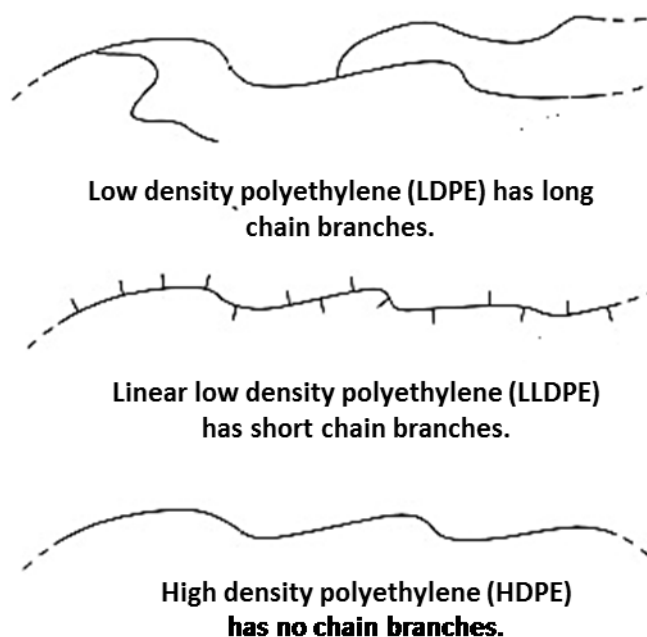


Figure 4. Examples of chain branches in LDPE, LLDPE and HDPE.

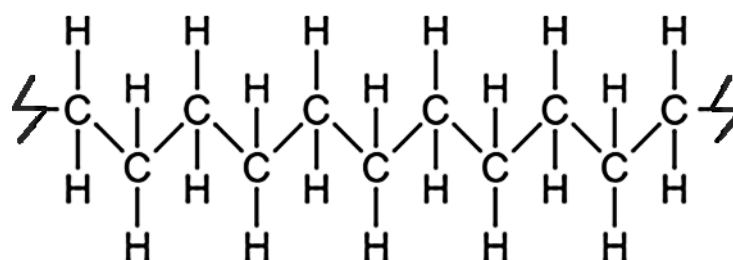


Figure 5. Zig-zag conformation of a PE chain.

Long and short chain branched PE grades (such as LDPE) are often made by free radical polymerisation. Conversely, it is difficult to control the level of chain branching using the free-radical polymerisation method relative to coordination polymerisation ^[86]; as chain-growth termination is randomly determined during free radical polymerisation (termination occurs when two chains collide, known as chain recombination), it is difficult to control the length and branching of individual chains ^[87]. Furthermore, as growing PE chains are flexible, a radical at the end of a chain may bend and abstract a hydrogen atom from a hydrocarbon group along the middle of the chain, thus forming a new radical site for chain growth; this is called intramolecular back-biting chain transfer and produces short chain branches. A free radical may also abstract a hydrogen atom from a surrounding PE chain and form a new radical site for chain growth propagation ^[88]; this is called intermolecular chain transfer and produces long chain branches. Low density PE (LDPE) can have both long and short chain branches; however, it is generally short chain branches for most commercial LDPE grades. On the other hand, long chain branches in LDPE increase the melt strength by chain entanglement ^[89]. Generally speaking, the density of most

short chain branched PE grades varies between 0.91-0.939 g cm⁻³ [90]; this range in density defines low to medium density PE (MDPE). When there is little (or no) chain branching present in PE, it is graded as linear PE or HDPE. Linear PE is much stiffer than branched PE as linear chains can pack together into a crystal lattice more effectively, resulting in higher crystallinity and density [91]. However, branched PE is tougher and easier to produce [92]. Linear PE is made using the coordination polymerisation method. Coordination polymerisation has a significant impact on the structural properties of vinyl polymers such as PE relative to equivalent polymers produced by free radical polymerisation; the polymers tend to be linear (have little or no chain branching) and have a considerably higher molar mass (indicating the chain lengths are longer) [93]. Polymers produced by coordination polymerisation are also stereoregular, indicating the spatial configuration of the monomers is consistent (such as PE, Figure 3). Ordered monomer configurations introduce crystallinity in otherwise amorphous polymers [52]. However, high crystalline content is not always desirable; some controlled branching during coordination polymerisation is required for better control over density to produce linear MDPE (LMDPE), LLDPE and even very low density PE (VLDPE). For example, copolymerising ethylene monomers with an alkyl-branched comonomer (via coordination polymerisation) produces LLDPE which has short branches. The latter exemplifies that coordination polymerisation may also be used if short chain branching is required.

3.3 Particulate-Filled Polymers Used for Rotational Moulding

In 2012, the UK consumed approximately 15 % of the total European resin demand for RM [94], making it the one of the largest producers of rotationally moulded products in Europe. One obstacle to the growth of the rotational moulding industry lies in its dependence on PE to meet the performance demands of end users. PE is relatively thermally stable and so is well suited to rotomoulding but its stiffness is relatively low. Therefore, it would be desirable to modify PE in such a way that its properties are enhanced [14]. One feasible solution to this is a composite material composed pre-dominantly of PE. A successful composite material can be defined as a combination of two or materials that results in better properties than those of the individual components used alone [95]. Due to the economic and practical advantages of bulk thermoplastics such as PE, the addition of particulate materials (or filler particles) has proved to be an effective method of stiffness enhancement. The plastics industry is one of the most cost competitive markets for materials engineering, particularly for mineral suppliers who rely heavily on their products to enhance existing polymers [96]. Filler materials give practically infinite possibilities for thermoplastics; consider the numerous combinations of thermoplastics with an equally large selection of fillers such as talc particles or carbon fibres [97, 98]. The attributes of particulate-filled

polymer composite materials could be low cost, decreased density (if hollow particles are used), increased strength or improved thermal conductivity [99]. It is known that the addition of mineral fillers to PE (and all thermoplastics with a glass transition temperature (T_g) below room temperature) results in a higher modulus [100].

Whilst one of the primary roles of filled polymers is to reduce costs, this role is normally superseded by the reinforcing effects or reduction in mould shrinkage. Furthermore, the introduction of fillers influences end product properties such as density and processability. Ideally, particulate-filled PE composite materials for RM should as much as possible maintain the toughness, processing window and relative economy of PE. Many studies have confirmed the introduction of particulate fillers to PE can enhance mechanical properties and dimensional tolerances [101, 102]. However, increasing the stiffness of PE via the addition of filler particles may reduce toughness. Furthermore, the addition of filler particles increases the melt viscosity of PE, hindering its flow during processing [103]. Therefore, it is recognised that the deterioration of properties in particulate-filled PE composites may also depend on the level of filler addition. Such composite materials for RM demand a good assessment of the inevitable compromise between stiffness, toughness and melt flow properties with the addition of filler particles.

The effectiveness of particulate-filled polymer composites relative to unfilled polymers is generally due to the base polymer properties, filler particle properties, level of filler particle addition, strength of filler-matrix interaction and manufacturing methods [21]. To gain a true appreciation of the influence each variable has on filled PE composites, it is necessary to understand the theory of particulate-filled polymer composites and the effects of filler reinforcement on the properties of polymers.

3.3.1 *Particulate-filled polymer composite theory*

In scientific literature, a vast number of theoretical models are available to approximate the effect of particulate fillers on the modulus and yield stress of thermoplastics [104]. Generally, the most noticeable difference to thermoplastics with the addition of filler particles is the increase in modulus (if the filler particles are of higher modulus than the matrix) [105]; this is due to the constraints imposed on the movement of the matrix by the filler particles (i.e. the matrix ligaments are sandwiched between the filler particles). The latter is generally due to a variety of factors such as filler particle size, shape, distribution, volume fraction (V_f) and interaction with the polymer matrix. The interaction of untreated filler particles with the polymer matrix (i.e. no coupling or dispersion agents are used, see Section 3.3.5) is mainly due to thermal contraction of the polymer around the filler particles when the composite is cooled. The latter generates a frictional force between the filler particle and the matrix that also constrains the movement of

the matrix. On the other hand, if the filler particles are treated with a chemical coupling agent to promote better matrix-filler interaction, the probable increase in filler-matrix interaction will also increase the modulus.

3.3.1.1 Modulus of particulate-filled polymer composites

Several authors have analysed the effects of particulate fillers on the modulus of polymers; Kerner's equations ^[106] which assumed perfect filler-matrix interaction were further modified by Goodier ^[107] to approximate the moduli of polymers filled with spherical particles. However, Goodier's equations did not take into account the maximum packing fraction (MPF) by volume of the filler particles. Therefore, Nielsen ^[108] further developed Goodier's equations to account for the MPF by volume of the filler particles. The resulting equation was in the form of:

$$\frac{E_c}{E_m} = \frac{1+ABV_f}{1+B\varphi V_f} \quad \text{Equation 1.}$$

Where:

$$A = k_E - 1 \quad \text{Equation 1.1}$$

$$B = \frac{\left(\frac{E_f}{E_m}\right)^{-1}}{\left(\frac{E_f}{E_m}\right)^{-1} + A} \quad \text{Equation 1.2}$$

$$\varphi = 1 + \left(\frac{1-P_f}{P_f^2}\right) V_f \quad \text{Equation 1.3}$$

k_E = Einstein co-efficient

E_c = Modulus of the composite

E_f = Modulus of the filler particle

E_m = Modulus of the matrix

V_f = Volume fraction of the filler particles

P_f = Maximum packing volume fraction of the filler particles

The Einstein co-efficient k_E is dependent upon filler particle shape and can be determined experimentally by rheological techniques ^[101]. The B parameter is a function of the moduli of the filler particle and the polymer matrix; this can be approximated to unity if $E_f \gg E_m$. The constant Ψ is the modification to Goodier's equation by Nielsen ^[108] in order to account for the volume fraction of filler in the composite. The latter can be determined by oil absorption tests (see Experimental Section 4.3.2). The modified Kerner equations have been used successfully in the

past by various authors ^[109, 110] to produce values of modulus close to what was experimentally determined on polymers with filler volume fractions of ≤ 0.5 .

3.3.1.2 Yield stress of particulate-filled polymer composites

Pukansky ^[111, 112] found that the yield stress of particulate-filled polymers is dependent on factors such as the surface area of the filler particles and the strength of filler-matrix interaction. The yield stress of particulate-filled thermoplastics can be higher or less than the unfilled matrix depending on the factors discovered by Pukansky ^[111, 112]. However, at filler volume fractions (V_f) low enough to allow yielding (i.e. ≤ 0.5 , such as the filler levels typically encountered in studies of particulate-filled polymer composites ^[14-22]), the yield stress of the composite (σ_c) is generally assumed to be a failure stress because it is generally more than the yield stress of the filler particle (σ_f). Therefore, a simple expression that relates the composite failure stress to the matrix area on the fracture surface (assuming no filler-matrix interaction) is available ^[113, 114] to calculate the yield stress of the composite:

$$\sigma_c = \sigma_m(1 - V_f) \quad \text{Equation 2.}$$

Where:

σ_c = Yield stress of the composite material.

σ_m = Yield stress of the matrix.

v_f = Volume fraction of filler.

3.3.2 *Origins of the filler particles*

Sand, garnet, fly-ash and cenosphere particles were selected for addition to PE to increase the modulus. The origins of these fillers are discussed in the following paragraphs.

3.3.2.1 *Silica sand*

Sand is composed of finely granulated rock and mineral particles of typically 0.1 - 0.8 mm in size ^[115]. It is a naturally occurring mineral usually found on beaches, riverbeds and deserts ^[116]. The composition of sand is generally a product of geological factors such as the type of local rock sources and environmental conditions. However, the most common constituent of sand (as found on inland continental environments) is Silica ^[117] (SiO_2 , generally in the form of Quartz). Due to its chemical inertness and hardness, Silica sand particles are the most resistant to weathering by water or wind. However, the common angular/irregular shape of Silica sand particles is due to erosion from contact with granite or gneiss quartz crystals ^[118].

3.3.2.2 Almandine garnet

Garnets are a group of silicate minerals that share similar property-structure relationships (e.g. crystallinity, hardness and density) but differ in terms of chemical composition ^[119]. The chemical composition of Garnets denote whether they belong to the pyrope, almandine, spessartine, grossular, uvarovite or andradite species ^[120]. Almandine garnet can be described as an alumino-iron mineral with a typical formula of $\text{Fe}_3\text{Al}_2(\text{SiO}_4)_3$ ^[121] and usually occurs in metamorphic rocks such as Mica schist's ^[122]. It is dark red/purple in colour, angular/irregular in shape and is commonly used as an abrasive.

3.3.2.3 Fly-ash and cenospheres

Fly-ash and cenosphere particles are a bi-product of coal combustion. The particles are ceramic and predominantly composed of Alumina, Silica and Iron ^[123]. Both cenosphere and fly-ash particles are spherical in shape however the cenosphere particles are hollow (filled with air) giving them a density lower than water ($0.4\text{-}0.8\text{ g cm}^{-3}$) ^[124]. The elemental composition of fly-ash and cenosphere particles depends on the coal used to produce them. However, fly-ash and cenospheres generally contain significant amounts of Silicon Dioxide (SiO_2), Calcium Oxide (CaO) and Aluminum (Al). Fly-ash and cenosphere particles are commonly used as additives to building materials (e.g. concrete and bricks) and polymers to enhance their properties ^[125]. However, fly-ash particles are typically an order of magnitude smaller than cenosphere particles with a considerably higher density ($1.7\text{-}2.9\text{ g cm}^{-3}$) ^[126] as they are solid particles.

3.3.3 Effects of filler reinforcements on polymer properties

Polyethylene is a semi-crystalline polymer. Its properties are determined by the relative amount of amorphous and crystalline phases, crystal modification size, perfection of crystallites, dimensions of spherulites and the number of tie molecules (e.g. interlamellar and interspherulitic ties) ^[127, 128]. However, modifying the crystal structure of PE may affect the remaining properties simultaneously, exemplifying why changes solely to the crystalline structure may not correlate well with the resulting physical properties. In the context of RM, fillers act as a foreign matter and tend to retard the sinterability and coalescence of the polymer melt, causing air bubbles in the moulded parts; these air bubbles reduce the impact properties and percent elongation of the moulded part ^[16]. However, fillers can have a significant effect on the crystal structure of polymers which should not be neglected ^[129].

Kendal claims that the mechanical properties in filled polymer composites are mainly affected by the strength of interaction between the polymer matrix and filler particles (matrix-filler interaction) ^[130]. The mechanical response of untreated particulate-filled composites are

determined partially by the physical attributes of the filler particles ^[131]. Data sheets from mineral suppliers to the plastics industry typically do not sufficiently characterise filler particles and their suitability for addition to polymers. However, such data sheets may disclose information such as particle size and distribution, shape, density and chemical composition. Chemical composition is important as it denotes the purity of the fillers (impurities such as transition elements lead to accelerated degradation of the matrix). Furthermore, the chemical composition of fillers has some influence over nucleation effects ^[132] and the reactivity of the filler particle surfaces with coupling agents i.e. Silanes ^[133]. However, further physical, mainly particle characteristics are required to forecast the performance of filler materials ^[136].

Particle size plays a dominant role in the properties of particulate-filled composites; the strength and modulus were seen to increase with the decrease in particle size ^[137]. Schlumpf ^[136] also identified that particle size distribution is an important factor when selecting appropriate filler particles for PE reinforcement. Large size particles can have a negative effect on failure characteristics and composite toughness. Small size particles show a tendency to aggregate increasingly with the decrease in size ^[31]; aggregation is a condition where the particles coalesce in a generally irreversible manner, when introduced to a polymer matrix they cannot be broken down into primary particles and hence lower the impact toughness of the composite. Furthermore, aggregated filler particles can act as crack initiation sites. On the contrary, Vu-Kahn and Fisa ^[137] saw a decrease in impact toughness with the decrease in particle size. Riley et al. ^[138] also observed that impact resistance decreased with decreasing particle size and with high aspect ratio particles (ratio of length to width). However, Tritignon et al. ^[139] observed no change in the tensile stress at yield with the decrease in particle size.

The effective surface area of the filler particles (related to their particle size and size distribution ^[140] also has an effect on the stiffness and impact strength of filled polymer composites. Another crucial element of filler materials is their shape, in fact many types of filler are characterised by their anisotropy ^[141] (aspect ratio) and it is said that the effectiveness of filler reinforcement is closely associated with this property. In some investigations an increase in modulus is seen with filler particles of a higher aspect ratio. For example, the plate-like nature of talc particles gives better mechanical properties than particles of a spherical nature ^[16, 130]. However, it is not clear how the aspect ratio of filler particles affects the microstructure of resulting composites. Considering the wealth of contradictory observations, it is reasonable to suggest, besides filler particle size and particle size distribution, the aspect ratio and shape should be taken into consideration when introducing particulate fillers as reinforcement for polymers.

3.3.4 *Filler-matrix interaction (interfacial regions)*

The performance of commodity particulate-filled composites is being pushed ever higher by the need to down-gauge part thickness and increase the creativity of industrial designs. This places increased demands on the interfacial properties of the composites as high strength is often required together with reasonable toughness ^[142]. The interface is the physical region where mechanical properties are altered due to a chemical reaction that promotes the adhesion of the filler particle surface to the matrix ^[143]. The adhesion strength and toughness of the interfacial region plays an important role in the performance of particulate-filled polymer composites ^[144]. These interfacial properties are heavily influenced by the type of surface coating applied to the fillers for addition to the polymer ^[145]. This provides a physicochemical link between the filler particle surface and the matrix. In polymeric composites, matrix-filler interaction has a profound effect on crystalline structure and the amount of crystalline phase (particularly for semi-crystalline polymers such as PE). In many cases, increases in flexural and tensile properties are seen with the appearance of an interfacial region between the filler particles and polymer matrix. It is certain that the strength of the interfacial region is a prominent factor in the overall properties of the composites in question ^[146]. With this in mind, it can be said that strength of the interfacial region would depend on the specific surface area it is applied to and the strength of adhesion. The size of the interface is proportional to the specific surface area of the filler; this is inversely proportional to the particle size. Many investigations have indicated the dependence on the specific surface area of the interfacial region ^[147, 148].

3.3.5 *Filler-matrix coupling agents and filler particle surface treatments*

Although previous investigations have identified that the performance of filled polymers are heavily dependent on filler particle related characteristics, it seems that optimum performance is only possible when the filler particle surfaces are treated for better compatibility with PE and dispersion within the matrix ^[149]. Filler materials are often treated with some form of chemical surface coating to optimise their performance or processability; such additives can be classed as coupling agents and dispersion agents. Coupling agents improve the filler particles strength of adhesion at the polymer interface by modifying their surfaces ^[150]. In doing so, coupling agents promote the polymer to strongly bond to the filler surface for better stress transfer from the polymer matrix to the stiffer filler particles. Dispersion agents (or wetting agents) reduce the surface energy of filler particles and improve dispersion within the polymer matrix ^[151]; maximising the interfacial area of fillers within a composite whilst reducing its surface energy results in better wetting of the filler by the matrix and often better dispersion. However, filler-matrix interaction is often reduced relative to filler particles not treated with dispersion agents. At low filler levels this can be beneficial to toughness; at high filler levels coupling agents perform

better ^[127]. Furthermore, better dispersion of the filler particles may serve the melt flow properties of the resulting composite blend. Highly filled polymer composites may benefit the most from such treatments.

At present, a wide range of coupling agents and chemical treatments (titanates, silanes, and maleic anhydride grafted polymers etc.) are available to chemically promote better filler-matrix adhesion. Chemical agents such as these can also better disperse the filler particles and increase interfacial area within the matrix. This results in increased stiffness but not necessarily increased toughness. The latter is dependent on the filler-level and the properties of the interfacial region. These aspects have been investigated by the MMU fillers group ^[152], Pukanzsky et al. ^[153] and Brechet et al. ^[154]. Some filler particle surface treatments increase filler dispersion quality at the expense of filler-matrix interaction, treatments of this nature are known as dispersants; stearic acid is the best example of this class. Dispersants can be more effective than coupling agents at increasing composite toughness at low filler levels, where filler-matrix de-bonding and void formation contribute to a very effective toughening mechanism. On the other hand, increases in the toughness and stiffness of filled polymeric composites may still be possible with coupling agents ^[16]. However, it is difficult to find an effective coupling agent in the case of PE because of its low polarity and lack of reactive groups ^[139]. Hydrocarbon based polymers like PE or polypropylene (PP) have a limited interaction with filler particles because of their low surface energy (polarity). Bernada ^[155] claimed that a linear PE chain is stable enough to resist any kind of chemical reaction with surface treated fillers.

Maleic anhydride grafted PE (MA-g-PE) is an effective coupling agent which acts via trans-crystallisation and entrapment of the filler by chemical adsorption of the anhydride groups to the filler surface ^[156]. The latter is achieved via ion pair interactions between a hydrolysed anhydride group, and the filler particle surface. Maleic anhydride may be grafted onto polyolefins such as PE by mechano-chemical means initiated with free radical, ionic or radiation initiation techniques ^[157]. Suppliers to the rotomoulding industry sell PE grades pre-grafted with maleic anhydride (MA) which is more cost effective and convenient; however, the exact level of MA grafted to the polymer remains propriety information of the supplier. On the other hand, the chemistry of the reactive extrusion process generally prohibits maleic anhydride levels in excess of 1 % wt. in PE ^[158].

3.4 Introduction to Finite Element Analysis

Computer aided engineering (CAE) technologies such as computer aided design (CAD) and finite element analysis (FEA) offer the capability to build, optimise and validate engineering designs within a virtual environment. Often referred to as virtual prototyping, CAE technologies can:

- Decrease development time.
- Simplify the revision process.
- Highlight considerations
- Assess performance.
- Bring designs to the market faster.

Modern CAE softwares essentially reduce a significant amount of the design process by automating the design sensitivity and optimisation process, eliminating the need to physically build multiple prototypes. In the context of RM, manufacturers and their clientele use FEA to estimate whether their load-bearing designs will be within the dimensional tolerance specified, withstand the loads required and endure the intended lifecycle. FEA is ultimately a numerical approximation ^[159] for solving boundary value and solid mechanics problems. It is the most extensively used numerical analysis method in mechanical engineering practice ^[160]. The mechanical response of structures that were previously difficult or practically impossible to analyse by hand can now be analysed using FEA software with relative ease. The fundamental concept of FEA is the assumption that any continuous quantity such as stress or deflection can be numerically approximated by a discrete mathematical model composed of iterative partial differential equations (PDE's). FEA software solves PDE's by first discretising them into their spatial dimensions. This discretisation is done locally at nodes (infinitely small points) that are connected by lines to form a mesh of simple shapes (e.g. tetrahedrons, called finite elements) around a 2D or 3D structure ^[161] (Figure 6). The solutions of PDE's are functions assigned to the nodes forming the finite elements ^[162]. Stress or strain is calculated at the nodes and then an approximation across the entire mesh of elements is provided (under the given equilibrium and loading conditions).

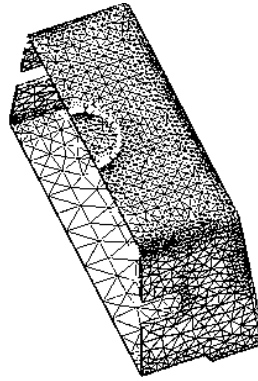


Figure 6. FEA mesh of a 3D structure. The triangular shapes are the elements and the points connecting the elements are the nodes (or nodal points).

The development and mathematical analysis of FE models is practically impossible to achieve by hand. Therefore, computers are used for such operations. However, FEA computer simulation times increase with the complexity of the FE model. Therefore, it is important to understand the finite element method (FEM) in order to design FE models with an optimal balance of simplicity to accuracy ^[163].

FEA software was primarily designed for application without requiring the user to understand its governing mathematics. However, skilful FEA users have a thorough understanding of the governing mathematics, model assumptions, boundary conditions and limitations of FEA software ^[164]. Conversely, it must be appreciated that FEA is a purely predictive approach; the virtual representation of a physical loading scenario (i.e. the FE model) is highly idealised to reduce the number of uncontrollable variables and provide swift solutions with good practical value (hypothetically). At present, the RM industry typically uses FEA to approximate the stress or deflection of load-bearing parts in the field. Therefore, it was recognised that numerical material data for FEA of the proposed particulate-filled PE composite material for RM should be developed. Due to the unusual properties of composite materials, FEA has often been applied to approximate their mechanical response in various applications ^[165]. In the 21st Century, most FEA software is capable of numerically approximating the behaviour of structures due to multiple phenomena such as thermal, chemical and electrical stresses combined ^[166, 167]. With the latter examples in mind, it is appreciated that the mathematical methods of FEA software should be properly understood.

3.4.1 *Partial differential equations*

Many natural phenomena such as stress-strain, thermodynamics, fluid dynamics and even quantum mechanics are approximately described by partial differential equations (PDE's) ^[168]. A partial differential equation (PDE) is an equation for some quantity u (dependent variable) which

is a function of the independent variables $x_1, x_2, x_3 \dots x_n$ (provided $n \geq 2$) and involves derivatives of u with respect to at least some of the independent variables ^[169]. Ordinary differential equations describe one-dimensional dynamic systems whereas partial differential equations can describe multi-dimensional systems; PDE's contain unknown multi-variable functions and their partial derivatives, relative to ordinary differential equations which contain single variable functions and their derivatives ^[170]. PDE's may be solved by hand (impractical for complex problems) or ordered to create a relevant computer model (e.g. a FE model). Various sets of PDE's have been developed to approximate natural phenomena such as the Helmholtz equation, Klein-Gordon equation and Poisson's equation.

PDE's may be solved analytically or numerically. Analytical solutions are closed form as the solution can be described as a single mathematical function ^[171]. The analytical solution is easily achievable for very simple problems and becomes impractical to obtain for complex PDE's with a large number of independent variables. In the ideal world, analytical solutions would arguably be the preferred choice as it provides a single mathematical function that describes the systems behaviour at any given instance. However, analytical solutions are usually difficult to understand or impractical to develop for complex problems which involve multiple variables. Numerical solutions use a numerical time-stepping procedure to provide a basic solution at any given time in the form of time-stepping graph, allowing observation of the change in variables with respect to time ^[172]. Numerical solutions approximate as close as possible to the analytical solution with respect to these time-steps. Therefore, the accuracy of the final solution is dependent upon the size of the time steps i.e. smaller time steps will give a solution more closely linked to the analytical solution. However, many iterative calculations are required for better accuracy; as the time steps decrease, the number of iterative calculations increases. The latter condition highlights the trade-off between time and accuracy for numerical and analytical solutions. However, modern advances in computing speed have greatly leaped the practicality of solving PDE's numerically. Currently, there are various numerical methods used to solve PDE's such as the finite volume method (FVM), the finite difference method (FDM) and the finite element method (FEM). For the purpose of this study, the FEM has been selected for further discussion.

3.4.2 *History of the finite element method*

Although the development of methods to solve PDE's can arguably be traced back as far as the late 16th Century ^[173], a paper by Courant et al. in 1928 ^[174] detailed the considerations for time-dependent PDE solutions. Furthermore, in 1943 R. Courant utilised the Rayleigh-Ritz method of minimisation of variational calculus and numerical analysis to deduce approximate solutions for vibrational systems ^[175, 176]. Prager and Synge used triangular elements to solve a 2D elasticity

problem using the hypercircle method in 1947 ^[177]. The works by R. Courant et al. were extremely influential on the first FEA computer software developed by the European and American aircraft industries in the 1950's, using expensive, large mainframe computers ^[178]. However, in 1955 Argyris published work on energy methods in structural analysis, thus creating the force method of FEA ^[179]. Moreover, in 1956 a paper on the stiffness and deflection of complex structures by M. J. Turner et al. ^[180] established a wider definition of numerical analysis for PDE's. R.W. Clough first used the term "Finite Element Method" in 1960 ^[181]. By the early 1970's, FEA was limited to expensive mainframe type computers only available to heavy industries such as automotive, aerospace, defence and even nuclear. However, the introduction of personal computers in the 1980's provided wider access to FEA software from numerous vendors.

3.4.3 *Theory and Requirements of the Finite Element Method*

The underlying theory of FEA is a selection of discrete PDE's defined at nodes that form a mesh of elements across a geometry. FEA software reduces the PDE's governing the underlying physics of the model into a series of trial functions to be evaluated at nodal points defined by the mesh ^[182]. The result is an approximation of stress, strain or displacement, at any nodal point or element or across the structure. Such an interpretation is a wide generalisation. However, it is highly flexible in terms of application and can have good practical value. In order to highlight the theory of FEA, a generalised solution for static linear-elastic isotropic problems is discussed in this section. Generally, it is common to determine the structural behaviour of a body that is in static equilibrium, indicating that the sum of all forces acting on the body equal zero. Therefore, in order to conduct FEA the following pre-requisites must be met ^[183]:

- The material properties are known e.g. the tensile modulus, yield stress and Poisson's ratio
- The geometry of the body in its unloaded state is fully defined (R). The latter is usually imported into the software in the form of a CAD file.
- The elastic constants (C_{ijkl}) of the solid are known.
- The boundary conditions i.e. the magnitude and distribution of the force (b) and/or displacements ($u^*(x)$) on a portion ($\delta_1 R$) of the body in its unloaded state are accurately defined.

The latter pre-requisites are sufficient if thermal effects acting on the body are negligible, the material is isotropic, the displacements are relatively small and there is no contact with other bodies. The FEM begins by summarising the following governing equations of the model to solve for the displacement field (u_{ij}), stress field (σ_{ij}) and strain field (ε_{ij}):

- The strain-displacement equation ^[184] $\rightarrow \varepsilon_{ij} = \frac{1}{2} \left(\frac{\partial u_i}{\partial x_j} + \frac{\partial u_j}{\partial x_i} \right)$ **Equation 3.**
- The elastic stress-strain law ^[185] $\rightarrow \sigma_{ij} = C_{ijkl} \varepsilon_{kl}$ **Equation 4.**
- The static equilibrium of stresses equation ^[186] $\rightarrow \frac{\partial \sigma_{ij}}{\partial x_i} + b_j = 0$ **Equation 5.**
- The boundary conditions on displacement $\rightarrow u_{ij} = u_{ij}^*$ on $\delta_1 R$ **Equation 6.**

PDE's 3 and 5 are generally solved using the principle of virtual work ^[187]; this re-defines the equations in integral form for easier manipulation. The main objective of the FEM is to calculate the displacement within a body subjected to external forces; if one were to visualise a solid body undergoing deformation due to external load, a suitably defined point on the body will move with the application of the load. The displacement vector ($u^*(x)$) will define the motion of this point at position x in the undeformed body. Once $u^*(x)$ has been determined, the distribution and magnitude of stress-strain fields across the entire body can be deduced.

3.4.4 *Finite element model development*

FEA may be conducted in three stages respectively; FE model development, analysis and refinement. Due to the wealth of options within FEA software, only a selection of analysis types, model refinement techniques and material properties used for investigations within this thesis are elaborated upon. Primarily, two types of analyses can be conducted within FEA software; static linear-elastic and non-linear. Static linear-elastic analyses are suitable for many simple to intermediate engineering problems. However, static linear-elastic simulations are highly idealised rendering them unsuitable for more complex scenarios. For example, the static term describing linear-elastic simulations indicates the entire load is applied at one instance. Therefore, a static linear-elastic analysis would not be suitable for vibratory or sinusoidal loading scenarios.

Non-linear analyses are more suitable when excessively large stresses/strains (beyond the yield stress of the material) and complex loading scenarios are anticipated. However, designing non-linear FE models requires significantly more time, information and careful representation of the loading scenario relative to static linear-elastic simulations. Furthermore, when designing non-linear FE models it is crucial to avoid the complexity of the model reaching the complexity of the problem in the physical world. To reduce simulation times, numerical elimination methods (such as Gaussian elimination) may be used for the analysis of FE models with thousands of functions. However, when the amount of calculations reaches several million, the non-linear solutions become too expensive in terms of time and computing memory. In such circumstances special iterative methods such as the Newton-Raphson method are used, although the solution time of these methods depends on the required accuracy ^[188]. Overall, it is clear that identifying a suitable

balance between FE model simplification and accuracy is critical for reducing simulation times, a judgement made better by skilful users who have a thorough understanding of the methods, boundary conditions and limitations of FEA.

3.4.4.1 *Static linear-elastic analyses*

Static linear-elastic FEA offers quick solution times at the expense of highly idealising the model; in essence, such models assume the structure and material to obey Hooke's Law, whereby the stress-strain response of the material is linear and the structure returns to its original state upon removal of the load ^[189]. The tensile modulus of a material is the gradient of its tensile stress-strain response up to the yield point. Beyond the yield point is the onset of non-linearity. Therefore, static linear-elastic simulations are suitable when stresses below the yield point of the material are anticipated. Generally, engineering designs require a high factor of safety to ensure that the stresses operate well below the yield point of the material. Therefore, static-linear elastic simulations are common procedure for FEA. Consequently, the matrix function describing the static linear-elastic assumption is:

$$\{F\} = [K]\{u\} \quad \text{Equation 7.}$$

Where:

$\{K\}$ = Global stiffness matrix of the structure

$\{F\}$ = External force matrix

$\{u\}$ = Displacement matrix

In order for the static linear-elastic assumption to be valid, the loads must be constant in magnitude and distribution ^[190], the applied stress should be lower than the yield stress of the material and the boundary conditions should remain constant from the instance of loading to the final deformed shape. Furthermore, static linear-elastic analysis assumes the entire load is applied at one instance and the stiffness of the structure is independent of any load or displacement ^[191]; a geometric stiffening phenomenon can occur when a structure is loaded resulting in decreased displacement with increased load, such factors are not fully accounted for in static linear-elastic FE models. However, the static linear-elastic assumption may be used in circumstances where steady state and constant magnitude are observed; for example, the structural response of a body travelling at a constant velocity or acceleration can be modelled as static. The static assumption loses its validity when, for example, the structure's stiffness causes the load to be removed before the full response can be gauged or when the load excites vibrations within the structure. Technically speaking, a static linear-elastic situation seldom exists in the physical world. However,

it is reasonable that such an assumption may give an accurate-enough indication of a structure's response.

3.4.4.2 *Non-linear analyses*

The behaviour of materials beyond the yield point is typically characterised by the tensile stress-strain response, which is required by FEA software for non-linear analyses. Equation 7 is deemed adequate for linear materials such as metals. For non-linear materials such as PP, PE and other semi-crystalline thermoplastics with a glass transition temperature (T_g) below ambient temperature, Equation 7 must be generalised. A whole branch of continuum mechanics is dedicated to the solutions of such problems ^[192]. During non-linear FEA, the material is assumed to be elasto-plastic; it deforms both elastically and plastically depending on the level of stress. However, this is a challenge to determine for plastics due to their non-linear behaviour, even below the yield point ^[193]. Non-linear FEA correctly assumes the stiffness of the structure to be load dependent; the deformation due to load consequently affects the overall stiffness of the structure. Therefore, a non-linear analysis may be applicable to structure's that undergo very small deflections due to a geometric stiffening effect, countering the notion that non-linear analysis is for large displacements only ^[194]. Changes in load type and direction due to deformation of the structure may also be accounted for during non-linear FEA. Overall, non-linear FEA can account for non-linearity in the material, the geometry and the boundary conditions (e.g. temperature, loads or constraints). Such parameters undoubtedly have an effect on the mechanical response of a physical structure. Boundary condition non-linearity refers to the non-linear behaviour of loads or constraints. For example, if the magnitude of stress located near the support points of a structure is beyond the yield stress of the material, non-linear FEA may be employed ^[195].

During non-linear FEA, time dependent loads are incrementally applied to a structure up to the maximum load for a theoretically more accurate solution (e.g. 10 N s^{-1} to a maximum of 1 kN); the values of load at each time increment (load-time) are used to solve the nodal functions of deflection. The resulting deflection values are then converted into load values for input into the nodal functions of deflection at the next load-time. FEA software uses these values of load and deflection to calculate nodal stress and strain at each load-time and provides a final solution after the final load-time. Iterative methods such as the Newton-Raphson technique are used to conduct non-linear FEA ^[196]. Actual stress-strain curves from physical testing are typically used as a reference by FEA software to calculate stress-strain realistically for non-linear FE models. Unlike static linear-elastic FEA, non-linear FEA can optimise the load-time increment by observing when the previous load increment solution is within 98% of the next load increments solution. However,

this may be user specified. The latter process is known as solution convergence. Therefore, the timing of the load increment should be sufficiently optimised to observe solution convergence [197].

3.4.5 *Finite element model refinement*

The fundamental purpose of FE model refinement is to increase mesh quality to reduce experimental error. FEA software calculates stress and strain at nodal points defining the mesh. Therefore, it is crucial that the mesh is properly defined. Determining the exact number, size and shape of elements to optimise a FE model is not possible. Moreover, refining a mesh to ensure low approximation errors and avoid long solution times simultaneously can be a difficult and time-consuming task [198]. However, the application of mesh refinement is certainly individual to the boundary conditions of model. Therefore, the importance of a good mesh for FEA cannot be overemphasized [199]. Conversely, over-refining the mesh may increase simulation time considerably for little gain in accuracy. To simplify the refinement process, the mesh can be iteratively refined until the solution of the model converges to a user specified limit e.g. the elemental solutions of stress or strain are within 98 % of the equivalent nodal solutions, the latter is called relative strain error convergence. Other common convergence options for FEA are:

- **Strain energy convergence** - The strain energy of the model is calculated by summing the strain energy of the elements. Strain energy convergence is a better criterion for optimizing an FEA mesh; the average strain energy of the elements is influenced by mesh size and elemental order, rather than structural geometry.
- **Stress convergence** – Convergence occurs when the solutions of stress reach a limiting value. Convergence is difficult to achieve with this method if stress concentration points are observed. The concentrated stress simply increases with the increase in mesh density. Some degree of mesh coarsening (reduction of nodal points) at points of stress concentration can reduce this effect.
- **Deflection convergence** - nodal deflection values are used for the convergence criterion.

Mesh refinement may be automated (known as adaptive meshing) or manually conducted by skilful users [200]. Adaptive mesh refinement usually increases the number of elements in areas of interest by decreasing their size. A FE mesh is characterized by the local mesh size “H”, the element order “P” and the nodal positions “R” for the solutions of stress or deflection across the mesh [201]. The H and P mesh refinement methods are extensively implemented within FEA

software. However, the implementation of each method can be different depending on analysis conditions. Adaptive mesh refinement methods started with H-refinement before Babuska et al. [202] introduced P-refinement and HP-refinement methods. H-adaptive meshing refines the mesh size by subdividing the elements. However, H-adaptive mesh refinement does not modify the polynomial order of the elements [203]. On the other hand, the algorithm for H-adaptive mesh refinement is relatively easy to apply on complicated geometries. The basic procedure of H-adaptive mesh refinement by element subdivision is portrayed in Figure 7.

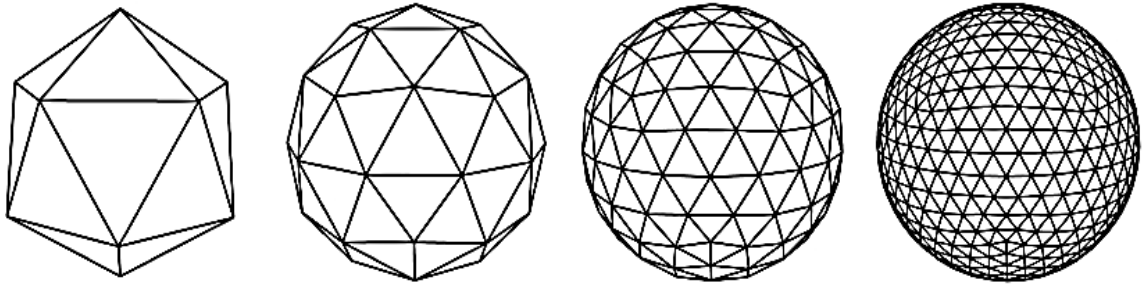


Figure 7. The basic subdivision of triangular elements during H-adaptive mesh refinement [204]

P-adaptive mesh refinement is simpler in mesh construction than H-adaptive. P-adaptive maintains a fixed mesh but increases the polynomial order of the nodal functions at each element; a nodal function of stress or deflection is affected by the number, position and properties of surrounding nodes. If there are several nodes within a small area of a structure's mesh, the resulting nodal functions will contain several algebraic terms, becoming polynomials. A larger number of algebraic terms increases the order of these polynomials, known as the element order. An example of this is illustrated in Figure 8.

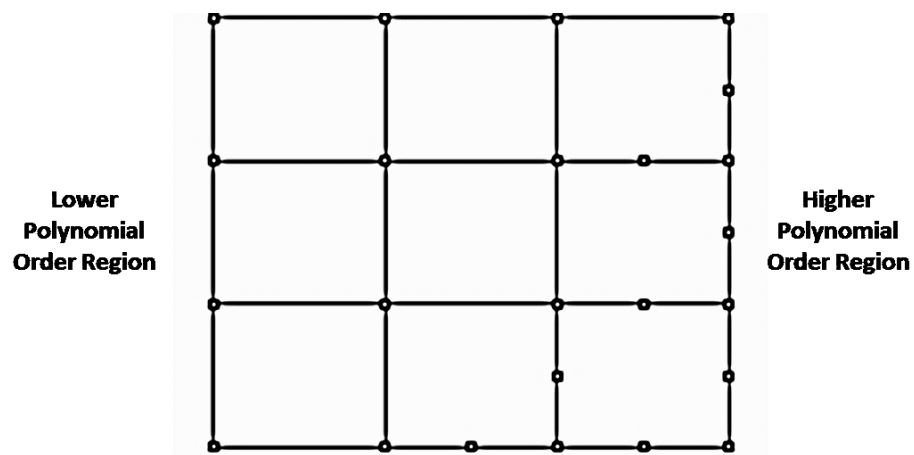


Figure 8. Regions of both lower and higher polynomial orders within a 2D FE mesh. The polynomial order of the nodal functions increases with increasing node count [205].

P-adaptive mesh refinement is particularly useful for complex elements that deform due to both compression and tension ^[206]. The HP-adaptive mesh refinement type combines the approach of both H and P-adaptive meshing ^[207]. R-adaptive mesh refinement maintains the number of nodes in the original mesh. However, the positions of these nodes are relocated to where better resolution is required ^[208]. All three methods (H, P and R-adaptive) have individually achieved success in FEA studies ^[209, 210, 211]. However, the consideration of all three adaptive mesh refinement methods (H, P and R) should be made during FEA. The accuracy of FEA is heavily dependent on the mesh size selected; a smaller mesh size can minimise the error incurred by extrapolating data between nodes. On the other hand, a fine mesh increases the computational cost of the analysis in terms of simulation time. Therefore, a skilful FEA user should have adequate experience and knowledge with each mesh refinement method to understand its application. To conclude, the following steps summarise the basic procedure of FEA software:

1. A 2D or 3D structure is graphically divided into small elements (sections or regions of shape).
2. A mechanical stress-strain response is defined at the elements by a set of PDE's. The PDE's are converted into polynomial functions suitable for a computer-aided solution.
3. The element functions are combined and a global structural function is obtained.
4. The load and boundary conditions are then incorporated in the global function
5. The individual functions are solved and a deflection for each node is calculated.
6. The deflection values are then inserted into the global function to solve for overall stress and strain of the structure.
7. Refinements are made to the original model, if necessary.

3.5 Finite Element Analysis of Rotomoulded Parts

In the context of RM, little published research regarding FEA is available ^[23]; the FEA of rotomoulded parts often remains confidential in the RM industry, creating an environment that promotes the retention (rather than the dissemination) of vital experience and data with regards to FEA. The RM industry mostly outsources FEA to external consultancies, understandably due to their own lack of expertise in using such software. Furthermore, if any preliminary design revisions resulting from FEA were made, rotomoulders can defend claims of negligence if a part fails in the field ^[212]. It is apparent that the accuracy of FEA software is dependent on the credibility of input data (material properties, geometry and load scenario). Parameters such as geometrical dimensions, material properties and model assumptions play an important role in the accuracy of FEA. With this in mind, it is appreciated that the geometry of rotomoulded products vary significantly relative to injection moulded products, due to the absence of applied pressure.

Therefore, conducting FEA on large rotomoulded products (such as underground water tanks where wall thicknesses can exceed 50 mm) presents a formidable challenge to engineers due to substantial differences between the FE model and the physical rotomoulded product. These differences are:

- The variation in wall thickness.
- The complex non-linear behaviour of PE at low strains.
- The lack of experimental data regarding the compressive behaviour and Poisson's ratio of PE.

Such factors are not entirely considered during the FEA of rotomoulded parts, leading to instances of unexpected behaviour in the field. Therefore, identifying the critical factors affecting the use of FEA for rotomoulded parts is explored within this thesis, in order to develop an inclusive FE modelling procedure. Consequently, the extensive use of FEA in the modern engineering world exemplifies the importance of developing a numerical material property database for the proposed new particulate-filled PE composite materials. The latter materials should instil confidence in rotomoulders who are expected to use them via accurate FEA approximations of their performance. Combining physical test data from rotomoulded parts with FEA was the selected approach; a venture seemingly unheeded in the RM industry today. Data from the material specification sheets of PE suppliers are often inappropriate for FEA and vary considerably. A common example of this is the tensile modulus of PE; due to the non-linearity of PE's stress-strain response, the tensile modulus is an over-estimation of its true capability. A high modulus composite material accompanied by accurate numerical material property data for FEA could expand the current application envelope for RM. The latter formed the rationale behind the composite development and FEA investigations in this thesis.

3.6 Summary of Literature Review

To conclude, the following points of interest from the literature review are summarised:

- RM has progressed considerably (and is continuing to progress) from a relatively primitive technique to a method highly regarded by manufacturers for complex, load bearing structures.
- PE is the most common material used in modern day RM products because of its cheap cost, good toughness and suitable melt flow properties, relative to alternative polymer

grades. However, the stiffness limitation of PE narrows the application envelope for manufacturers.

- Fillers have been known to reduce the cost of polymer products. However, this effect is generally superseded by the reinforcing effects. Filler characteristics such as shape, size, elemental composition and aspect ratio play significant roles in determining the effectiveness of particulate-fillers as reinforcements for polymers.
- Optimisation of particulate-filled polymers is only possible when the filler particles have been treated with chemical agents to increase the strength of adhesion between the polymer matrix and the filler particle (filler-matrix interaction) and disperse the particles evenly. The latter additives are known as coupling agents and dispersion agents respectively.
- PE is well known to have low polarity (chemically stable). Therefore, it is somewhat tedious to find a coupling agent to functionalise the PE matrix for better compatibility with the filler particle surfaces; this can increase matrix-filler interaction and thus increase the mechanical performance of the resulting composite.
- RM is a zero-shear process (unlike many conventional plastics moulding processes such as injection or blow moulding). The lack of pressure induced flow of the polymer melt challenges particulate-filled polymer composite materials; the melt flow properties of the resulting composites are often reduced.
- Computer aided engineering (CAE) technologies such as computer aided design (CAD) and finite element analysis (FEA) offer the capability to build, optimise and validate engineering designs within a virtual environment.
- In the context of RM, manufacturers and their clientele use CAE softwares such as FEA and CAD to estimate whether load-bearing parts will be within the overall dimensions specified, withstand the loads required and endure the intended lifecycle.
- FEA is ultimately a numerical approximation for solving boundary value and solid mechanics problems. It is the most extensively used numerical analysis method in mechanical engineering practice. The mechanical response of structures can be analysed using FEA software with relative ease.

- The fundamental concept of FEA is the assumption that any continuous quantity such as stress or deflection can be numerically approximated by a discrete mathematical model composed of iterative partial differential equations (PDE's).
- FEA software was first developed in the 1950's. By the early 1970's, FEA was limited to expensive mainframe type computers only available to heavy industries such as automotive, aerospace, defence and nuclear. However, the introduction of personal computers in the 1980's provided access to FEA software from numerous vendors.
- Primarily, two types of analyses can be conducted using FEA software; static linear-elastic and non-linear. Static linear-elastic analyses are suitable for many simple to intermediate engineering problems. However, static linear-elastic analyses are highly idealised for quicker solution times rendering them unsuitable for more complex scenarios.
- Non-linear FEA is more suitable when large stresses/strains (beyond the yield stress of the material) and complex loading scenarios are anticipated. However, designing non-linear FE models requires significantly more time, information and careful representation of the loading scenario. Overall, non-linear simulations can account for non-linearity in the material, the geometry and the boundary conditions.
- Identifying a suitable balance between simplification and accuracy in order to reduce simulation times is crucial; a judgement made better by skilful FEA users who have a thorough understanding of analysis methods, boundary conditions and limitations.
- The fundamental purpose of FE model refinement is to increase mesh quality to reduce experimental error. The accuracy of FEA is heavily dependent on the mesh size selected; a smaller mesh size can minimise the error incurred by extrapolating data between nodes. On the other hand, a finer mesh increases the cost of the analysis in terms of time and computer operating speed.
- Adaptive mesh refinement usually increases the number of elements in areas of interest by decreasing the size of elements. A FE mesh is characterized by the local mesh size "H", the element order "P" and the nodal positions "R".
- H-adaptive mesh refinement subdivides elements but maintains the order of the element. Moreover, the algorithm for H-refinement is easy to apply to complicated geometries. P-

adaptive mesh refinement is simpler in mesh construction than H-adaptive. P-adaptive maintains a fixed mesh but increases the polynomial order of the nodal functions at each element.

- In the context of RM, little published research regarding FEA is available. The RM industry mostly outsources FEA to external consultancies, understandably due to their own lack of expertise using such techniques.
- The FEA of large rotomoulded products presents a formidable challenge to engineers due to substantial differences between the FE model and the physical rotomoulded product, such as wall thickness variation and the non-linear behaviour of PE.

4. Experimental

This section details the experimental methods used for both the development of particulate-filled PE composite materials and FEA of the rotomoulded safety step product, using numerical data from physical testing of the particulate-filled PE composite materials.

4.1 Polyethylene Grades and Coupling Agent

Material data sheets for all the polymers used in this study are available within the Appendix Section 5.

4.1.1 *Maleic anhydride grafted polyethylene (MA-g-LLDPE)*

Prior to initial investigations, the industrial sponsor Rotomotive Ltd. had developed an optimal polyethylene based formulation for the rotational moulding of dry blended composite materials containing high levels of large particle fillers. This material was in powder form and consisted of 75 % wt. Linear Medium Density Polyethylene (LMDPE) and 25 % wt. Maleic Anhydride grafted Linear Low Density Polyethylene (MA-g-LLDPE). The MA grafted in the LLDPE is a coupling agent introduced to improve the strength of interaction with fillers; the level of MA used was found by experiment to be optimum for the large particle composite application concerned. The commercial names of the LMDPE and MA-g-LLDPE used in this study are 'Revolve N250' and 'Revolve N211' respectively, they are available from Matrix Polymers Ltd. UK; Table 1 displays their properties.

4.1.2 *High density polyethylene (HDPE)*

The HDPE reference was M40060S from SABIC. It is said to have a narrow molecular weight distribution and good mouldability. Articles produced from this grade exhibit excellent impact strength, good stress crack resistance (SCR) and low warpage with a glossy finish. Table 1 also displays the properties for this particular HDPE grade.

Table 1. Properties of MA-g-LLDPE, LMDPE and HDPE.

Physical Properties	MA-g-LLDPE		LMDPE		HDPE	
	Test Standard	Value	Test Standard	Value	Test Standard	Value
Density (g cm ⁻³)	ISO 1183	0.921	ISO 1183	0.935	ASTM D1505	0.96
Melt Flow Rate (dg min ⁻¹)	ISO1133	5	ISO1133	7	ASTM D1238	4
Tensile Yield Strength (MPa)	ISO 527	11	ISO 527	16.8	ASTM D638	33
Impact Strength (J)	ARM-I	80	ARM-I	101.6	ASTM D256	69
Estimated Price (£/metric tonne)	3000		1250		2500	

4.2 Candidate Filler Particles

Material data sheets for the filler particles used in this study are available within the Appendix Section 6. The mineral fillers (see Table 2) were natural silica sand, almandine garnet and both coarse and fine fractions of alumino-silicate spheres (cenospheres and fly-ash respectively).

Table 2. Details of the filler particles used in this study.

Details	Fly-ash	Cenospheres	Garnet	Sand
Supplier	Rocktron Ltd.	Dean and Tranter Ltd.	GMA Garnet Australia	Bathgate Silica Sand
Chemical Analysis	SiO ₂ .Al ₂ O ₃	SiO ₂ .Al ₂ O ₃	3FeO.Al ₂ O ₃ .3Si ₂	SiO ₂
Shape	Spherical	Spherical	Irregular	Irregular
Density (g cm ⁻³)	2.3	0.74	4.08	2.67
Hardness (Mohs Scale)	5-6	5-6	7.5-8	6-7
Approximate Price (£/metric tonne)	750	350	250	60

4.3 Polyethylene and Filler Particle Characterisation

4.3.1 Determination of melt flow rate (MFR)

The MFR of PE grades used in this study were determined using a Ray-Ran melt flow indexer. The procedure for determining the MFR, (in accordance with ASTM D1238) was as follows:

1. A small amount of PE (ca. 4-5 g weighed on a Sartorius model AC 120 S four figure balance) was placed into the extruder barrel of the Ray Ran MFR apparatus. At the end of the extrudate barrel is a small die of approximately 2mm in diameter.
2. The PE was compressed into the extruder barrel (using a metal plunger) in 0.5 g intervals to avoid the formation of air bubbles.
3. The sample was then preheated for 5 min at approximately 190 °C.
4. A 2.16 kg piston was then placed into the barrel (on top of the PE) to introduce the shear force required to extrude the PE through the die at the output end of the barrel.
5. A sample of the melt was then taken after a period of ten minutes and weighed to give the resulting MFR (expressed as g/10 minutes or dg min⁻¹).
6. Each determination was replicated four times and an average value reported.

4.3.2 *Estimation of filler particle maximum packing fraction (MPF)*

MPF tests (essentially oil absorption tests) were carried out in order to estimate the maximum amount of filler that can be incorporated into a PE matrix. Rather than linseed oil (as would be used in a conventional oil absorption test), liquid paraffin was used as the liquid medium. Liquid paraffin is chemically very similar to PE; in fact the basic structure (mixed alkanes) is identical to PE, the alkyl chains in liquid paraffin are however much shorter. Linseed oil (mainly linolenic acid) is more polar than PE and could therefore give unsuitable data. The test involved placing a known mass of filler (ca. 1 g weighed on a Sartorius Model AC 120 S four figure balance) on to a clean white tile. Liquid paraffin was added drop-wise to the pile of filler from a burette. A palette knife was used to mix the filler and liquid paraffin mixture, making sure that it was spread into a neat pile. Just enough liquid paraffin was added to fully wet out the powder particles such that a homogeneous putty-like mass was formed whilst mixing with the spatula. The latter change in property forms a surprisingly well defined end point. Reproducibility was typically ± 0.01 % vol. Each determination was replicated three times and the average titre reported. The maximum packing fraction (MPF) was then calculated by volume and mass, using Equations 8 and 9 respectively. Equation 8 was used to convert mass into volume and vice versa, for input into Equations 9 and 10.

$$\rho = \frac{m}{v} \quad \text{Equation 8.}$$

Where:

m = Mass of powdered material (g)

v = Volumetric displacement of water (ml)

ρ = Density of material (g cm⁻³)

$$V_{pf} = \frac{V_f}{V_f + V_l} \quad \text{Equation 9.}$$

Where:

V_{pf} = Maximum packing fraction volume (between 0 and 1)

v_f = Volume of filler (cm³)

v_l = volume of liquid paraffin (cm³)

$$M_{pf} = \frac{M_f}{M_f + M_l} \quad \text{Equation 10.}$$

Where:

M_{pf} = Maximum packing fraction by mass (between 0 and 1)

m_l = Mass of liquid paraffin (g)

m_f = Mass of filler (g)

4.3.3 *Determination of filler particle densities*

4.3.3.1 *Sand, garnet and fly-ash*

The densities of sand, garnet and fly-ash were calculated directly by slowly sprinkling a pre-determined mass (ca. 200 g weighed on a Mettler model PE11 one figure balance) of each material into a measuring cylinder containing water to measure the resulting volumetric displacement. The corresponding values of mass and volume were then used to calculate the density using Equation 8. Three repeat tests were conducted and the average density and standard deviation was calculated. Candidate fillers used in this work were not porous, this is apparent in scanning electron microscope (SEM) images of the filler particles (Results and Discussion Section 5.3.1, Figures 44-48) where the filler particles have a solid non-porous surface. Fly-ash and cenosphere particles are essentially hollow spheres filled with air.

4.3.3.2 *Cenospheres*

Cenospheres float on water due to their low density relative to water. Therefore, a liquid of lower density than water was used for cenosphere density tests; petroleum ether (60-88 °C boiling range, density 0.67 g cm⁻³). Prior to conducting the test, a jar and lid were weighed using a Mettler model PE11 one figure balance. The jar was then totally filled with petroleum ether, sealed with the lid (to prevent the petroleum ether from evaporating) and the total mass of the jar, lid and petroleum ether was recorded. Next the jar was emptied, rinsed thoroughly and dried before repeating the same process again with the addition of cenospheres. The mass of petroleum ether in the jar (both with and without cenospheres) was deduced and converted to volume using Equation 8. The difference between the two measured volumes (as a result of

cenosphere addition) was then calculated; the resulting volume and known mass of cenospheres were then used to calculate the density, using Equation 8. Three repeat tests were conducted and the average density and standard deviation was calculated.

4.3.4 Verification of filler particle size distribution

Sieve analyses on the large particle fillers were conducted using a Rotap shaker, test sieves and pan. The latter equipment is a vertical stack of sieves, whereby the top sieve is of a larger size than the sieve underneath. For this investigation, the sieve sizes (in descending order from the top) were 500, 425, 300, 212, 150 and 90 μm , leading to a pan at the very bottom to collect remaining particles. The shaker is used to ensure the filler particles are effectively drawn through the sieves. The test procedure was as follows:

- Sieves were arranged in the order specified and a 100 g sample was placed into the top sieve.
- A lid was placed on the top sieve and secured to the Rotap sieve shaker.
- A 10 minute timer was set on the control pad of the sieve shaker and the start button was pressed via the analogue control panel.
- After 10 minutes, the top sieve was placed on the scale and the tare was set to zero.
- The sieve was then removed, any remaining material was cleaned and the new weight of the sieve was then recorded.
- This process was then repeated with all the remaining sieve sizes. The weights were totalled and recorded.

4.3.5 Determination of PE/filler composite densities

4.3.5.1 Densometer method

Composite PE/filler density was determined using an Ohaus Voyager Pro densometer. The densometer has a combined weighing scale and jug facility which allows the user to weigh a solid material in air and water, both of which the densometer records. The densometer then uses Archimedes principle to calculate the density, utilising the values of apparent weight in air and apparent weight in water using Equation 11.

$$\frac{\rho_m}{\rho_w} = \frac{m}{m - m_w}$$

Equation 11.

Where:

ρ_m = Density of material (g cm^{-3})

ρ_w = Density of water (g cm^{-3})

m = Mass of material in air (g)

m_w = Apparent mass of material in water (g)

4.3.5.2 Ashing method

Ashing to determine the density of melt compounded PE/fly-ash composites was conducted using a Carbolite electric oven, a glass desiccator containing silica gel beads (to absorb moisture) and ceramic crucibles. The desiccator had a valve on the lid for air pressure relief. A thin layer of petroleum jelly was applied by hand on the surface of the lid and desiccator to create an airtight seal. The following test procedure was applied:

1. The crucibles were treated in the oven for 2 hours at 860 °C to burn off any organic residues.
2. The PE/fly-ash composite samples and crucibles were weighed using a Sartorius Model AC 120 S four figure balance.
3. One crucible was filled with fly-ash and the other crucibles were filled with the PE/fly-ash composite samples.
4. All crucibles were placed in the desiccator, sealed air-tight and placed in the oven at 100°C for two hours to remove any moisture.
5. The crucibles and their contents were weighed and placed back into the oven at 800 °C for two hours to burn off the PE in the PE/fly-ash materials.
6. The remaining filler content in the crucibles were weighed. Equations 12, 13 and 14 were used to calculate composite filler content and ultimately total composite density (using Equation 15).

$$F_r = m_f / m_{fd}$$

Equation 12.

Where:

F_r = Residue fraction of fly-ash after 800 °C

m_f = Mass of fly-ash (g)

m_{fd} = Mass of fly-ash after the 100°C drying period (g)

$$M_{fc} = m_{cr}/f_r$$

Equation 13.

Where:

m_{fc} = Mass of fly-ash in composite (g)

m_{cr} = Mass residue of composite after 800 °C period (g)

f_r = Residue fraction of fly-ash

$$F_c = \frac{m_{fc}}{m_{fd}} \times 100$$

Equation 14.

Where:

F_c = Fly-ash content (% wt.)

m_{fc} = Mass of fly-ash in composite (g)

m_{fd} = Mass of composite after the 100 °C drying period (g)

$$\rho_T = \frac{1}{(m_f/\rho_f) + ((1-m_f)/\rho_p)}$$

Equation 15.

Where:

ρ_T = Total composite density

m_f = Mass of filler material (g)

ρ_f = Density of filler (g cm⁻³)

ρ_p = Density of polymer (g cm⁻³)

4.4 Blending of Filler Particles and Polyethylene to Form Composite Materials

4.4.1 *Dry blended formulations*

Composites were prepared by pre-mixing the filler and PE in the bowl of a planetary type powder mixer (Brevet model SHM2 domestic cake mixer). The total mass of the charge was 500 g weighed using a Mettler model PE11 one figure balance. Mixing took place for 10 minutes at slow speeds. The composite was finally formed in a separate compression moulding operation described in Section 4.5.

4.4.2 *Two roll milled formulations*

Blends were mixed using a Bridge laboratory two roll mill with 150 mm diameter x 300 mm long rolls. The distance between the crowns of the rolls (known as the “nip”) is adjustable. The rolls rotate at different speeds in opposing directions; the ratio of rotation speed between the front and rear rolls is the friction ratio. The polymer melt within the nip is therefore subjected to high shear stresses, which leads to dispersive mixing. The steam heated front and rear rolls were set at

137 °C and 146 °C, respectively. Corresponding steam pressures were 430 kN m⁻² and 550 kN m⁻², respectively. A friction ratio of 2 was used. Mixing was carried out by cross cutting and took between 5 and 30 minutes depending on filler type and amount. A diagram to demonstrate the two roll mills mixing process is provided in Figure 9; the PE powder is poured onto the hot rolls (when the nip is closed) and rotation is initiated. A band of polymer melt then forms on the hotter front roll and a rolling bank of polymer melt forms above the nip. Once the band is formed, filler particles can be introduced to the rolling bank. Distributive mixing is effected by cross-cutting the band of polymer melt, this introduces material from the rolling bank to the nip. After incorporation of all the ingredients, the mixes were sheeted off by cutting quickly across the band and taking it off as a “hide” where possible. The hide was left to cool on a clean stainless steel bench.

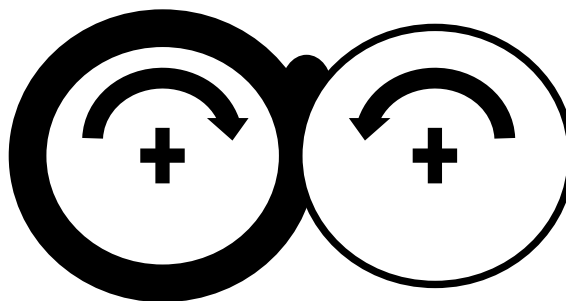


Figure 9. Diagram of two roll mill (side view). The PE melt sticks to the hotter roll (on the left) during processing. Notice the rolling bank of polymer within the “nip”.

4.4.3 *Twin screw extrusion compounded formulations*

Blends were compounded using a Thermo-Prism 24HC modular 28:1 L:D ratio twin screw extruder (TSE). The screw speed was generally set between 500 and 900 rpm, the head pressure between 40-60 bar and the temperature between 160-230 °C, depending on the type of filler and amount. The TSE was fitted with a three-hole die and the vacuum vent facility was used. Figure 10 shows a side view schematic of the TSE.

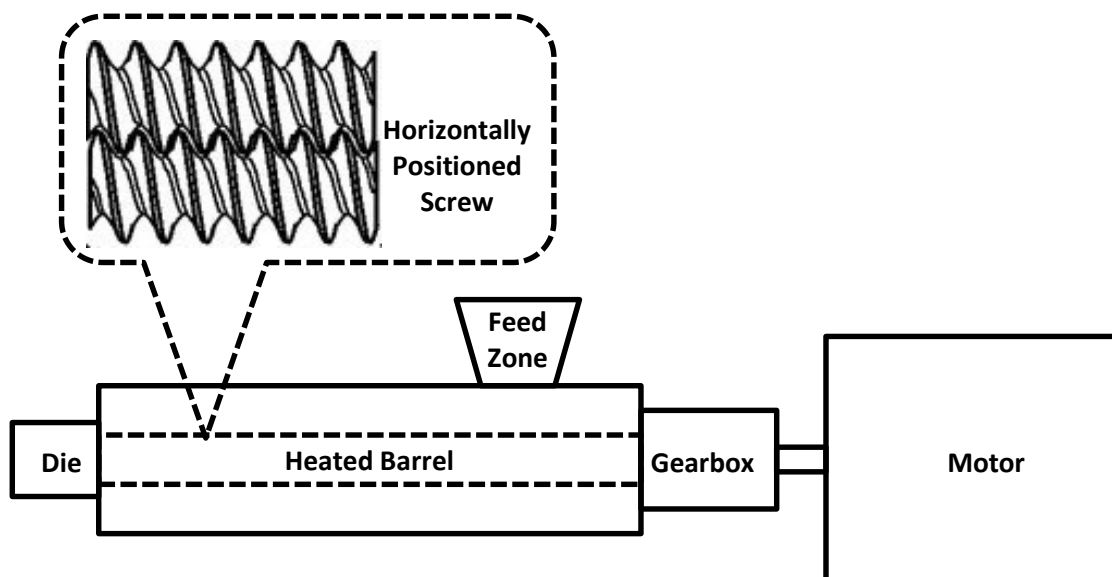


Figure 10. Schematic of the twin screw extruder (side view).

The PE and filler particles were loaded into separate Brabender Technologie feeders; a volumetric feeder was used for the polymer and a gravimetric feeder was used for the filler material, at the feed zone of the screws. The combined output rate was between 12 and 14 kg hr⁻¹ and the feeders were individually programmed with the correct output rate to give the desired filler content. The extrudate strands (from the die) were passed through a cooling trough (2.5 m long x 0.28 m wide) containing water at 18-20 °C to the pelletiser integrated at the end of the cooling trough. The benefits of the blending techniques investigated in this study (dry blending, two roll mill and TSE) are discussed in detail within the Results and Discussion Sections 5.4, 5.5 and 5.6 within this thesis. Conclusions arisen from physical testing to verify the effectiveness of each method are also detailed within these sections. A full list of the compounds prepared by two roll mill blending and twin screw extrusion are available within the Appendix Section 1. The corresponding Results and Discussion Section numbers for these compounds are also provided.

4.5 Moulding of PE/Filler Composites

4.5.1 *Composite plaques prepared at Manchester Metropolitan University*

Plaques were compression moulded in a 250 mm x 200 mm x 4 mm mould frame using a 500 kN Bradley and Turton hydraulic press fitted with electrically heated platens. The moulding was cooled by transferring the filled mould to a 500 kN Francis Shaw hydraulic press fitted with water cooled (15 °C) platens. The moulding cycle was as follows:

1. 500 g of the composite mix/pellets were placed within the frame mould which had been pre-treated with Frekote 700-NC mould release agent and then pre-heated in the electrically heated press for 2 minutes.
2. The filled frame mould was then placed into the electrically heated press and the platens were closed such that the top plate of the mould fully contacted the top platen. The contents of the mould were then allowed to heat through for 5 minutes before fully closing the mould to a maximum hydraulic line pressure of 100 kN. Considering the area of the mould is 0.05 m², the maximum pressure exerted on the polymer melt is 1.96 MPa. However, it has to be appreciated that once a frame mould is closed no further pressure can be applied to the polymer melt in the mould.
3. After a period of ten minutes, the filled mould was removed from the hot press and placed into the water cooled press, the platens were quickly closed and cooling continued for 10 minutes.
4. The moulding was then removed from the mould frames using a rubber mallet (if necessary).

Tensile (ASTM D638), flexural (ASTM D790) and impact test pieces were cut from the composite plaques using an OMAX water jet cutter, using the built in CAD package within the control system of the machine. The water jet cutting process is a form of micro-erosion, it works by concentrating an extremely large volume of water through a small orifice in a nozzle, producing a high pressure jet of water (ca. 600 MPa) containing abrasive particles to accelerate rapidly and impact the surface to be cut. The width of the cut is 0.6 mm. The principle benefit of the high pressure water cutting process is that it does not generate heat on the cutting edge of the material due to the part being submerged in water, leaving a smooth finish with minimal defects. Dimensions were programmed to be 10 mm x 100 mm for the flexural and impact specimens with the thickness varying between 4 and 6 mm (depending upon filler type and content). Individual specimen dimensions were measured to the nearest 0.1 mm before any testing took place. Water jet cut test specimens were dried in a Carbolite electric oven at 50 °C for 3 hours to ensure all composites had the same thermal history and to reduce any possible adverse effects from the plaques being submersed in water during the cutting process.

4.5.2 Composite plaques prepared at Rotomotive Ltd.

Plaques were compression moulded using a 200 mm x 180 mm x 4 mm frame mould at Rotomotives facility in Northampton, UK. Two Halfords model hand pumped 4 metric tonne hydraulic bottle jacks were used to press the custom made platens together for each press. One

had heated platens set at 230 °C and the other was used as a cooling platen (with no integrated cooling system). The moulding cycle was as follows:

1. Composite pre-mix was added to the pre-heated mould frame treated with Frekote 700-NC mould release agent and the top plate placed on top of the pile of pre-mix.
2. The filled mould was then placed into the hot press and the platens closed to a force of 39 kN, considering the projected area of the mould, the maximum pressure exerted on the polymer melt was approximately 1.08 MPa.
3. After a period of ten minutes, the filled mould was removed from the hot press and placed into the cold press and quickly closed.
4. When sufficiently cooled, the moulding was removed from the mould frame using a rubber mallet (if necessary).

Whilst the pressure exerted on the polymer melt (just before mould closure) by the press at Manchester Metropolitan University is almost double that of the press at the Rotomotive facility, it has to be appreciated that for frame moulds the estimated moulding pressures are essentially meaningless as no further pressure can be exerted after mould closure. Flashing of the mould will cause the pressure to drop below the estimated value. Therefore, when using a frame mould, the clamping force will have insignificant effect on composite properties. At the Rotomotive facility, Tensile (ASTM D638) and flexural (ASTM D790) test pieces were punched from the composite plaques using custom made metal die punches and hydraulic press. Specimens manufactured at the Rotomotive facility were not tested in Charpy impact mode.

4.5.3 Injection moulding of PE/fly-ash flexural test specimens

PE/fly-ash flexural test pieces (adhering to ASTM D790) were injection moulded using a Battenfeld model BA230CD+ injection moulding machine. TSE compounded PE/fly-ash composite pellets were placed in the hopper at the feed throat of the machine. The melt temperature was between 190-200 °C and the clamp pressure was between 6-8 MPa, dependent upon fly-ash content. Moulded flexural test pieces were ejected into a box underneath the machine. Spurs were cut off the flexural test pieces using pliers.

4.5.4 Bench-scale rotational moulding of PE/fly-ash rectangular test boxes

Small rectangular box test mouldings made using various formulations of compounded PE/fly-ash were rotomoulded using a Roto-Lab model Roto-Sampler machine (Figure 11).



Figure 11. Rotomoulded PE/fly-ash rectangular box test moulding (front view)

The dimensions of the rectangular box test mouldings were approximately 155 mm length x 50 mm height x 40 mm width. The peak internal air temperature of the mould during the heating cycle was between 188-244 °C, recorded using a heat sensitive label. The heating cycle took typically between 15 minutes and the cooling cycle took typically between 45 minutes, dependent on fly-ash content. The following step-by-step procedure was used to operate the rotomoulding machine:

1. The oven was set to the required temperature via the analogue control panel of the machine and allowed to pre-heat.
2. The mould was charged with material (in powder or pellet form)
3. The mould was mounted securely onto the arm in the oven of the machine.
4. The heating cycle was set via the analogue control panel of machine.
5. A heat sensitive label was attached inside the mould and a breather pipe (to ensure moulding at ambient pressure) was inserted into the mould breather hole.
6. Rotation of the machine arm was initiated via the control panel and the oven door was closed.
7. Upon completion of the heat cycle (signified by an analogue timer), the oven door was opened and the oven air temperature was measured via the analogue display of the machine, the arm was then allowed to cool whilst rotating.
8. At 100 °C, the mould was dismantled from the arm and cooled using a domestic fan
9. The oven door was closed and allowed to preheat for the next moulding.
10. Once the mould had cooled below 50 °C it was opened and the moulding was removed by hand. The moulds inner surface was then cleaned to repeat the process.

Shot charges for the rectangular box test mouldings were in pellet form. Shot weights were calculated based on a 3 mm target wall thickness (to conform to the box's original dimensions) using Equation 16.

$$M_s = at\rho \quad \text{Equation 16.}$$

Where:

M_s = Shot charge mass (kg)

a = Surface area of part (m²)

t = Intended wall thickness (m)

ρ = Density of material (kg m⁻³)

4.5.5 *Commercial-scale rotational moulding of unfilled PE and PE/fly-ash safety steps*

Safety steps (Figure 12) were rotomoulded using a 1981 ORME 10-arm 6-plate single shuttle machine fitted with a K-paq temperature logger for process monitoring. The peak internal air temperature of the mould during the heating cycle varied between 170-215 °C and took typically between 15-35 minutes. The cooling cycle took typically between 60-90 minutes. Both heating and cooling cycle times were dependent upon material type. The following step-by-step procedure was used to operate the machine:

1. The oven was set to the required temperature via the analogue control panel of the machine and allowed to pre-heat.
2. The safety step mould and temperature logger were then mounted onto the arm of the machine in the cooling station.
3. Cooling and heating cycles were then set via the analogue control panel of machine.
4. The safety step mould lid was opened, charged with material (in powder or pellet form) and clamped to close.
5. A breather pipe (to ensure moulding at ambient pressure) was inserted into the mould tool breather hole along with the thermocouple for the temperature logger.
6. Rotation of the machine arm was initiated via the control panel of the machine and the oven door was opened.
7. The rotating arm was moved into the oven via the analogue control panel of the machine for the heat cycle.
8. Upon completing the heat cycle (signified by a ringing bell), the oven door was opened and the arm was moved back into the cooling station and allowed to cool whilst rotating. Ceiling mounted fans above the cooling station were running,

however, due to the heat generated by the nearby oven, the cooling station air temperature was approximately 37 °C.

9. Once cooled, the mould tool was opened and the moulding was gently removed using a crowbar.
10. The moulds inner surface was wiped with a damp cloth to remove any remaining particles and charged with material again to repeat the process.

Replicate steps were cut in half (lengthways) 24 hours after production for wall thickness measurements in the corners and the mid-point of the top and bottom surfaces (Figure 13).

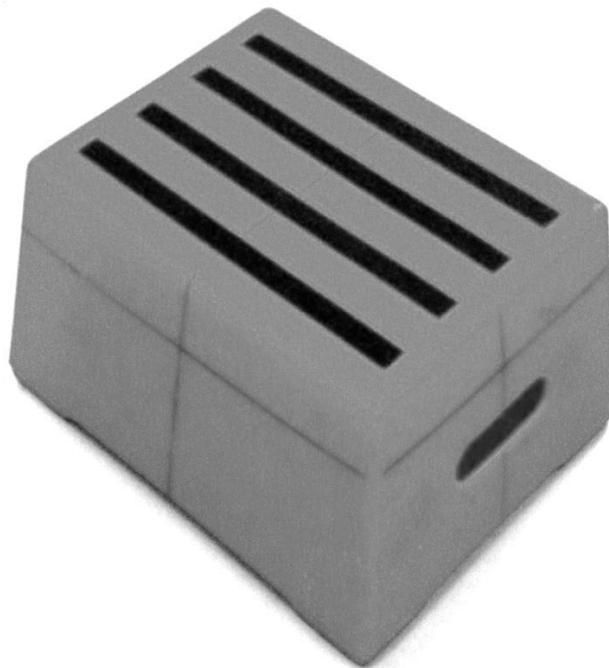


Figure 12. The rotomoulded safety step. The overall dimensions of the safety step were approximately 485 x 280 x 195 mm.

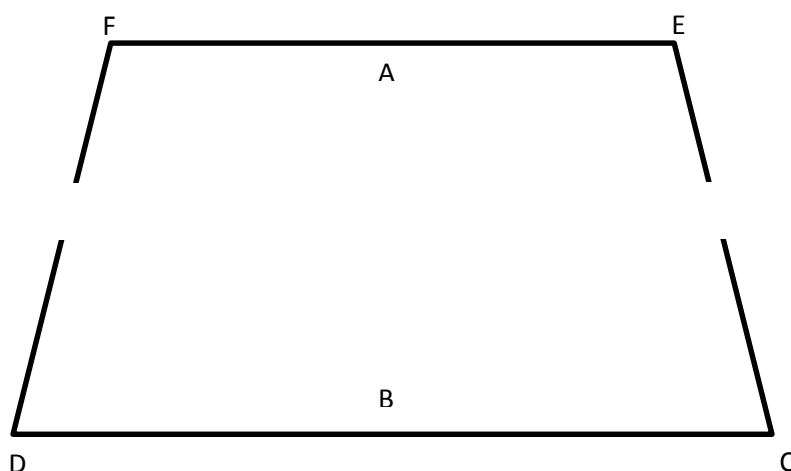


Figure 13. Rotomoulded safety step wall thickness measurement points. A and B are the mid-section points. C, D, E and F are the corner points. The safety step handle cut-outs are represented by the gaps in the left and right sidewalls.

4.5.5.1 Unfilled PE safety steps

Three commercial PE grades supplied by Matrix Polymers Ltd. in powder form were used to mould all of the unfilled PE safety steps; Revolve N250 (LMDPE), N307 (HDPE) and M601 (super-linear HDPE). The N-250 LMDPE is the original commercial safety steps PE grade; it is considered to have a wide processing window, excellent mouldability and good impact strength. N-307 HDPE boasts excellent impact strength and is especially suitable for large tanks. M601 “super-linear” HDPE has both high stiffness and toughness, making it ideal for leisure marine products such as kayaks and boats. A selection of material properties for these PE grades is available within Table 3, the shot charge weights of the unfilled PE safety steps were calculated using equation 16.

Table 3. Properties of LMDPE, HDPE and super-linear HDPE used for rotomoulded safety steps

Physical Properties	LMDPE		HDPE		“Super-Linear” HDPE	
	Test Standard	Value	Test Standard	Value	Test Standard	Value
Density (g cm ⁻³)	ISO 1183	0.935	ISO 1183	0.939	ISO 1183	0.949
Melt Flow Rate (dg min ⁻¹)	ISO1133	7	ISO1133	3.5	ISO1133	3.5
Tensile Yield Strength (MPa)	ISO 527	16.8	ISO 527	17.7	ISO 527	21.4
Impact Strength (J)	ARM-I	101.6	ARM-I	108	ARM-I	118

4.5.5.2 PE/fly-ash safety steps

PE/fly-ash composite safety steps were moulded at 0, 12.5, 25 and 50 % wt. fly-ash loading (Table 4). The PE grade used for PE/fly-ash composites was in powder form and consisted of 75 % wt. LMDPE and 25 % wt. MA-g-LLDPE; refer to Experimental Section 4.1 for details this PE blend.

Table 4. PE/fly-ash composite safety step materials

MA-g-LLDPE/LMDPE (% wt.)	Fly-ash	
	% wt.	% vol.
100	0	0
87.5	12.5	7.2
75	25	14.4
50	50	28.8

The shot charge weight of the composite PE/fly-ash safety steps were in pellet form and were calculated by volume using Equation 8, based on the 5 kg weight of the original safety step at 7 mm nominal wall thickness. A total composite density for the PE/fly-ash composite materials was calculated using Equation 15, for input into Equation 8.

4.6 Measurement of Mechanical Responses

Examples of how raw test data translated into the properties presented in this thesis are available within the Appendix Section 2.

4.6.1 Tensile Testing

Tensile testing to failure was carried out in accordance with ASTM D638 using a Hounsfield H10KS tensometer fitted with a 10 kN load cell. The ambient temperature was 23 °C (± 1 °C); this was measured using a thermocouple temperature probe situated close to the tensometer. Cross head speed was 50 mm min⁻¹. Low strains were measured using an LVDT (the Hounsfield 100s extensometer) and higher strains measured using the integrated 100 R extensometer. Gauge length was 50 mm. The specimens were clamped using manually tightened grips. Before testing, the sample dimensions were measured to the nearest 0.1 mm using a digital calliper. After collection of the data, the raw load - deflection data points were exported to MS Excel for further processing.

4.6.1.1 Determination of tensile parameters from the raw data

The tensile modulus and stress at yield values were calculated using the Hounsfield Q-Mat software as part of the test routine selected. Modulus values generated by the Q-Mat software

were checked via linear regression of the raw data and values were found to be similar to those generated by the software. 8 replicate tensile samples of each material were measured; a maximum of three outlier results were removed for each parameter to give the five closest values. Averages and standard deviations were calculated using the five closest values obtained for each material. It is appreciated that, in a selection of graphs from the results and discussion section of this report the standard deviation error bars are small relative to the size of the data point marker, giving the impression that they are absent. However, standard deviation was calculated throughout this study. Therefore, this data is tabulated within the Appendix Section 3 for selected plots; the relevant table number is provided in the Results and Discussion Sections.

4.6.2 *Flexural testing*

Flexural testing (in three point bend mode according to ATSM D790) was carried out to 10 mm deflection using a Hounsfield H10KS tensometer fitted with a 1 kN load cell. The ambient temperature was 23 °C (± 1 °C); this was measured using a thermocouple temperature probe situated close to the tensometer. The span between the sample supports was 64 mm, crosshead speed was 5 mm min⁻¹ and a 0.05 N preload was applied before collecting data. Force and crosshead displacement were recorded up to failure and the crosshead auto-returned to the start position.

4.6.2.1 *Determination of flexural parameters from the raw data*

The raw load deflection data from the three point bend tests was first converted in to stress (in outer fibre) versus strain (in outer fibre) data using equations 17 and 18 respectively. Calculations were performed using MS Excel. The parameters determined from flexural stress-strain data were the secant modulus at 1 % strain ($E_{sf(1\%)}$), the flexural modulus (E_f) and the flexural stress at 10 mm deflection, yield or break (E_σ).

$$\sigma_f = \frac{3PL}{2bd^2} \quad \text{Equation 17.}$$

Where:

σ_f = Stress in outer fibre at mid-span

P = Load at a given point on the load deflection curve

d = Depth of tested beam

b = Width of tested beam

L = Support span

$$\varepsilon_f = \frac{6Dd}{L^2} \quad \text{Equation 18.}$$

Where:

ε_f = Strain in the outer surface

d = Depth of tested beam

D = Maximum deflection of the centre of the beam

L = Support span

The load-deflection curves for semi crystalline polymers above T_g (particularly when filled) are non-linear, even at low strains. The strain at the onset of deviation from linearity generally decreases with increasing filler content. In unfilled polymers non-linearity arises due to viscoelastic effects which are significant at the relatively low strain rates encountered in polymer testing. In composites the deviation from linearity can be related to filler-matrix de-bonding. The secant modulus at 1 % strain (a deliberately high value; well in to non-linearity for some of the filled samples) has been determined as a qualitative measure of filler-matrix de-bonding; when compared with the flexural modulus obtained at close to zero strain it is the best estimate of the true stiffness of the composite. The difference between the $E_{sf(1\%)}$ and E_f values can provide some insight in to the linearity of the stress-strain data. If $E_{sf(1\%)}$ is slightly less than, or equal to, E_f it can be concluded that the stress-strain data is sensibly linear up to 1 % outer fibre strain. In the case of composites such linearity can be an indicator of good filler-matrix interaction. However, if $E_{sf(1\%)}$ is less than E_f , damage (i.e. filler-matrix debonding) to the composite is indicated. The secant modulus at 1% strain (Figure 14) was calculated using Equation 19. Whilst it was appreciated that the Hounsfield H10K tensometer did not record data up to the pre-load, the preload applied was very small (0.05 N) and the data obtained from 0 to 0.05 N was insignificant, even for the least stiff samples (i.e. the unfilled matrix materials). The pre-load was applied in order to ensure data was recorded at zero deflection, rather than at some random point along the x-axis that corresponded to application of the load.

$$\text{Secant Modulus} = \frac{\sigma_{x\% \varepsilon} - \sigma_{0\% \varepsilon}}{x\% \varepsilon} \quad \text{Equation 19.}$$

Where:

$\sigma_{x\% \varepsilon}$ = Stress value at chosen % strain

$\sigma_{0\% \varepsilon}$ = Stress value at zero strain/after toe elimination

$x\% \varepsilon$ = Chosen % strain value

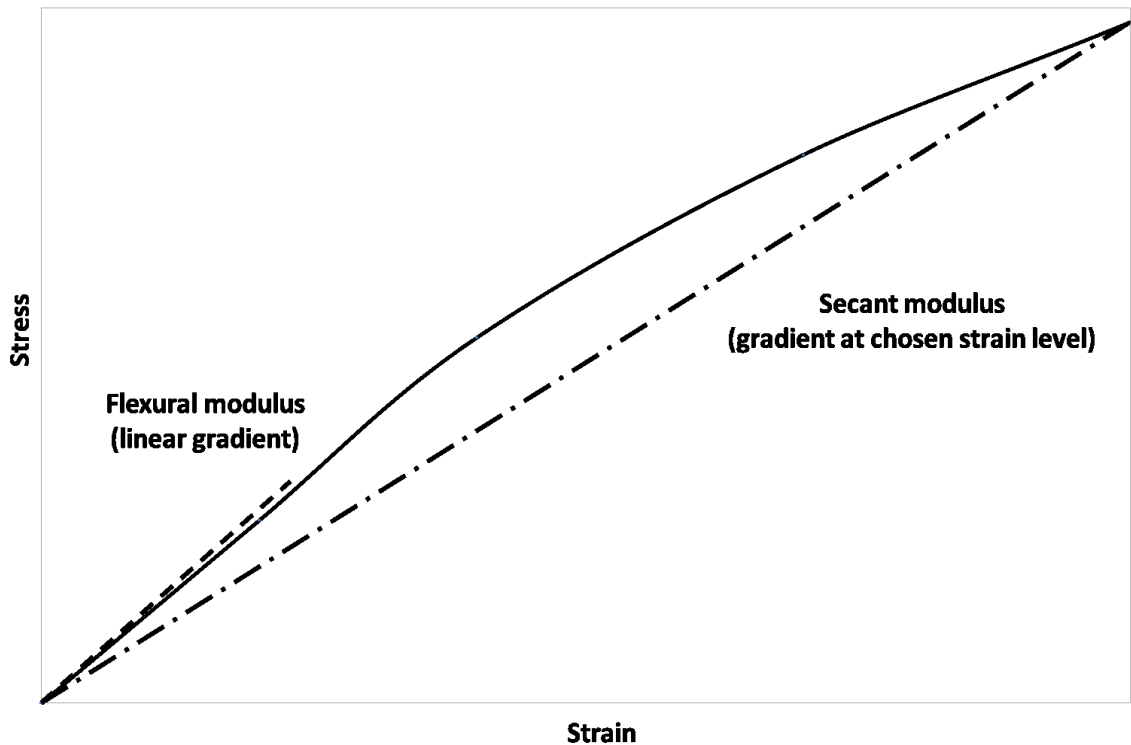


Figure 14. The difference between flexural modulus and secant modulus at chosen strain.

The flexural modulus was calculated from linear regression of the first 10 stress versus strain data points which showed the highest rate of change. The latter was checked by plotting the first 200 data points and checking the region of maximum slope; this usually occurred from the first recorded data point thanks to inclusion of a pre-load in the method. However, there were cases where the sample was very slightly twisted and small amount of force was required to flatten the sample on its supports. In such cases, the maximum rate of increase in stress was some distance from the first recorded data point and an appropriate compensation was made. The flexural stress at 10 mm deflection was calculated by Hounsfield's QMAT tensometer software. 8 replicate flexural samples of each material were measured; a maximum of three outlier results were removed for the secant modulus at 1 % strain , flexural modulus and flexural stress at 10mm deflection to give the five closest values of each parameter. Averages and standard deviations were calculated using the five closest values obtained for each material.

4.6.3 High temperature flexural testing of PE/fly-ash composites

Flexural testing to 10 mm deflection (in three point bend mode) at 85, 100, and 115 °C was carried out in accordance with ATSM D790 using a Hounsfield HTE50 tensometer fitted with a 50 kN load cell and a heat chamber containing a 3 point bend test rig. The heat chamber temperature was controlled via the tensometers computer. The span between the sample supports was 64 mm, crosshead speed was 5 mm min⁻¹ and a 0.05 N preload was applied before

collecting data. Force and crosshead displacement were recorded up to failure and the crosshead auto-returned to the start position.

4.6.3.1 Determination of flexural parameters from the raw data

The flexural modulus was calculated by Hounsfield's QMAT tensometer software. Section 4.6.2.1 describes the procedure to determine the flexural stress at 10 mm deflection for the PE/fly-ash composite materials.

4.6.4. Poisson's ratio testing of PE/fly-ash composites

Poisson's ratio determination of the PE/fly-ash composite safety step materials was carried out using the advanced video extensometer at the National Composites Certification and Evaluation Facility (NCCEF) within the University of Manchester. 5 tensile test pieces were cut from PE/fly-ash composite plaques via an OMAX water jet cutter, using the built in CAD package within the control system of the machine (Section 4.5.1). Sample dimensions were programmed to be 195 x 35 x 3.5 mm with a gauge section of 80 x 25 mm. The thickness varied between 3-4 mm (depending upon filler content). Specimens were dried in a Carbolite electric oven at 50 °C for 3 hours to evaporate any water potentially absorbed by the composite during the water jet cutting process. Individual specimens were measured to the nearest 0.001 mm before testing. Tensile testing to failure was carried out in accordance with ASTM D638-10 using an Instron 5982 tensometer fitted with a 100 kN load cell. The specimens were held using hydraulic grips. Cross head speed was 5 mm min⁻¹. Axial and transverse strains were measured using an Instron AVE 2663-821 video extensometer at 10 samples per second. The system was controlled using Instron's Bluehill software. Test pieces were marked on the centre of their gauge lengths with a permanent pen using both vertical and horizontal dots in the four principal directions. The markings provided a reference grid for the video extensometer to measure strain in the axial and transverse directions during the test. The ambient temperature was 23 °C (± 1 °C); this was measured using a thermocouple temperature probe situated close to the tensometer. After collection of the data, the numerical axial and transverse strain data points were exported to MS Excel for further processing.

4.6.4.1 Determination of Poisson's ratio from the raw data

The transverse and axial strain of the test specimens (to failure) was provided by the tensometers integrated computer in % format. Equation 20 was then used to calculate a value of Poisson's ratio at every point of strain (up to the yield point) using MS Excel.

$$v = \frac{\Delta x}{\Delta y}$$

Equation 20.

Where:

v = Poisson's ratio

Δx = transverse strain (%)

Δy = axial strain (%)

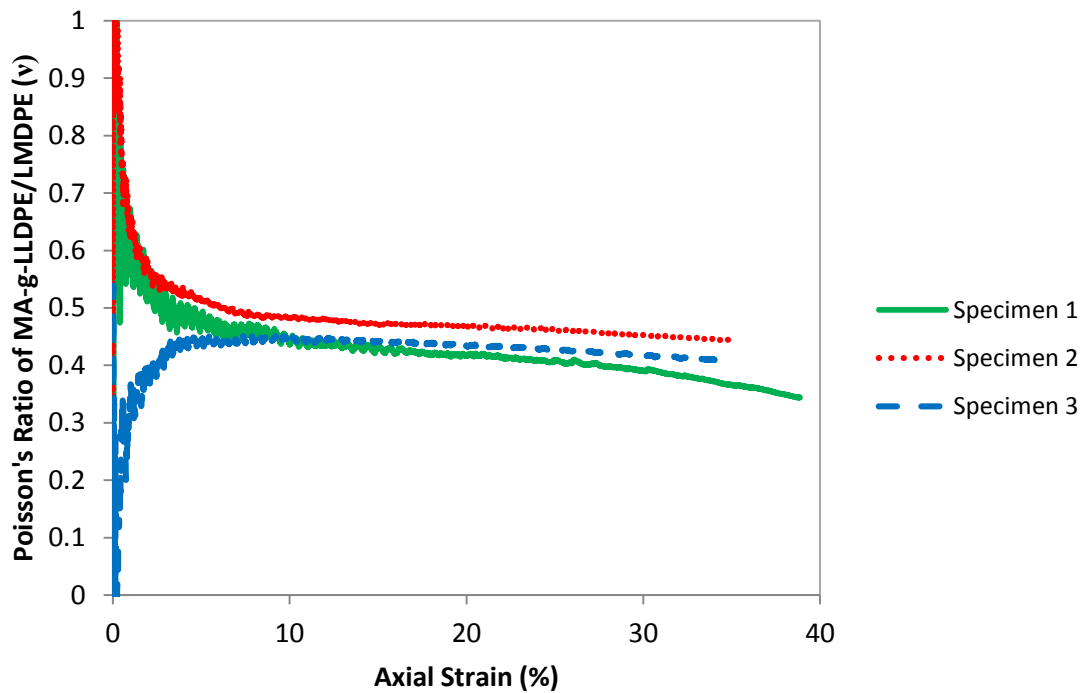


Figure 15. Poisson's ratio of MA-g-LLDPE/LMDPE vs. axial strain.

The resulting values of Poisson's ratio were plotted against axial strain for each material. Figure 15 displays the latter for three identical MA-g-LLDPE/LMDPE specimens (see Experimental Section 4.1.1 for details of this grade) and clearly portrays the challenge in measuring the Poisson's ratio of PE. It was found that consistent values of Poisson's ratio for the PE/fly-ash composite materials could not be calculated at the low to medium levels of strain. However, significantly more consistent values of Poisson's ratio were calculated at the higher levels of strain (approaching the yield point). The latter observation is counter-intuitive; due to the high-resolution advanced video extensometer, it was thought that consistent values of Poisson's ratio would be found at the lower levels of strain. From observation of the data, it was seen that all the PE/fly-ash composites were providing consistent values of Poisson's ratio at approximately 10 % axial strain, except for the 50 % wt. fly-ash/PE composite which provided consistent values of Poisson's ratio at approximately 5 % strain. Due to the strong consistency in behaviour between the tensile specimens of each PE/fly-ash composite material tested, it was decided to calculate an average axial and transverse % strain response up to the yield point for the latter materials. An average

Poisson's ratio was then calculated using the first 100 average transverse and axial % strain values after 5 % average axial strain for 50 % wt. fly-ash PE/composites and 10 % average axial strain for the remaining PE/fly-ash blends. Standard deviations were also calculated. The latter effectively resulted in a value of Poisson's ratio close to or at the yield point, rather than within the elastic region.

4.6.5 Charpy impact testing of PE/fly-ash composites

8 samples were tested using a Zwick model 5102 non-instrumented swinging pendulum type impact tester. The span between the sample supports was 40 mm. For this study the samples (nominally 10 x 4 mm in cross section) rested between the supports on their 4 mm side, such that the 10 mm wide side was struck by the tup (Figure 16). Care was taken to ensure that only the external moulding surface (mould side) of the specimen was facing the tup. This unconventional loading mode was used in order to more closely replicate the loading scenario of rotomoulded part in the field; when the mould side (external surface) of a rotomoulded part is loaded in compression, the air side (inner surface) undergoes tension. Un-notched Charpy impact samples were measured to the nearest 0.1 mm using a digital calliper. The most appropriate tup (0.5 J, 1 J, 2 J or 4 J) was selected using a spare test piece. The average free swing energy (E_{free}) of the selected tup was calculated from 8 free swings. All samples were then impact tested and the impact strength was calculated using Equation 21 (the figure of 1000 appears in the denominator, as a factor of 1/1000 will convert $J m^{-2}$ to $kJ m^{-2}$).

$$\text{Impact energy absorbed} = \frac{E_i - E_f}{1000(b*d)} \quad \text{Equation 21.}$$

Where:

E_i = Impact Energy (J)

E_f = Free Swing Energy (J)

b = breadth (m)

d = depth (m)

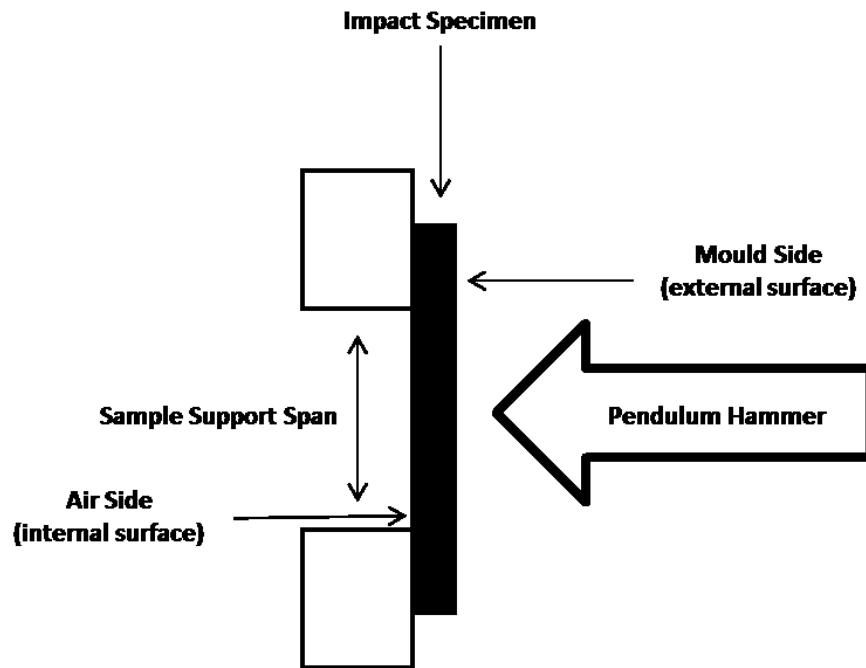


Figure 16. Charpy impact test setup (plan view).

4.6.6 Compression testing of rotomoulded safety steps

Compression tests on all unfilled PE and PE/fly-ash safety steps were conducted using a Hounsfield HK50S tensometer fitted with a 50 kN load cell. Crosshead speed was 1 mm min^{-1} . The ambient temperature was $23 \text{ }^\circ\text{C} (\pm 1 \text{ }^\circ\text{C})$; this was measured using a thermocouple temperature probe situated close to the tensometer. A total load of 600 N was applied on the top centre of all the safety steps by a 75 mm \varnothing , 25 mm thick compression platen through a 100 mm \varnothing , 6 mm thick aluminium disc (Figure 17). Force and crosshead displacement were recorded up to the 600 N and the crosshead auto-returned to the start position. The real time stress-strain curve generated by the tensometers integrated computer revealed that the 600 N load was well below the yield stress of the materials. However, replicates of all the PE/fly-ash composite safety steps were further compression tested to a maximum of load 5.5 kN using the same test procedure; this exceptionally high load is nearly double that of the maximum load rating of 2.6 kN specified in the British Standard for the testing of safety stools (BS EN 14183:2003 E). The latter load was purposely selected in an effort to record the compression response of the PE/fly-ash safety steps beyond the yield point of the material for comparison with non-linear FEA.

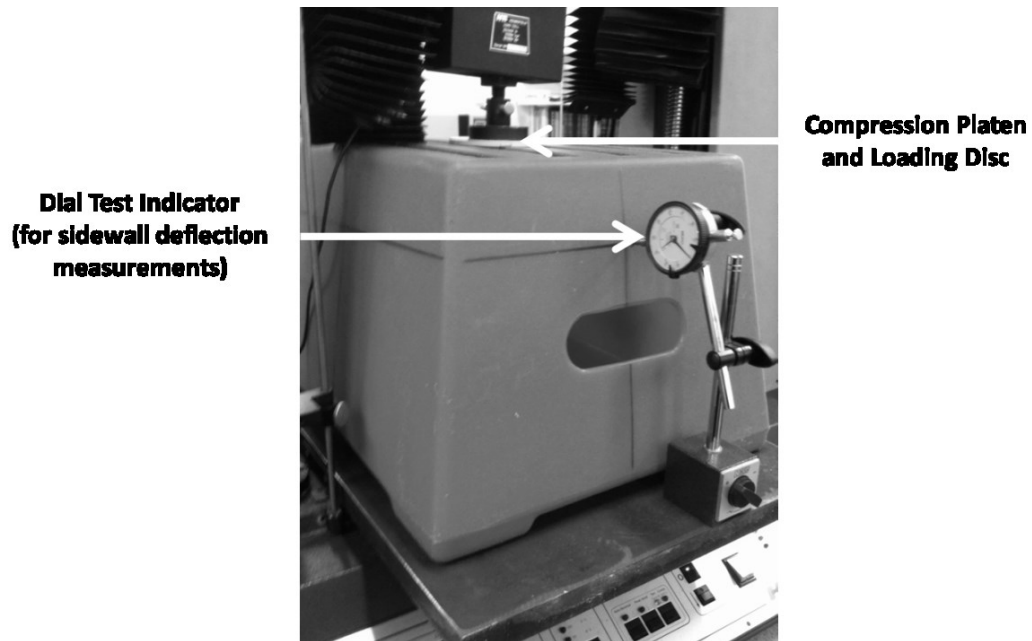


Figure 17. Safety step compression test set up. Dial test indicators (DTI's) were installed on opposing sides of the safety steps for sidewall deflection measurements.

Prior to compression testing of the safety steps, a static linear-elastic FE model using a CAD file of the step (in “.IGES” format) was set up within SOLIDWORKS Simulation. The aim was to identify locations of maximum sidewall deflection due to the safety steps geometry. Therefore, specific material properties were not required. However, standard material properties for low density PE available within SOLIDWORKS Simulation were applied; 172 MPa tensile modulus, 13.27 MPa tensile yield strength and a Poisson's ratio of 0.439. FEA predicted the maximum deflection of both sidewalls of the safety step to occur approximately 50 mm down from the top centre of the sidewalls. Consequently, two Mitutoyo dial test indicators (DTI's) were installed at these predicted locations of maximum sidewall deflection for the safety steps (Figure 17). Sidewall deflections during the actual test were measured at 20 N intervals. One hour after the test, the permanent deflection of both sidewalls was also measured.

4.6.7 Tensile testing of safety step materials

Straight surfaces were cut out from the side walls of the safety steps using a Baileigh industrial model BSV16 band saw. Tensile test pieces (Figure 18) were cut from these surfaces via an OMAX water jet cutter using the CAD package built into the control system of the machine (see Section 2.5.2.). Samples were tensile tested to failure in accordance to the same procedure described in Sections 4.6.1 and 4.6.1.1. However, six replicate test pieces of each material were measured. A maximum of two outlier results were removed to give the four most representative values in order to generate averages and standard deviations.

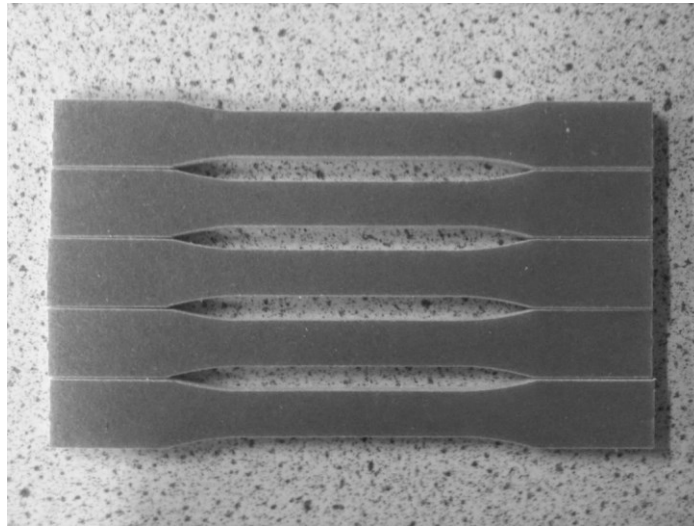


Figure 18. ASTM D638 tensile test pieces cut from flat sides of the safety steps.

4.6.8 *Compression testing of safety step materials*

Straight surfaces were cut out from the sidewalls of the safety steps using a Baileigh industrial model BSV16 band saw. Compression test pieces were cut from these surfaces via an OMAX water jet cutter, using the built in CAD package within the control system of the machine. The test pieces were 7 mm thick and 13 mm wide with two specimens at 15, 20, 25, 30 and 35 mm height. The samples were squared off at 90° on the top and bottom surfaces using a Proto-Trax model SMX3500 milling machine to ensure the top and bottom circular loading platen surfaces were flush with the top and bottom surfaces of the compression test pieces. Specimens were compression tested using a Hounsfield HK10S tensometer fitted with a 10 kN load cell (Figure 19). Both circular compression platens were 75 mm \varnothing and 25 mm thick. A crosshead speed of 1 mm min⁻¹ was used. To ensure the samples remained upright during testing, two samples of the same height were stuck together using double-sided tape (Figure 20). The double-sided tape joined the samples with little constraint. A Maplin model N43HH USB digital microscope was focused upon the tape-adhered joint between both of the identical test pieces to more closely identify premature buckling during the test. The resulting compressive load-deflection data was exported to MS Excel by Hounsfield's QMAT tensometer software for conversion to stress-strain using Equations 22 and 23. The consequent compressive stress-strain curves were added to tensile stress-strain curves of equivalent materials.

$$\sigma = \frac{F}{A}$$

Equation 22.

Where:

σ = Stress (MPa)

F = Force (N)

A = Area (mm²)

$$\epsilon = \frac{\Delta l}{l_0}$$

Equation 23.

Where:

ϵ = Strain (no units)

l_0 = original length (mm)

Δl = change in length (mm)

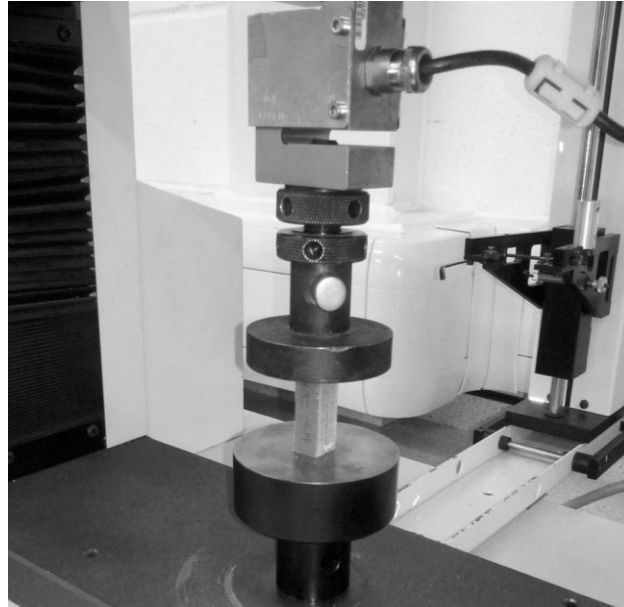


Figure 19. Safety step material compression test.

The range in height of the compression test pieces was purposefully selected in order to observe an optimal height to thickness ratio; if the ratio of height to thickness was too low (i.e. the test piece was short and stubby), it would result in decreasing deflection with the increase in force. However, if the ratio of height to thickness was too high (i.e. the sample was tall and slim) then the likelihood of premature failure due to buckling increases.

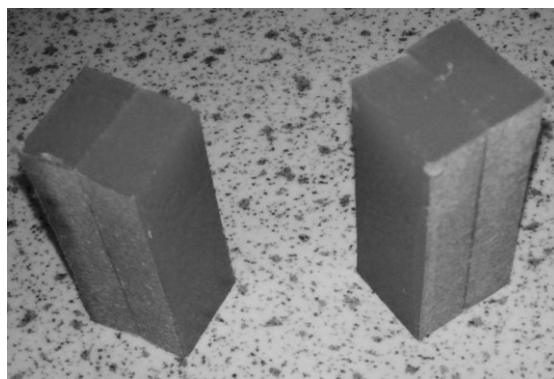


Figure 20. Two sets of compression test samples enjoined by double-sided tape, left 20 mm height, right 30 mm height.

4.6.8.1 Removal of machine compliance error

Movement of internal components (such as the crosshead bearings) within the tensometer can constitute significant error during testing. In order to identify and remove this error for the small scale compression tests (referred to as the machine compliance error), the same test equipment and procedures described in Section 4.6.8 were applied. However, no test specimen was used; the top platen was effectively compressed against the bottom platen and numerical force-deflection data was obtained from the integrated PC. The resulting force deflection data was plotted on an x-y scatter graph using MS Excel and 400 data points (out of 1000 in total) were taken after the initial toe of the force-deflection curve. After selecting these 400 data points (Figure 21), the corresponding x-data points were substituted by y-data points and vice versa (Figure 22), then plotted in MS Excel and a linear equation command was applied, giving an equation in the form of:

$$y = mx + c. \quad \text{Equation 24.}$$

Where:

m = gradient of the slope

c = the y-axis intercept

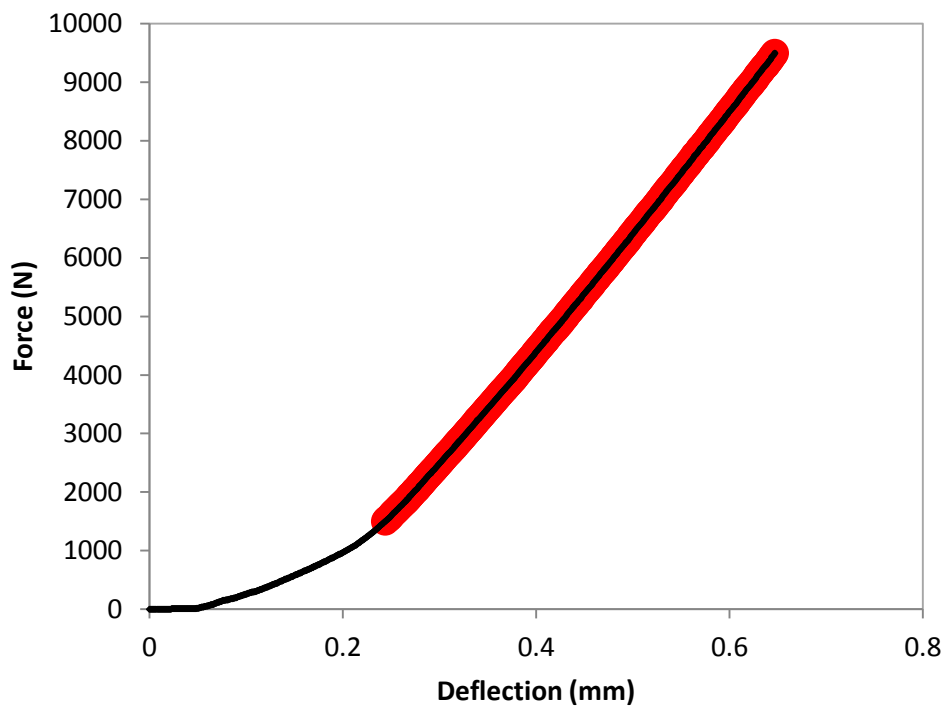


Figure 21. Hounsfield H10KS tensometer compression compliance curve. The red area indicates the section of the curve selected (400 data points).

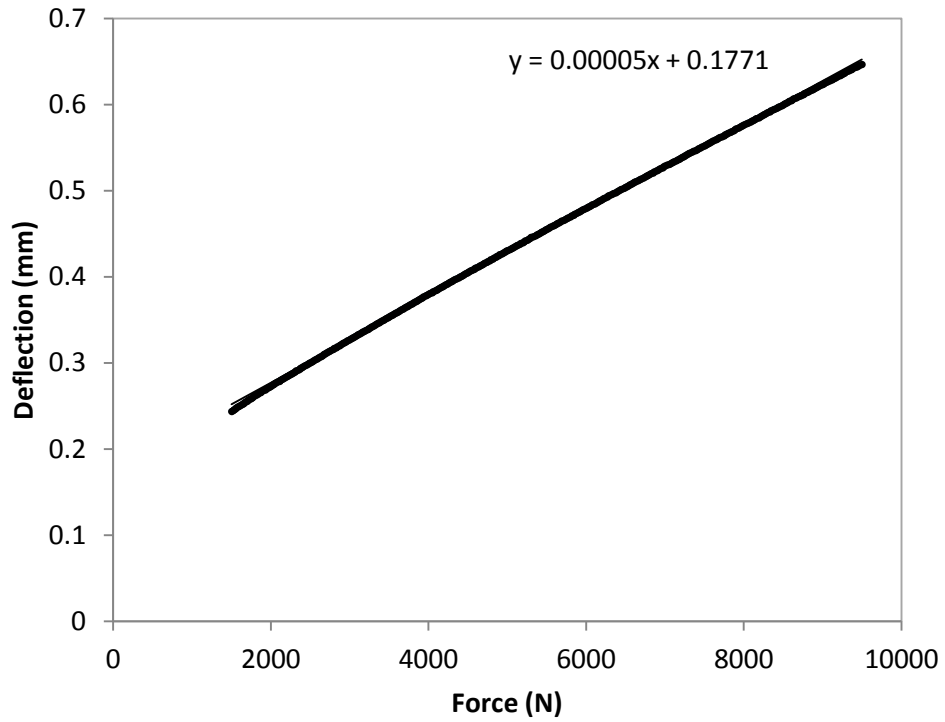


Figure 22. Inverse of Hounsfield HK10S compression compliance curve (x-data points substituted by y-data points and vice versa).

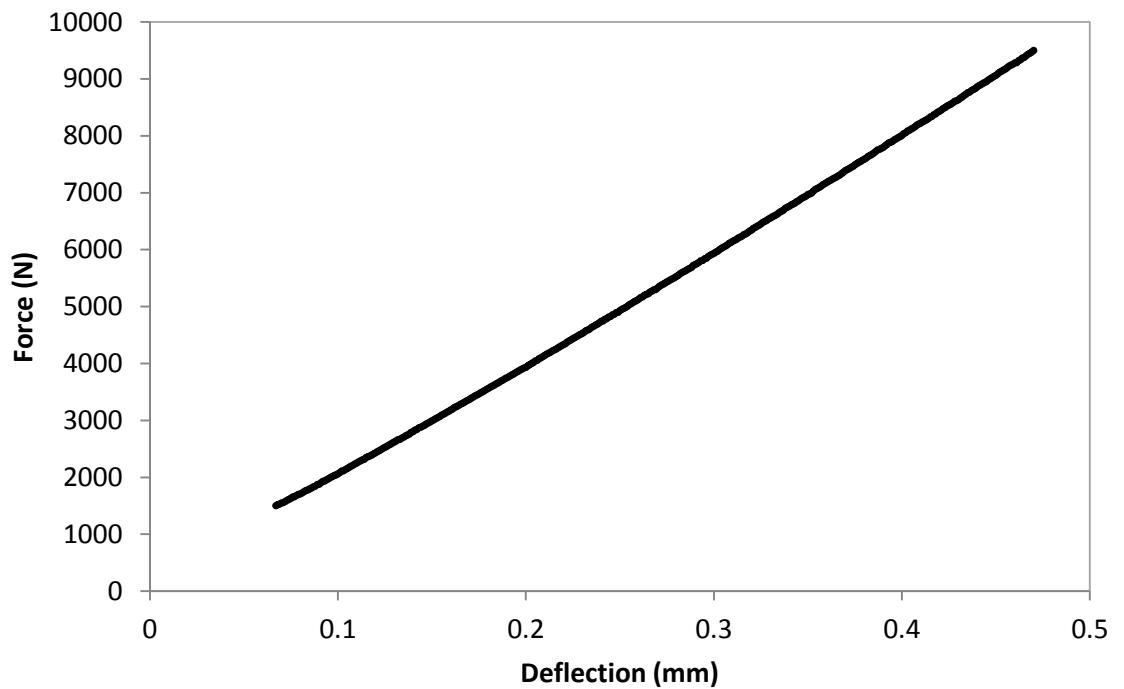


Figure 23. Hounsfield HK10S compression compliance curve with toe eliminated and machine compliance error accounted for.

The 'c' term in Equation 24 denotes where the line intercepts the y-axis (i.e. the deflection axis). In the case of Figure 22, the line crosses the y-axis at 0.1771 mm. Therefore, this value of 0.1771 was subtracted from the original deflection curve values to eliminate the toe. Furthermore, the value of 0.00005 displayed in Figure 22 is the gradient of the machine compliance error. The load-deflection curves from compression tests were altered to include the machine compliance error gradient by modifying their deflection values; this was done via subtracting the deflection values from corresponding force values and multiplying the result by 0.00005. The result was effectively a curve with the toe eliminated and the machine compliance gradient error accounted for (Figure 23). This error gradient was then incorporated into compressive stress-strain calculations of the safety step materials for better accuracy.

4.7 Surface Image Analysis of Rotomoulded PE/Fly-Ash Rectangular Box Test Mouldings

Small PE/fly-ash composite rectangular box test mouldings were rotomoulded using a Roto-Lab model Roto-Sampler machine (Section 4.5.4). Small pinholes were observed on the external surfaces of the PE/fly-ash test box mouldings. Therefore, flat sides of the rectangular box test mouldings were cut out using a Baileigh Industrial model BSV16 band saw for image analysis. The resulting specimens were mounted on a Griffin and George scissor jack platform. A Nikon model D3100 DSLR camera, fitted with a Nikon model DX AF-S 35 mm 1:1.8G lens, Yongnuo model MR85 LED macro-ring flash and Yongnuo model RF603N radio trigger, was mounted on a SLIK model U8000 tripod at 90° perpendicular to the external surface of the rectangular box moulding specimens (Figure 24).

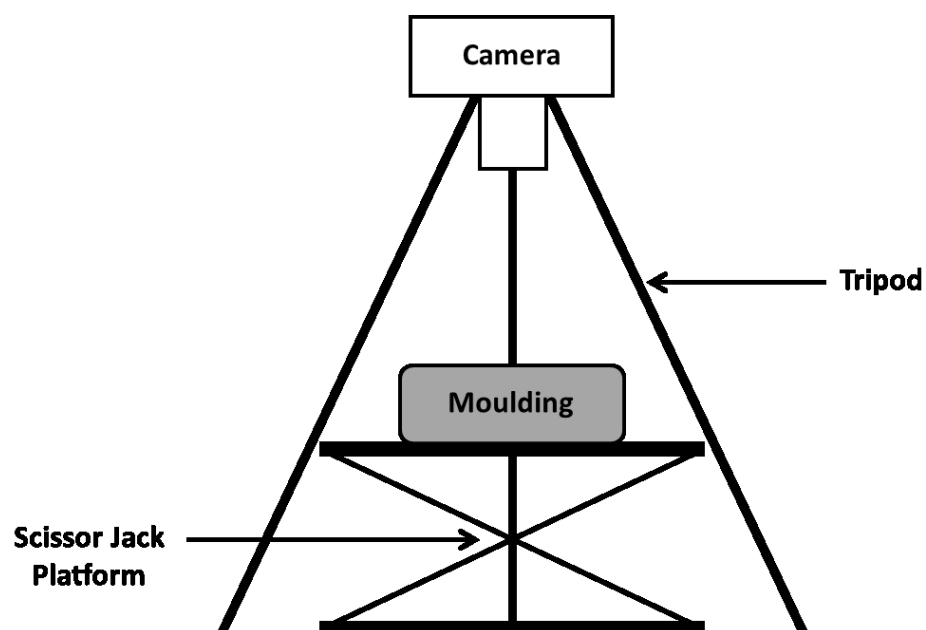


Figure 24. Apparatus used for surface porosity imaging of bench scale PE/fly-ash mouldings (front view).

A generic model MCDC2 remote trigger was used to capture images of the mouldings for surface porosity analysis using “ImageJ” analysis software. The following step-by-step procedure was followed:

1. All images were cropped in Windows 2010 photo viewer to remove all unwanted background items before analysis.
2. An image was opened for analysis within ImageJ software, noting the aspect ratio in pixels.
3. A straight line was drawn on the image and a pixel/mm calibration was set, using a known scale within the image (in this case, the scissor jacks platforms surface area was 150 mm x 150 mm).
4. The image was sharpened and a threshold was applied to highlight the areas of interest (i.e. porous holes).
5. A duplicate image of the thresholded image was then created and a Gaussian blur filter technique was applied using a large value for blur radius (relative to the porous hole radii in the image).
6. The original image was then subtracted from the Gaussian-blurred image, resulting in an image that highlight the porous hole outlines in black. A suitable porous hole diameter detection range was then specified and the resulting porous holes were measured by ImageJ.
7. Numerical data for the porous hole count and diameter were provided by ImageJ and saved to MS Excel for post-processing (Figure 25).

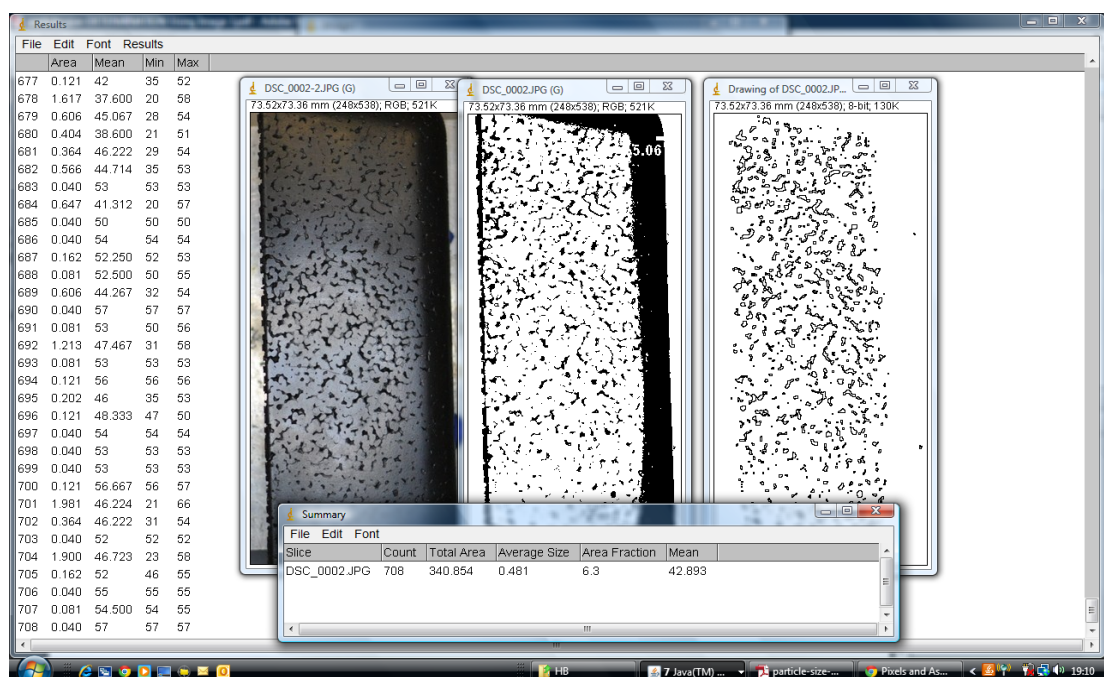


Figure 25. ‘Image J’ surface porosity image processing and analysis results.

4.8 Scanning Electron Microscopy and Energy Dispersive X-ray Analysis

Scanning electron microscopy (SEM) permits the observation and characterisation of various heterogeneous organic and inorganic materials on a micrometer (μm) to nanometer (nm) scale ^[213], typically producing images at magnifications of up to $10^6\times$ ^[214]. During SEM, an area or volume of a sample is irradiated with a precisely focused electron beam that can be swept in a raster fashion to image an entire sample or statically focused to image a specific point on a sample. Various signals such as secondary electrons, backscattered electrons and x-rays are emitted from atoms in the sample upon interaction with the electron beam ^[215]. These signals are used to analyse various characteristics of the sample such as surface topography and elemental composition. With regards to surface imaging, the signals of most interest are the secondary and backscattered electrons as they are emitted due to differences in the surface topography of the sample ^[216].

With regards to elemental composition, the signals of most interest are x-ray emissions; the atoms in a sample have a unique a set of peaks on the x-ray emission spectrum ^[217]. Upon excitation of an atom by an external source of charged particles (i.e. an electron or proton beam) an electron from a low-energy inner shell is ejected, prompting an electron replacement from a high-energy outer shell. The difference in energy between the inner and outer shells of the atom is released in the form of x-rays ^[218]. The number and energy of x-rays are detected by an energy dispersive spectrometer integrated with the SEM. X-ray emissions are a product of the difference in energy between the two shells and the atomic structure of the elements in the sample ^[219]. Therefore, the elemental composition of a sample can be identified from x-ray emissions. The latter process is called energy dispersive x-ray (EDX) analysis.

SEM was used to image the filler particles and fracture surfaces of tensile test specimens. EDX analysis was used to determine the elemental composition of the fillers. The latter was achieved by a Jeol model JSM 5600 SEM fitted with an Oxford instruments 7800 series EDX detector.

4.8.1 *Sample preparation*

1. A double sided self-adhesive carbon pad was stuck on to the specimen face of a fresh stub and the protective film removed, exposing the adhesive surface attached to the stub.
2. A small amount of the filler sample was sprinkled on to the pad and the excess removed with a jet of compressed air.
3. The sample was then sputter coated with gold to render its surfaces electrically conductive and reduce the tendency to charge.

4.8.2 *Scanning electron microscope and energy dispersive x-ray operating conditions*

For the filler particle surface imaging, the SEM was run at an accelerating voltage of 15 kV, using the secondary electron detector. Digital images of each specimen were acquired at a range of magnifications. Care was taken to ensure that the image was representative of the sample. EDX was carried out using spot analysis with an accelerating voltage of 15 kV, the spot size was adjusted to provide an acceptable detector dead time in the region of approximately 30 %. The levels of all the elements detected were recorded. To ensure that the data was representative, three replicate areas were examined and the data averaged.

4.9 Differential Scanning Calorimetry

Differential scanning calorimetry (DSC) was conducted to investigate the effect of blending method and filler addition on the melting, crystallisation and re-melting of the PE based matrix materials developed for this PhD study. DSC is defined by Höhne et al. as a method of measuring the change of the difference in heat flow rate to a sample and a reference sample during a controlled temperature program ^[220]. It is a method of measuring the thermal transitions of a material. In principle, DSC converts a temperature difference to an energy per unit mass value associated with a phase transition of a material (e.g. the energy per unit mass required to melt a solid material to a liquid) ^[221]. DSC is widely applied to polymeric materials to analyse their microstructural properties. The melting temperature (T_m) of polymers is dependent upon their molecular composition, molecular structure and thermal history. Consequently, the percentage crystallinity of a polymer can be estimated using the melting and crystallisation energy-temperature peaks from a DSC thermogram alongside reference heats of fusion found in literature ^[222] (refer to Appendix Section 4 for typical DSC thermogram traces). The melting point (T_m) of a polymer is defined by the peak of its energy-temperature curve. The heat of fusion of a polymer is the area under the energy-temperature peak from the beginning to the end of the baseline. The crystallinity of the polymer can then be calculated by dividing the measured heat of fusion by the heat of fusion for an equivalent 100 % crystalline polymer ^[223] (see Equation 25).

The DSC instrument used for this study was a Perkin-Elmer DSC-7, a power compensation type instrument. The following heat – hold – cool – heat cycle was used:

- Heat from 20 °C to 240 °C at 20 °C min⁻¹
- Hold at 240 °C for 5 minutes
- Cool from 240 °C to 20 °C at 20 °C min⁻¹
- Hold at 20 °C for 2 minutes

- Heat from 20 °C to 240 °C at 20 °C min⁻¹

Samples were heated in a nitrogen atmosphere (flow rate 30 cm³ min⁻¹). The following parameters were recorded during DSC:

1st Heat (for determination of the specimens melting characteristics in its as-moulded component)

- Onset of melting temperature
- Peak melting temperature
- Melting temperature range
- Heat of fusion (for calculation of crystalline content. The samples were held at 240 °C for five minutes to ensure complete melting and total eradication of previous thermal history)

Cool from melt (to provide controlled crystallisation)

- Onset of crystallisation temperature
- Crystallisation exotherm peak temperature
- Crystallisation temperature range
- Heat of crystallisation (for calculation of crystalline content obtained during controlled crystallisation)

2nd Heat (to examine the melting of crystal structures formed as a result of controlled crystallisation)

- The same parameters as recorded during the 1st heat were recorded

Sample mass was typically between 4 and 10 mg. Samples were crimped in to aluminium pans and the DSC head was purged with nitrogen (flow rate 50 cm³ min⁻¹). The crystalline content of unfilled PE materials was determined using Equation 25. For PE/filler composites, crystallinity content was also calculated using Equation 25. However, Equation 26 was used to calculate ΔH_f for input into Equation 25.

$$\text{Crystallinity (\%)} = \frac{\Delta H_f}{\Delta H_{f0}} \times 100 \quad \text{Equation 25.}$$

Where:

ΔH_f = Heat of fusion (J g^{-1})

ΔH_{f0} = Heat of fusion for 100 % crystalline PE (277 J g^{-1}) [224]

$$\Delta H_f = \frac{A}{M(1-V_f)} \quad \text{Equation 26.}$$

Where:

ΔH_f = Heat of fusion (J g^{-1})

A = Area of the Energy-Temperature Peak (mJ)

M = Mass of the sample

V_f = Volume Fraction of filler

4.10 Finite Element Analysis of the Rotomoulded Safety Steps Sidewall Deflection

SOLIDWORKS 2013 was the software selected for FEA investigations due to its highly intuitive user interface and extensive suite of CAD tools integrated with virtual prototyping applications such as FEA (known as SOLIDWORKS Simulation). Forces, pressures, accelerations and temperatures applied on one structure or between multiple structures can be solved via SOLIDWORKS Simulation. Furthermore, data obtained from thermal or fluid-flow studies can be implemented for multi-physics analyses. SOLIDWORKS Simulation has an extensive database of properties for a variety of materials including polymers, metals and ceramics integrated within the software. However, the option to implement materials data from physical testing is also available. Moreover, in the case of model failure SOLIDWORKS Simulation guides the user with a failure diagnostics tool to locate and resolve problems with meshing, boundary conditions or analysis options. Currently, many computer software packages such as HyperWorks, COMSOL and ANSYS are available for the FEA of stresses. Although the latter software may differ somewhat in capability, the vast majority of FEA software can trace their underlying mathematics to the 1960's [225] when NASA were developing the first commercial FEA computer software package (NASTRAN). Due to its well-integrated CAD/FEA capability and the relatively simple loading scenario of the rotomoulded safety steps, SOLIDWORKS Simulation 2013 was selected for FEA investigations.

In principle, SOLIDWORKS Simulation splits a 2D or 3D geometry into a vast array of nodes. Lines connecting these nodal points small create an overall mesh of tetrahedron elements (for 3D geometries), triangle elements (for 2D geometries) or beam elements. SOLIDWORKS Simulation then uses the displacement formulae of the finite element method (FEM) to solve for stress and

strain at every nodal point and element and provide a total solution for the entire geometry (Literature Review Section 3.4). Solutions are calculated either directly (with the entire load applied at one instance) or iteratively.

4.10.1 *Finite element model development*

In order to use the FEA application within SOLIDWORKS Simulation, a CAD file of the safety step (in “.IGES” format) was uploaded into the software. A simulation tab within the user interface was then selected, prompting a pop-up window offering FEA options (Figure 26). Primarily, static linear-elastic and non-linear FE analyses were selected for comparison with physical test measurement of the PE/fly-ash safety steps sidewall deflection. Overall, static linear-elastic analyses required values of tensile modulus, density, tensile stress at yield and Poisson’s ratio (Figure 27).

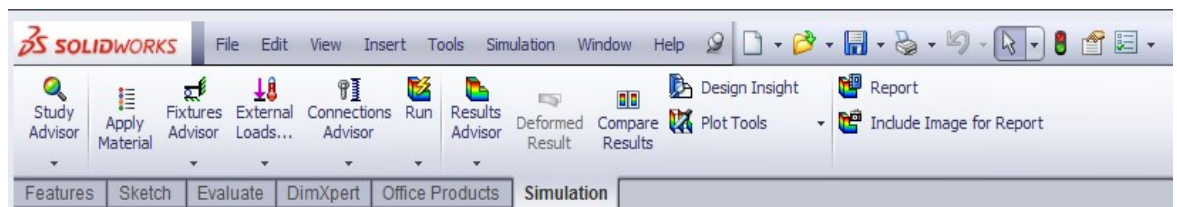


Figure 26. SOLIDWORKS Simulation toolbar options.

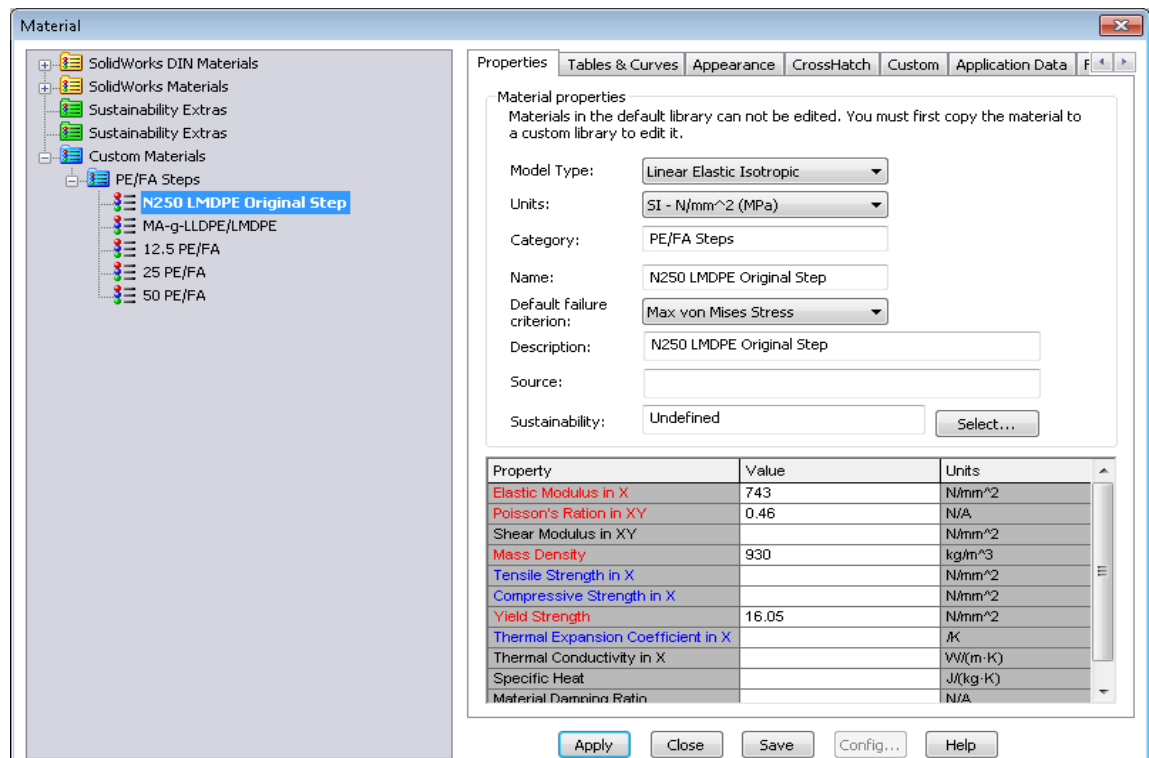


Figure 27. A pop-up window within SOLIDWORKS Simulation to apply material properties to the 3D safety steps geometry.

Non-linear analyses required a Poisson's ratio value and a full numerical tensile stress-strain curve (Figure 28). The latter numerical material properties required for both static linear-elastic and non-linear FE analyses were calculated from physical testing of the rotomoulded PE/fly-ash safety step materials. Static linear-elastic analysis offered potentially quicker solution times relative to non-linear FEA at the expense of highly idealising the model; such models assume the material is linear and the structure returns to its original shape when the load is removed. For static linear-elastic analysis, a factor of safety is a common design goal as it is difficult (thus uncommon) to model the mechanical response of a structure beyond the yield point of its material. Non-linear FEA was selected due to the non-linear stress-strain relationship of PE; non-linear FEA uses full tensile stress-strain curves from physical testing for application in an iterative type solver to provide solutions more closely linked to the real stress-strain response of the material (see Literature Review Section 3.4.4.2). Therefore, non-linear FEA was anticipated to provide more accuracy at the expense of longer solution times, due to the larger amount of input data required.

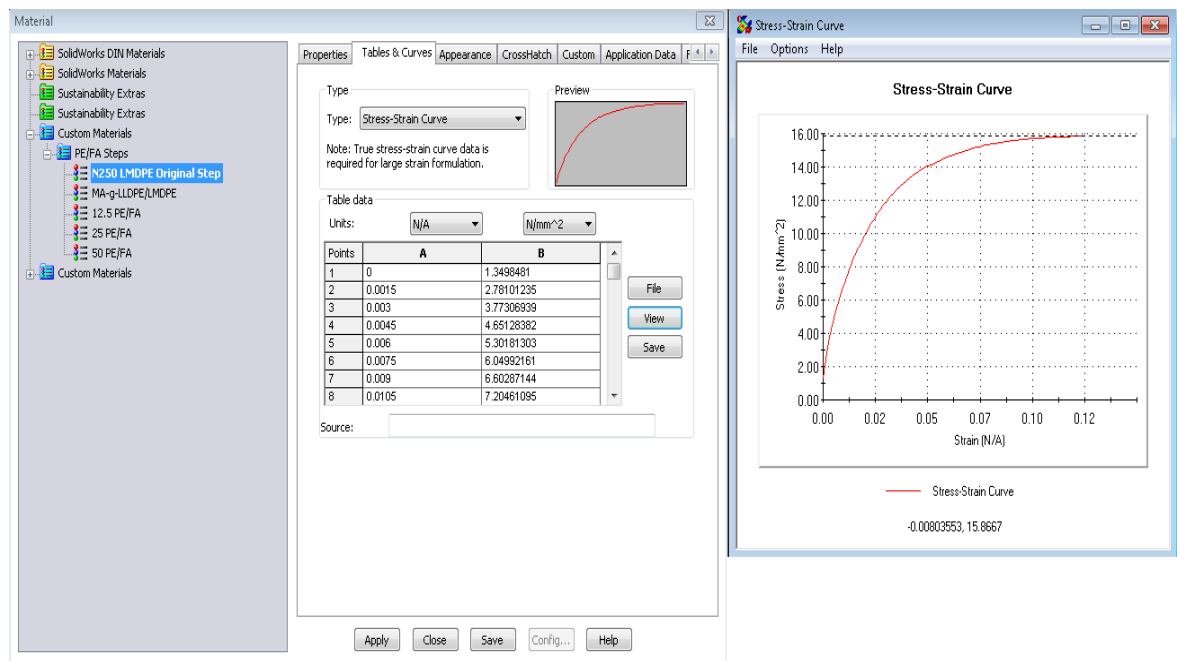


Figure 28. A pop-up window within SOLIDWORKS Simulation to specify a stress-strain curve for the safety step materials.

After specifying the analysis type and material properties, the loads and constraints of the FE model were defined by highlighting faces or edges of the 3D safety step geometry (Figure 29) and specifying the magnitude and direction of the load using the toolbar in Figure 30. A 5.5 kN force (or 4.6 kN for the 50 % wt. fly-ash/PE composite safety step, see Results and Discussion Section 5.12.2) was applied through a 0.0314 m² area (100 mm diameter disc) on the top centre surface of the step in order to replicate the physical test scenario. Ground contacts of the safety step (the feet) were secured using stabilising springs (to contain, rather than eliminate, slight movements

during loading) and the effect due to gravity was accounted for. During actual compression tests of the safety steps, the maximum deflection of the compression platen (or crosshead) at 5.5 kN varied depending on the PE/fly-ash composite material used. Therefore, a displacement was also applied on the top centre surface of all safety step FE models (instead of a load) according to the maximum crosshead displacement of each PE/fly-ash safety step recorded from physical testing. The latter was conducted to gauge the effect of applying a displacement instead of a load on FEA results.

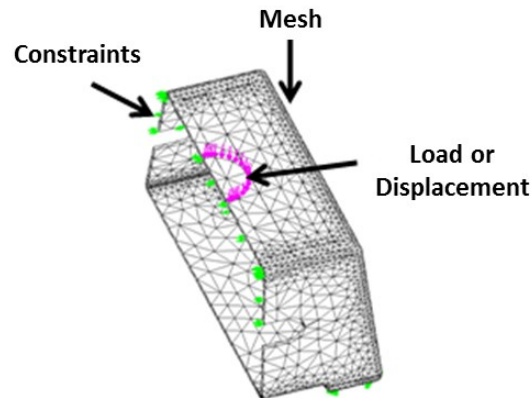


Figure 29. 3D geometry of safety step with loads, constraints and mesh applied within SOLIDWORKS. The geometry was cut in half lengthways along its line of symmetry to simplify the model.

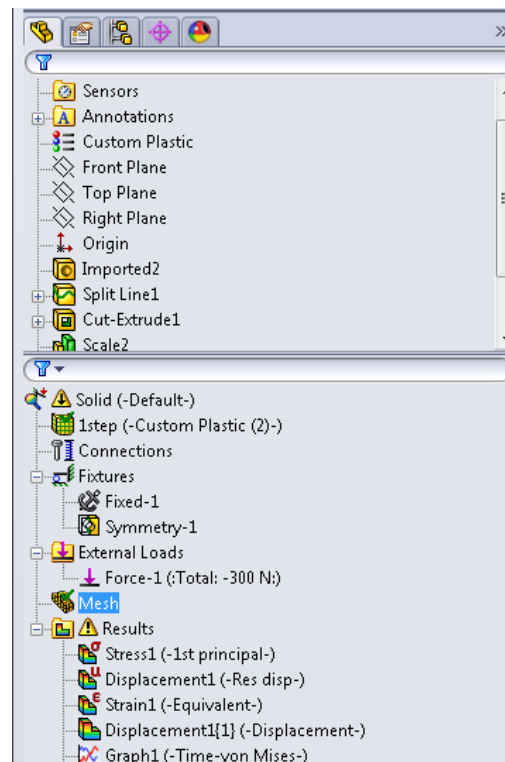


Figure 30. SOLIDWORKS Simulation toolbar displaying a list of parameters for application or observation.

4.10.2 *Finite element model simplification and refinement*

To simplify the safety step FE model, the 3D step geometry was cut in half lengthways along its line of symmetry (Figure 29). Therefore, the area and magnitude of the applied force was also halved. The line of symmetry allowed the software to calculate stress-strain in half of the geometry and replicate the results for the remaining half, reducing simulation time considerably (as the geometry is symmetrical). With the essential details defined (geometry, loads, constraints and material properties), a coarse mesh size was selected for initial FEA simulations (Figure 31).

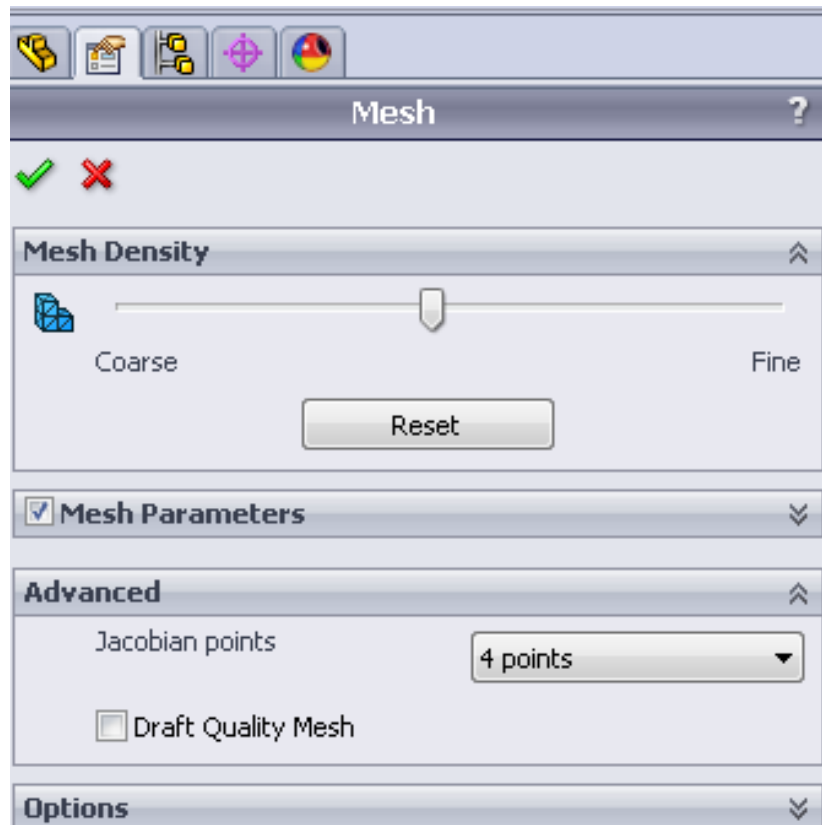


Figure 31. A pop-up window to vary element mesh density between coarse (larger elements) and fine (smaller elements). The element size generated are dependent upon the geometry.

To refine the static-linear elastic FE models for better accuracy, both P-adaptive and H-adaptive mesh refinement methods were applied (Literature Review Section 3.4.5). The seamless integration of CAD and FEA is one advantage of using SOLIDWORKS Simulation; the exact geometry is well defined, this helps to ensure both the H and P-adaptive mesh refinement solutions converge (Figure 32). Convergence occurs when the iterative changes in mesh size (H-adaptive) or element order (P-adaptive) result in a small change to the solution. The solution convergence criterion for H and P-adaptive mesh refinement was 98 % (i.e. the automated meshing process stops when the total strain energy change between all the elements is within 2 %) with a maximum of 5 mesh refinement loops for H-adaptive and 4 mesh refinement loops for P-adaptive. A maximum element order of 5 was used for P-adaptive mesh refinement (Figure 33).

For the non-linear FE models, the solution criteria was a start time of 0 with an end time of 1 second and a load-time increment of 0.01 seconds with the large displacement option turned on (Figure 34). The iterative calculation method used by SOLIDWORKS Simulation for all non-linear FEA was the Newton-Raphson technique. During the meshing process, SOLIDWORKS Simulation automatically defined beam or solid elements to the safety steps geometry.

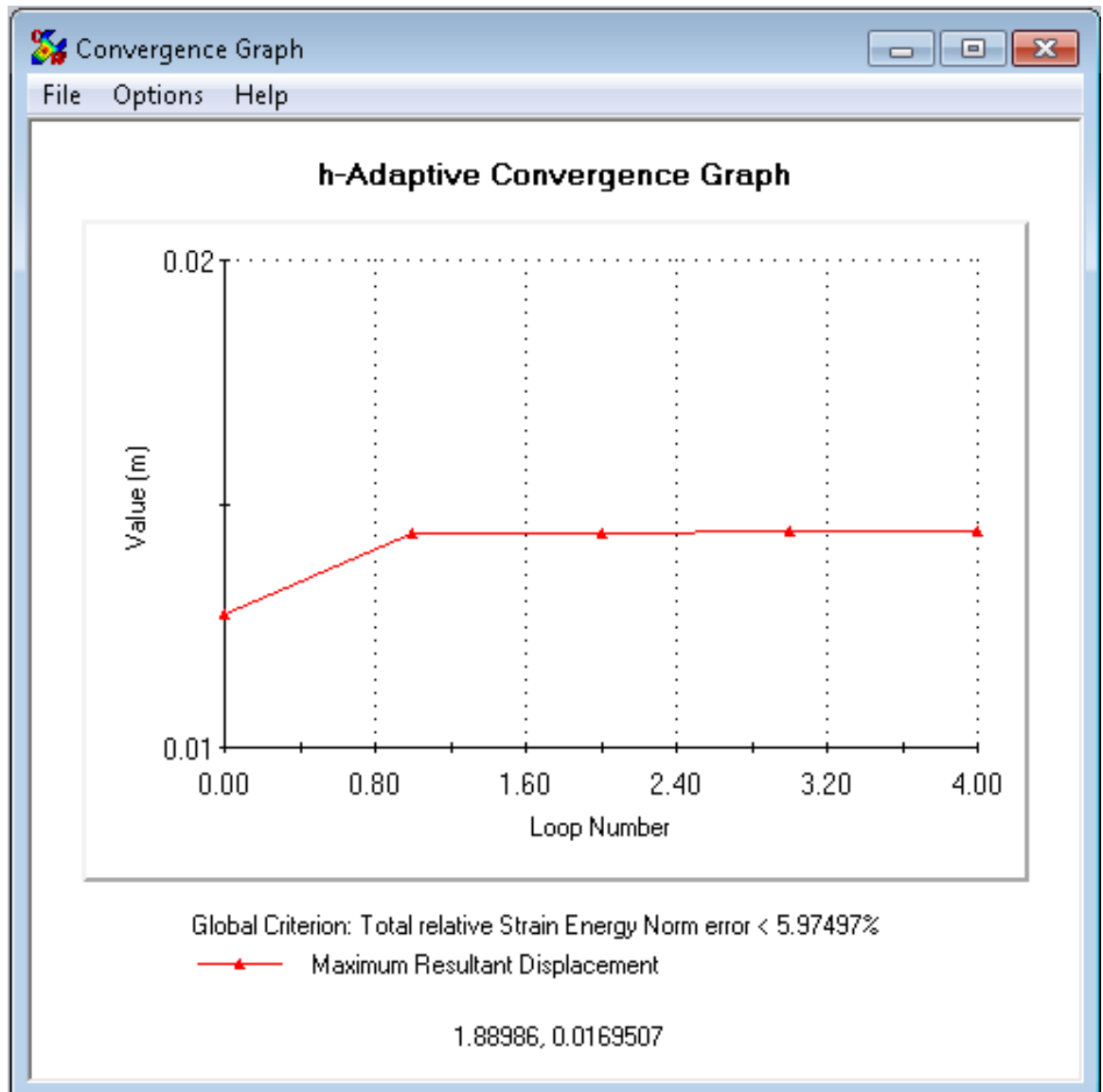


Figure 32. H-adaptive solution convergence graph produced by SOLIDWORKS Simulation.

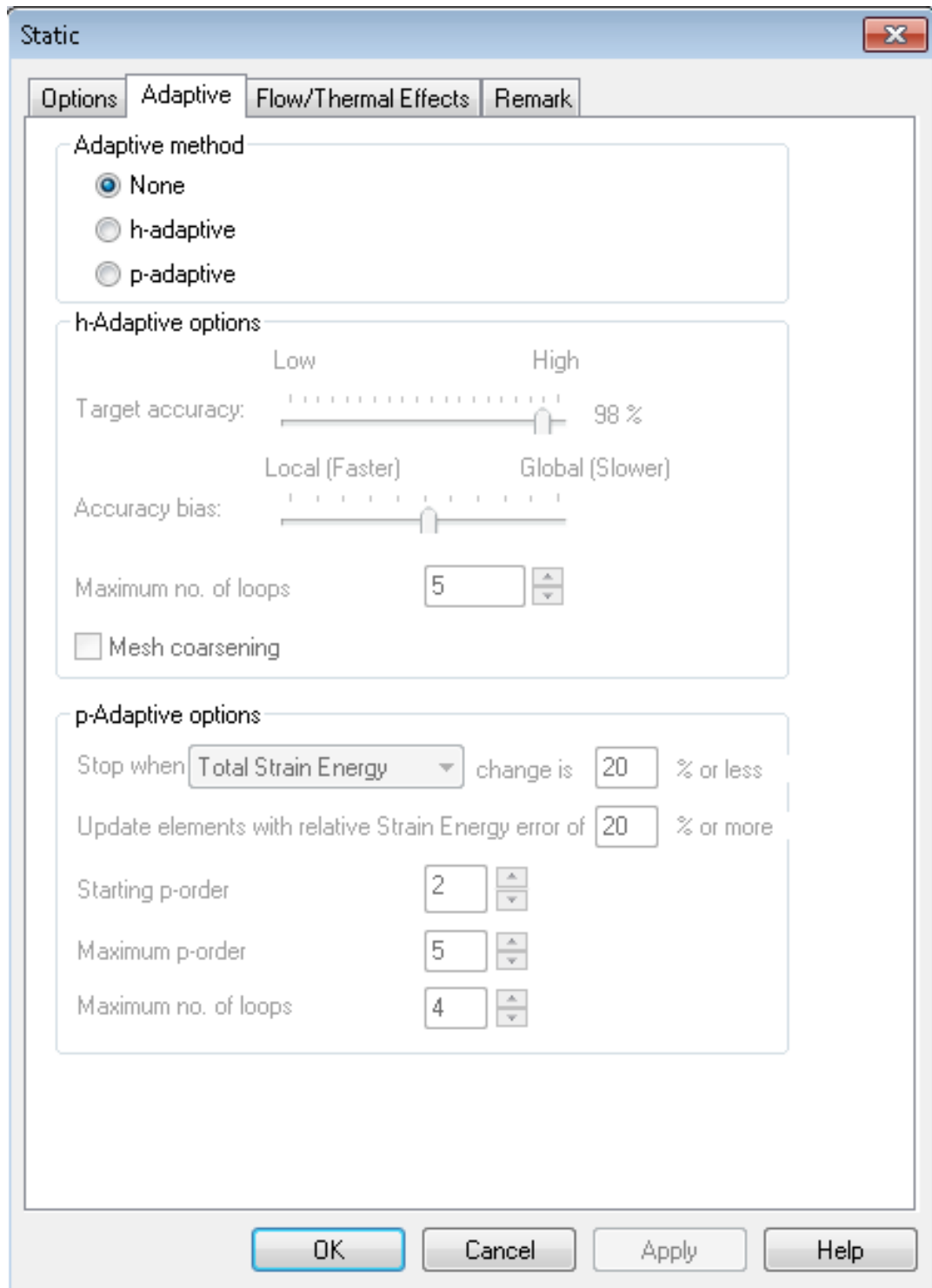


Figure 33. A popup window within SOLIDWORKS Simulation software to specify H-adaptive and P-adaptive mesh refinement options.

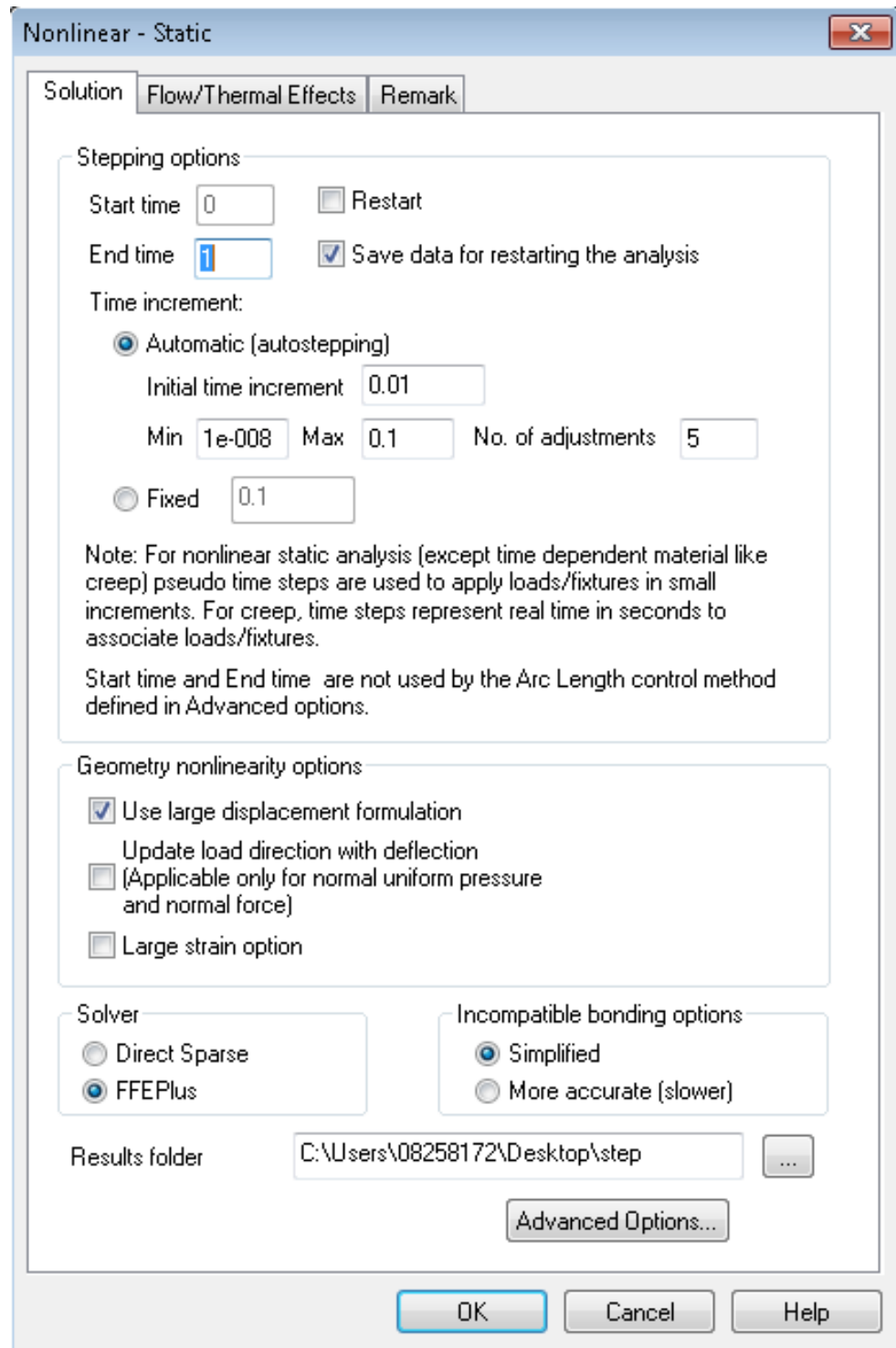


Figure 34. A popup window within SOLIDWORKS Simulation to specify non-linear FEA solution options.

4.10.3 *Finite element model analysis*

FEA solutions took approximately 5 minutes for static linear-elastic models and 45 minutes for non-linear models using a 32 GB RAM PC. FEA solutions were provided by the software in the form of images that use colours to highlight the intensity and magnitude of stress or deflection across the safety steps geometry (red is high, blue is low). The sidewall of the safety step was highlighted and probed to identify the magnitude of deflection at this location (Figures 35 and

36). The resulting data was plotted using MS Excel for comparison with physical test measurements of the safety steps sidewall deflection.

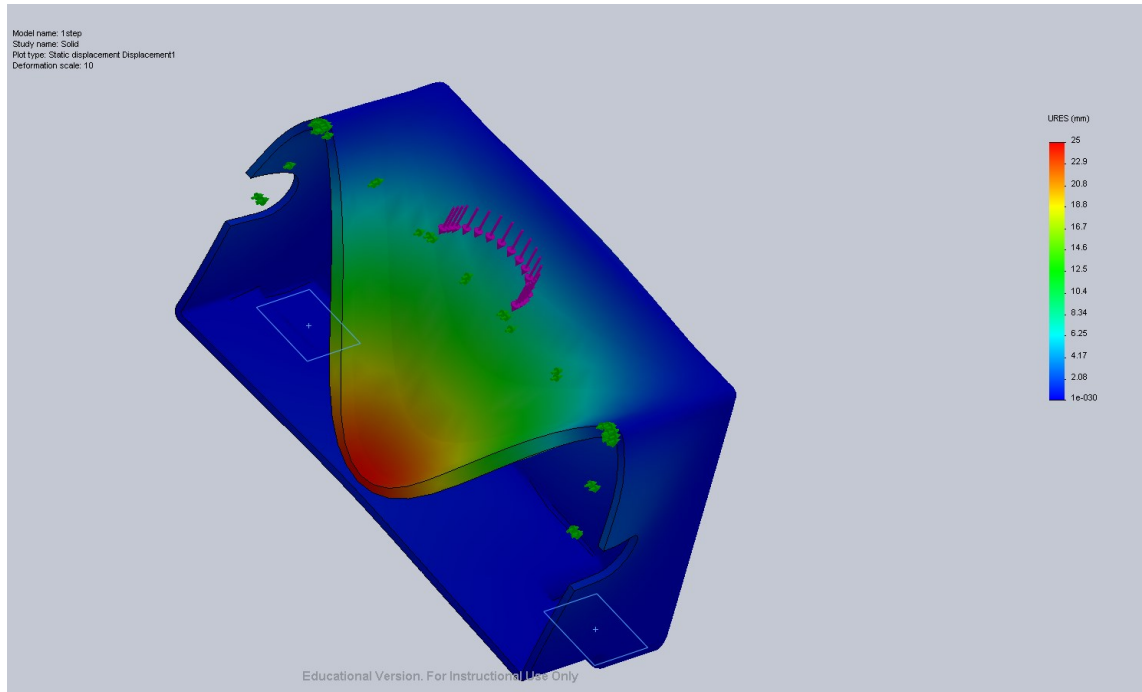
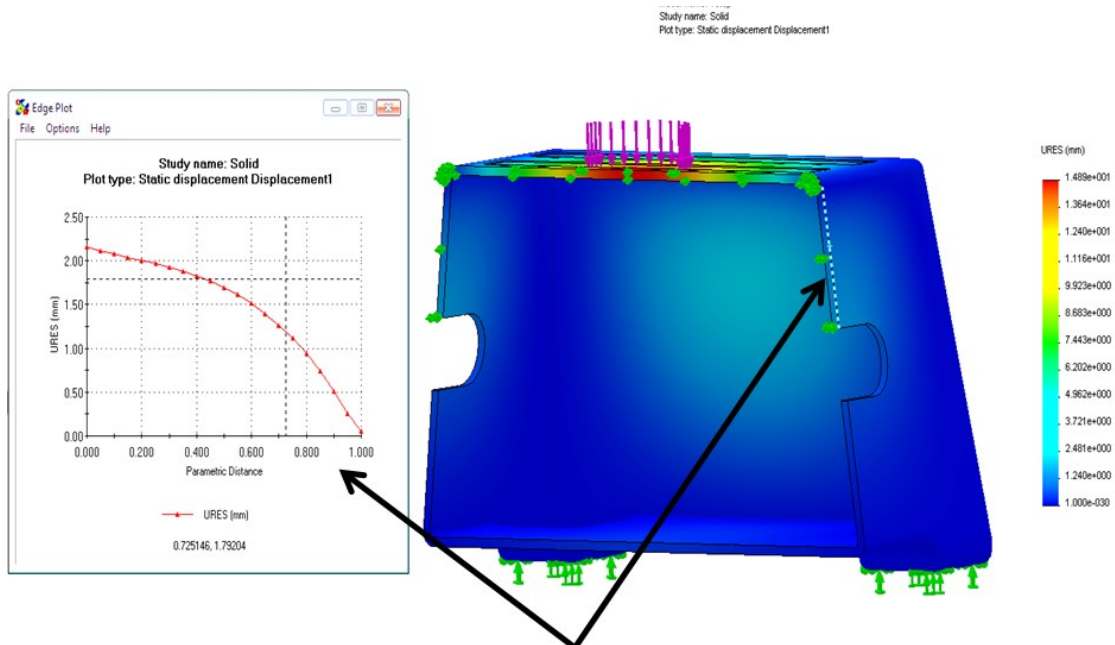


Figure 35. Deformed shape of safety step after application of load within FEA.



Sidewall deflection highlighted and probed for analysis



Figure 36. Sidewall deflection of safety step highlighted and plotted after FEA.

5. Results and Discussion

5.1 Summary of Work

Phase 1 of this study focused upon the development of PE/filler composites for the proposed new generation of high stiffness rotational moulding materials. The influence of garnet, sand, cenosphere and fly-ash particles on the mechanical properties of PE was investigated. The garnet, sand and cenosphere particles are larger in size relative to the finer fly-ash particles. Fly-ash and cenospheres are an industrial by-product from coal fired power stations; fly-ash is by far the major product and cenospheres are a minor product. Energy dispersive X-ray (EDX) spectroscopy analysis confirmed the filler particles were free from impurity before application. PE/filler composites of various filler content were mixed either by dry blending or melt compounding. The resulting blends were then compression moulded or rotomoulded and analysed for mechanical response in tensile, flexural and impact modes. In order to promote better interfacial coupling between the filler particle surface and PE matrix (filler-matrix interaction), a maleanised PE blend consisting of 75 % wt. LMDPE and 25 % wt. MA-g-LLDPE was used for PE/filler composites. Development of a stiffer maleanised PE was attempted by blending HDPE with MA-g-LLDPE at various concentrations for comparison with equivalent MA-g-LLDPE/LMDPE blends; the results indicated a strong relationship between the crystalline content and modulus of PE. Improvements in tensile and flexural properties were observed with the addition of the candidate filler particles to the maleanised PE system. However, the finer fly-ash particles offered exceptionally good enhancements with every increase in filler loading and maleanised PE investigated. Therefore, the PE/fly-ash based composite materials were selected for further study.

The 75 % wt. fly-ash/LMDPE displayed improvements in tensile modulus and tensile stress at yield with every increase in MA-g-LLDPE loading investigated. The same was true for equivalent HDPE based composites except in the case of tensile stress at yield up to 10 % by wt. MA-g-LLDPE loading; due to the seemingly better compatibility of LMDPE with the MA-g-LLDPE and the better suitability of LMDPE for rotomoulding in terms of cost and processability, it was decided to remain with the 25 % wt. MA-g-LLDPE/75 % wt. LMDPE for further investigations. The improvements in tensile and flexural properties of the PE/fly-ash composite materials were accompanied by reduced impact toughness for the PE/fly-ash composites, particularly at higher fly-ash loadings (50 % wt.) where the stiffness enhancement was more prominent. High temperature flexural tests revealed the addition of fly-ash to the selected maleanised PE system improved the heat distortion behaviour of the resulting injection moulded composites relative to

the unfilled matrix. TSE melt blended PE/fly-ash composites were rotomoulded into safety steps and compression tested for comparison with unfilled PE safety steps. Tensile tests using specimens cut from flat surfaces of the safety steps were also conducted and compared with compression moulded equivalents. Only the 50 % wt. fly-ash PE composites offered stiffness comparable to that of higher density rotomoulding PE grades. However, pinholes on the surfaces of rotomoulded PE/fly-ash box test mouldings were evident with the increase in fly-ash; the latter confirmed the challenge in moulding such highly filled PE using the zero-shear RM process. On the other hand, it was seen that the variation in wall thickness of the rotomoulded PE safety steps decreased with the addition of fly-ash; the increased melt viscosity may have allowed for better dispersion of the melt during rotomoulding.

Phase 2 of this study focused upon developing a numerical database of material properties required for computer simulation of the compression tests conducted on rotomoulded PE/fly-ash composite safety steps. FEA was used to approximate the sidewall deflection of the safety steps for comparison with actual sidewall deflection measurements. This exercise also served as a method of identifying the numerical material parameters required for FEA of the new high stiffness PE/fly-ash composite material; it was found that the tensile modulus, stress at yield, Poisson's ratio and tensile stress-strain response play an influential role in the outcome of FEA. Furthermore, the geometry of the structure, mesh quality and boundary conditions of the FE model (e.g. loads or constraints) are critical to the accuracy of FEA. With the parameters for FEA identified, physical tests were conducted on rotomoulded PE/fly-ash materials and the corresponding data was applied within FEA software; the resulting approximations of sidewall deflection coincided reasonably well with physical measurements (depending on the analysis type, mesh and material data of the FE model), confirming the practical value of the numerical material data. However, in some instances significant differences between FEA and the actual safety step are probably due to the effect of various complex factors such as the non-linear behaviour of PE and the variation in wall thickness of rotomoulded parts. These differences between FE model assumptions and physical rotomoulded parts arguably contribute to the accuracy of FEA, exemplifying the importance of properly understanding the FEM for rotomoulded parts.

During this study, both the tensile and flexural properties of the test materials were determined. It was seen that the tensile properties of all PE/filler composites coincided well with the flexural properties. In order to rationalise the volume of data discussed in this thesis, it was decided that in the majority of cases only the tensile properties of PE/filler composites will be discussed, along with a selection of other important data such as MFR and Charpy impact properties.

5.2 Characterisation of Materials for Composite Development

5.2.1 *Effect of polymer structure*

The principal PE matrix used in this investigation comprised of a blend of MA-g-LLDPE (25 % wt.) with LMDPE; the presence of the MA coupling additive warrants the description “maleanised PE”. For composites manufactured without the MA-g-LLDPE coupling additive, the matrix comprised of a blend of 25 % wt. LLDPE (without MA grafting) with 75 % wt. LMDPE; the latter is described as “analogue PE”. MA-g-LLDPE was introduced to improve filler-matrix interaction; the level of MA-g-LLDPE selected was experimentally determined by the industrial partner for the large particle composite application concerned, where the composites were made using a dry blending approach. The melt flow rate (MFR) of both the maleanised and non maleanised PE is displayed within Table 5 below, both of which the industrial sponsor Rotomotive Ltd. confirmed to be suitable for rotomoulding by previous investigation. The difference in MFR between both the maleanised and non-maleanised PE grades was negligible, indicating the introduction of maleic anhydride to PE (in this instance) has no real impact on the MFR. However, it was appreciated that the addition of fly-ash particles to PE does have a negative impact on the MFR (Section 5.8).

Table 5. Melt flow rate of maleanised and analogue PE used in this work.

Melt Flow Rate	Maleanised PE	Standard Deviation	Analogue PE	Standard Deviation
dg min ⁻¹	3.424	0.025	3.415	0.014

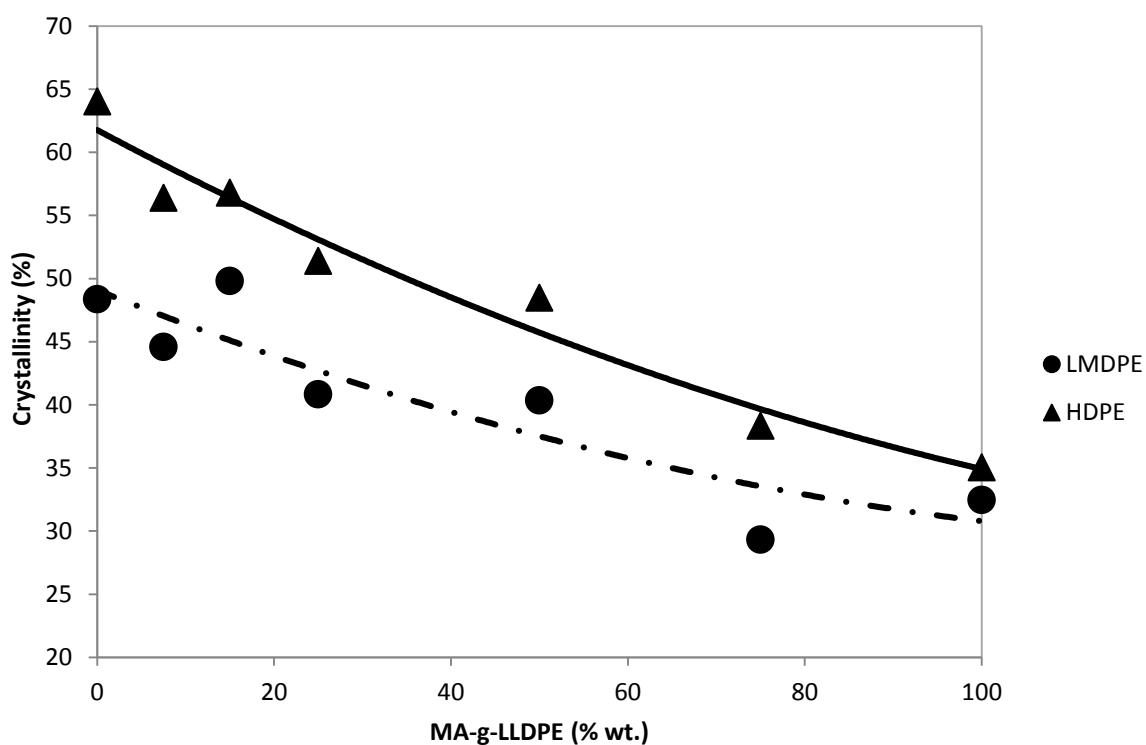
5.2.2 *Dual polyethylene blends*

5.2.2.1 *Dry blended formulations*

Dry blending MA-g-LLDPE with HDPE (replacing LMDPE) was conducted in an attempt to further improve the mechanical properties of the base PE used for composites in this work. Differential Scanning Calorimetry (DSC) data indicated HDPE and LMDPE are inherently of higher crystallinity than MA-g-LLDPE (with HDPE having the highest crystalline content). When combined with MA-g-LLDPE their % crystallinity progressively decreases; these crystalline regions are effectively the mechanical reinforcing phases of PE. Figures 37-39 display graphs of results (note that in some instances the error bars appear absent as they were smaller than the plot symbols). Tables containing standard deviation data for tensile parameters found in this investigation are available within the Appendix Section 3. The relevant Appendix table number is provided in the figure caption. A compilation of all DSC data is provided in Appendix Section 4. Table 6 identifies the various concentrations of HDPE or LMDPE with MA-g-LLDPE; eight replicate samples of each blend combination were tested, five of the most consistent values were selected and averaged.

Table 6. Combinations of MA-g-LLDPE with HDPE or LMDPE.

MA-g-LLDPE (% wt.)	LMDPE or HDPE (% wt.)
0	100
7.5	92.5
15	85
25	75
50	50
75	25
100	0

**Figure 37.** Crystalline content of LMDPE or HDPE with the addition of MA-g-LLDPE.

Increasing the level of MA-g-LLDPE in HDPE or LMDPE progressively reduced the tensile properties. Evidently, similar progressive decreases in tensile properties were observed when LMDPE was dry blended with the maleanised LLDPE. In this case the drop in properties is not as steep as observed with the HDPE/maleanised LLDPE blends because LMDPE has properties closer to that of the maleanised LLDPE. Figures 37-39 indicate that 100 % LMDPE and HDPE specimens have inherently better modulus and yield strength in comparison to equivalent specimens compounded with MA-g-LLDPE. HDPE's superior mechanical performance relative to LMDPE can be attributed to its inherently more crystalline structure, confirming the strong relationship between the structural formation of polymers and their mechanical properties. The latter results indicate that HDPE may be a better matrix than LMDPE, if composite stiffness is the major objective.

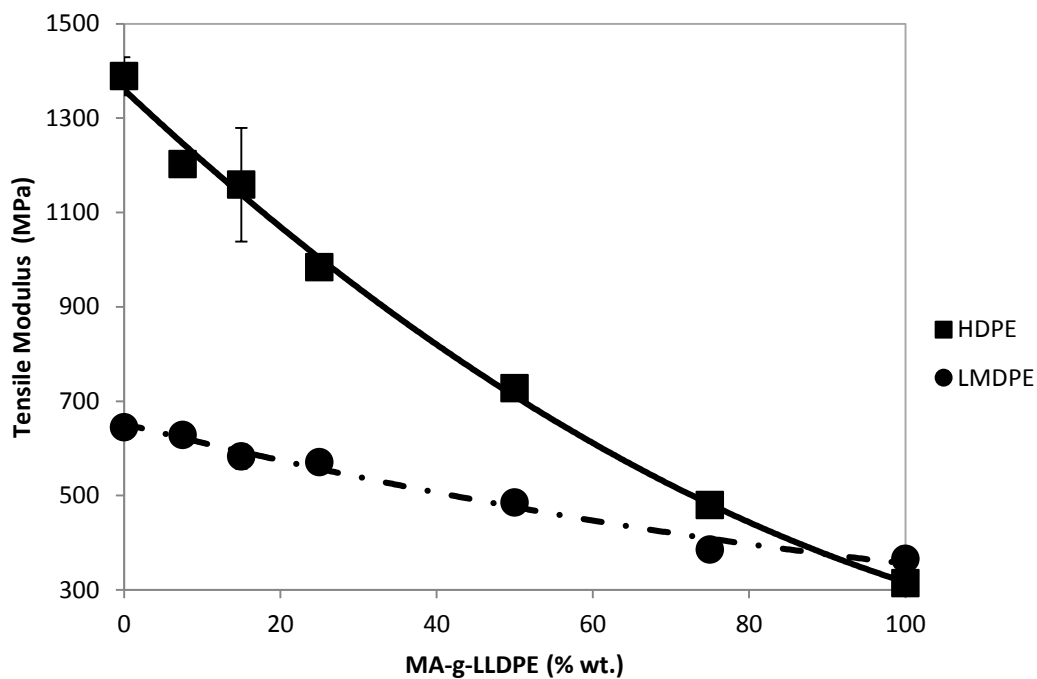


Figure 38. Tensile modulus of HDPE or LMDPE with the addition of MA-g-LLDPE (Tables 35 and 36 in the Appendix Section 3 display standard deviations).

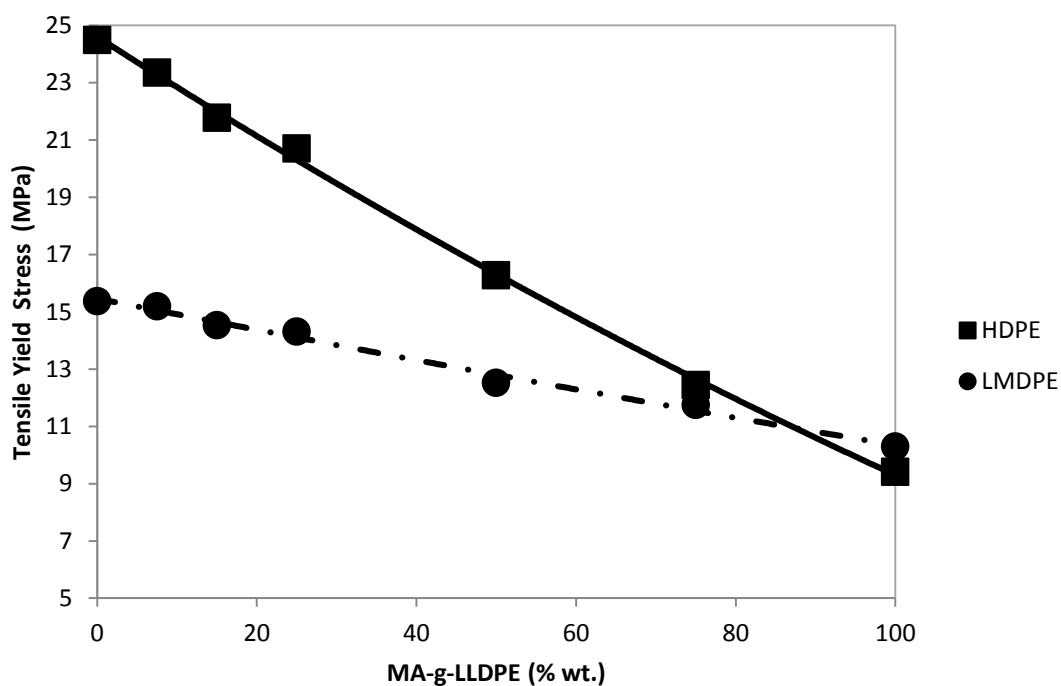


Figure 39. Tensile stress at yield of HDPE or LMDPE with the addition of MA-g-LLDPE (Tables 35 and 36 in the Appendix Section 3 display standard deviations)

5.2.2.2 Twin screw extrusion compounded formulations

It was suggested to melt blend (instead of dry blending) HDPE with MA-g-LLDPE, mould specimens and test for mechanical response. The twin screw extrusion (TSE) compounding technique offers some excellent benefits:

- Continuous mixing process.
- Ideal for blending particles of different size fraction (micro/macro mixing).
- Electro-mechanical control over shear force and temperature, unachievable by two roll mill or dry blending.
- Blends are more homogenous, promoting good dispersion with ease of reproducibility.

TSE compounding is a continuous process where polymer and/or filler are introduced inside the bore of a pre-defined space envelope containing two identical co-rotating, co-penetrating, self-cleaning screws. The surface temperature of the bore and screws are above the melting temperature of the polymer used, therefore the polymer and/or filler is continuously melt blended under high pressure and temperature (Experimental Section 4.4.3). The resulting viscous blend leaves the bore of the extruder at high pressure through a small die, where by the extrudate strands pass through a cooling trough containing water to an integrated pelletiser. Table 6 displays blend information for this investigation, Figures 40-43 display tensile test results against DSC data.

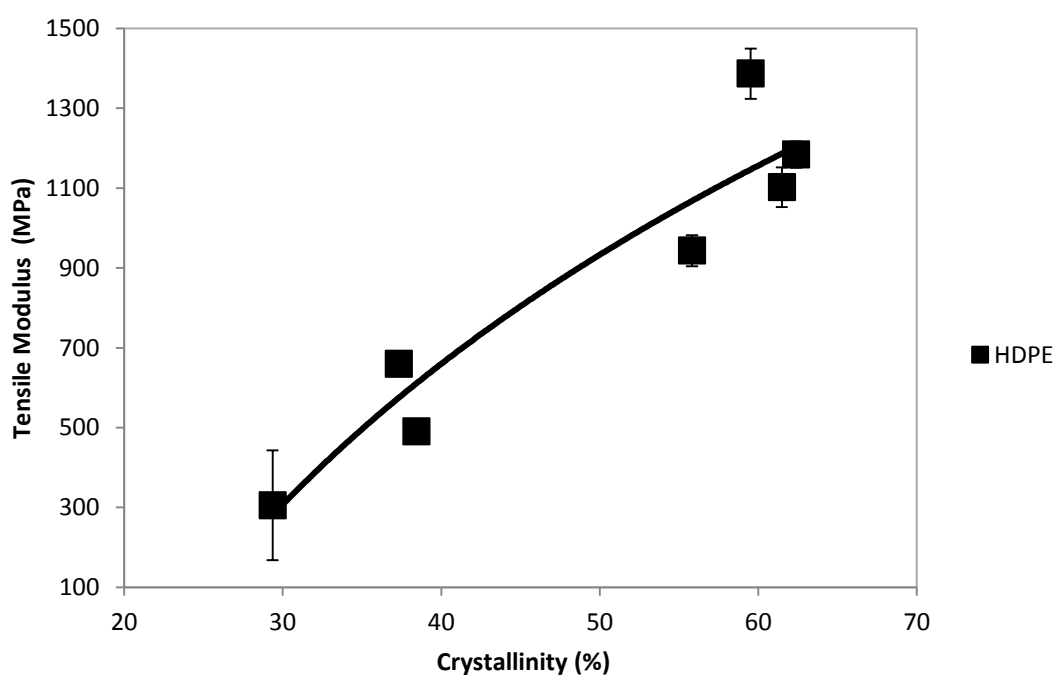


Figure 40. Tensile modulus vs. crystallinity content of HDPE compounded with MA-g-LLDPE
(Table 37 in the Appendix Section 3 displays standard deviations)

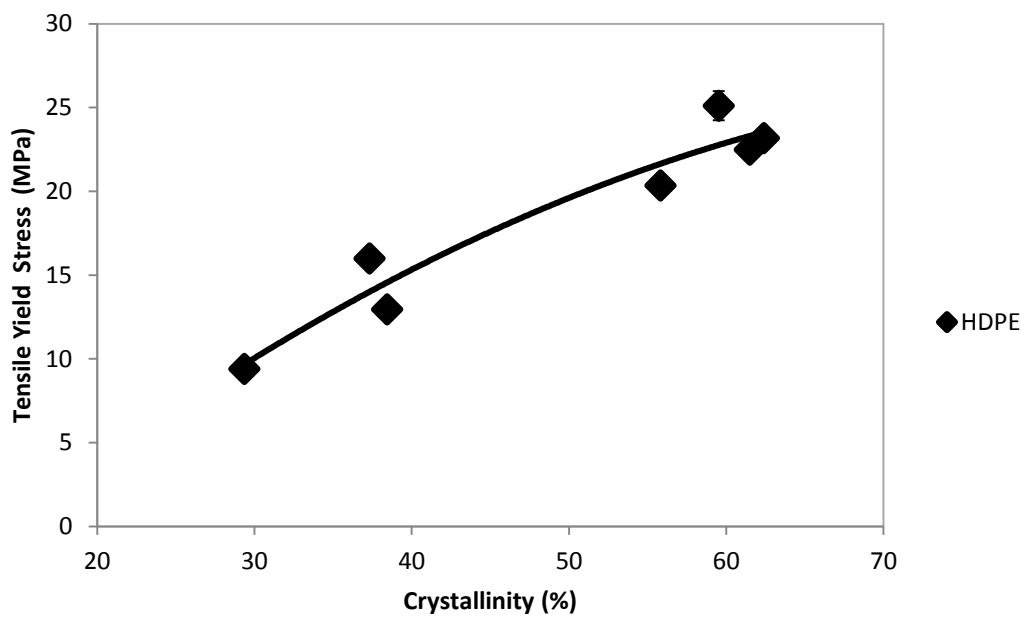


Figure 41. Tensile stress at yield vs. crystallinity content of HDPE compounded with MA-g-LLDPE (Table 37 in the Appendix Section 3 displays standard deviations).

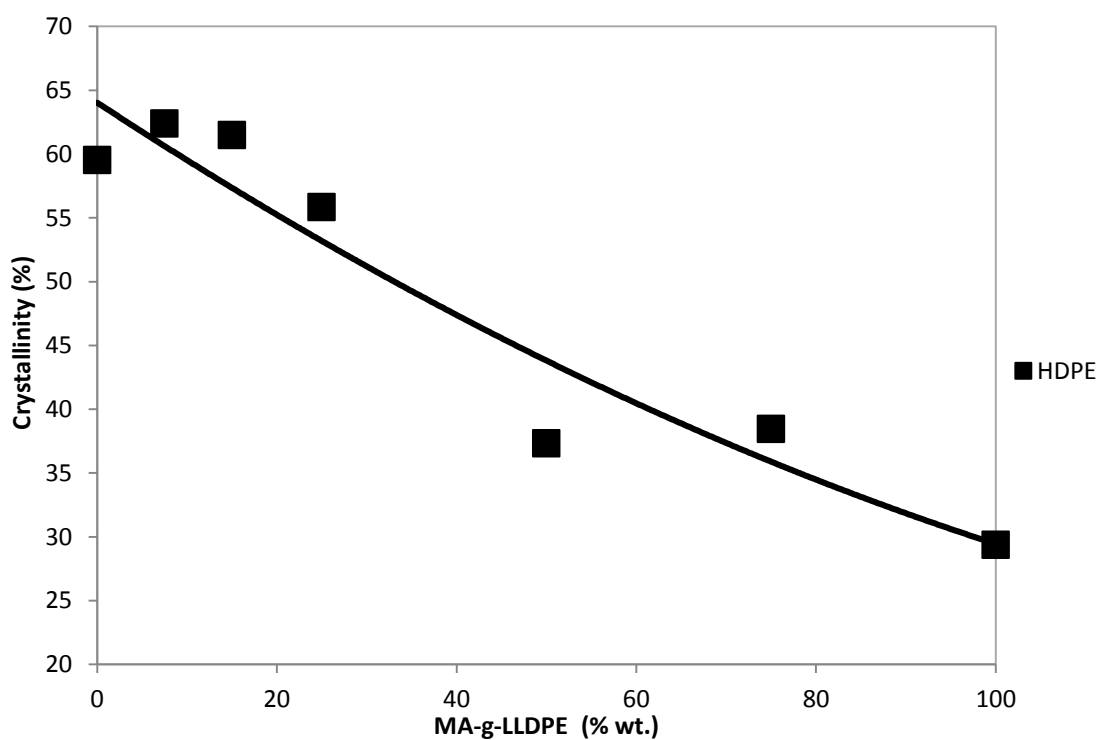


Figure 42. Crystalline content of HDPE with the addition of MA-g-LLDPE/LMDPE.

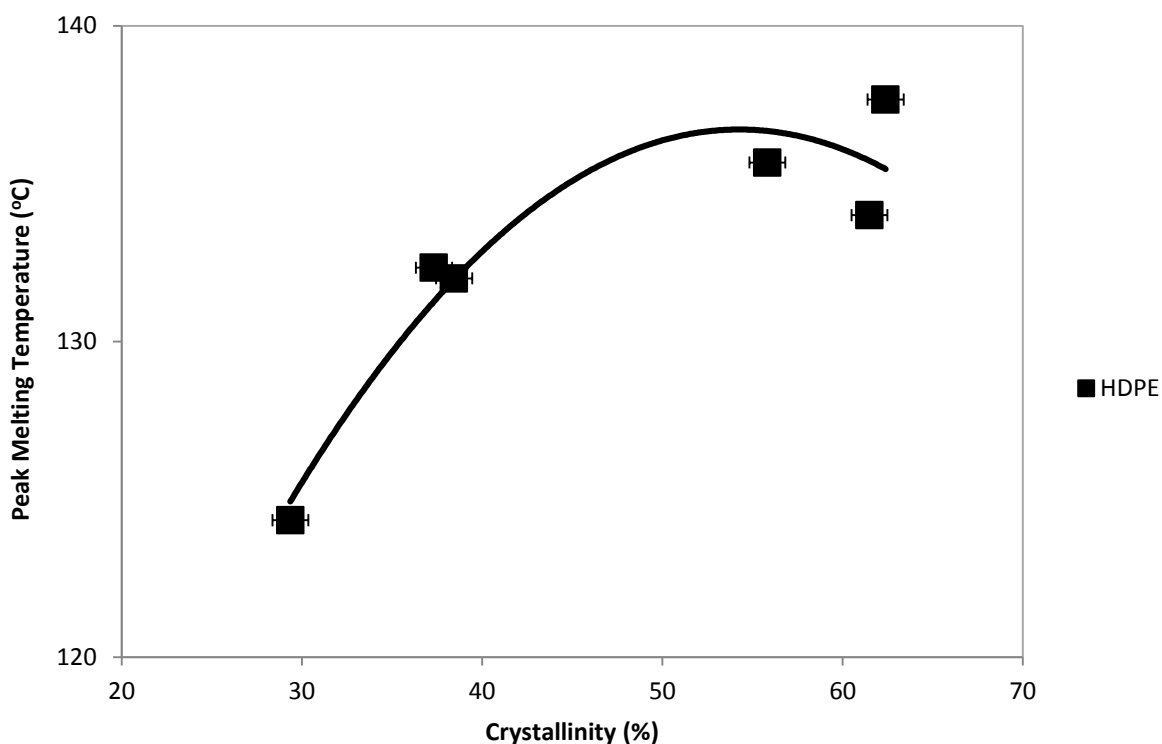


Figure 43. Peak melting temperature vs. crystallinity of HDPE compounded with MA-g-LLDPE.

The addition of MA-g-LLDPE to HDPE reduced the tensile parameters investigated (Figures 40 and 41) in comparison to 100 % HDPE. This decrease in mechanical properties is attributed to the rise in the level of amorphous (non-crystalline) material in the blend as the amount of MA-g-LLDPE is increased. The crystalline content within PE has a profound influence on mechanical properties; for example, in HDPE the hydrocarbon chains have a lower degree of branching, this allows the chains to pack together more easily into a uniform crystalline structure. MA-g-LLDPE contains a larger degree of chain branching therefore making it difficult to pack chains in a uniform fashion, giving a lower crystalline content than HDPE (Figure 42). The higher melting point of HDPE also indicates that the length of chains involved in a crystal structure is increased due to a very low level of branching (Figure 43). Due to the relatively large number of branches in MA-g-LLDPE, the amount of chains that can pack into a crystal lattice reduces, leading to reduced crystalline content, lamellar thickness and melting temperature. Figures 40-43 confirm the intimate relationship between the crystallinity, melting temperature and mechanical properties of PE.

Melt blending HDPE with MA-g-LLDPE offered better performance relative to LMDPE compounded with MA-g-LLDPE. However, DSC and mechanical test results on equivalent specimens prepared by dry blending and compression moulding revealed that only small improvements were evident relative to equivalent melt compounded samples. The crystallinity, mechanical properties and melting temperature still decreased in HDPE with increasing levels of

MA-g-LLDPE. Although increases in crystallinity were observed with the addition of HDPE (replacing LMDPE) to MA-g-LLDPE, it was decided to remain the current 25% wt. MA-g-LLDPE/ 75 % wt. LMDPE formulation for initial investigations; LMDPE is popular amongst rotomoulders because of its good balance between the desired melt flow behaviour and mechanical properties

5.2.3 *Key findings from the characterisation of materials for composite development*

For the purpose of clarity, the key findings of this investigation are summarised in the following bullet points:

- The difference in MFR between the maleanised and non-maleanised PE grade is negligible; the introduction of maleic anhydride to PE (in this instance) has no real impact on the MFR.
- HDPE and LMDPE are inherently of higher crystallinity than MA-g-LLDPE (with HDPE having the highest crystalline content). When combined with MA-g-LLDPE their % crystallinity and tensile properties progressively decreases; these crystalline regions are effectively the mechanical reinforcing phases of PE.
- Dry blending LMDPE with the maleanised LLDPE (rather than TSE compounding) progressive decreases the tensile properties. In this case the drop in properties is not as steep as observed with the HDPE/maleanised LLDPE blends because LMDPE has properties closer to that of the maleanised LLDPE. However, only small improvements were evident with melt compounded samples, relative to dry blended equivalents.

5.3 Analyses of Selected Candidate Fillers

The sand, garnet and cenosphere particles selected for this study were also used in preliminary studies carried out by the industrial sponsor; these fillers were therefore considered as valuable references on which to base the current project. The sand and garnet particles are considered large by normal (i.e. conventionally melt processed) particulate-filled composite standards. It has to be appreciated that the composites under investigation here are formed via rotational moulding (RM); this process is unique in that it relies on the inherent self-adhesion and coalescence of individual polymer melt particles. Therefore, the addition of fillers should ideally have minimal impact on the viscosity of the composite melt. Under such circumstances, large particles of low specific surface area and low aspect ratio (i.e. unity-spheroid or cubic) are likely to be a sensible choice.

The cenospheres were selected due to their low density (they are essentially hollow silica spheres filled with air); it was envisaged that highly filled composites of low density could be formed. Cenospheres are also a waste product of fossil fuelled electric power generation, use as a filler would avoid them going to land fill. Fly ash essentially consists of solid spherical silica particles that are an order of magnitude smaller than the sand, garnet and cenospheres. Fly ash has been used in previous work conducted by the fillers group at MMU [226]. Fly ash is also a waste product of fossil fuel combustion. It was initially considered that fly ash could be used in conjunction with cenospheres in an attempt to maximise filler volume fraction in that the small fly ash particles would fit in to the interstices between the larger cenospheres. The diversity in shape, size, and density between candidate fillers used in this work gives good reasoning behind their selection. Specific information regarding filler particle characteristics (size distribution, shape and surface elemental content) is discussed within this section.

5.3.1 *Imaging of the candidate filler materials*

Scanning Electron Microscope (SEM) imaging was used to analyse the particle size, shape and surfaces of the candidate fillers for this work (Figures 44-48). The presence of smaller particles on the fly-ash particles surfaces were observed with SEM imaging (Figure 48). Consequently, Energy dispersive x-ray (EDX) analysis was used to analyse the elemental composition at the surface of the filler particles, the results of which are available within Section 5.3.2.

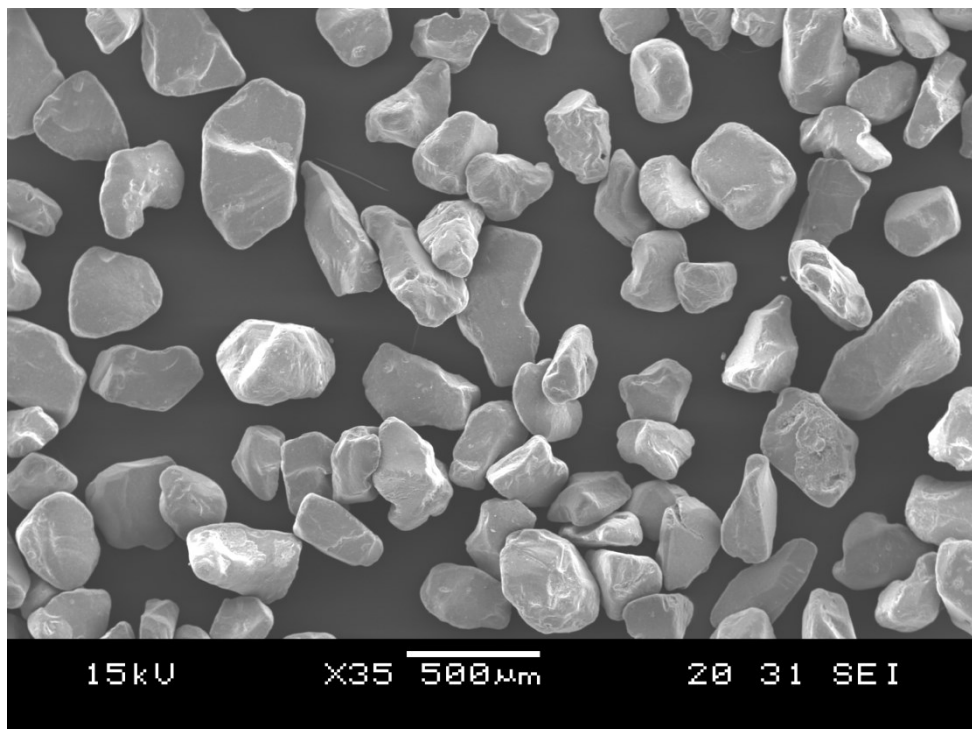


Figure 44. Garnet particles.

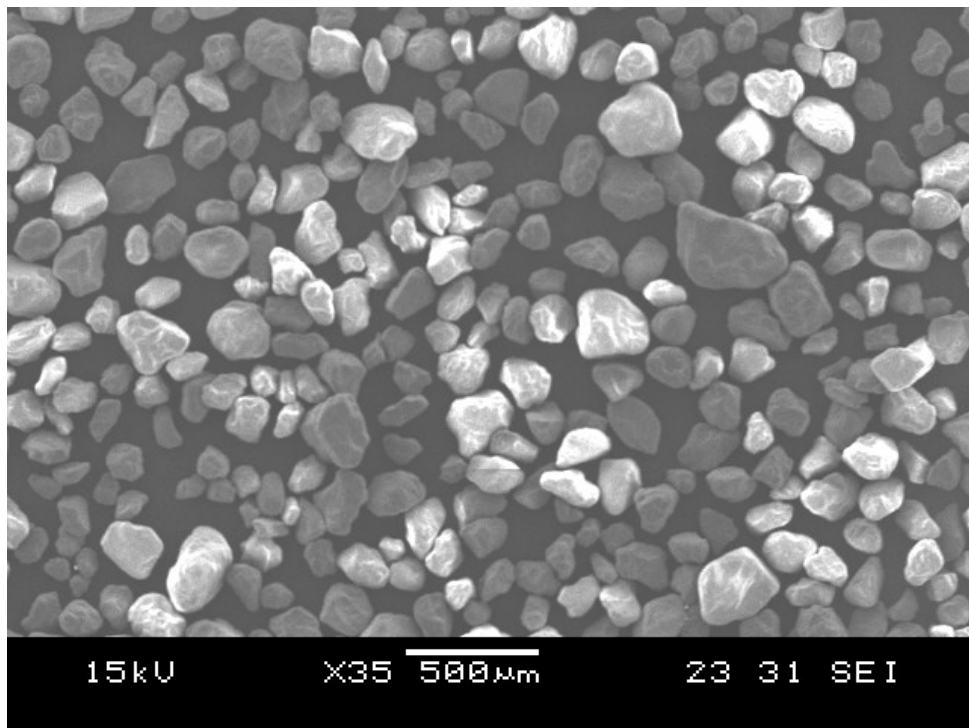


Figure 45. Sand particles.

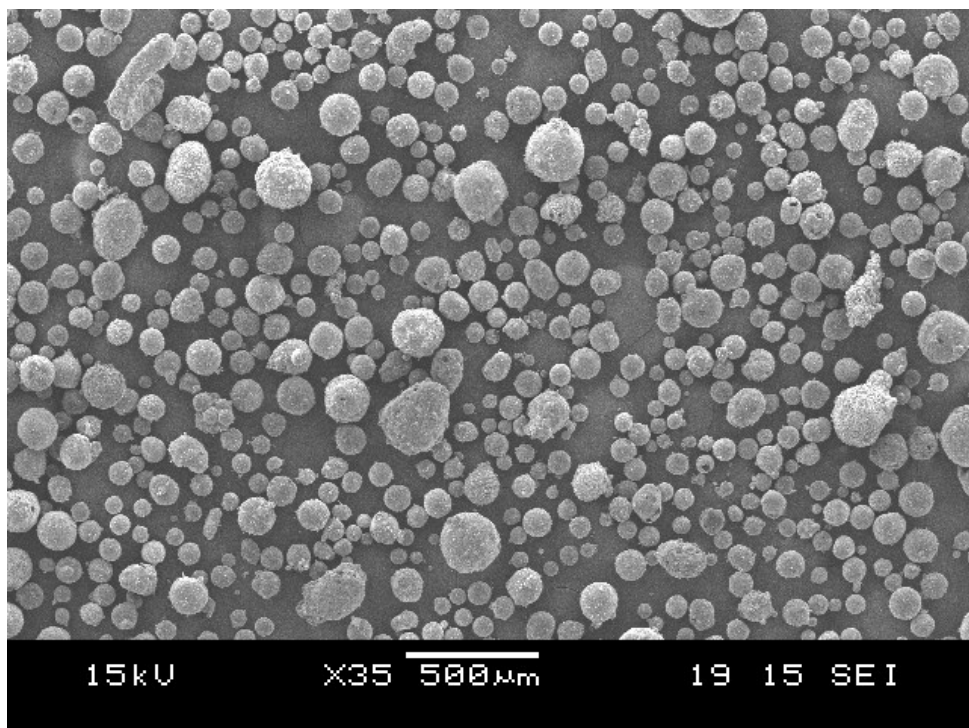


Figure 46. Cenosphere particles.

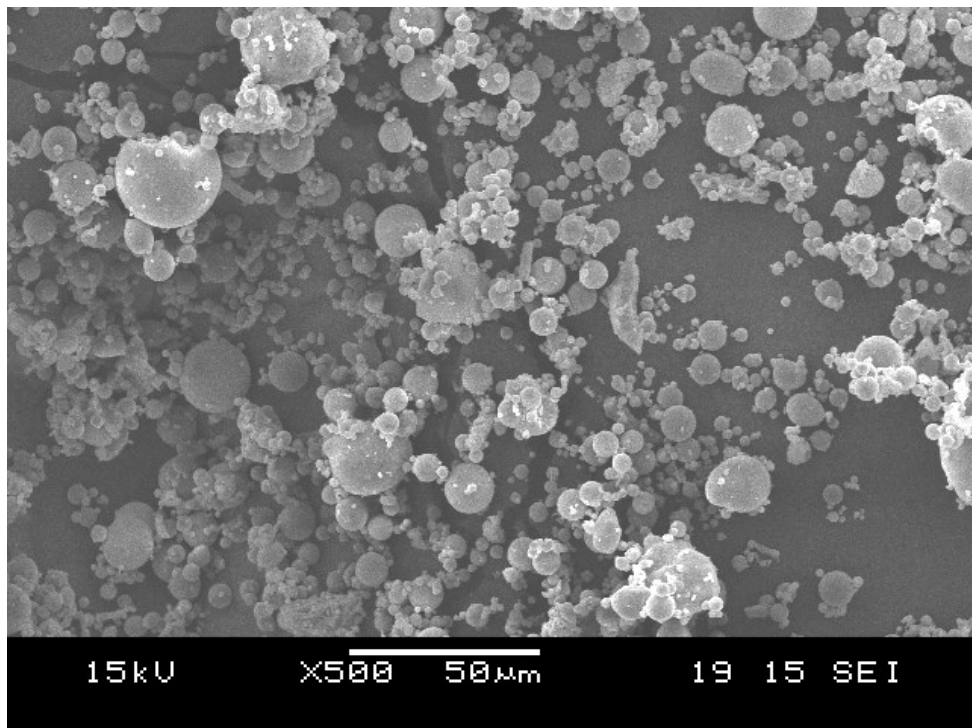


Figure 47. Fly-ash particles (note the large increase in magnification).

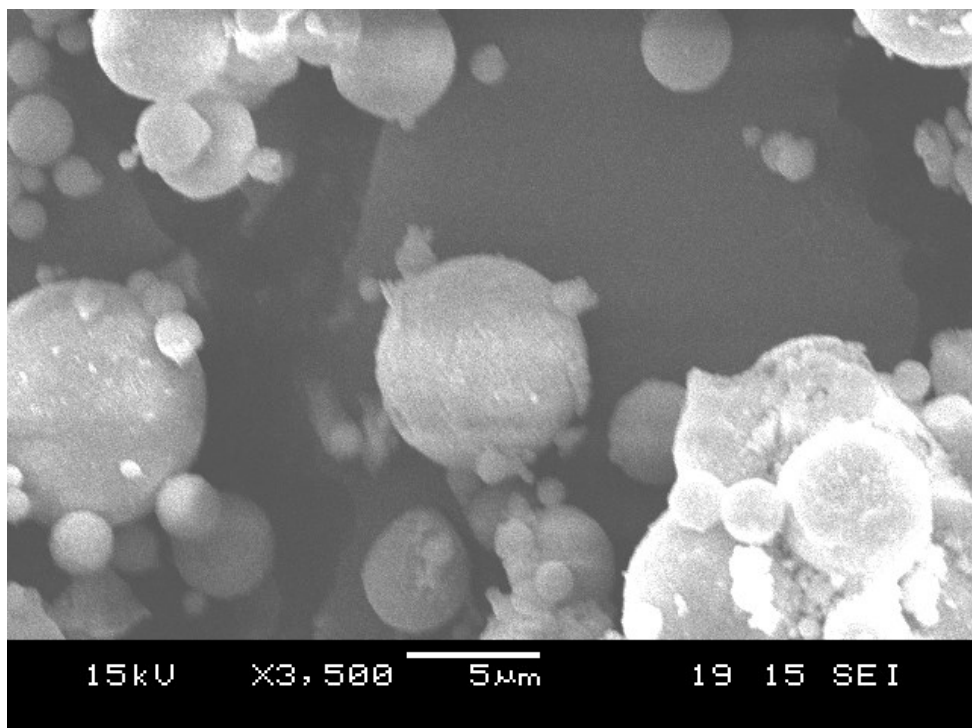


Figure 48. Fly-ash particles.

5.3.1.1 Sieve analysis for construction of particle size distribution

Sieve analysis on the candidate fillers was conducted to assess their particle size distribution (PSD). Figures 49 and 50 identify the PSD data obtained by sieve analysis for garnet, sand, cenosphere and fly-ash particles. It was observed that the fly-ash particles are under 90 μm in size whereas the cenosphere particles (essentially larger size fractions of fly-ash obtained from coal

fired power stations) are generally an order of magnitude larger. This coincides well with the larger magnifications required for SEM imaging of the fly-ash and cenosphere particles (Figure 46-48). However, the garnet and sand particles (relative to cenospheres and fly-ash) are larger in size, with the majority of garnet particles passing through 150-212 μm sieves. Conversely, the majority of sand particles (which are similar in shape and elemental composition to that of garnet particles, (refer to Section 5.3.2) pass through 90-150 μm sieves. These observations coincide with SEM images of garnet and sand particles (Figures 44 and 45). Overall, the fly-ash particles are considerably smaller than the other candidate fillers and the garnet particles are the largest. However, garnet and sand particles are irregular in shape whereas cenospheres and fly-ash are spherical.

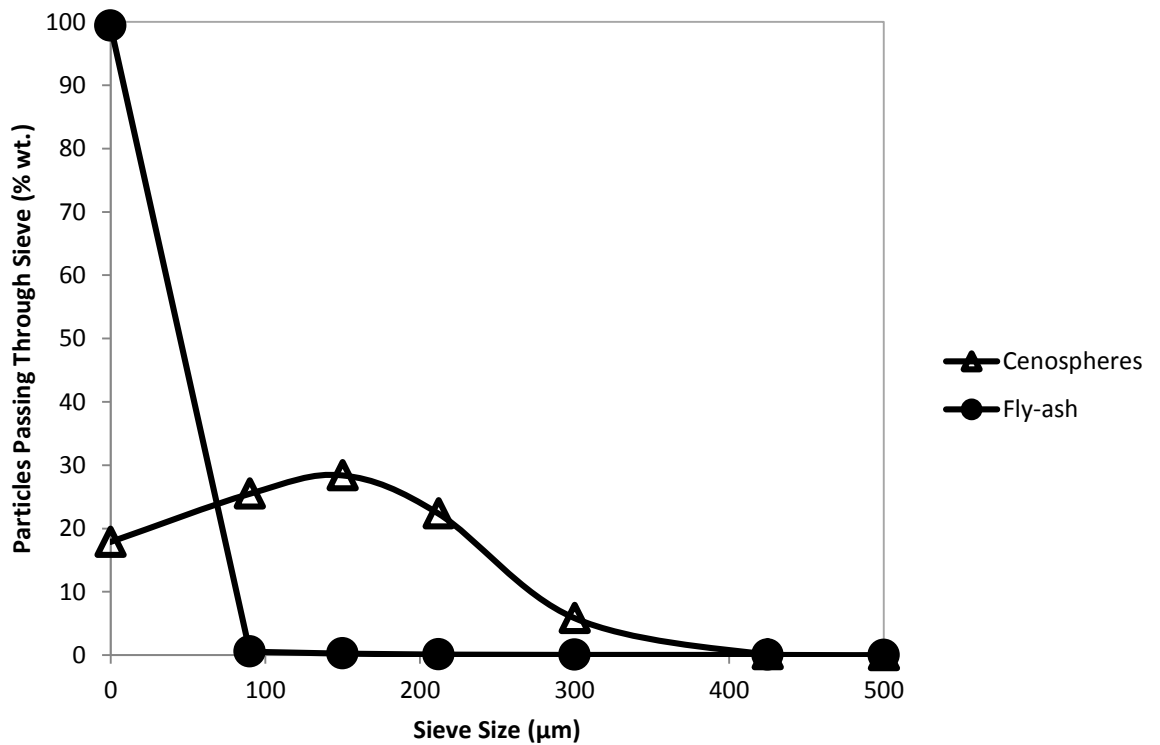


Figure 49. Particles size distribution of fly-ash and cenosphere particles.

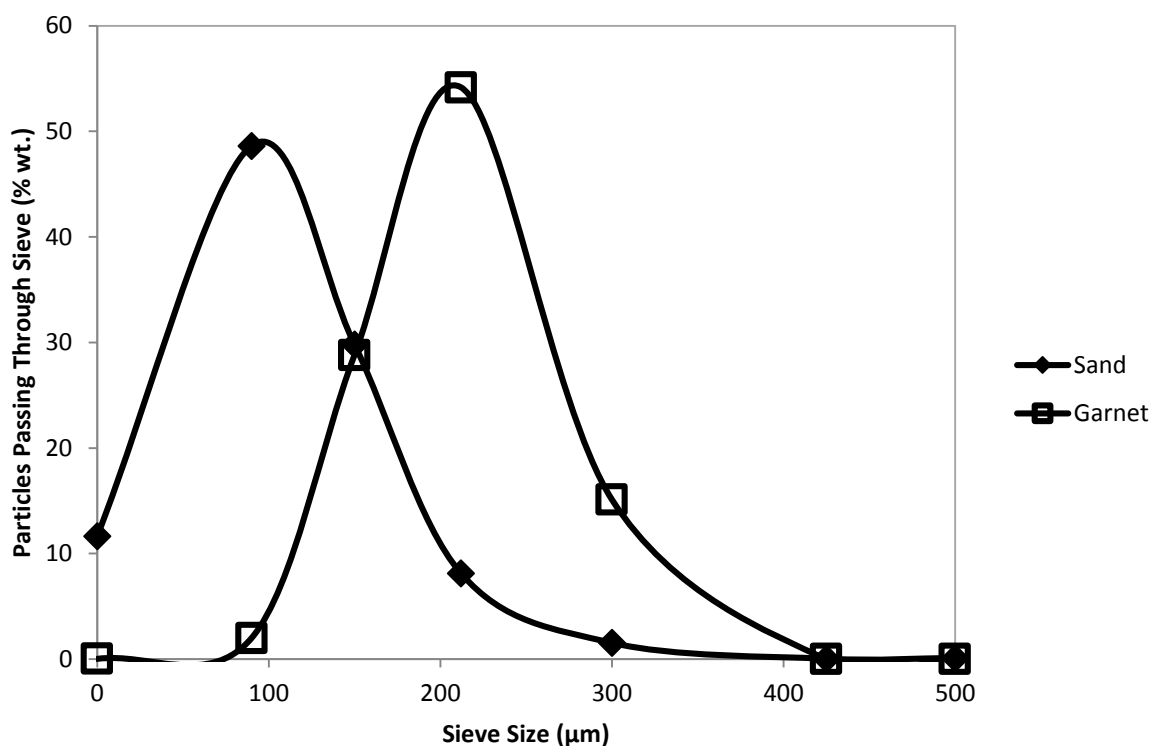


Figure 50. Particle size distribution of sand and garnet particles.

5.3.2 Energy dispersive x-ray analysis

The sand and garnet particles (Figure 51) comprise of the same elements (C, O, Mg, Si, Fe and Al) except in the case of Mn and K which are exclusive to garnet and Ca which is exclusive to sand. Sand is mainly silicon dioxide (SiO_2) and garnet is mainly $\text{Fe}_3\text{Al}_2\text{Si}_3\text{O}_{12}$. However, sand has a considerably larger percentage by wt. of its common elements with garnet particles, especially in the case of Mg, Si, Al and Fe. Fly-ash and cenospheres (Figure 52) share the common elements C, O, Mg, Si, Fe, Al, Ca, Ti and K. Both the fly ash and the cenospheres will differ in elemental composition according to the mineral content in the coal from which they originate; the latter will obviously vary geographically. Fly ash is sometimes washed before being released as filler grade material. The latter is true of the Mintron 7 fly-ash (Experimental Section 4.2) obtained from Fiddlers Ferry power station for this study. In recent work submitted for publication, Mintron 7 has been compared to a fly ash sourced from South Africa. Mintron 7 was found to be the superior filler as it interacted strongly and irreversibly with an unsaturated coupling agent and thus promoted improved composite mechanical properties to the South African fly-ash [226].

To conclude, the elements identified were unsurprising; candidate filler particle surfaces hosted elements which form the very chemical composition of the fillers themselves. However, the content of carbon apparent in garnet and sand samples could be from the adhesive tape used to stick the particles on the mounting stub before EDX analysis. It is reasonable to expect that fly ash

and cenospheres could contain some carbon, bearing in mind that they are the combustion residue of coal.

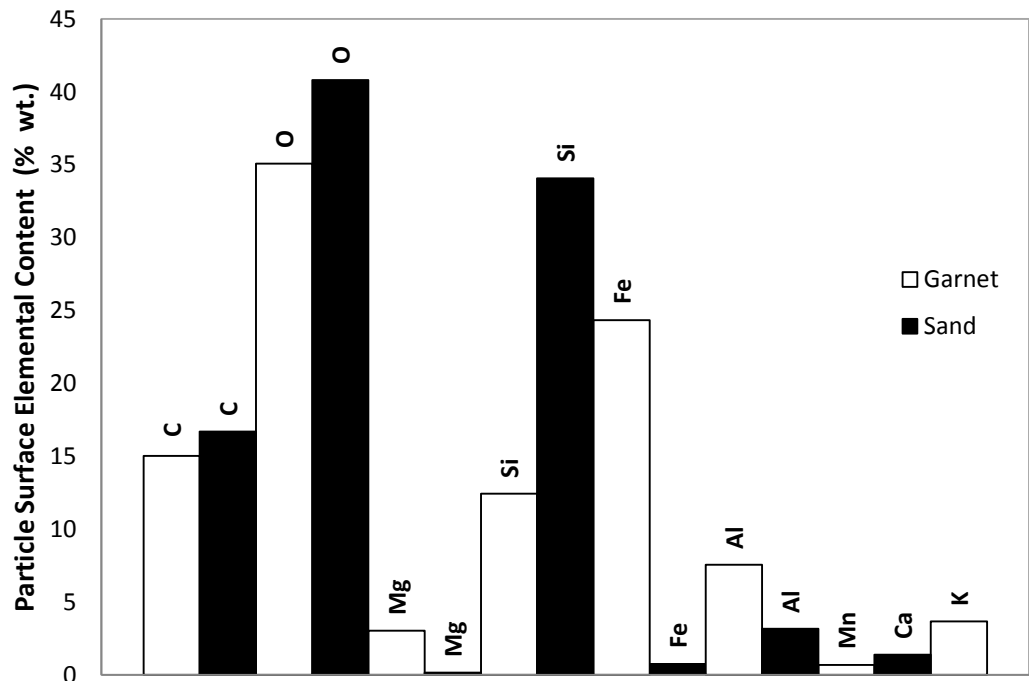


Figure 51. Elemental content on the surfaces of garnet and sand particles.

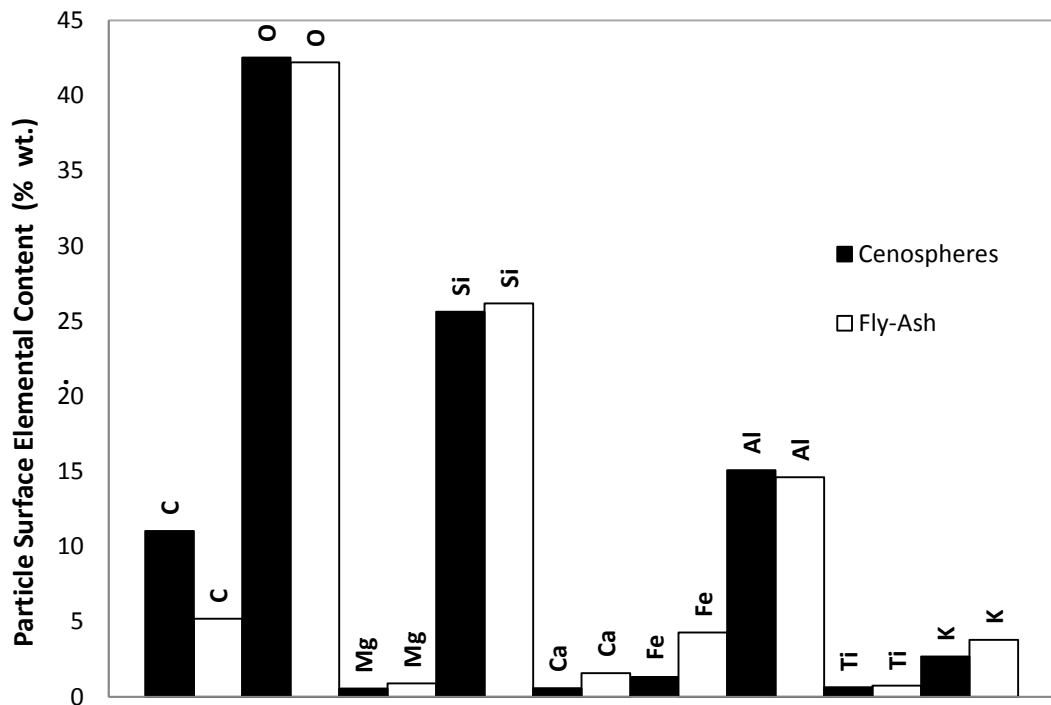


Figure 52. Elemental content on the surfaces of fly-ash and cenosphere particles.

5.3.3 *Density of the candidate filler materials*

Liquid displacement density tests were conducted on all candidate fillers (Experimental Section 4.3.3); the corresponding results were required for composite design specification (mass, volume, stiffness). In the case of the hollow, spherical cenospheres, particle rupture can occur when blended with PE, this can be detected via composite density tests; the cenospheres are hollow spheres filled with air, if crushed during processing the density of the composite will be higher than expected, removing the advantage of conferring low density to the composite. Table 7 displays results of density tests for each filler candidate. Garnet has the highest density followed by sand. Fly-ash particles are effectively small size cenosphere fractions but have a higher density than cenospheres; cenospheres are hollow particles filled with air, hence the low density relative to fly-ash particles. The selected filler candidates used for this work possess a useful range in terms of density, presenting the opportunity to adjust composite density via a combination of two or more fillers; this is advantageous if modifying component mass is the major objective.

Table 7. Densities of filler candidates used in this work.

Density	Sand	Standard Deviation	Cenosphere	Standard Deviation	Fly-ash	Standard Deviation	Garnet	Standard Deviation
g cm ⁻³	2.67	0.05	0.74	0.07	2.3	0.02	4.08	0.03

5.3.4 *Determination of maximum packing fraction*

Determining the maximum packing fraction (MPF) of the candidate filler particles in liquid paraffin (Experimental Section 4.3.2) was a quick, accurate method of approximating the maximum volume of filler particles that can be accommodated by the PE matrix; in some cases, the reinforcement of particulate-filled polymer composites can be maximised by incorporating as much filler as possible into the polymer matrix.

5.3.4.1 *Single filler systems*

Table 8 displays the MPF in liquid paraffin, by mass and volume, of the candidate fillers used for this work. The latter data identifies interesting characteristics of the fillers when taking into account their individual densities, particle shape and size. Determination of the MPF by volume is an informative method of estimating the maximum amount of filler accommodated by the PE matrix. Garnet, fly-ash and cenospheres gave essentially similar results; a slightly unexpected observation considering that the fly-ash particles are much smaller than the cenosphere, garnet and sand particles. Poor dispersion of the particles may have limited the MPF of fly-ash particles. Moreover, the smaller fly-ash particles may have agglomerated; this coalescence of particles forms irregular shapes of various sizes which increases the volume of interstitial voids between particles.

Table 8. MPF of the filler candidates.

Filler	Medium	Mass Fraction	Standard Deviation	Volume Fraction	Standard Deviation
Sand	Liquid Paraffin	0.86	0.06	0.67	0.06
Garnet	Liquid Paraffin	0.85	0.03	0.54	0.01
Cenospheres	Liquid Paraffin	0.51	0.02	0.58	0.02
Fly-ash	Liquid Paraffin	0.76	0.01	0.55	0.01

On the other hand, sand particles maintain the largest maximum packing fraction within liquid paraffin by volume. The high volumetric packing fraction of sand may be due to the size distribution and the angular shape of the sand particles; the angular shape may result in more efficient packing.

5.3.4.2 Dual filler systems

Following initial tests to establish the MPF for the single fillers i.e. cenospheres, sand and garnet (Table 8), it was decided combine the latter fillers with fly-ash; the fly-ash particles are an order of magnitude smaller. Theoretically, particles with finer fractions could occupy interstitial voids between larger particles and increase the MPF for better stiffness enhancement. Furthermore, combining two fillers could also allow for fine adjustments to the composites mechanical properties (i.e. density or stiffness). Table 9 displays the combinations of sand, cenospheres or garnet with fly-ash that were examined.

Table 9. Combinations of sand, garnet or cenospheres with fly-ash particles for MPF tests.

Sand, Garnet or Cenospheres (% wt.)	Fly-ash (% wt.)
0	100
7.5	92.5
15	85
25	75
50	50
75	25
100	0

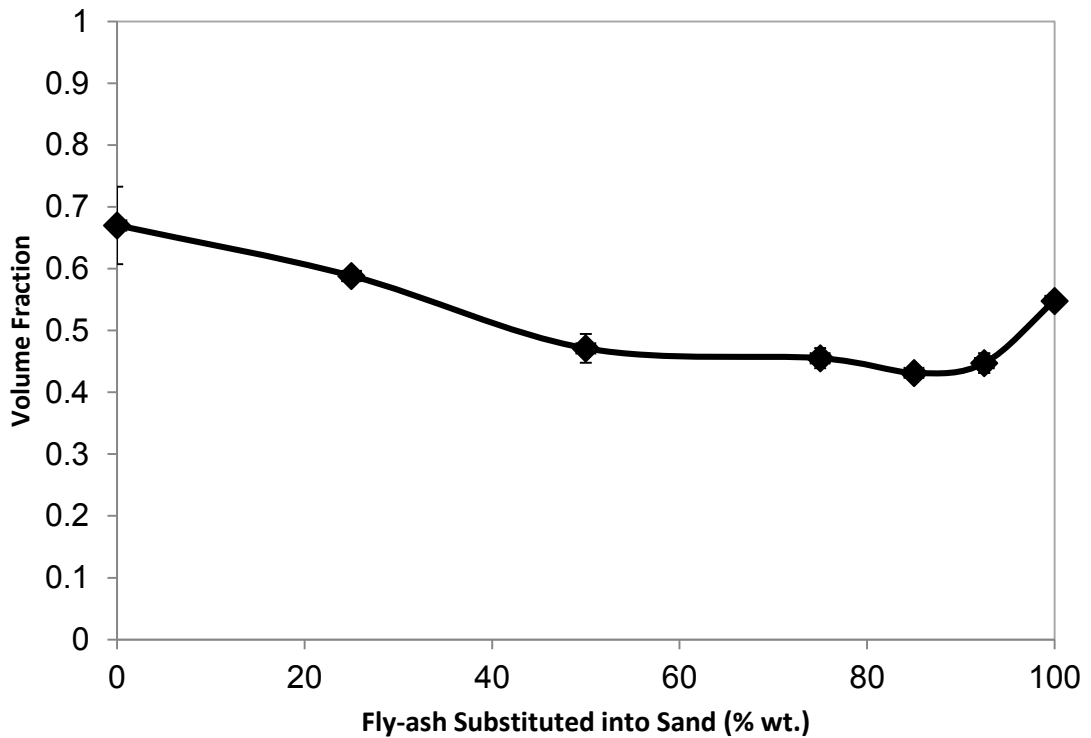


Figure 53. MPF versus fly-ash to sand ratio.

Sand/fly-ash and garnet/fly-ash combinations in liquid paraffin unexpectedly decreased the MPF by volume (Figures 53 and 54). This is probably due to their particle characteristics (shape and distribution) preventing finer, spherical fly-ash fractions from penetrating interstitial voids. Cenospheres combined with up to 50 % wt. fly-ash resulted in a small improvement outside experimental error MPF by volume (Figure 55), implying a degree of interstitial filling had occurred. Whilst this increase in MPF is significant in terms of it being outside experimental error, the actual level of increase is not significant. However, if no interstitial filling had occurred at all, the combination of fly-ash with cenospheres would decrease the value of MPF by volume in a linear fashion proportional to the ratio of cenospheres to fly-ash.

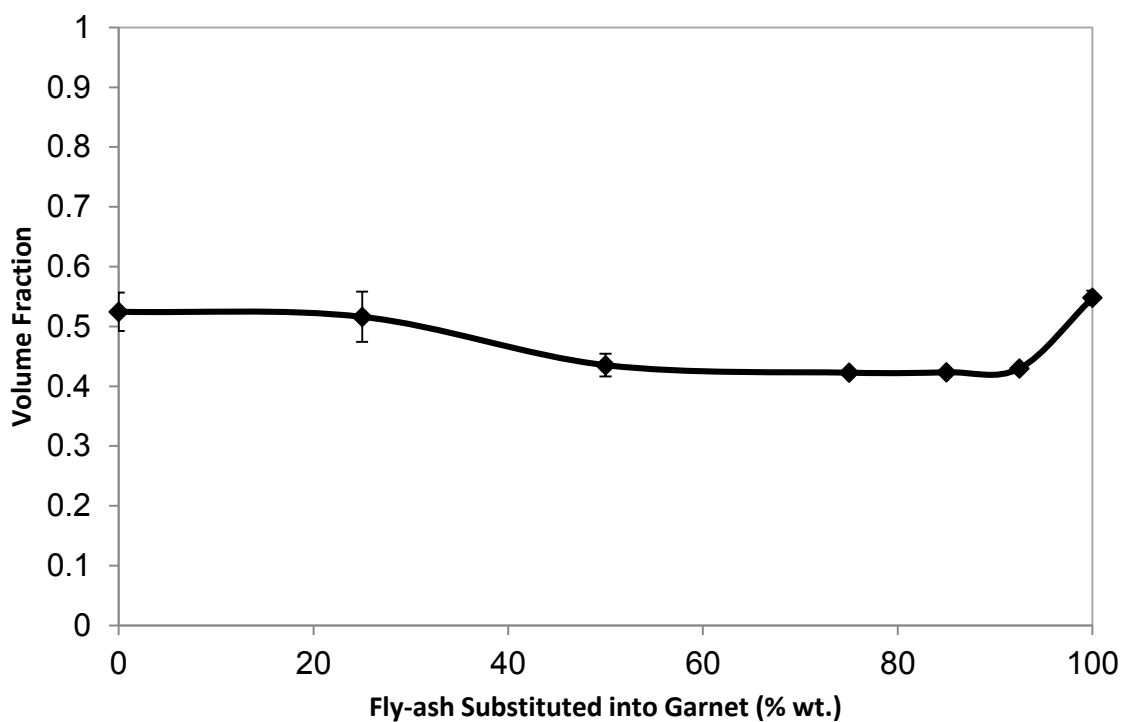


Figure 54. MPF versus fly-ash to garnet ratio.

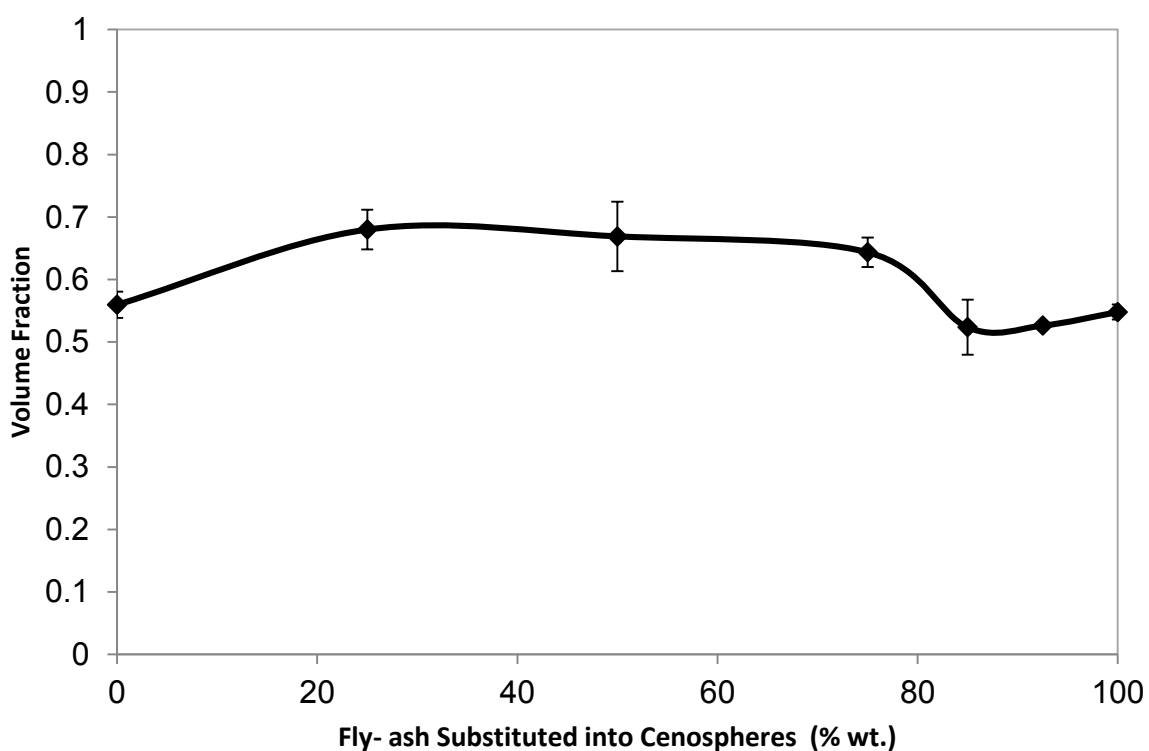


Figure 55. MPF versus fly-ash to cenosphere ratio.

5.3.5 Key findings from analysis of the filler particles

Combining different filler particles in order to increase their MPF in PE is one particularly novel aspect of this research. For the purpose of clarity, the key findings of this investigation are summarised in the following bullet points:

- The fly-ash particles are under 90 μm in size whereas the cenosphere particles are generally an order of magnitude larger. However, the garnet and sand particles (relative to cenospheres and fly-ash) are larger in size, with the majority of garnet particles passing through 150-212 μm sieves. Conversely, the majority of sand particles (which are similar in shape and elemental composition to that of garnet particles), pass through 90-150 μm sieves.
- Garnet and sand particles are irregular in shape whereas cenospheres and fly-ash are spherical.
- The sand and garnet particles comprise of the same elements (C, O, Mg, Si, Fe and Al) except in the case of Mn and K which are exclusive to garnet and Ca which is exclusive to sand. Sand is mainly silicon dioxide (SiO_2) and garnet is mainly $\text{Fe}_3\text{Al}_2\text{Si}_3\text{O}_{12}$. However, sand has a considerably larger percentage by wt. of its common elements with garnet particles, especially in the case of Mg, Si, Al and Fe.
- Fly-ash and cenospheres share the common elements C, O, Mg, Si, Fe, Al, Ca, Ti and K. Both the fly ash and the cenospheres will differ in elemental composition according to the mineral content in the coal from which they originate; the latter will vary geographically.
- Garnet, fly-ash and cenospheres have essentially similar MPF results; a slightly unexpected observation considering that the fly-ash particles are much smaller than the cenosphere, garnet and sand particles. Poor dispersion of the particles may have limited the MPF of fly-ash particles. Moreover, the smaller fly-ash particles may have agglomerated; this coalescence of particles forms irregular shapes of various sizes which increases the volume of interstitial voids between particles.
- The sand particles maintain the largest maximum packing fraction within liquid paraffin by volume. The high volumetric packing fraction of sand may be due to the size distribution and the angular shape of the sand particles; the angular shape may result in more efficient packing.
- Sand/fly-ash and garnet/fly-ash combinations in liquid paraffin unexpectedly decreased the MPF by volume. This is probably due to their particle characteristics (shape and distribution) preventing finer, spherical fly-ash fractions from penetrating interstitial voids.

- Cenospheres combined with up to 50 % wt. fly-ash resulted in a small improvement outside experimental error MPF by volume (Figure 55), implying a degree of interstitial filling had occurred. Whilst this increase in MPF is significant in terms of it being outside experimental error, the actual level of increase is not significant.

5.4 Comparison of Composite Formation Processes for Large Particle Composites (Dry Blending of Pre-Mix versus Two Roll Mill Melt Blending and Moulding)

The initial PE/filler composites were dry blended in the bowl of a Brevil Model SMH2 domestic planetary mixer before moulding. Dry blending was the quickest method of mixing materials for compression moulding; the relatively short production time for dry blended PE/filler composites provided the opportunity to establish firm test protocols quickly. The dry blending approach was also successfully used by the industrial sponsor Rotomotive Ltd. for the large particle application concerned. Therefore, a database of properties was available to compare with the data found in this study. However, it was appreciated that uniform filler particle dispersion quality and sufficient matrix-filler interaction may not be achievable via dry blending and compression moulding; particle dispersion quality and the strength of filler-matrix interaction have a significant effect on the mechanical properties of PE/filler composites. Therefore, a melt blend route was attempted using a two roll mill; the latter method offered the following benefits:

- Both rolls are above the melting temperature (T_m) of PE, physically incorporating the filler particles by shear within a liquid PE matrix.
- The separation and relative rotational speed of individual rolls can be varied by the operator; this allows the level of shear to be precisely tailored.
- Better filler-matrix interaction; the filler particle surface is more intimately wetted by a sheared polymer melt.

Table 10. Blend details of two roll milled and dry blended composites.

MA-g-LLDPE/LMDPE (% wt.)	Filler (% wt.)
100	0
75	25
50	50
40	60
30	70
25	75
20	80
15	85

To assess the effect of blending method on the mechanical properties of PE/filler composites (Table 10), the tensile properties of dry blended PE/filler prepared composites were analysed in comparison to equivalent two roll mill prepared specimens (Figures 56-59). The dry blended PE/cenosphere composites at filler loadings above 60 % wt. were difficult to process thus rendering them brittle and unsuitable for testing. A CNC water jet cutter (operating to a tolerance of $\pm 0.1\text{mm}$) was used to cut flexural and tensile test pieces from composites produced by compression moulding at MMU; these composites were prepared by pre-blending the filler and PE matrix in the melt state using a two roll mill. However, the test materials produced at Rotomotive Ltd. by dry blending the filler with PE and compression moulding were die stamped. The die stamping method was reasonable for the unfilled matrix and the more lightly filled composites, although as filler content increased it became evident that the edges of the test pieces were damaged via this method (manifested as stress whitening). Water jet cutting was a superior method for the production of test pieces relative to die stamping; the edges of even the highly filled composite test pieces were clean with no stress whitening evident. There is obvious potential for the two different test piece preparation methods to confound differences in properties between the composites prepared by melt blending and those prepared by dry blending. It can nevertheless be said with some confidence that composite stiffness will not be affected by the test piece preparation method, as the samples are not stressed to failure during such examination. Due to the presence of defects at the edges of the die stamped samples, it is reasonable to expect them to fail prematurely. Therefore, it can be argued that the ultimate properties (tensile strength and tensile stress at yield) cannot be compared with those composites prepared by water jet cutting. Despite this argument it appears that the superiority of dry blending for production of composites based on larger particles (particularly garnet and to a lesser extent sand) in terms of tensile yield strength is still observable, regardless of the fact the dry blended samples were die stamped (Figure 58).

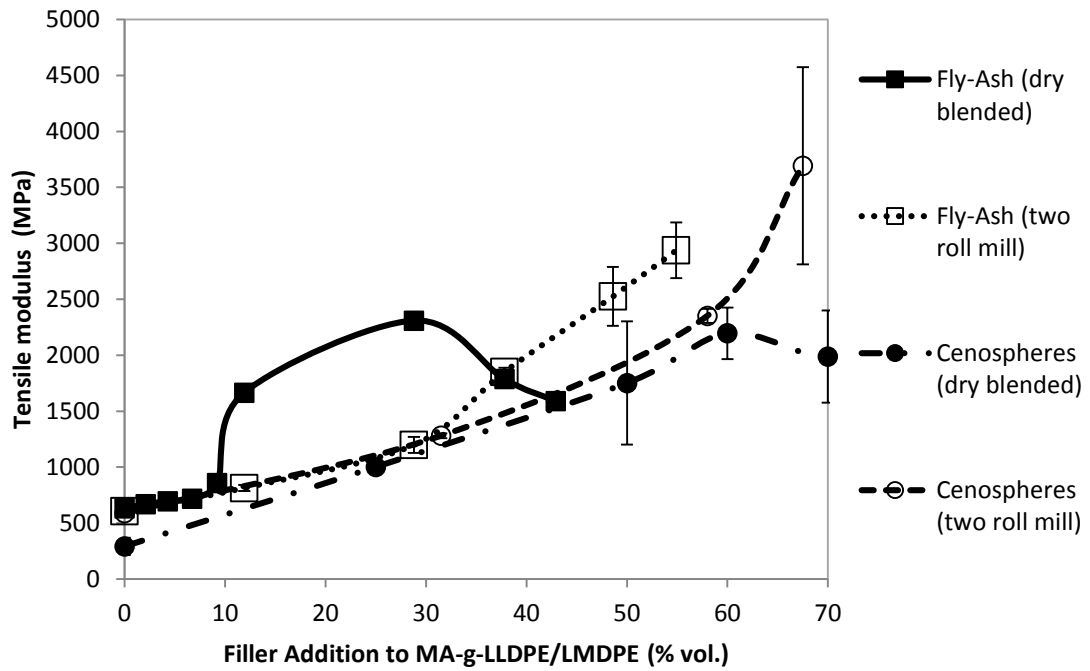


Figure 56. Tensile modulus of fly-ash and cenosphere filled PE composites.

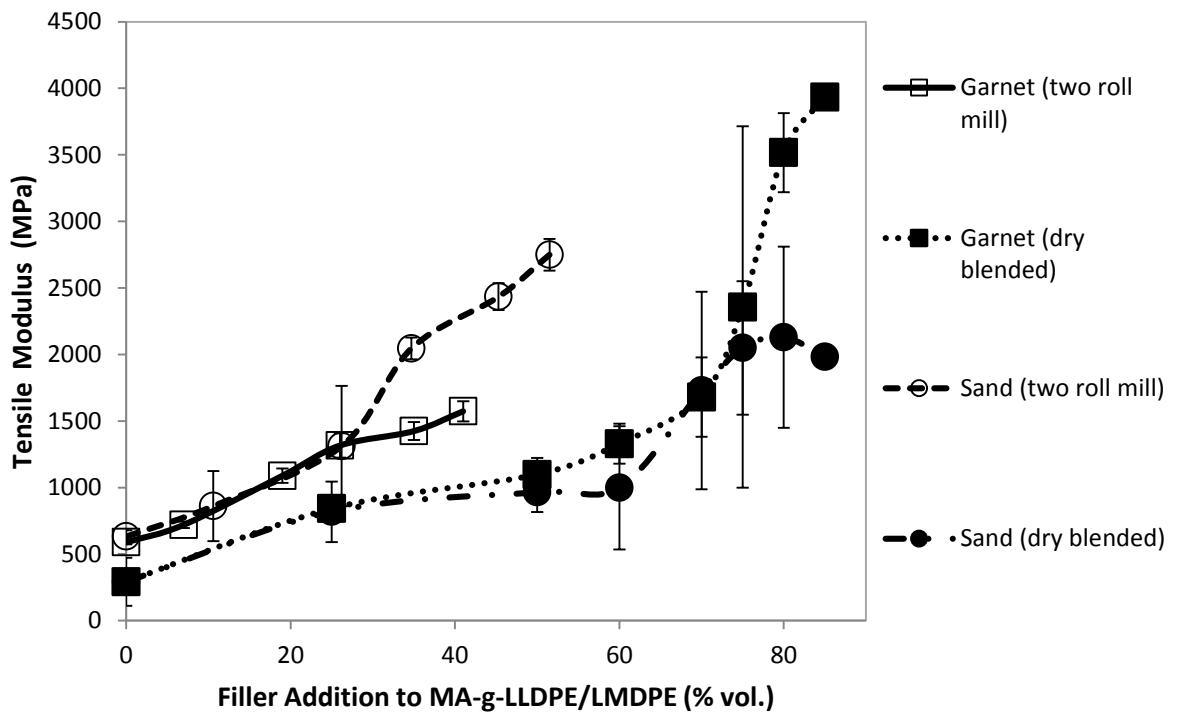


Figure 57. Tensile modulus of garnet and sand filled PE composites.

Figures 56 and 57 indicate two roll milled composites offer significant improvements in tensile modulus for all candidate fillers investigated. A doubling of tensile modulus is considered to be a good result for this study; it is evident that this can be achieved at a filler loading of about 30 % vol. Interestingly, all two roll milled PE/filler composites (with the exception of dry blended PE/fly-ash) increase in modulus with every level of filler investigated. At filler volume fractions less than

ca. 29 % vol., the dry blended PE/fly-ash composites show higher tensile moduli relative to melt blended equivalents (Figure 56). However, beyond 29 % vol. fly-ash the tensile modulus of the dry blended composites decreases. The increased moduli of the dry blended PE/fly ash composites may be due to occluded polymer in the interstices of fly ash aggregates. Occluded polymer is known to increase the effective volume fraction of the filler as the occluded polymer has properties closer to those of the filler rather than the bulk matrix ^[227, 228]. The decrease in tensile modulus may be related to poor wetting of the filler particles by the matrix combined with poor dispersion of the filler beyond ca. 29 % vol.; a similar decrease in the tensile modulus of polypropylene (PP) composites with the addition of Rattan powder particles was also observed by Nurshamila et al. due to poor wetting and dispersion of the filler particles ^[229].

However, the increases in tensile modulus of the two roll milled composites with increasing filler content can be attributed to a better transfer of stress from the flexible PE matrix to the stiffer filler particles, as a result of improved matrix-filler adhesion; the shear force element in the two roll mill technique mixes the filler particles more effectively, subsequently improving matrix-filler adhesion and promoting a tighter packing of particles (filling of interstitial voids) in comparison to dry blending. The latter behaviour was also observed by Deepthi et al. ^[230] in HDPE/cenosphere composites blended by TSE compounding; the tensile modulus and strength were seen to increase with every filler content investigated. However, the specimens were injection moulded under high pressure and temperature. The latter could have also contributed towards the improvement in tensile properties.

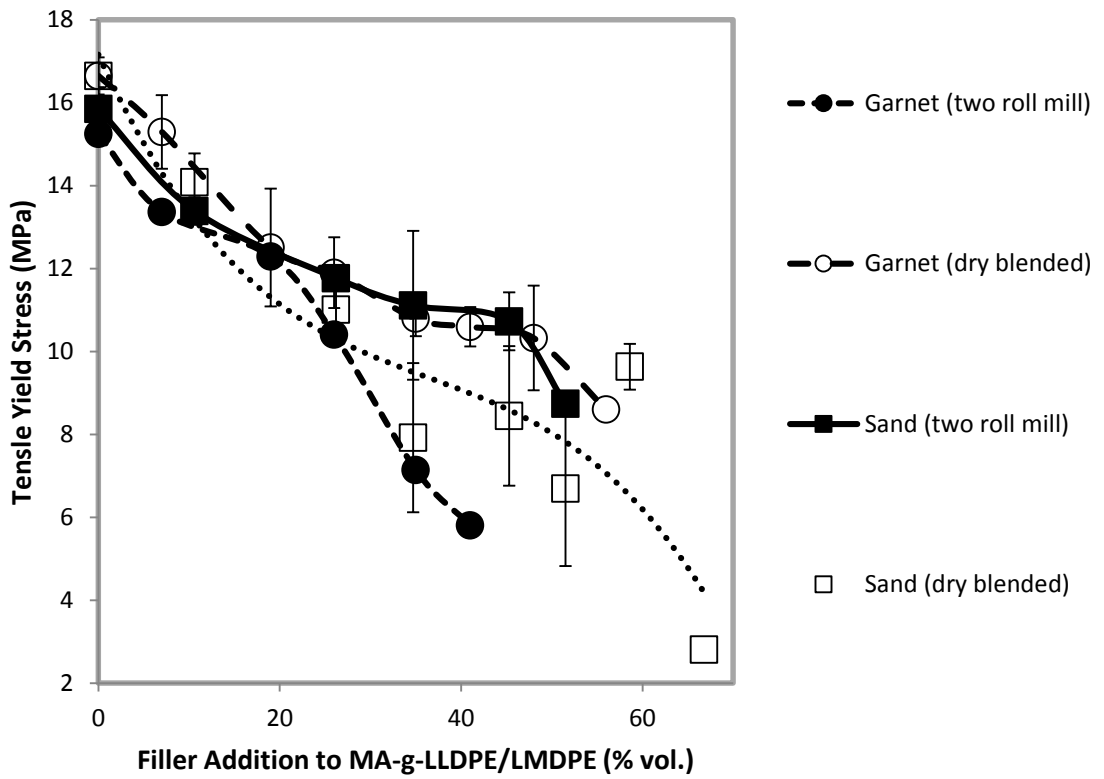


Figure 58. Tensile stress at yield of garnet and sand filled PE composites.

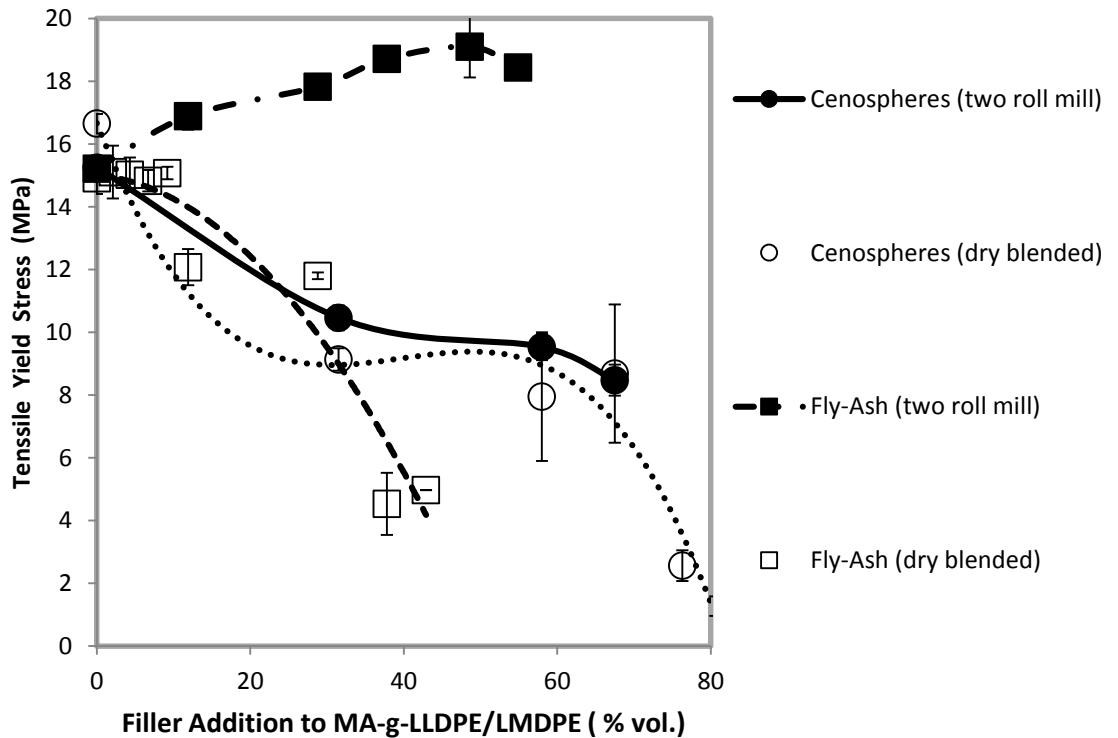


Figure 59. Tensile stress at yield of fly-ash and cenosphere filled PE composites.

The decreases in the tensile stress at yield for sand, garnet and cenosphere filled PE composites at all filler loadings investigated (regardless of blending technique, Figures 58 and 59) indicated weak

matrix-filler adhesion; the PE matrix tore away from the filler surface (de-wetting or de-bonding) relatively easily. The dry blended PE/garnet composites decrease in tensile strength with the addition of garnet at a slower rate than equivalent melt blended samples. This may be related to the increased shear associated with two roll mill mixing, resulting in degradation of the PE matrix. The melt blended PE/fly-ash composites show an increase in tensile strength at yield or break (whichever occurs first) with the increase in fly-ash addition (Figure 59). This observation is consistent with the generation of strong matrix-filler adhesion. Cenospheres did not show the same behaviour, even when melt blended with the PE matrix. It is likely that this could be mainly due the large size of the cenospheres. The two roll milled cenosphere and fly-ash PE composites performed better in comparison to dry blended equivalents and gave better performance relative to equivalent sand and garnet PE composites (Figures 56 - 59).

5.4.1 *Estimation of tensile modulus and yield stress for filled polyethylene composites*

The increases in tensile modulus of the PE/filler composites (Figures 57-58) with increasing filler content is not surprising; the PE matrix ligaments are sandwiched between the filler particles which constrains movement of the matrix. Furthermore, thermal contraction of the polymer around the filler particles (when the composite is cooled) generates a frictional force between the filler particle and the matrix that also constrains movement of the matrix. Constraining the movement of the matrix results in a more effective transfer of stress from the matrix to the stiffer filler particles. Moreover, in the case of the PE/fly-ash composites, the possible generation of an interfacial region between the fly-ash particles and PE matrix (as a consequence of introducing MA-g-LLDPE to the composite blend) has probably promoted filler-matrix interaction. Better filler-matrix interaction may also be responsible for improvements in tensile modulus of the two roll milled PE/fly-ash blends. Such factors explaining the improvements in tensile modulus are generally due to filler particle size, shape, distribution, volume fraction (V_f) and interaction with the polymer matrix. Therefore, Equation 1 from Literature Review Section 3.3.1.1 was used to estimate the modulus of the PE/filler composites used in this study. Einstein coefficient (K_E) values for circular particles (i.e. cenospheres and fly-ash) and angular shaped particles (i.e. garnet and sand) were found to be 2.5 and 4 respectively from existing literature ^[101]. Values of moduli (E_f) for the sand, garnet, fly-ash and cenosphere particles were also found from existing literature to be 70 GPa ^[231], 250 GPa ^[232] and 150 GPa ^[233] (for fly-ash and cenospheres) respectively.

It is clear that Equation 1 underestimates the tensile modulus of all the PE/filler composites investigated (Figure 60-63). However, Equation 1 does calculate an increase in modulus with the increase in filler content up to a limit of approximately 50 % vol. filler. The latter deviation between experimentally determined values of tensile modulus and equivalent values determined

by Equation 1 are probably due to complex factors unaccounted for by Equation 1. For example, it is possible that degradation induced cross-linking of the matrix during processing has occurred; increasing the filler content effectively reduces the matrix surface area and increases the shear force required during processing. The latter harsh conditions could have supported the establishment of cross-links in the matrix. Cross-linking of the matrix may have contributed towards the increases in modulus of the PE/filler composites relative to the theoretical modulus calculated using Equation 1. Interestingly, degradation induced cross-linking of the matrix could also explain the increase in tensile yield stress of analogue (non-maleanised) PE containing the two highest fly-ash levels in Figure 79. This can be verified using MFR measurement, or more ideally oscillatory viscometry.

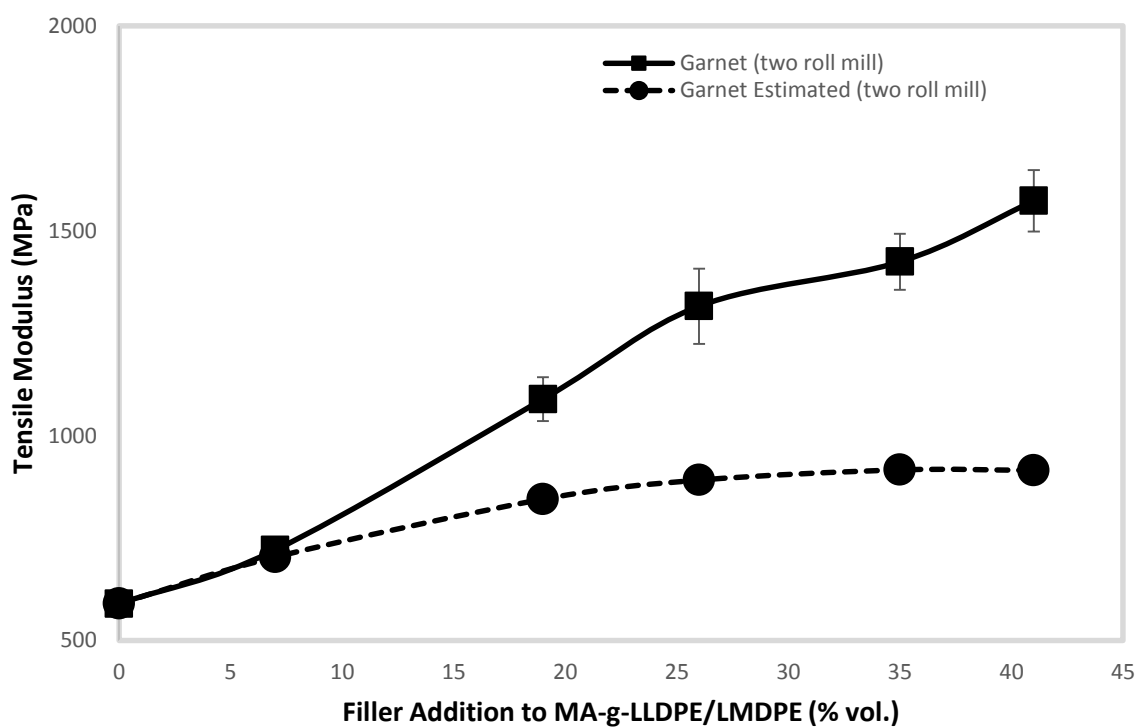


Figure 60. The actual and estimated tensile modulus of garnet filled PE composites.

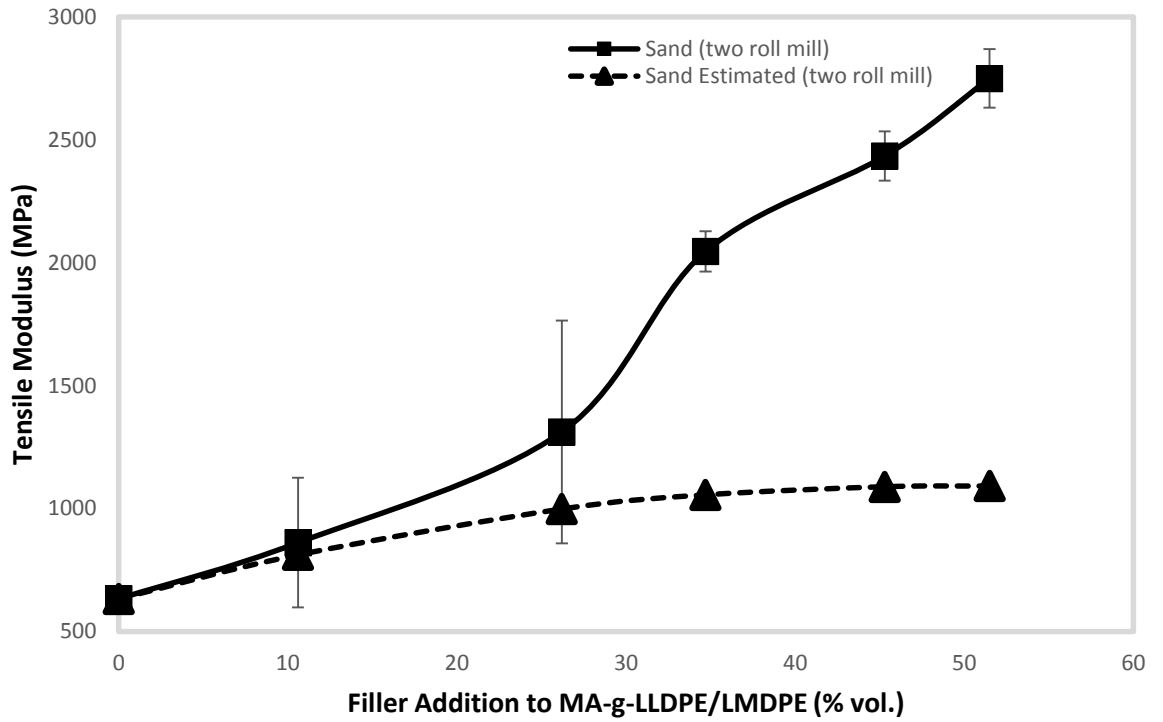


Figure 61. The actual and estimated tensile modulus of sand filled PE composites.

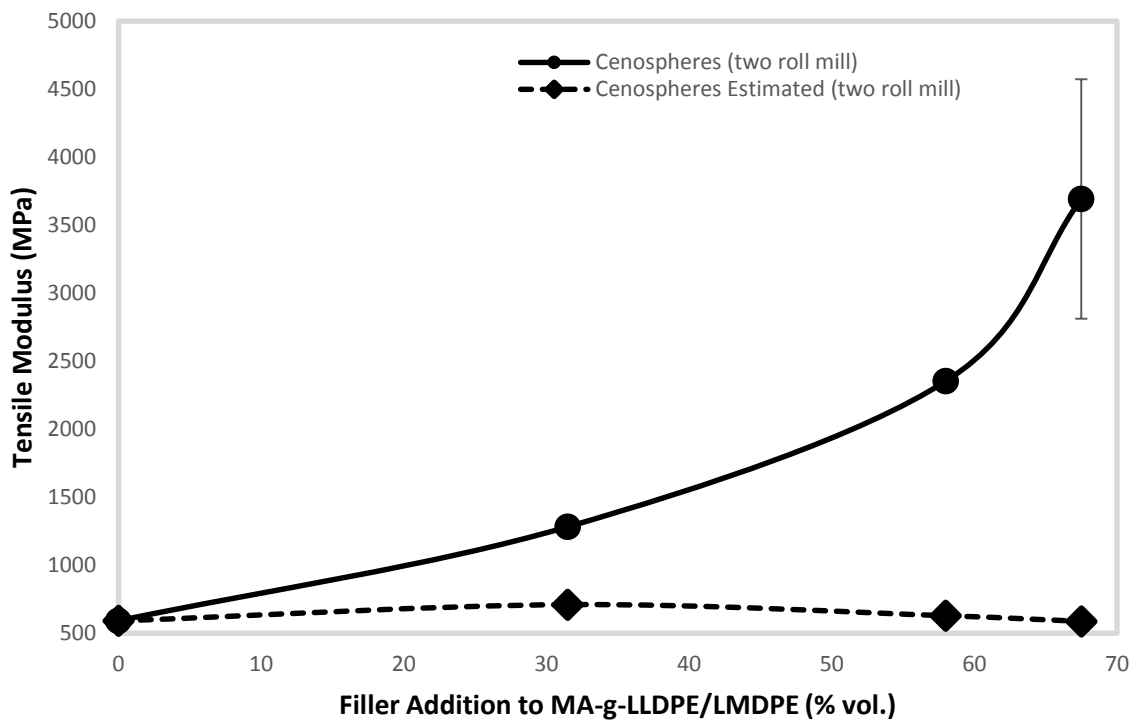


Figure 62. The actual and estimated tensile modulus of cenosphere filled PE composites.

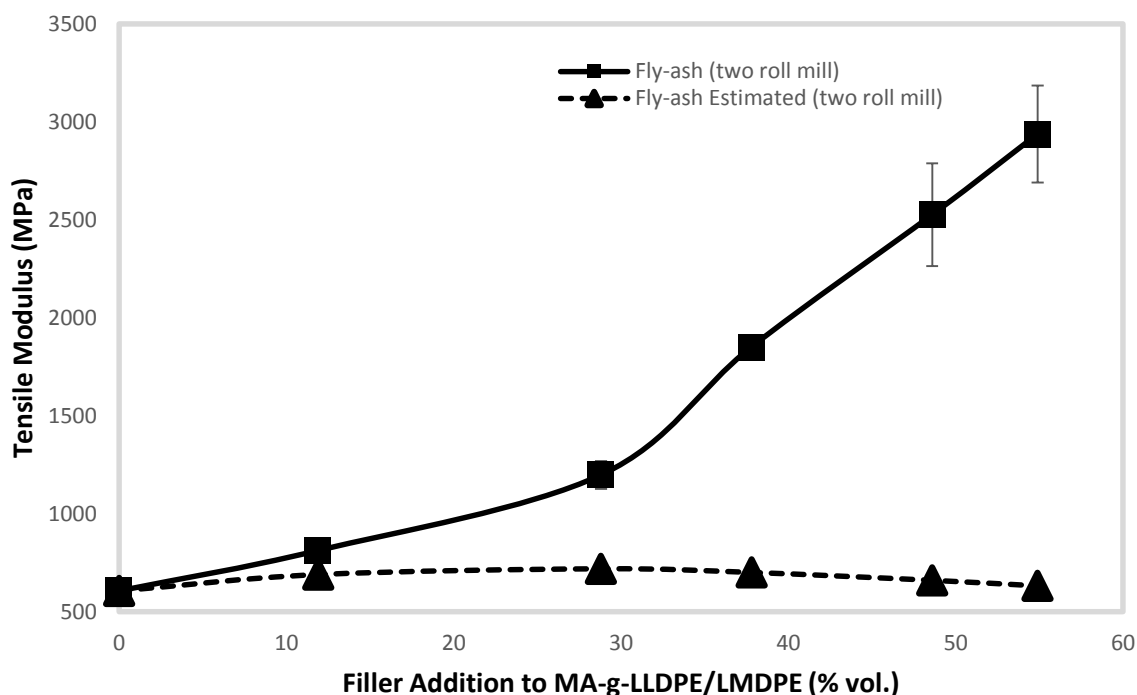


Figure 63. The actual and estimated tensile modulus of fly-ash filled PE composites.

The decrease in tensile yield stress of the large particle garnet, sand and cenosphere PE composites with increasing filler level is unsurprising; little interaction was observed between the latter filler particles and MA-g-LLDPE/LMDPE (Figures 58 and 59). At low filler levels this was especially true; the ductile PE matrix withstood the majority of the stress in the composite and continued to deform post-yield. However, at higher filler loadings the matrix yielded simultaneously with filler-matrix de-bonding and fractured, due to the loss in matrix surface area within the composite. The loss in matrix surface area can be calculated by 1 minus the volume fraction of filler ($1 - V_f$)^[234]. Therefore, Equation 2 (Literature Review Section 3.3.1.2) was used to estimate the yield stress of the two roll mill blended PE/filler composites detailed in Table 10.

Figures 64 - 67 show both the actual and estimated tensile yield stress of the PE/filler composites with the increase in filler content. It is apparent that Equation 2 provided a reasonably accurate approximation of yield stress for the garnet, sand and cenosphere PE composites at filler levels below approximately 35 % vol. At filler levels above 35 % vol. Equation 2 underestimated the yield stress of the composite; at higher filler levels the latter PE/filler composites fracture, this switch over from ductile behaviour at yield (with the lower levels of filler) to brittle failure (with the high levels of filler beyond ca. 35 % vol.) indicates that, even though little or no matrix-filler interaction is present, the relatively high volume of filler is providing some modulus enhancement to the composite. In the case of the PE/fly-ash composites (Figure 67), Equation 2 severely underestimates the tensile yield stress; due to well-established interfacial regions between the

fly-ash particles and the MA-g-LLDPE/LMDPE matrix, the PE/fly-ash composites actually increase in tensile yield stress, a factor which is unaccounted for in Equation 2. However, It appears that Equation 2 provides good approximations of yield stress for relatively low to medium filled polymer composites (below 40 % vol.) if little or no matrix-filler interaction is assumed. On the other hand, in the case of highly filled composites or filled composites with better matrix-filler interaction, the shape, size, dispersion, orientation, yield stress of the filler particles and strength of matrix-filler interaction play a more influential role in estimating the yield stress of filled polymer composites ^[235].

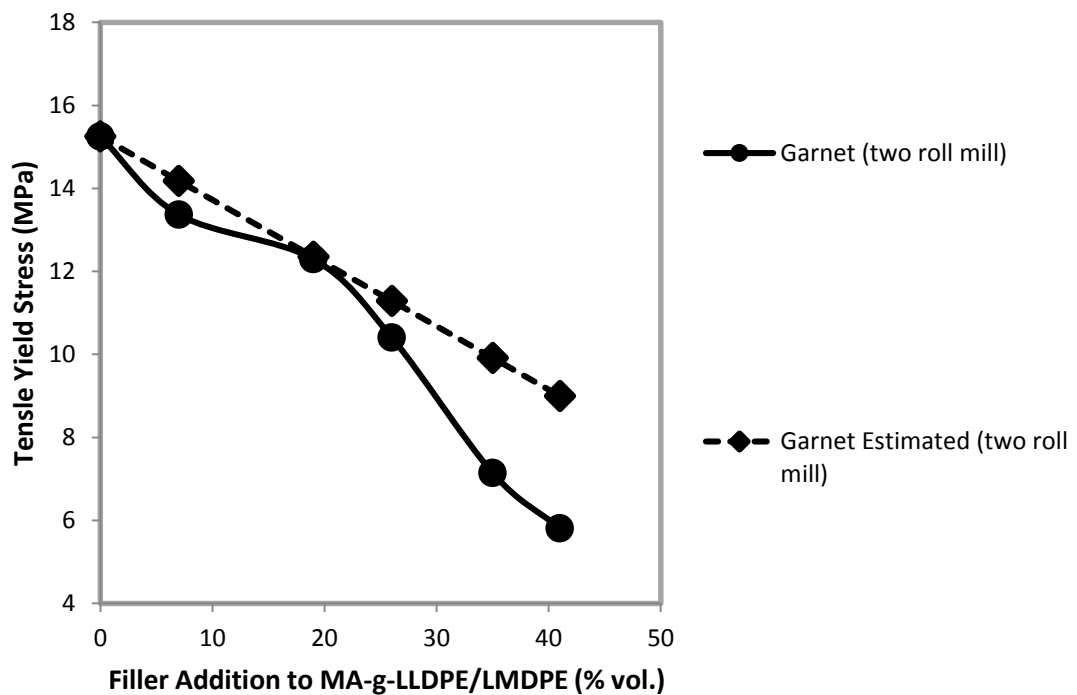


Figure 64. The actual and estimated tensile yield stress of garnet filled PE composites.

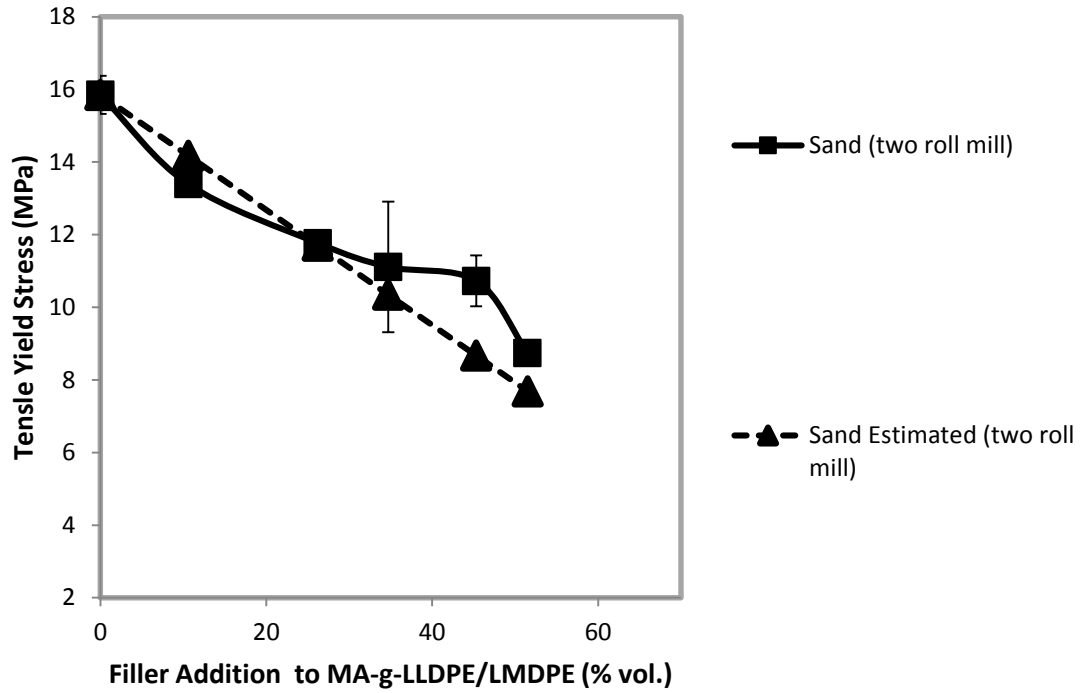


Figure 65. The actual and estimated tensile yield stress of sand filled PE composites

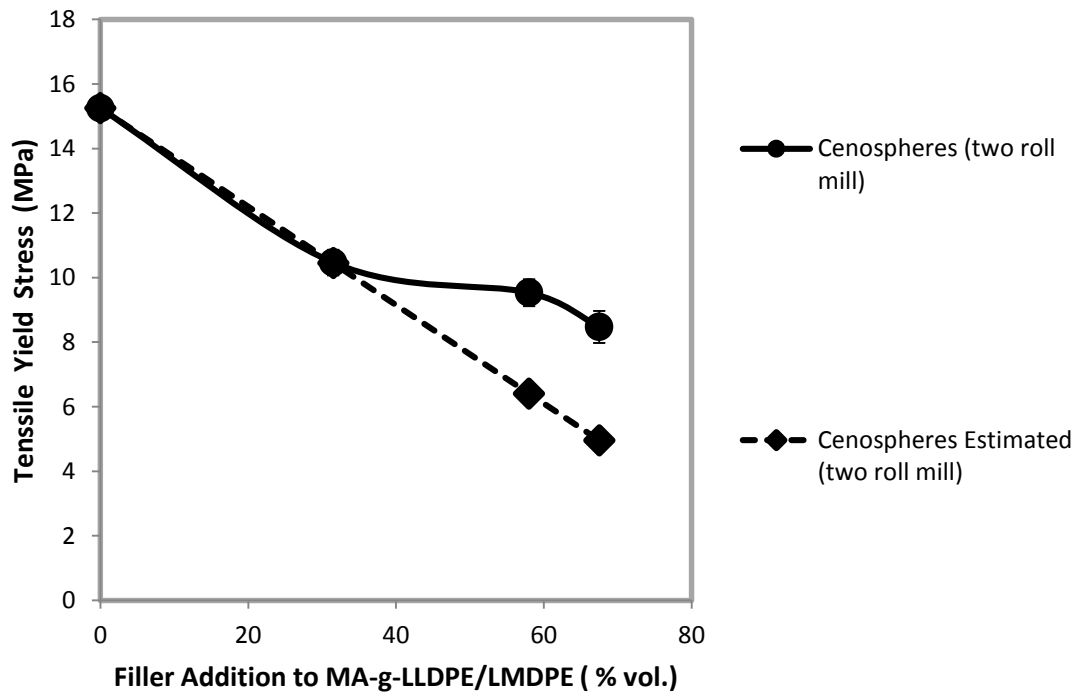


Figure 66. The actual and estimated tensile yield stress of cenosphere filled PE composites.

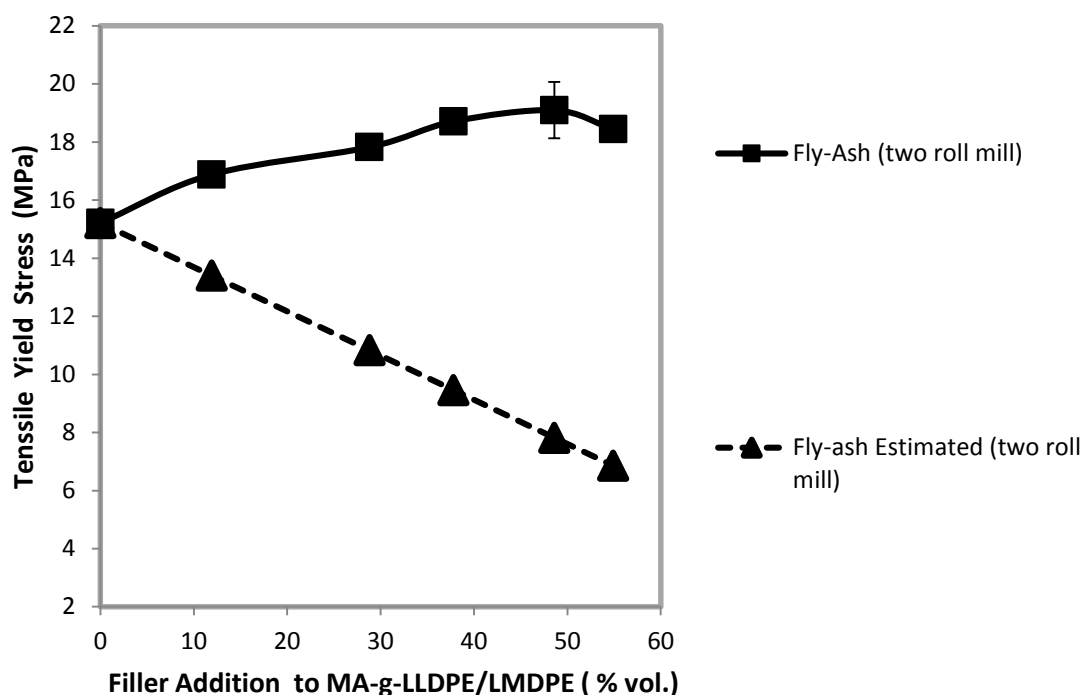


Figure 67. The actual and estimated tensile yield stress of fly-ash filled PE composites

5.4.2 Key findings from the comparison of composite formation processes

Investigating the effect of various polymer-filler blending methods forms another particularly novel aspect of this research in the context of rotational moulding. For the purpose of clarity, the key findings of this investigation are summarised in the following bullet points:

- The two roll milled composites offer significant improvements in tensile modulus for all candidate fillers investigated. A doubling of tensile modulus is considered to be a good result for this study; it is evident that this can be achieved at a filler loading of about 30 % vol. Interestingly, all two roll milled PE/filler composites (with the exception of dry blended PE/fly-ash) increase in modulus with every level of filler investigated.
- At filler volume fractions less than ca. 29 % vol., the dry blended PE/fly-ash composites have higher tensile moduli relative to melt blended equivalents. However, beyond 29 % vol. fly-ash the tensile modulus of the dry blended composites decreases; the decrease in tensile modulus observed may be related to poor wetting combined with poor dispersion of the filler beyond ca. 29 % vol.
- The increases in tensile modulus of the two roll milled composites with increasing filler content can be attributed to a better transfer of stress from the flexible PE matrix to the stiffer filler particles, as a result of improved matrix-filler adhesion. The shear force element in the two roll mill technique could promote better mixing of filler particles,

subsequently improving matrix-filler adhesion and promoting a tighter packing of particles (filling of interstitial voids) in comparison to dry blending.

- The two roll milled cenosphere and fly-ash PE composites performed better in comparison to dry blended equivalents and gave better performance relative to equivalent sand and garnet PE composites.
- Equation 1 underestimates the tensile modulus of all the PE/filler composites investigated (Figure 60-63). However, Equation 1 does calculate an increase in modulus with the increase in filler content up to a limit of approximately 50 % vol. filler. The latter deviation between experimentally determined values of tensile modulus and equivalent values determined by Equation 1 are probably due to degradation induced cross-linking of the matrix during processing. This can be verified using MFR measurement, or more ideally oscillatory viscometry.
- Equation 2 provided a reasonably accurate approximation of yield stress for the garnet, sand and cenosphere PE composites at filler levels below approximately 35 % vol. At filler levels above 35 % vol. Equation 2 underestimated the yield stress of the composite. In the case of the PE/fly-ash composites, Equation 2 severely underestimates the tensile yield stress due to well-established interfacial regions between the fly-ash particles and the MA-g-LLDPE/LMDPE matrix.

5.5 Use of Two Roll Mill Blending for Mixed Large/Small Particle Composites

Previous tests had suggested a small contribution of fly-ash to cenospheres (i.e. 25 % wt. of the overall blend, Figure 55) may give a marginal increase in MPF; it was thought the increase in MPF may better reinforce the PE matrix. Therefore, it was decided to two roll mill small contributions of fly-ash with cenospheres to PE and test for tensile response, ensuring the fly-ash content is 25 % wt. of the total filler content (Table 11).

Table 11. Combinations of fly-ash and cenospheres for addition to PE.

LMDPE/MA-g-LLDPE (% wt.)	Fly-ash (% wt.)	Cenospheres (% wt.)
100	0	0
75	6.25	18.75
50	12.5	37.5
40	15	45
30	17.5	52.5
25	18.75	56.25

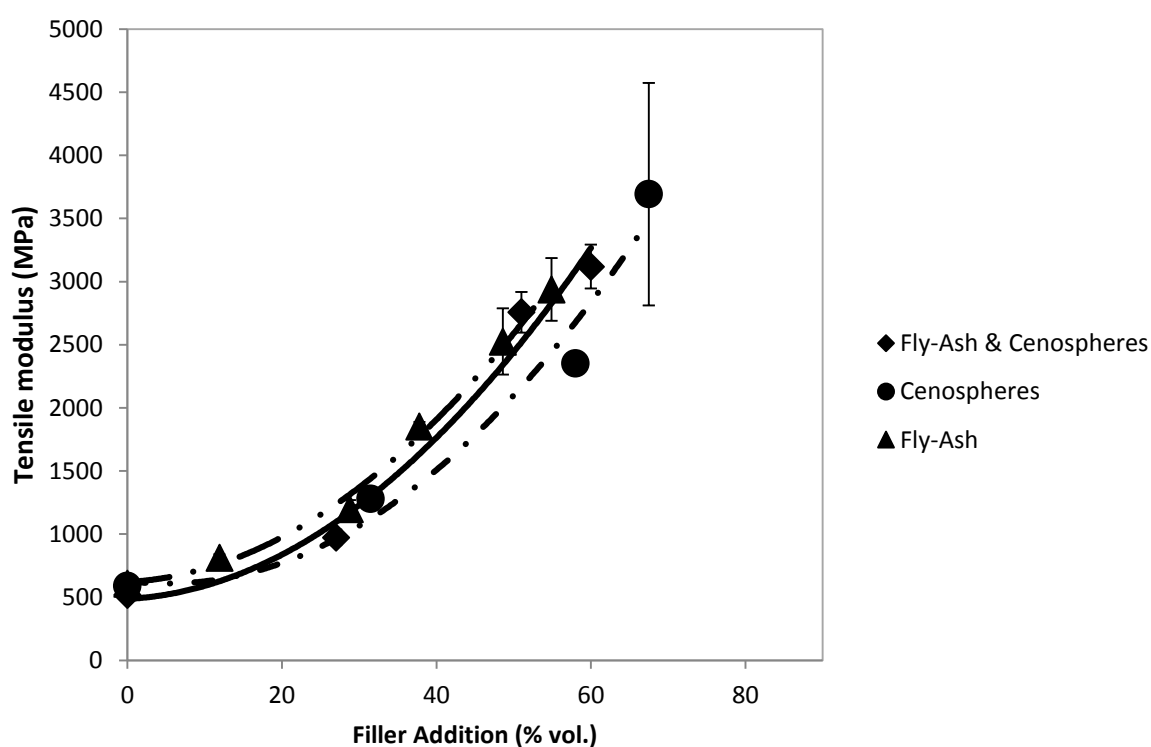
**Figure 68.** Tensile modulus of fly-ash and cenosphere PE composites.

Figure 68 portrays that the two-roll milled PE/fly-ash-cenosphere composites have higher values of tensile modulus in comparison to PE/cenosphere composites alone (the latter had inferior performance with regards to tensile modulus). However, the reduced performance of PE/fly-ash-cenosphere composites relative to PE/fly-ash composites (which withstood the greatest tensile stress at yield (Figure 69) and tensile modulus (Figure 68)) could be due to the non-uniformity of filler particle characteristics, possibly hindering matrix filler adhesion potential; a similar result was also observed by Yoo et al. [236] when combining glass fibres with montmorillonite (MMT) particles to increase the tensile properties of Polyamide 6. Although notable increases in modulus were observed with the latter combined fillers, the MMT particles alone provided a better modulus enhancement to Polyamide 6, even at low MMT contents (0-10 % wt.). It was concluded

that inconsistent particle orientation and filler-matrix interaction might have contributed towards the reduction in modulus observed with the combination of both fillers.

Furthermore, the tensile stress at yield (Figure 69) of the PE/fly-ash composites increased with every filler loading investigated indicating good matrix-filler interaction. However, at low filler levels the PE/fly-ash-cenosphere composites (Figure 69) have a higher tensile stress at yield relative to the PE/cenosphere composites; again this could be due to the non-uniformity of filler particle characteristics, possibly hindering matrix-filler adhesion potential at high fly-ash-cenosphere loadings.

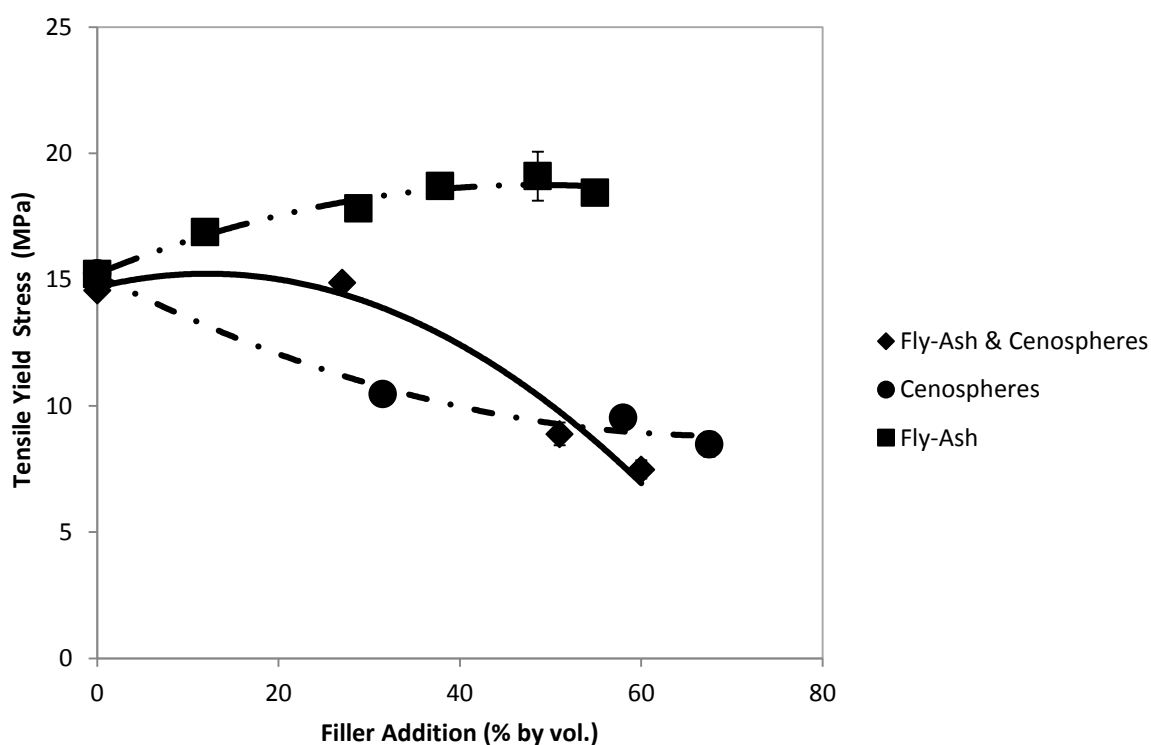


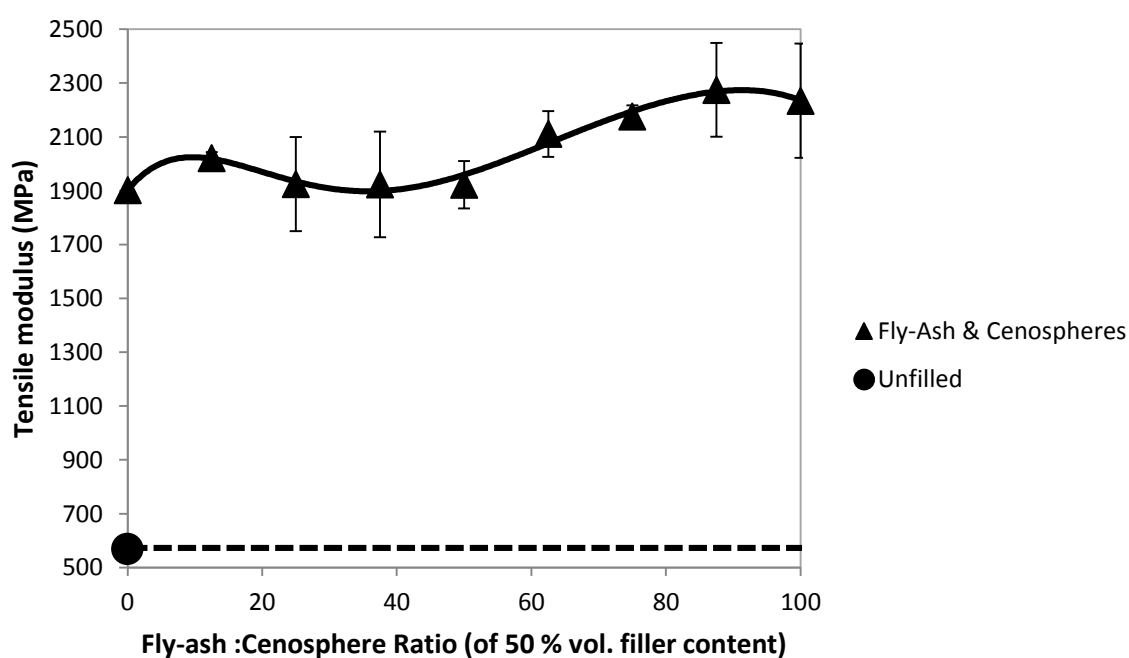
Figure 69. Tensile stress at yield of fly-ash and cenosphere PE composites.

Conversely, in terms of tensile modulus (Figure 68), the PE/fly-ash-cenosphere composites performed optimally at approximately 50 % vol. filler. Therefore, it was decided to two roll mill a variety of combinations of fly-ash with cenospheres in PE, maintaining overall filler content of 50 % vol. Table 12 identifies the blend details, Figures 70-71 display tensile properties found in this investigation.

Table 12. Ratio of fly-ash to cenospheres to maintain a volume of 50% filler.

LMDPE/MA-g-LLDPE (% vol.)	Fly-ash (of 50 % vol.)	Cenospheres (of 50 % vol.)
100	0	0
50	0	100
50	12.5	87.5
50	25	75
50	37.5	62.5
50	50	50
50	62.5	37.5
50	75	25
50	87.5	12.5
50	100	0

Cenosphere particles are considerably larger than fly-ash particles and therefore cannot pack together as effectively to reduce the size of interstitial voids. Furthermore, fly-ash particles seemingly respond better to the current coupling agent system (MA-g-LLDPE). This could explain the relatively small impact on the performance of cenosphere PE composites with the addition of fly-ash; in fact as the fly-ash level approaches 100 % (of 50 % vol. overall filler) both tensile modulus and tensile yield stress increase. The tensile modulus (Figure 70) shows no change up to a fly-ash/cenospheres ratio of 37.5/62.5. Beyond the latter, a slight rise is observed; the increase in tensile modulus (relative to the composite containing cenospheres only) for the composite containing fly-ash only is outside experimental error and indicates that smaller particles are more effective at improving stiffness, due to the increased interfacial area within the composite.

**Figure 70.** Tensile modulus of PE/fly-ash-cenosphere composites, maintaining an overall filler content of 50 % vol.

Tensile yield stress versus fly-ash:cenosphere ratio (at a total filler volume fraction of 50 %) is plotted in Figure 71 together alongside the tensile yield stress of the unfilled matrix. An increase in tensile yield stress was observed with the increase in fly-ash content to the filler blend; however, only the composite containing fly-ash had a yield stress greater than that of the unfilled matrix. On the other hand, there is a mild inflexion in the data around 50 % fly-ash:cenosphere ratio that is outside experimental error (some error bars are smaller than the data points, see Table 38 in the Appendix Section 3 for standard deviation data). The general conclusion that was drawn from these mechanical responses is that blends of cenospheres and fly-ash particles are not successful as stiffness reinforcement for PE; the large cenosphere particles may act as stress concentrators in the MA-g-LLDPE/LMDPE matrix with fly-ash particles (which are an order of magnitude smaller in size than cenospheres). As this matrix is of lower toughness than the MA-g-LLDPE alone, it is not surprising that premature failure occurs.

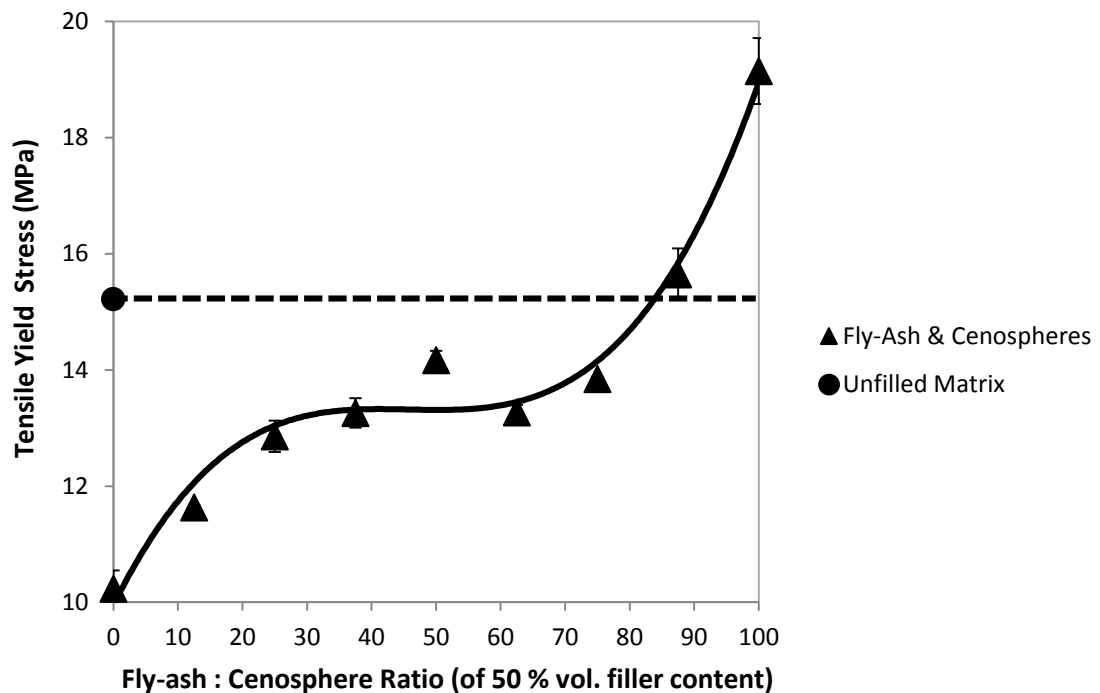


Figure 71. Tensile stress at yield of PE/fly-ash-cenosphere composites, maintaining an overall filler content of 50 % vol. (Table 38 of the Appendix Section 3 displays standard deviations).

5.5.1 Key findings from using the two roll mill to blend large/small particle composites

Combining two fillers (fly-ash and cenospheres) has never been attempted in the context of particulate-filled composites for rotomoulding. For the purpose of clarity, the key findings of this investigation are summarised in the following bullet points:

- The two-roll milled PE/fly-ash-cenosphere composites have higher values of tensile modulus in comparison to PE/cenosphere composites alone (the latter had inferior performance with regards to tensile modulus). However, the reduced performance of PE/fly-ash-cenosphere composites relative to PE/fly-ash composites could be due to the larger cenosphere particles acting as defects and hence causing premature failure. The cenospheres are effectively residing within a matrix which is itself a composite of PE and fly ash. The latter combination will be stiffer and probably more defect sensitive than PE, causing the effect of the cenosphere defects to be even greater than in a composite consisting of cenospheres and PE only.
- The tensile stress at yield of the PE/fly-ash composites increased with every filler loading investigated, indicating good matrix-filler interaction and sufficiently good filler dispersion. However, at low filler levels the PE/fly-ash-cenosphere composites have a higher tensile stress at yield relative to the PE/cenosphere composites; again this could be due to the non-uniformity of filler particle characteristics, possibly hindering matrix-filler adhesion potential at high fly-ash-cenosphere loadings.

5.6 Evaluation of Twin Screw Extrusion Compounding for Production of Small Particle Composites

Melt blended PE/fly-ash composites showed strong matrix-filler interaction which was manifested as the composite strength increasing with the volume fraction of fly ash (Figures 68, 69). Such behaviour is consistent with formation of a percolated network of well bonded filler-matrix interfacial regions which are stronger than the bulk matrix. Twin screw extrusion (TSE) compounding is arguably a more effective melt blending method than two roll milling; the residence time in TSE is shorter and unlike the two roll mill, the melt is not open to the atmosphere. These factors reduce the level of melt oxidation. TSE is also a continuous process and is therefore used for the commercial production of filled polymers.

Consequently, it was decided to TSE melt blend PE/fly-ash composites, Table 13 displays composite compositions. Garnet and sand particles were considered too large and abrasive and the cenospheres were considered too large and fragile to run through the extruder; breakage of the cenosphere particles would risk the benefit of low density being lost. PE/fly-ash composites prepared by TSE and two roll milling had the same tensile modulus versus fly-ash volume fraction characteristics when experimental error is considered (Figure 72). The tensile stress at yield or failure (whichever came first) of PE/fly-ash composites is also approximately identical for composites melt blended by TSE or the two roll mill, only the TSE produced composite containing

55 % vol. fly-ash is stronger (Figure 73). The insignificant differences between melt blending by two roll mill and TSE show that the level of filler dispersion obtained using the two methods is similar and probably close to optimum, bearing in mind the spherical shape and large size of the fly-ash particles relative to other fillers used in thermoplastics (e.g. talc and calcium carbonate). Differences in the extent of degradation of the matrix in the fly-ash composites are also insignificant despite the two roll mill blending process being open to atmospheric oxygen.

Table 13. Fly-ash and maleanised PE combinations for twin screw extrusion compounding.

MA-g-LLDPE/LMDPE (% wt.)	Fly-ash (% wt.)
100	0
75	25
50	50
40	60
30	70
25	75

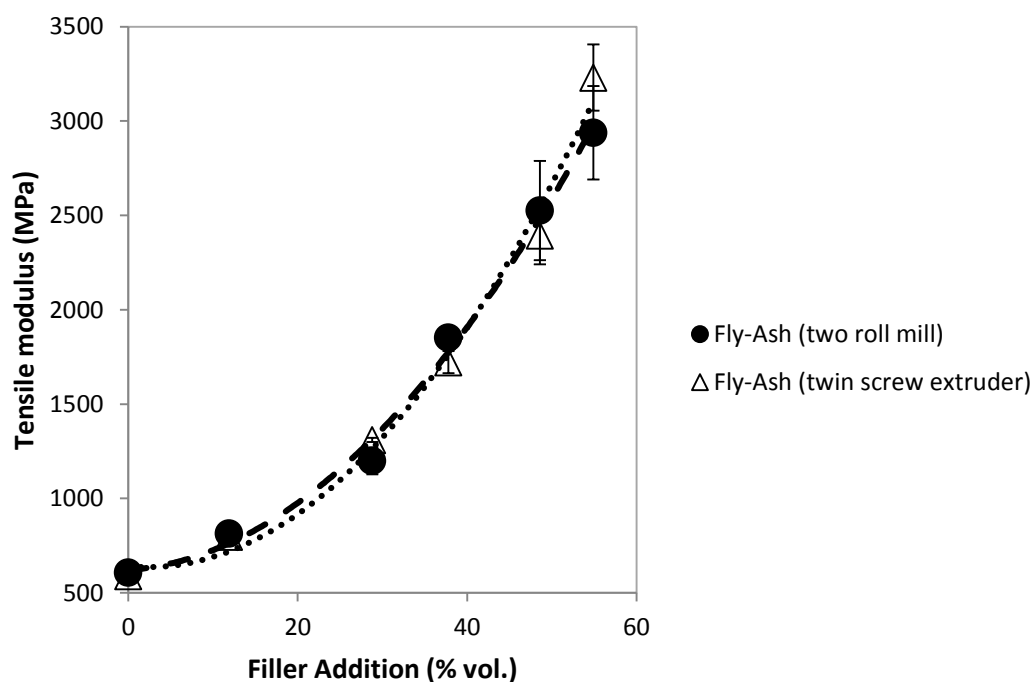


Figure 72. Tensile modulus PE/fly-ash composites dry blended vs. melt compounded.

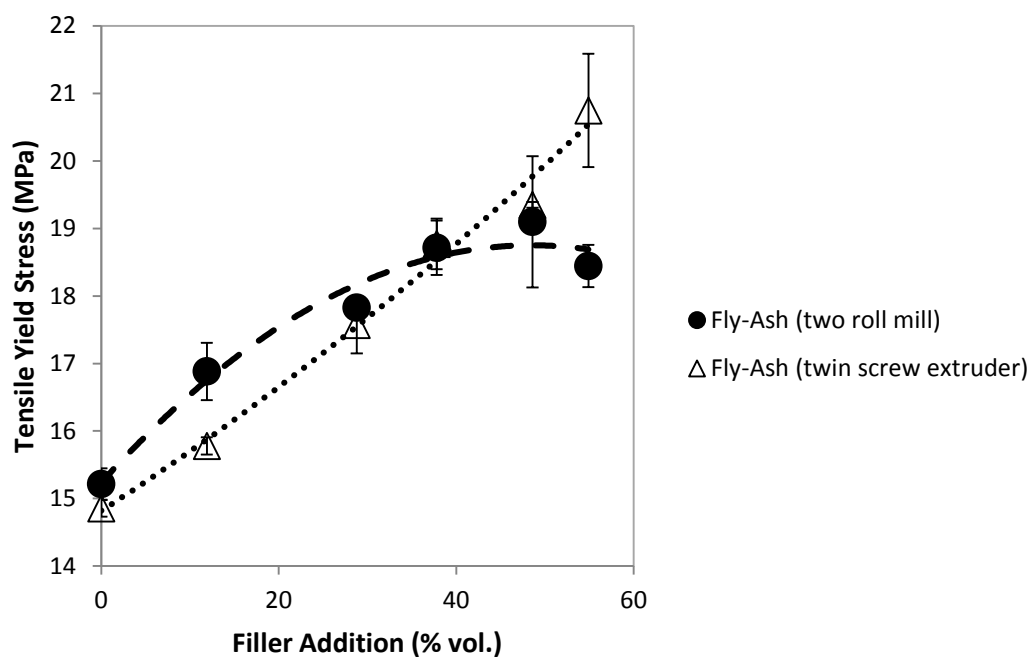


Figure 73. Tensile stress at yield PE/fly-ash composites dry blended vs. melt compounded.

Un-notched Charpy impact tests of TSE compounded PE/fly-ash specimens (Figure 74) revealed increases in impact energy absorbed up to 50 % wt. loading (28.8 % vol.). This may be due to a crack pinning effect; as a crack propagates through a polymer containing particles that locally obstruct its path, the crack front may propagate around the outer edge between particles. The propagation of such a crack front consumes more energy than cracks with a straight front [237, 238, 239]. This is referred to as crack pinning and is one method of toughness reinforcement in filled polymer composites (Figure 75).

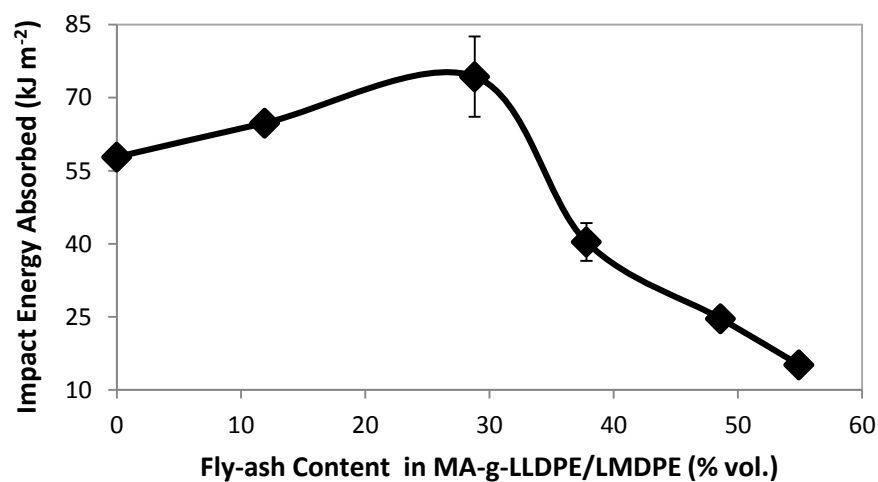


Figure 74. Un-notched Charpy impact test results for twin screw extruded PE/fly-ash blends.

(Table 39 of the Appendix Section 3 displays standard deviations).

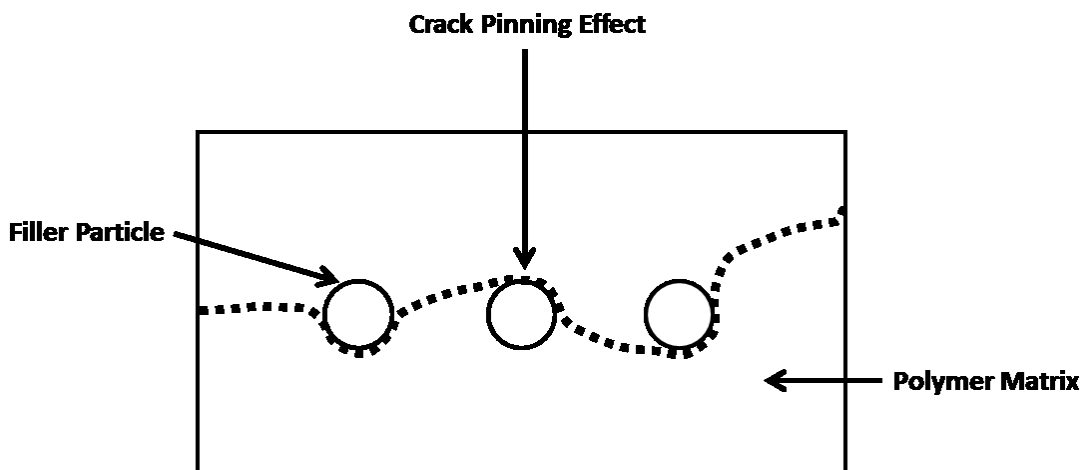


Figure 75. The crack pinning effect in filled polymeric composites.

Beyond 28.8 % vol. fly-ash, the impact energy absorbed decreases in an almost linear fashion resulting in sudden brittle failure. Un-notched Charpy Impact strength fell sharply between 28.8 and 37.8 % vol. then somewhat less sharply between 37.8 and 54.9 % vol. fly-ash. The sharp fall may be due to a change in fracture mechanism arising from the average distance between filler particles becoming too small for the crack pinning mechanism to operate. The rate of reduction slows due to possible percolation of filler-matrix interfacial regions, resulting in a further modification of the fracture mechanism. Consequently, it was thought that these interfacial regions may have a different crystalline content to the bulk matrix; this was resolved by differential scanning calorimetry (DSC) of the PE/fly-ash composite materials specified in Table 18 of Section 5.9.2. Figure 76 confirmed that the addition of fly-ash in this instance has a negligible impact on the crystalline content of MA-g-LLDPE/LMDPE.

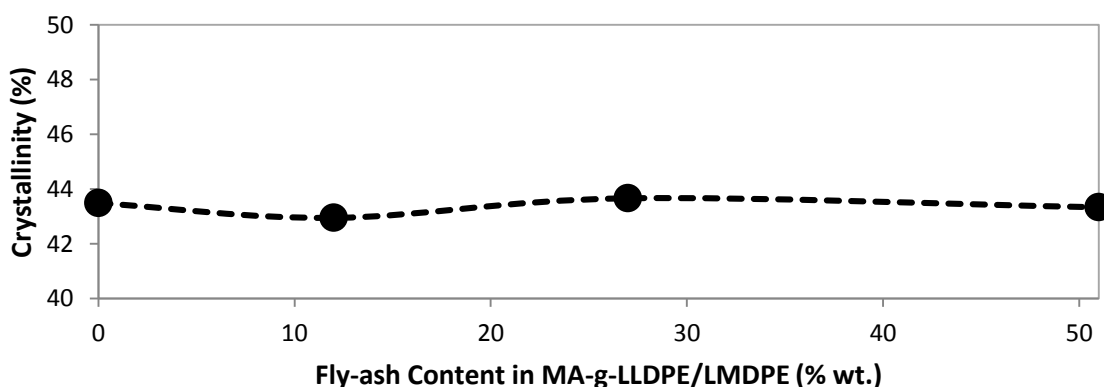


Figure 76. Crystallinity of MA-g-LLDPE/LMDPE with the addition of fly-ash. A compilation of all DSC data is provided in Appendix Section 4.

Preliminary SEM imaging of two roll milled 25 % wt. fly-ash/PE composites (Figure 77) revealed that fly ash particles were still visible on the fracture surfaces; indicating that whilst high tensile stress was realised, the composites still failed at the filler-matrix interface.

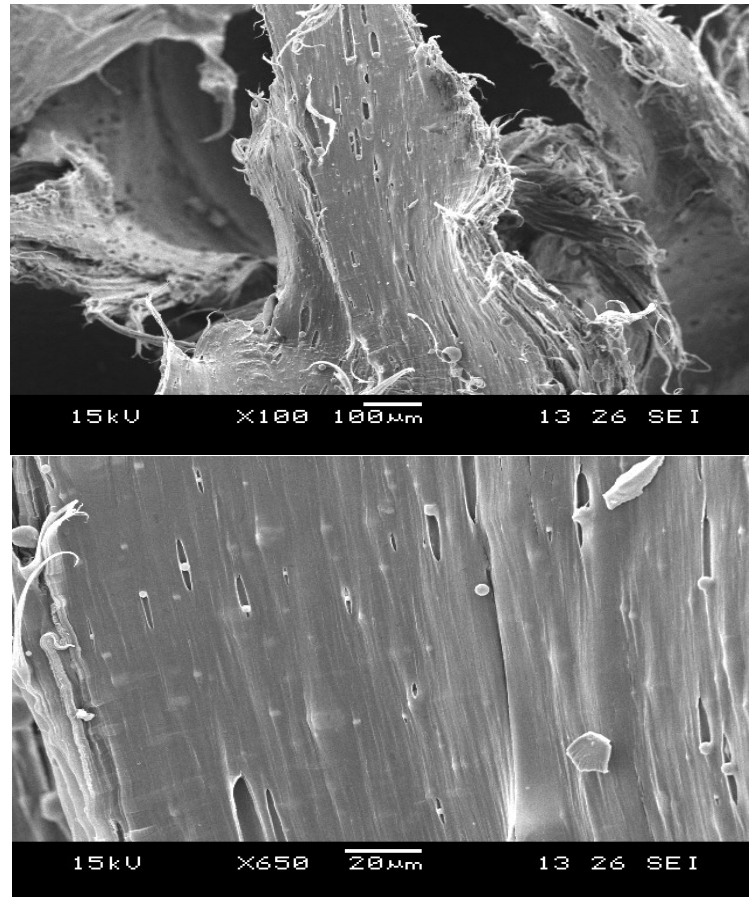


Figure 77. SEM images of the tensile fracture surface of a 25 % wt. fly-ash/PE composite specimen (650 and 100x magnification).

5.6.1 *Key findings from using the twin screw extruder to blend small particle composites*

Investigating the effect of various polymer/filler blending methods is seldom conducted in studies on particulate-filled composites for rotational moulding. For the purpose of clarity, the key findings of this investigation are summarised in the following bullet points:

- PE/fly-ash composites prepared by TSE and two roll milling had the same tensile modulus versus fly-ash volume fraction characteristics when experimental error is considered.
- The tensile stress at yield or failure (whichever came first) of PE/fly-ash composites is also approximately identical for composites melt blended by TSE or the two roll mill, only the TSE produced composite containing 55 % vol. fly-ash is stronger.

- The insignificant differences between melt blending by two roll mill and TSE show that the level of filler dispersion obtained using the two methods is similar and probably close to optimum, bearing in mind the spherical shape and large size of the fly-ash particles relative to other fillers used in thermoplastics (e.g. talc and calcium carbonate).
- Differences in the extent of degradation of the matrix in the fly-ash composites are also insignificant despite the two roll mill blending process being open to atmospheric oxygen.
- Un-notched Charpy impact tests of TSE compounded PE/fly-ash specimens revealed increases in impact energy absorbed up to 50 % wt. loading (28.8 % vol.). This may be due to a crack pinning effect.
- Beyond 28.8 % vol. fly-ash, the impact energy absorbed decreases in an almost linear fashion resulting in sudden brittle failure. Un-notched Charpy Impact strength fell sharply between 28.8 and 37.8 % vol. then somewhat less sharply between 37.8 and 54.9 % vol. fly-ash. The sharp fall may be due to a change in fracture mechanism arising from the average distance between filler particles becoming too small for the crack pinning mechanism to operate. The rate of reduction slows due to possible percolation of filler-matrix interfacial regions, resulting in a further modification of the fracture mechanism.
- The addition of fly-ash in this instance has a negligible impact on the crystalline content of MA-g-LLDPE/LMDPE.

5.7 Verification of Maleic Anhydride Coupling Agent Effect on Small Particle Composites Produced by Twin Screw Extrusion Compounding

The MA-g-LLDPE grade and dosage used in this study was selected by the industrial sponsor after extensive studies on large particle composites (Experimental Section 4.1.1). TSE trials have revealed that the MA-g-LLDPE at a loading of 25 % wt. on the LMDPE matrix is effective at coupling the fly-ash particles to the matrix, such that the composite strength increases with fly-ash loading up to the maximum level studied of 55 % vol. This indicates that the Mintron 7 fly-ash used interacts strongly with the maleic anhydride groups (or more likely the dicarboxylic acid formed after hydrolysis of the anhydride). This observation is not surprising; recent work, that has been submitted for publication ^[226] has verified, using flow micro-calorimetry and diffuse reflectance Fourier transform infrared spectroscopy, strong interaction between an unsaturated carboxylic acid coupling agent and Mintron 7 fly-ash. Ion pair interactions between carboxylate group from the acid and metal ions on the fly-ash surface were formed.

To further gauge the effectiveness of the maleanised PE on the properties of LMDPE/fly-ash composites, it was decided to blend the PE/fly-ash composites in Table 13 using LMDPE containing 25 % wt. of a similar non-maleanised LLDPE to the feedstock used to synthesise the MA-g-LLDPE. The latter is termed “analogue PE”. It is well known the type of coupling agent and amount used has an impact on the mechanical performance of particulate-filled polymer composites. The current PE system is 25 % wt. MA-g-LLDPE with 75 % wt. LMDPE. It is reasonable to assume a level of roughly 1 % by wt. maleic anhydride (MA) in the MA-g-LLDPE. However, the exact level remains proprietary. Table 14 identifies blend information for this trial and Figures 78-80 identify the tensile and impact properties.

Table 14. Fly-ash analogue PE combinations investigated.

Analogue PE (% wt.)	Fly-ash. (% wt.)
100	0
75	25
50	50
40	60
30	70
25	75

The tensile modulus of maleanised PE/fly-ash composites (Figure 78) is identical to that of equivalent non-maleanised PE composites up to approximately 48 % vol. At the highest loadings the analogue PE/fly-ash composites are slightly stiffer. This is probably due to a slightly higher crystalline content in the interfacial region of the composites based on the analogue PE. Attachment of the MA-g-LLDPE to the fly-ash particles may decrease crystallinity, reducing the stiffness of the interfacial regions and tensile modulus; Hassan et al. [240] also observed a reduction in the crystallinity of maleic anhydride grafted polypropylene (MA-g-PP)/glass fibre composites via DSC examination, relative to equivalent composites without the MA coupling agent.

The tensile stress at yield or break (whichever comes first) is plotted against fly-ash volume fraction in Figure 79; the MA-g-LLDPE modified composites increase in strength linearly (over the range investigated) with increasing fly-ash level. In contrast, the composites modified with the non-maleanised LLDPE show a decrease in strength which appears to be linear up to 38 % vol. fly-ash. Interestingly, the analogue PE based composites containing the two highest fly-ash levels show noticeably increased strength. This effect may be due to degradation induced cross-linking of the matrix, it can be verified using MFR measurement, or more ideally oscillatory viscometry.

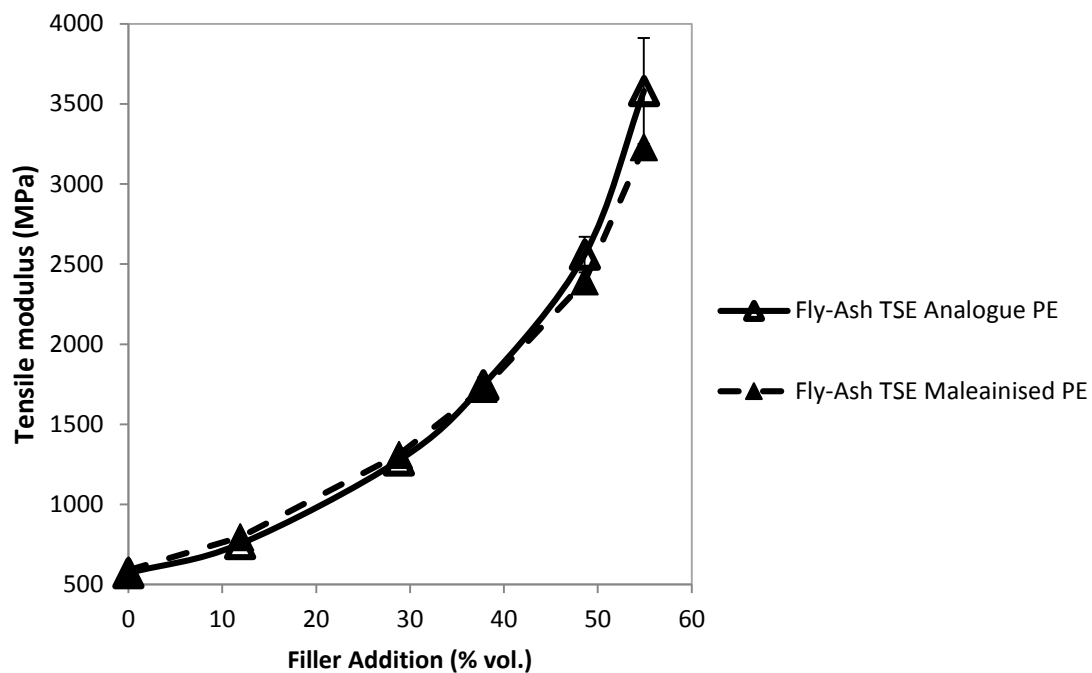


Figure 78. Tensile modulus of analogue PE/fly-ash composites versus maleanised PE equivalents.

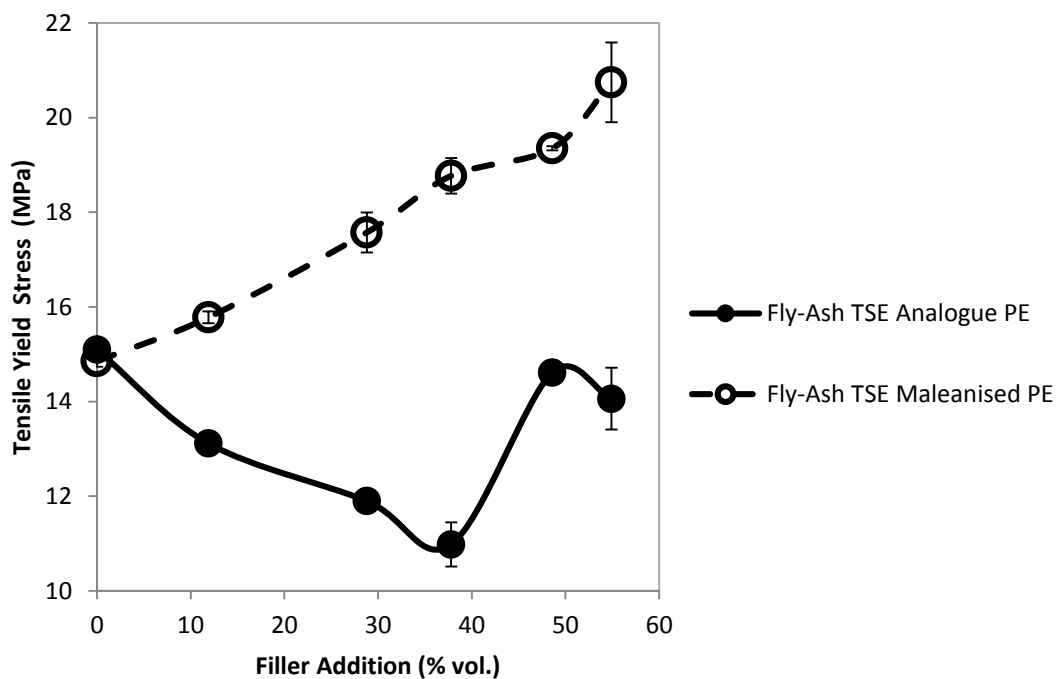


Figure 79. Tensile yield stress of analogue PE/fly-ash vs. maleanised PE equivalents.

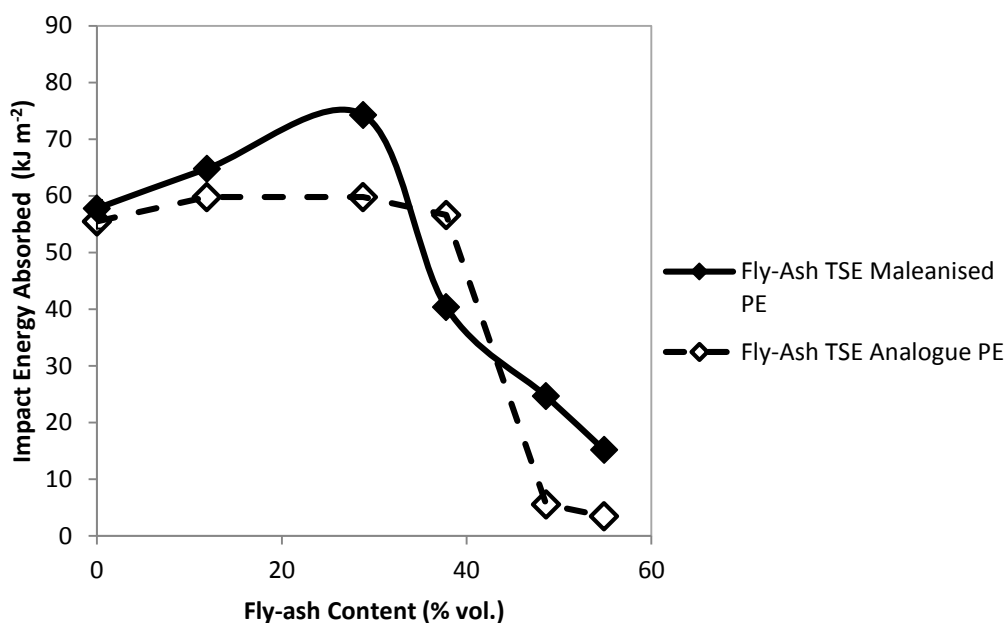


Figure 80. Un-notched Charpy impact results of analogue PE/fly-ash vs. maleanised PE equivalents. (Standard deviation data available within Tables 39 and 30 of Appendix Section 3).

Due to the spherical shape of the fly-ash particles and the absence of significant amounts of sub-micron particles (Figures 47 and 48) it is unlikely that the MA-g-LLDPE modification will improve the degree of fly-ash dispersion. Overall, it is strongly evident that the current MA-g-LLDPE coupling system offers clear advantages with regards to tensile properties. Toughness is important. With this in mind, un-notched Charpy impact testing was conducted on the PE/fly-ash composites. The maleanised PE modified composites gave better Charpy impact properties up to 28.8 % vol. fly-ash loading (Figure 80) in comparison to equivalent analogue PE composites. However, there is a switch over of the data at 60 % wt. (37.8 % vol.) fly-ash. The relatively high effectiveness of a coupling agent over such a wide range of volume fractions is unusual and may indicate that more than one toughening mechanism is in operation. The fact that the MA-g-LLDPE has a lower stiffness than the LMDPE may be a factor which helps improve toughness at lower volume fractions. Under the latter conditions, there will be a large amount of MA-g-LLDPE relative to the amount of filler and the MA-g-LLDPE is likely to encapsulate the filler particles. Both these factors are likely to increase toughness due to a reduction in the yield stress of the bulk matrix and a filler-matrix interfacial region of relatively low stiffness. At higher volume fractions (beyond 50 % vol.) there is less MA-g-LLDPE in relation to the filler and due to the high interfacial area, interfacial properties dominate. The improved filler-matrix adhesion arising from the MA-g-LLDPE modification is responsible for the increased toughness, relative the equivalent unmodified composites, at higher fly-ash volume fractions.

5.7.1 *Key findings from verifying the effect of Maleic Anhydride on PE/fly-ash composites*

For the purpose of clarity, the key findings of this investigation are summarised in the following bullet points:

- The tensile modulus of maleanised PE/fly-ash composites is identical to that of equivalent non-maleanised PE composites up to approximately 48 % vol. At the highest loadings, the analogue PE/fly-ash composites are slightly stiffer. This is probably due to a slightly higher crystalline content in the interfacial region of the composites based on the analogue PE.
- The MA-g-LLDPE modified composites increase in strength linearly (over the range investigated) with increasing fly-ash level. In contrast, the composites modified with the non-maleanised LLDPE show a decrease in strength which appears to be linear up to 38 % vol. fly-ash.
- The analogue PE based composites containing the two highest fly-ash levels show noticeably increased strength, relative to maleanised equivalents. This effect may be due to degradation induced cross-linking of the matrix, it can be verified using MFR measurement, or more ideally oscillatory viscometry.
- The maleanised PE modified composites give better Charpy impact properties up to 28.8 % vol. fly-ash loading in comparison to equivalent analogue PE composites. However, there is a switch over of the data at 60 % wt. (37.8 % vol.) fly-ash. The relatively high effectiveness of a coupling agent over such a wide range of volume fractions is unusual and may indicate that more than one toughening mechanism is in operation. The fact that the MA-g-LLDPE has a lower stiffness than the LMDPE may be a factor which helps improve toughness at lower volume fractions.
- The improved filler-matrix adhesion arising from the MA-g-LLDPE modification is responsible for the increased toughness, relative the equivalent unmodified composites, at higher fly-ash volume fractions.

5.8 Comparison of Maleic Anhydride Coupling Agent Effect on HDPE and LMDPE Small Particle Composites Produced by Twin Screw Extrusion Compounding

The strong performance of fly-ash particles with the current maleanised PE suggests good matrix-filler interaction; a strong interfacial region between the filler particle surface and the PE matrix has been established. The extent of filler particle surface coating by the MA-g-LLDPE/LMDPE has a

profound effect on the physical properties of filled polymeric composites. In the case of PE/fly-ash composites, increases in tensile modulus and stress at yield were seen with the increase in fly-ash loading. Increases in Charpy impact properties were also observed up to 28.8 % vol. fly-ash. The level of MA coupling agent in the MA-g-LLDPE used was originally found by experiment to be optimum for large particle composites by the industrial sponsor Rotomotive Ltd. However, the fly-ash particles are considerably smaller than the larger particle composites developed at Rotomotive Ltd.

Therefore, the effect of MA-g-LLDPE on the tensile and impact properties of TSE melt blended, compression moulded, 70 % wt. fly-ash filled LMDPE and HDPE was investigated (see Table 15); the high 70 % wt. fly-ash loading was selected due to the exceptional improvements in stiffness seen at that level for compression moulded materials. As rotational moulding is a zero shear process, rudimentary rotational moulding and oven sintering trials were carried out by the industrial partner; these trials revealed that whilst good mechanical properties were obtainable at high filler levels with compression moulded plaques, a resistance to flow at zero shear placed a question mark over the viability of using high filler loadings. Therefore, MFR tests were also conducted on the resulting composites. However, it was appreciated that the MFR tests conducted for this investigation were not under zero-shear conditions.

Table 15. Blend details of HDPE or LMDPE with Fly-ash

MA-g-LLDPE (% wt.)	LMDPE or HDPE with and without 70 % wt. fly-ash (% wt.)
0	100
1	99
2.5	97.5
5	95
10	90
17.5	82.5
25	75

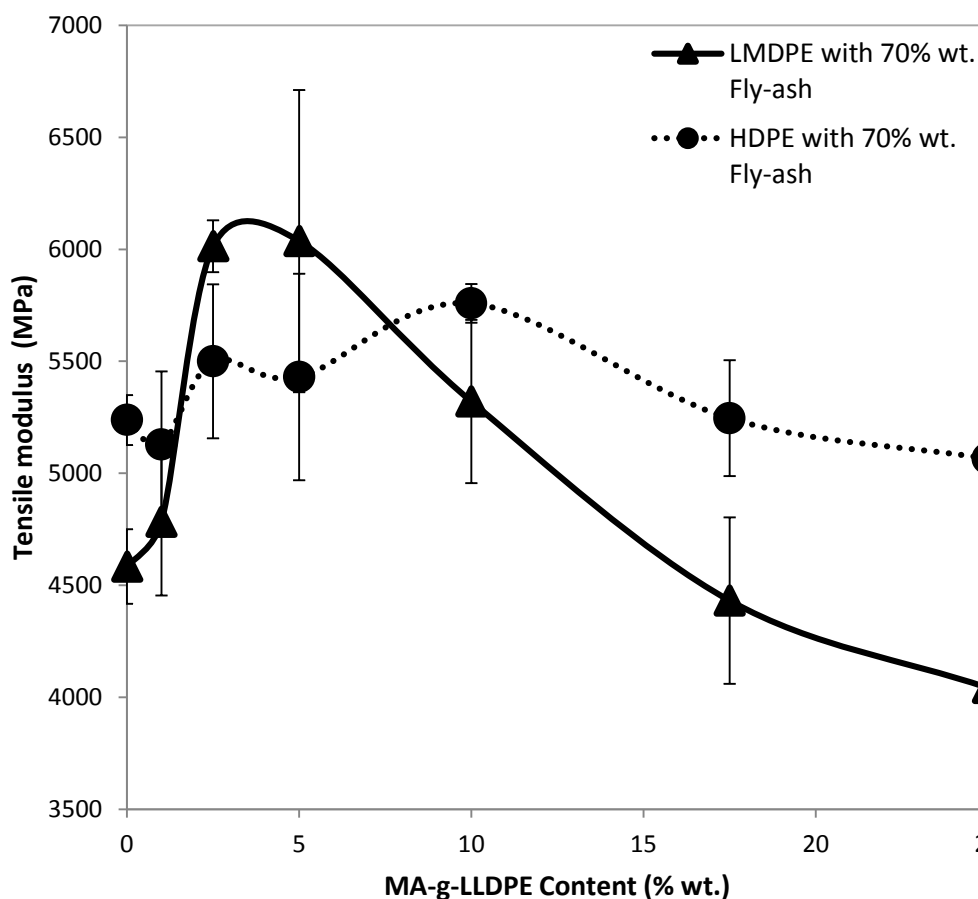


Figure 81. Tensile modulus of unfilled and 70 % wt. fly-ash filled HDPE or LMDPE with addition of MA-g-LLDPE.

With regards to tensile modulus, the 70 % wt. fly-ash filled LMDPE and HDPE specimens initially responded well to the introduction of MA-g-LLDPE coupling agent (Figure 81), particularly between 2.5 and 10 % wt. MA-g-LLDPE loading. Similar enhancements to the tensile strength of HDPE/rice hull composites was observed by Petchwattana et al. [241] with the addition of MA, which was optimum at the smallest rice hull particle size investigated (ca. 75 μm in length). The latter observation supports the theory that smaller particles (such as fly-ash, ca. $\leq 100 \mu\text{m}$ in diameter) are more effective at reinforcing the modulus and strength of polymer composites, relative to large particles which effectively decrease the surface area of the filler particles for attachment to the matrix. However, it is appreciated that rice hull particles have a high aspect ratio and are effectively long, thin fibres. On the other hand, the fly-ash particles have an aspect ratio of approximately 1 due to their spherical shape; the high aspect ratio of the rice hull particles may have also contributed to the tensile improvements observed in MA-g-HDPE.

However, at MA-g-LLDPE levels exceeding 10 % wt. in 70 % wt. fly-ash filled LMDPE or HDPE composites, the tensile modulus deteriorated with increasing MA-g-LLDPE addition. This

reduction in stiffness may be due to the interfacial region being of lower stiffness due to excessive amounts MA-g-LLDPE covering the filler particles.

Differential Scanning Calorimetry (DSC) data from previous testing (Figure 37, Section 5.2.2) indicated HDPE and LMDPE are inherently of higher crystallinity than MA-g-LLDPE (with HDPE having the highest crystalline content). When combined with MA-g-LLDPE their crystallinity progressively decreases; these crystalline regions are effectively the mechanical reinforcing phases of PE. Crystalline content has a profound influence on mechanical properties of PE; for example, in HDPE the chains have a lower degree of branching, this allows the chains to pack together more easily into a uniform crystalline structure. MA-g-LLDPE contains a larger degree of chain branching therefore making it difficult to pack chains in a uniform fashion. The initial increases in tensile modulus of the 70 % wt. fly-ash filled LMDPE or HDPE composites with increasing MA-g-LLDPE content suggests improved matrix-filler interaction, resulting in better coupling between the filler particles surfaces and the PE matrix. The exceptionally high values of tensile modulus overall (relative to the unfilled matrix) for the 70 % wt. fly-ash filled HDPE and LMDPE composites indicates the fly-ash has good interaction in both LMDPE and HDPE with the presence of MA-g-LLDPE/LMDPE.

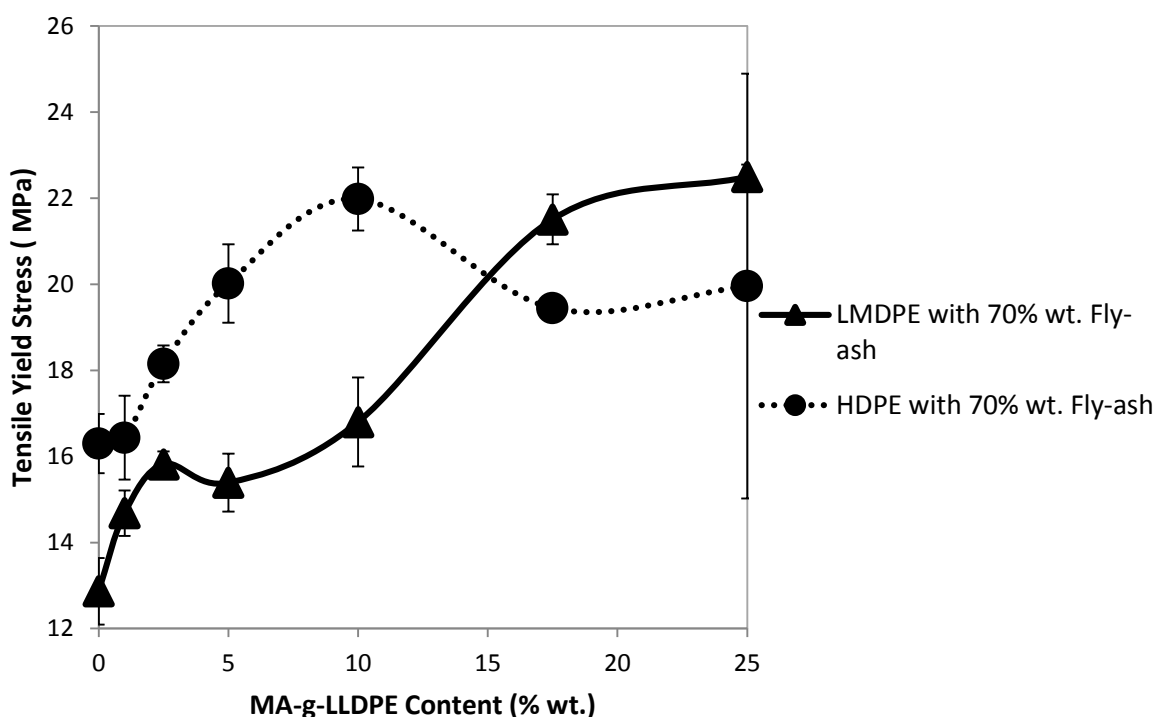


Figure 82. Tensile yield stress of unfilled and 70 % wt. fly-ash filled, HDPE or LMDPE with addition of MA-g-LLDPE.

The 70 % wt. fly-ash filled LMDPE and HDPE specimens also increased in yield stress (Figure 82) with the increase in MA-g-LLDPE, with the HDPE/fly-ash displaying optimal tensile performance between 5 and 10 % wt. MA-g-LLDPE loading. The 70 % by wt. fly-ash filled LMDPE displays improvements in tensile stress at yield which stabilises at 25 % MA-g-LLDPE addition; this suggested the establishment of a thick interfacial region which has high compatibility with the matrix, preventing the PE from tearing away at the filler particle surfaces (de-wetting or de-bonding). The decrease in tensile strength of the 70 % wt. fly-ash filled HDPE composites after 10 % wt. MA-g-LLDPE loading (Figures 81 and 82) may be due to a reduction in stiffness of the interfacial region. There is arguably better miscibility between the LMDPE and MA-g-LLDPE in comparison to the HDPE due to similarity of lamellar thickness, hence the better results. The tensile improvements observed at every level of MA-g-LLDPE addition to the 70 % wt. fly-ash filled LMDPE composites can also be attributed to a better transfer of stress from the PE matrix to the stiffer filler particles, as a result of improved matrix-filler adhesion; the increasing trend may be due to coupling by entrapment. LMDPE's better compatibility with MA-g-LLDPE covered filler particles also indicates trans-crystallisation is possible, giving composites with higher strength than the unfilled PE matrix.

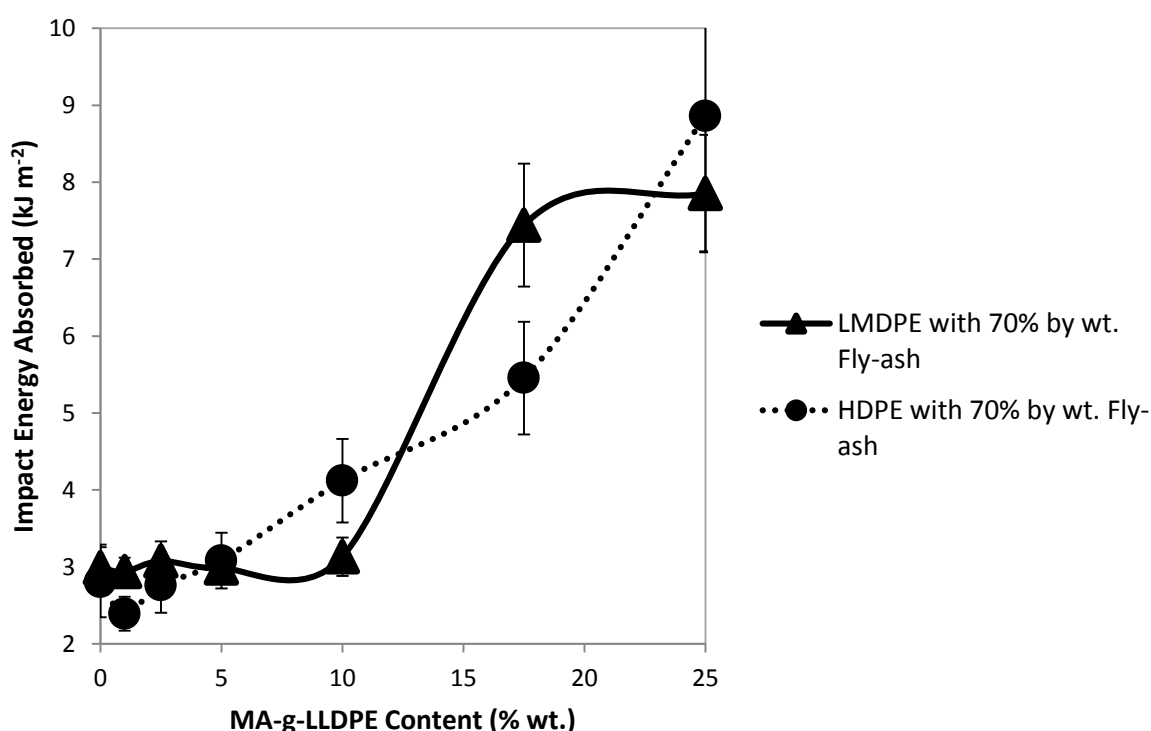


Figure 83. Impact energy absorbed of fly-ash filled HDPE or LMDPE with the addition of MA-g-LLDPE.

Overall, the impact energy absorbed by the 70 % wt. fly-ash filled LMDPE and HDPE (Figure 83) increased with the increase in MA-g-LLDPE. However, the 70 % wt. fly-ash/LMDPE composites at

and beyond 10 % wt. MA-g-LLDPE have a sharper increase in impact properties relative to equivalent HDPE composites, probably due to greater similarity of lamellar thicknesses. The increase in impact strength of polymer composites with the presence of MA is not surprising; Kord [242] observed an increase in the impact strength and tensile properties of PP/wood fibre composites with increasing levels of MA (up to 2 % wt.). The latter result is remarkable considering the brittleness of PP above its T_g relative to PE. On the other hand, the wood fibres are of considerably different shape, size and aspect ratio relative to the smaller spherical fly-ash particles.

5.8.1 Key findings from the comparison of Maleic Anhydride effects on HDPE and LMDPE fly-ash composites

Varying the level of coupling agent to assess its effect on the properties particulate-filled polymer composites for rotational moulding forms another novel aspect of this research. For the purpose of clarity, the key findings of this investigation are summarised in the following bullet points:

- With regards to tensile modulus, the 70 % wt. fly-ash filled LMDPE and HDPE specimens initially responded well to the introduction of MA-g-LLDPE coupling agent, particularly between 2.5 and 10 % wt. MA-g-LLDPE loading. However, at MA-g-LLDPE levels exceeding 10 % wt. in 70 % wt. fly-ash filled LMDPE or HDPE composites, the tensile modulus deteriorated with increasing MA-g-LLDPE addition. This reduction in stiffness may be due to the interfacial region being of lower stiffness due to excessive amounts MA-g-LLDPE covering the filler particles.
- The exceptionally high values of tensile modulus overall (relative to the unfilled matrix) for the 70 % wt. fly-ash filled HDPE and LMDPE composites indicates the fly-ash has good interaction in both LMDPE and HDPE with the presence of MA-g-LLDPE/LMDPE.
- The 70 % wt. fly-ash filled HDPE specimens increased in yield stress with the increase in MA-g-LLDPE, displaying optimal tensile performance between 5 and 10 % wt. MA-g-LLDPE loading. The decrease in tensile strength of the 70 % wt. fly-ash filled HDPE composites after 10 % wt. MA-g-LLDPE loading may be due to a reduction in stiffness of the interfacial region.
- The 70 % by wt. fly-ash filled LMDPE displays improvements in tensile stress at yield which stabilises at 25 % MA-g-LLDPE addition; this suggested the establishment of a thick

interfacial region which has high compatibility with the matrix, preventing the PE from tearing away at the filler particle surfaces (de-wetting or de-bonding).

- LMDPE's better compatibility with MA-g-LLDPE covered filler particles indicates trans-crystallisation is possible, giving composites with higher strength than the unfilled PE matrix.

5.9 Analysis of Rotationally Moulded Small Particle Composites

The TSE melt blended, compression moulded PE/fly-ash composites gave considerable increases in stiffness with the addition of fly-ash, due to good interaction between the fly-ash particles and the MA-g-LLDPE coupling agent additive; the highest filled PE/fly-ash composites (70 % wt.) were at least six times the tensile modulus of the unfilled matrix (Figure 78). However, the latter materials had not yet been rotationally moulded; it was therefore decided to investigate the properties of two PE/fly-ash rotomoulded products; a small rectangular box (test moulding) and a larger safety step (production moulding). The small rectangular box test mould was based on an aluminium bread baking tin. The safety step is a commercially available product typically used by aircraft technicians for inspecting the underside of fuselages and wings.

5.9.1 Rotomoulded rectangular box test mouldings

Small rotomoulded rectangular box test mouldings made using various formulations of compounded PE/fly-ash (Table 16) were produced at the industrial sponsors facility (Rotomotive Ltd., Experimental Section 4.5.4).

Table 16. Small Rectangular Box Mouldings

MA-g-LLDPE/LMDPE (% wt.)	Fly-ash. (% wt.)
100	0
75	25
50	50
40	60
30	70

Upon visual inspection, small pinholes were seen on the both the internal (air side) and external (mould side) surfaces of the moulding, becoming greater in number with the increase in fly-ash

content (see Figure 84). Therefore, it was decided to photograph the moulding surfaces using a DSLR camera (Experimental Section 4.7). Images were then uploaded into “imageJ” analysis software to identify the the count, size and area fraction of the pinholes for correlation with MFR and fly-ash content; the latter parameters painted an informative picture of the relationship between MFR, fly-ash content and and material processability. Figures 85 and 86 (stacked graphs) reveal how the number and area fraction of the pinholes increase with the addition of fly-ash and decrease with rising MFR (ie. reduction in fly-ash addition). However, the average hole diameter progressively gets larger up to 28.8 % vol. fly-ash loading (50 % wt.) and then decreases at 31.7 and 34.6 % vol. Figures 85 and 86 also demonstrate the impact of fly-ash addition to the melt flow properties of the resulting composite; with every fly-ash level, the MFR decreases. The latter observation confirms that the melt flow properties play a significant role in the overall quality of a rotomoulded part; high levels of filler particles can disrupt the rheology of the PE melt, decrease the MFR and thus produce mouldings with defects.

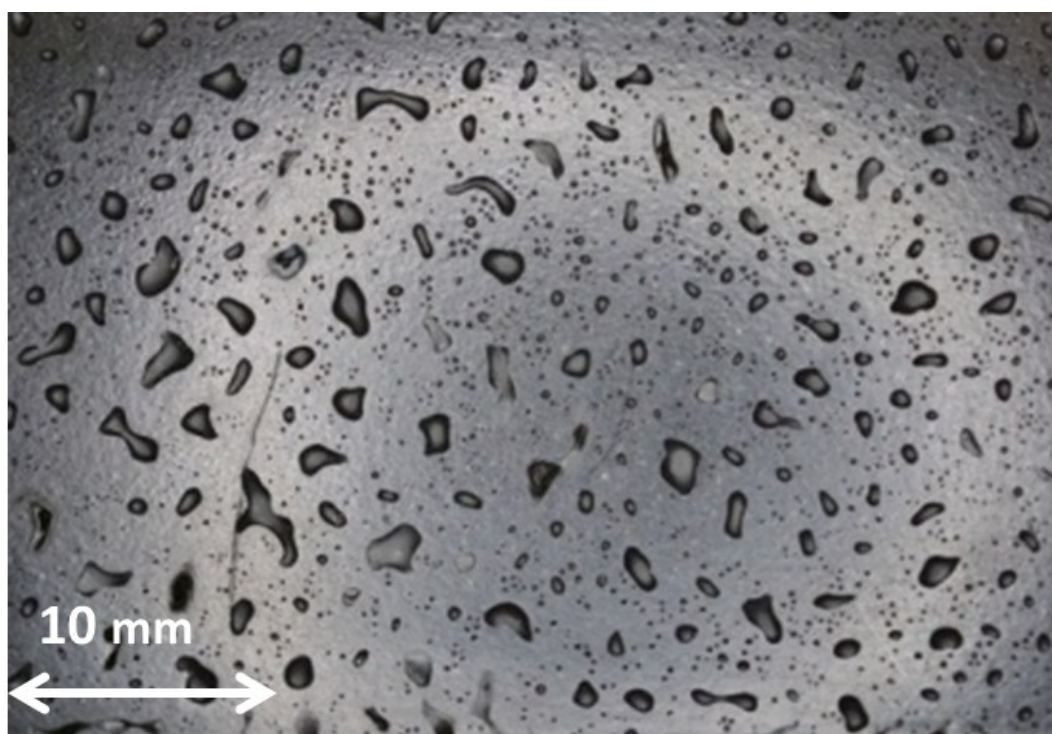


Figure 84. Pin holes on the surface of rotomoulded rectangular box test moulding (50 % wt. fly-ash/PE).

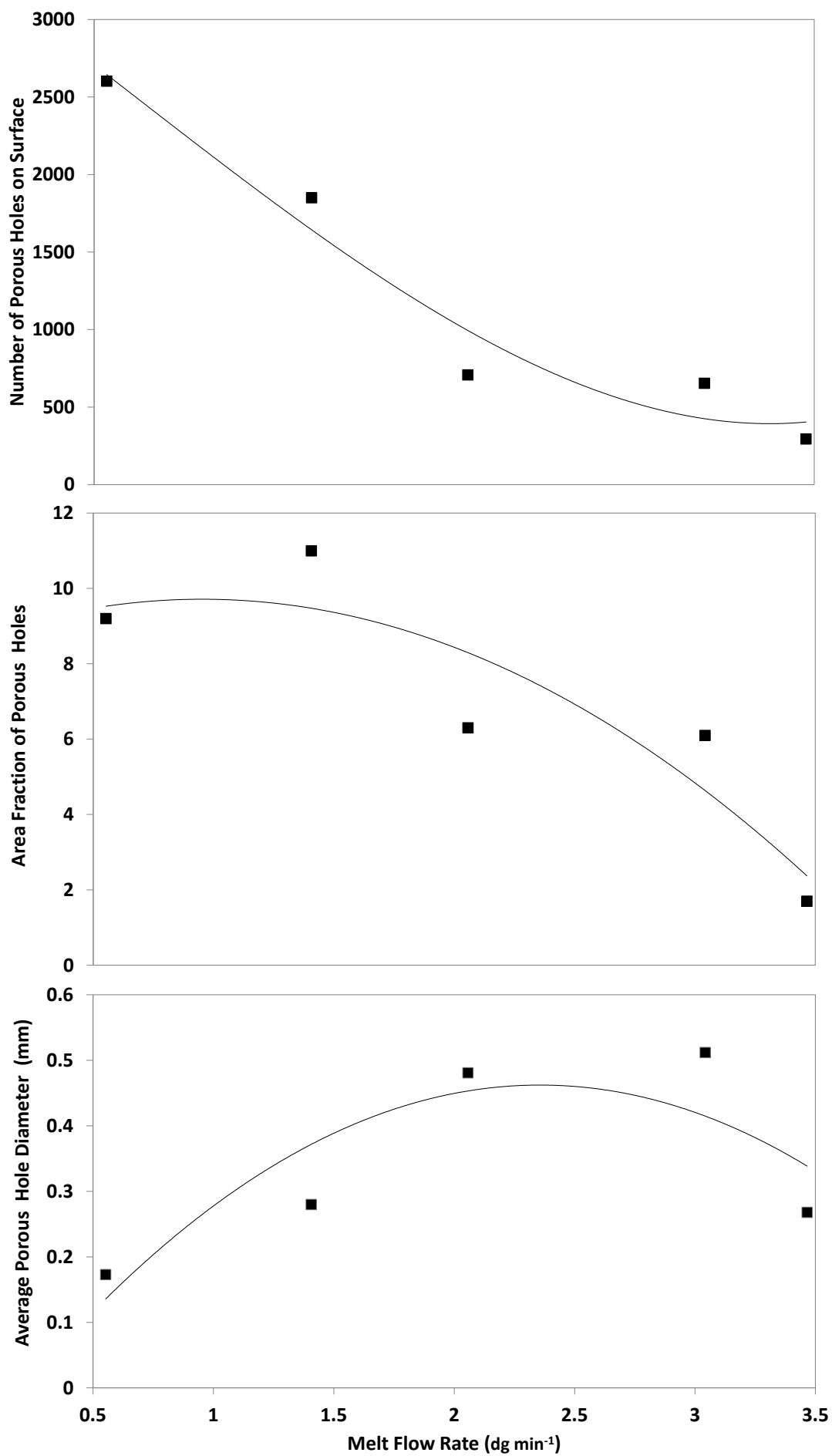


Figure 85. Pinhole count, area fraction and diameter vs. MFR of MA-g-LLDPE/LMDPE with fly-ash.

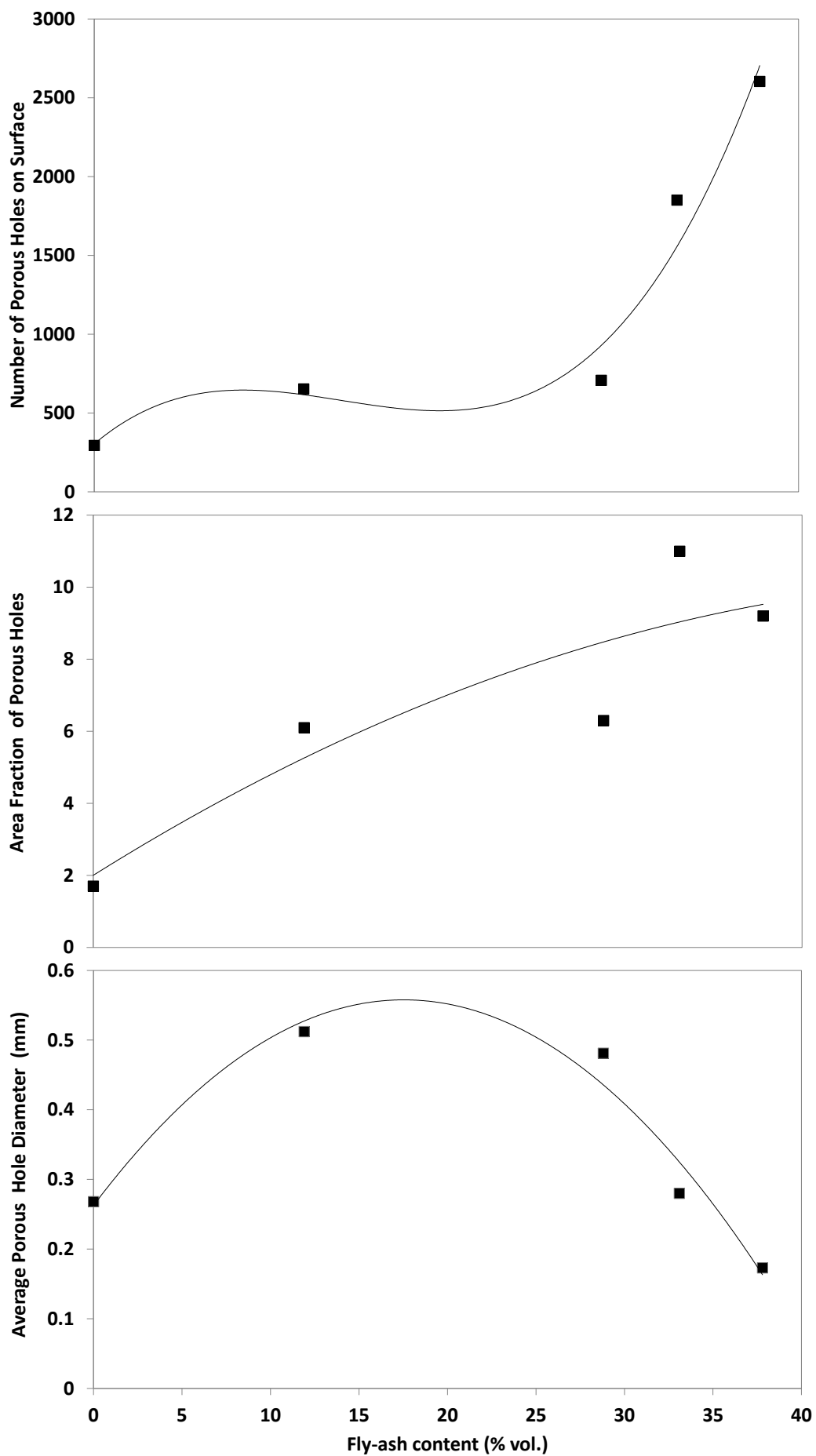


Figure 86. Pinhole count, area fraction and diameter vs. fly-ash content in MA-g-LLDPE/LMDPE.

5.9.2 Rotomoulded safety steps

The TSE compounded, compression moulded PE/fly-ash composites at 28.8 % vol. fly-ash loading had at least twice the tensile modulus of unfilled PE, partially due to good interaction between the fly-ash particles and the MA-g-LLDPE coupling agent additive (Figures 78 and 79). The doubling in stiffness of rotomoulded PE due was the main aim of this research. Thus far, the PE/fly-ash composite test materials were produced using a high pressure compression moulding process, relative to the zero-shear encountered in rotomoulding. Consequently, it was decided to rotomould safety steps (refer to Figure 87 and Experimental Section 4.5.5) using the maleanised PE/fly-ash composites up to 28.8 % vol. fly-ash loading and compare these with a selection of equivalent steps moulded using three other competitive grades of unfilled PE (Table 17); two of those grades were HDPE designed for liquid storage tanks, canoes and kayaks (N307 and M601, Experimental Section 4.5.5.1). The safety steps were compression tested and tensile test pieces were cut from their flat surfaces for analysis (Experimental Section 4.6.6, 4.6.7). The step mouldings also provided insight into the “rotomouldability” of the stiffer maleanised PE/fly-ash composite material. MFR determinations on the PE/fly-ash blends used to rotomould the rectangular box test mouldings (Table 16, Figure 88) revealed that the addition of fly-ash to the MA-g-LLDPE/LMDPE blend has a largely negative impact on the on the melt flow behaviour of the resulting composites, particularly for composites containing more than 28.8 % vol. fly-ash.

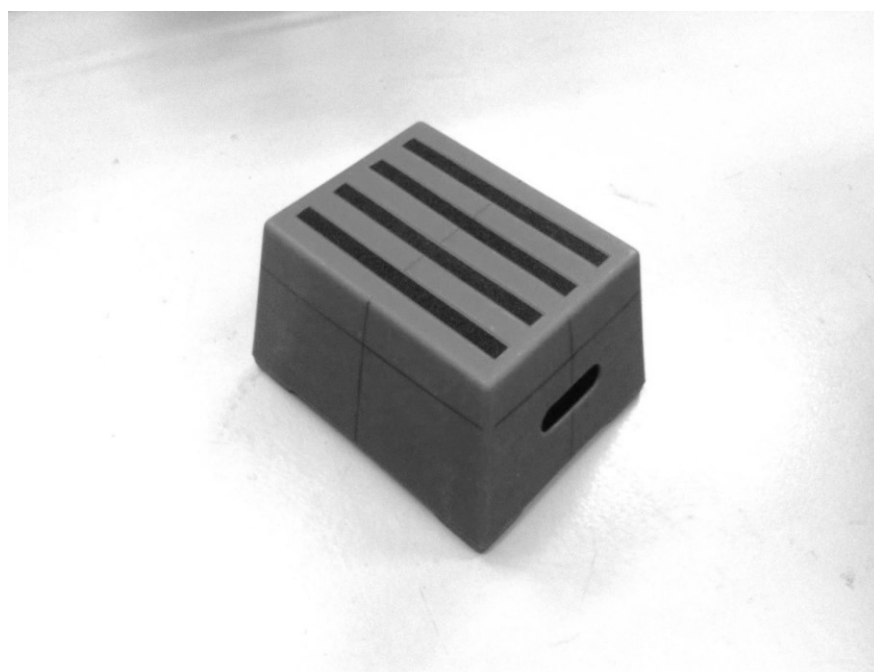


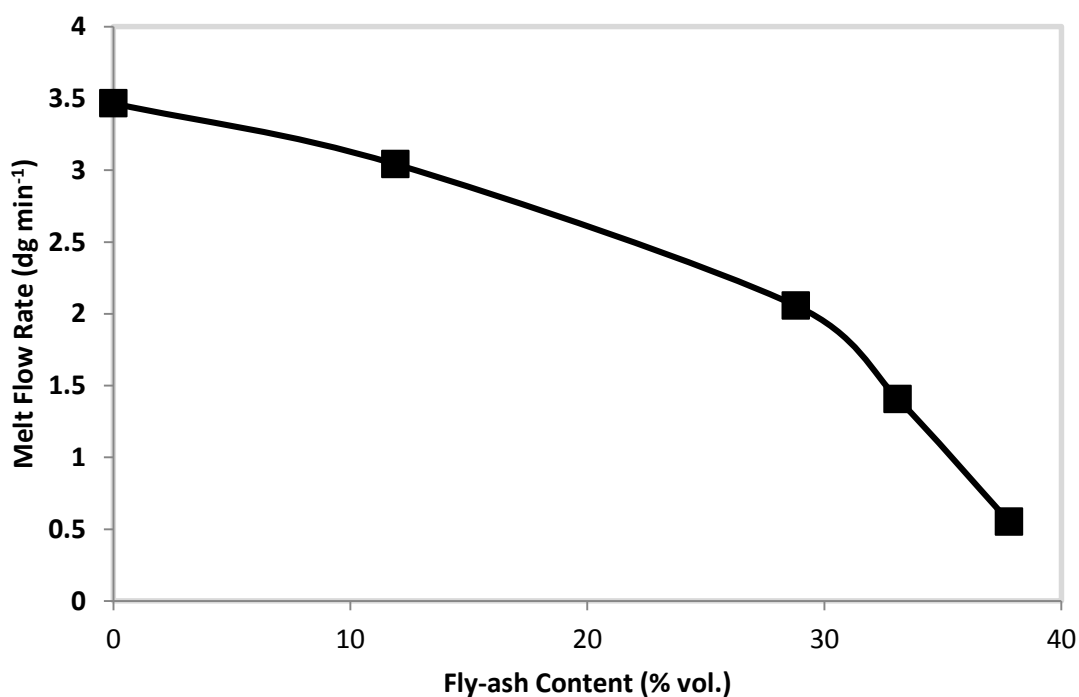
Figure 87. Rotomoulded PE safety step.

Table 17. Unfilled PE grades used for rotomoulded safety steps.

Target Wall Thickness (mm)	PE Grade
7	N-250 LMDPE
7	N-307 HDPE
7	M-601 HDPE

Table 18. PE/fly-ash formulations for rotomoulded safety steps.

Target Wall Thickness (mm)	MA-g-LLDPE/LMDPE (% wt.)	Fly-ash (% vol.)	Fly-ash (% wt.)
7	50	28.8	50
7	75	14.4	25
7	87.5	7.2	12.5
7	100	0	0

**Figure 88.** MFR of MA-g-LLDPE/LMDPE with the addition of fly-ash, specified in Table 16.

Liquid displacement and ashing tests were also conducted (Figure 89) in order to determine the density of the PE/fly-ash composites (Experimental Section 4.3.5); the ashing type test provided a pinpoint accurate verification of the filler content due to combustion of the polymer within the composite, leaving the fly-ash residue.

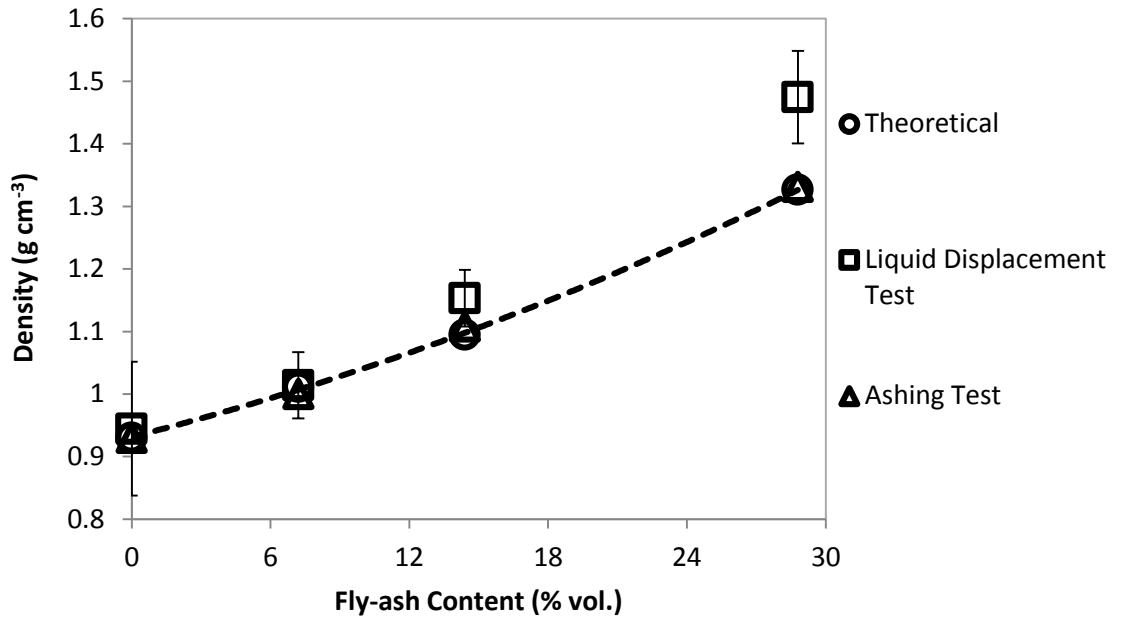


Figure 89. Density of rotomoulded PE/fly-ash safety step materials.

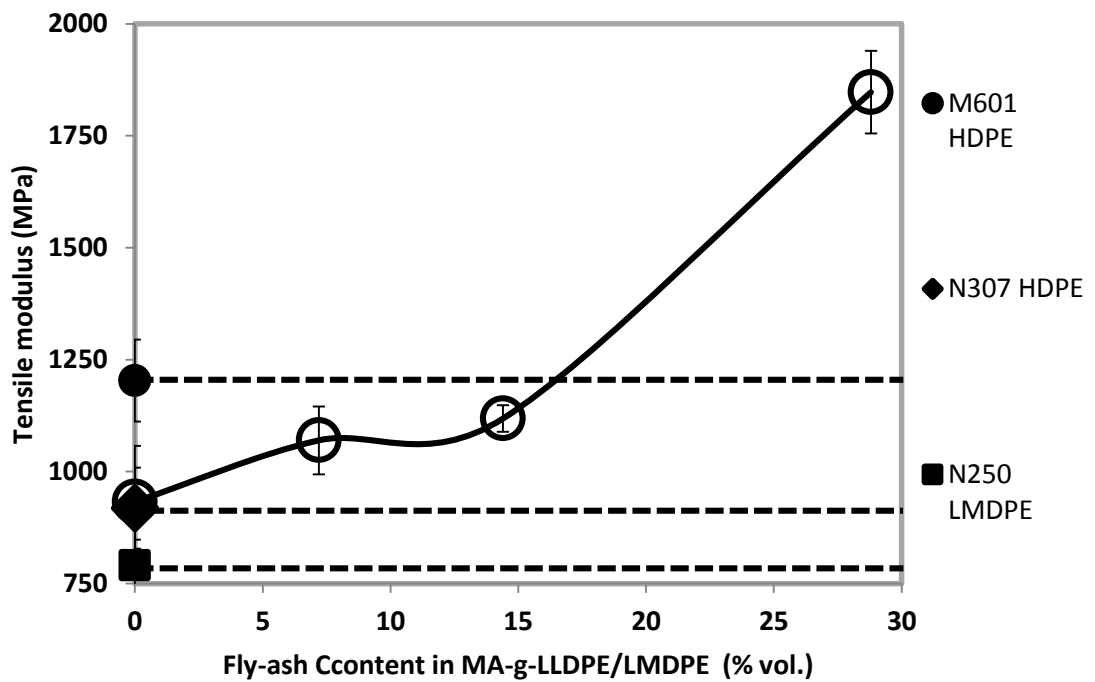


Figure 90. Tensile modulus of rotomoulded MA-g-LLDPE/LMDPE with the addition of fly-ash versus unfilled rotomoulded PE grades.

Figures 90 and 91 display the tensile modulus and stress at yield of samples cut from the PE/fly-ash safety steps, all of which had a target wall thickness of 7 mm (conforming to the original design specification of the commercial LMDPE safety step product, Table 17). The average tensile modulus and stress at yield for the unfilled N250 LMDPE, N307 HDPE and M601 HDPE

rotomoulded safety steps were also plotted against equivalent parameters from PE/fly-ash safety steps. It is arguable that, in terms of tensile modulus (which increased with every fly-ash level investigated) the 14.4 and 28.8 % vol. fly-ash/PE composite material competed extremely well against the N307 tank grade and the M601 canoe/kayak grade, both of which have good stiffness for RM applications. The latter PE grades are more expensive (Table 3, Experimental section 4.5.5.1) relative to the more popular N250 LMDPE rotomoulding grade PE. The increase in tensile modulus of the PE/fly-ash composite materials with every level of fly-ash investigated can be attributed to a better transfer of stress from the flexible PE matrix to the stiffer filler particles, as a result of improved matrix-filler adhesion. However, the 14.4 % vol. fly-ash/PE composite performed consistently well in terms of tensile modulus and stress at yield. Moreover, the sharp jump in tensile stress at yield for both 7.2 and 14.4 % vol. fly-ash/PE composites suggests the MA-g-LLDPE coupling agent has good functionality with the surfaces of the spherical fly-ash particles, even with the zero-shear conditions encountered in rotomoulding. Moreover, it is evident from Figure 91 that the fly-ash content could be increased to some point between 14 and 28 % vol.

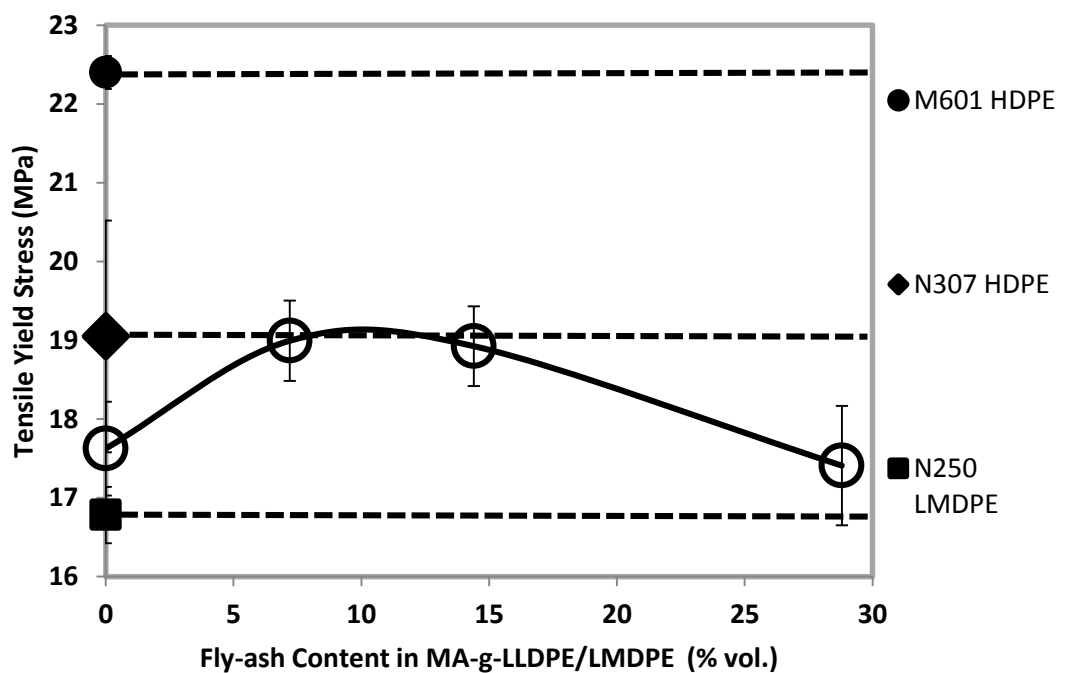


Figure 91. Tensile yield stress of rotomoulded MA-g-LLDPE/LMDPE with the addition of fly-ash versus unfilled rotomoulded PE grades.

Charpy impact tests were also conducted to analyse the PE/fly-ash composite systems impact properties. It is evident from Figure 92 that the increase in fly-ash content decreases the impact toughness of the composite; the sharp fall may be due to a change in fracture mechanism arising from the average distance between filler particles becoming too small for a crack pinning mechanism to operate (as seen at 7.2 % vol. fly-ash loading).

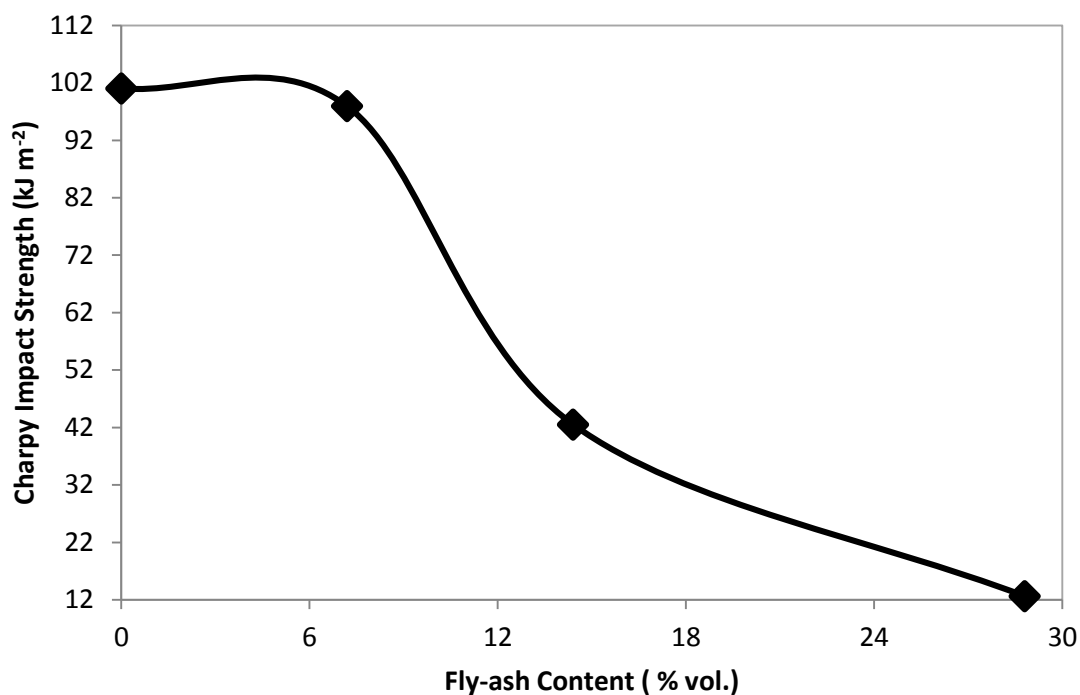


Figure 92. Charpy Impact properties of MA-g-LLDPE/LMDPE with the addition of fly-ash.

The rotomoulded safety steps detailed in Tables 17 and 18 were compression tested to 600 N (Experimental Section 4.6.6). Force-deflection curves are shown in Figures 93 and 94. It is clear from Figure 93 that the 14.4 and 28.8 % vol. fly-ash/PE safety steps undergo considerably less deflection of the loaded surface relative to the unfilled N307 HDPE and M601 HDPE safety steps under compression. Even the unfilled maleanised PE safety step is stiffer than the unfilled N250 LMDPE safety step (Figure 94). The overall stiffness of the PE/fly-ash steps increases with the increase in filler content; the superior stiffness of the PE/fly-ash composites showcases its great potential for rotomoulding applications. However, it was appreciated that the significant variations in wall thickness of all the rotomoulded safety steps may play an important role in their geometrical stiffness (Figure 95).

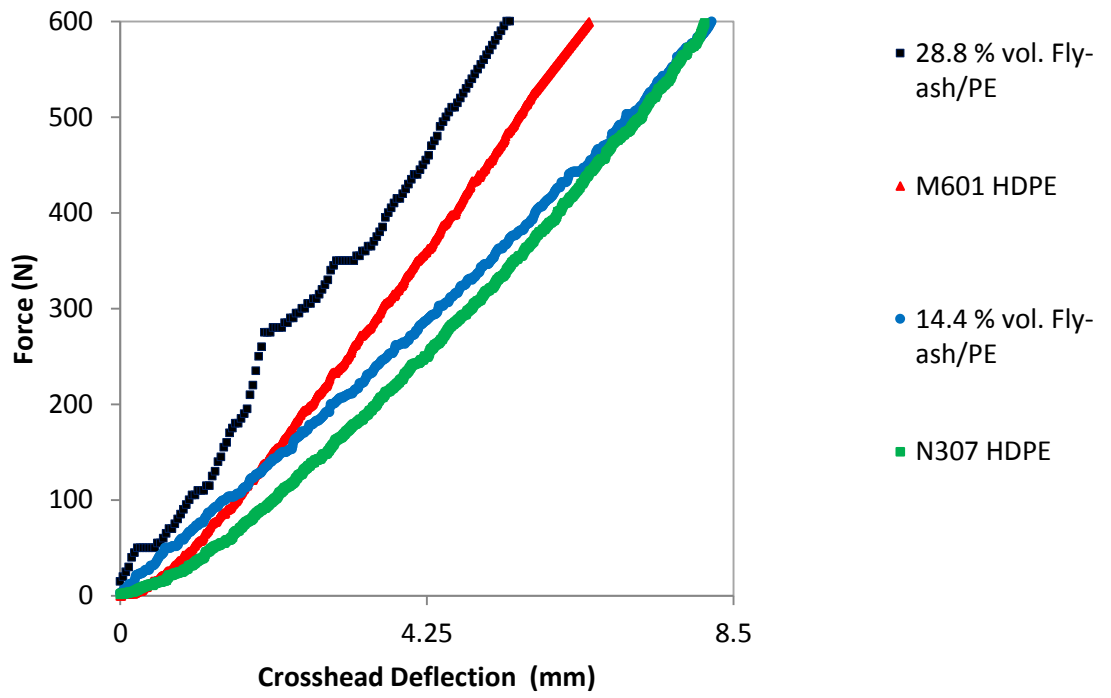


Figure 93. Force-deflection curves of rotomoulded PE/fly-ash safety steps vs. unfilled PE equivalents.

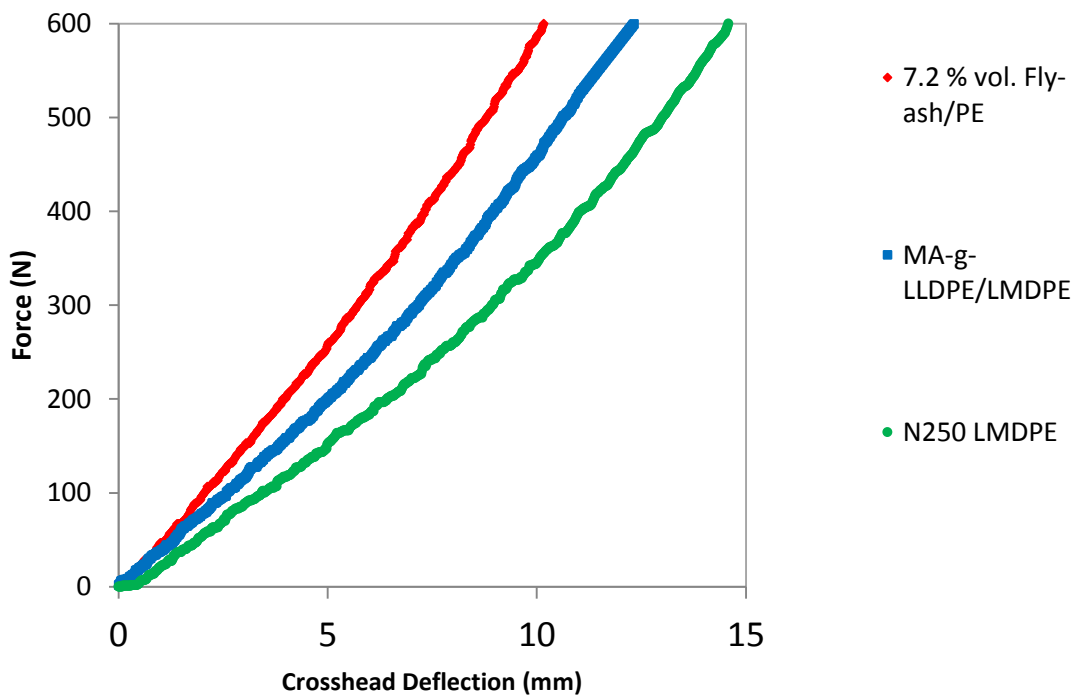


Figure 94. Force-deflection curves of rotomoulded PE/fly-ash safety steps vs. unfilled PE equivalents.

Considering the significant variation in wall thickness of the rotomoulded PE/fly-ash safety steps, it was decided to measure their wall thickness in all four corners and halfway across the top and bottom surfaces (Figure 95).

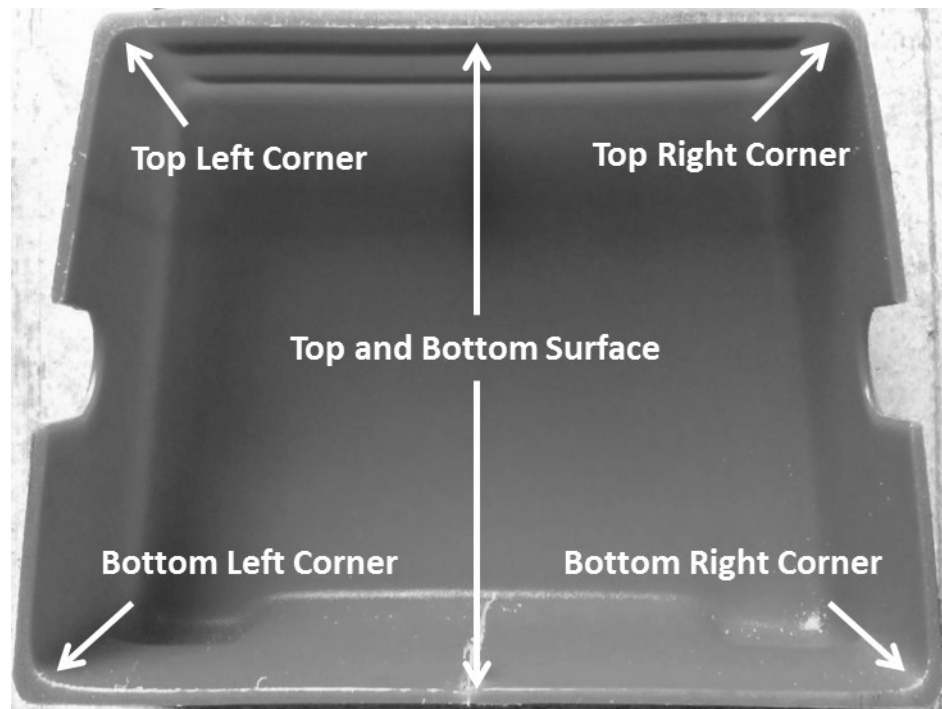


Figure 95. Rotomoulded safety step cross section for measurement of wall thickness. The measurement points were halfway across the top and bottom surface and the corners.

It is clear from Figure 96 that the wall thicknesses of the PE/fly-ash safety steps investigated are considerably different to the target of 7 mm. This is probably due to the absence of pressure during the rotomoulding process to better disperse the polymer melt and prevent excess material from congregating into the corners of the mould. However, the corner thicknesses of the MA-g-LLDPE/LMDPE safety steps decrease with the addition of fly-ash. Figure 97 confirms the addition of fly-ash significantly decreases the MFR of the resulting composites; the viscosity of the PE/fly-ash composites in the melt state is high as a consequence of modification to the melt rheology by the fly-ash particles. Interestingly, this increase in melt viscosity may be promoting better distribution of the melt in the mould; the top middle surface actually increases in thickness with the increase in fly-ash loading, confirming the PE/fly-ash safety steps lose material (i.e. thickness) from the corners and gain material in the top surface with the increase in fly-ash loading. The decrease in wall thickness at the bottom middle surface of the safety steps with the increase in fly-ash loading is understandable; due the angle of the safety steps sidewalls (Figure 95), the

bottom corners gain considerably more material (i.e. thickness) during rotomoulding. Therefore, less material is available from which to disperse across the bottom surface of the step.

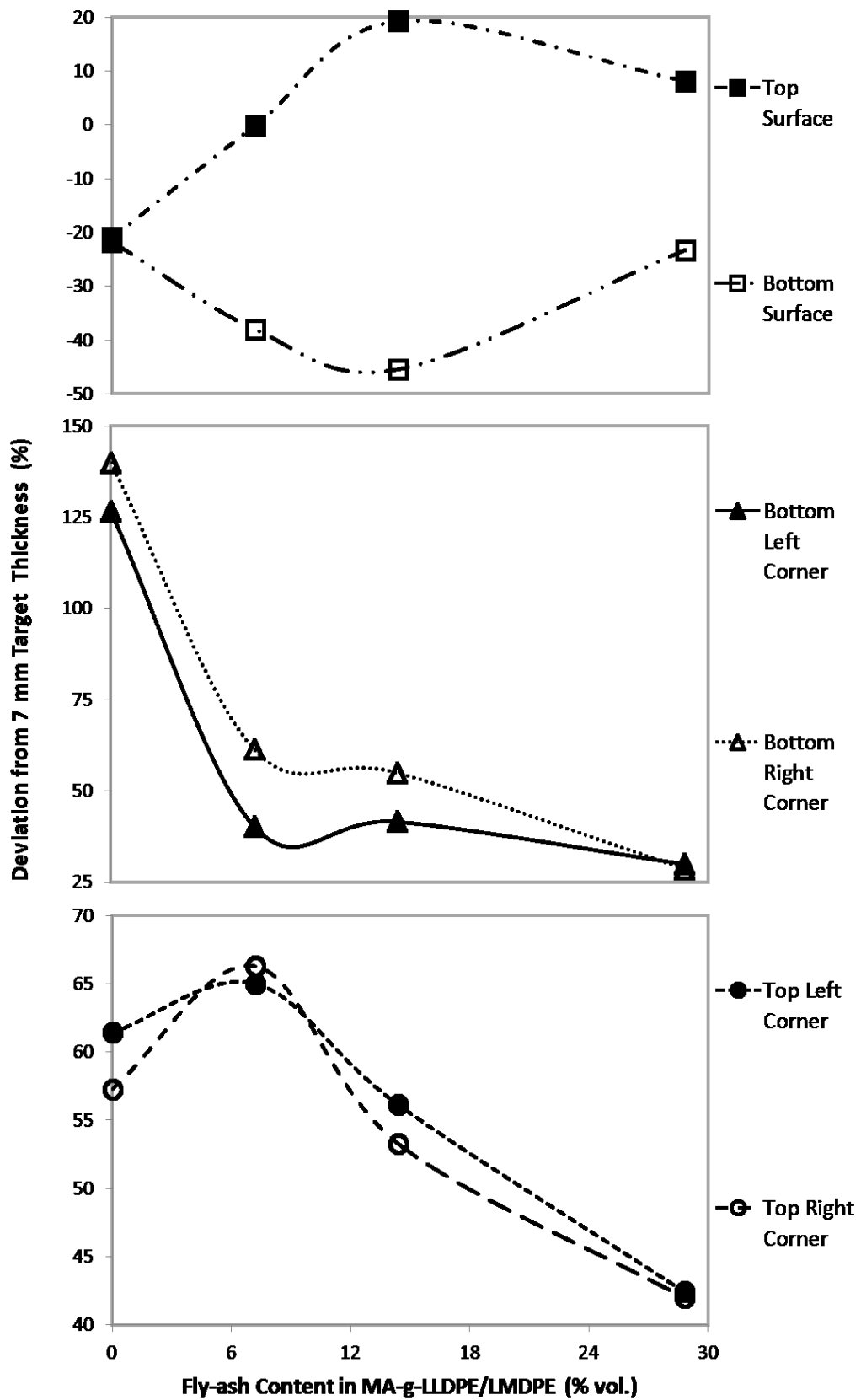


Figure 96. Percentage wall thickness deviation of the rotomoulded PE/fly-ash safety steps from the 7 mm target vs. fly-ash content.

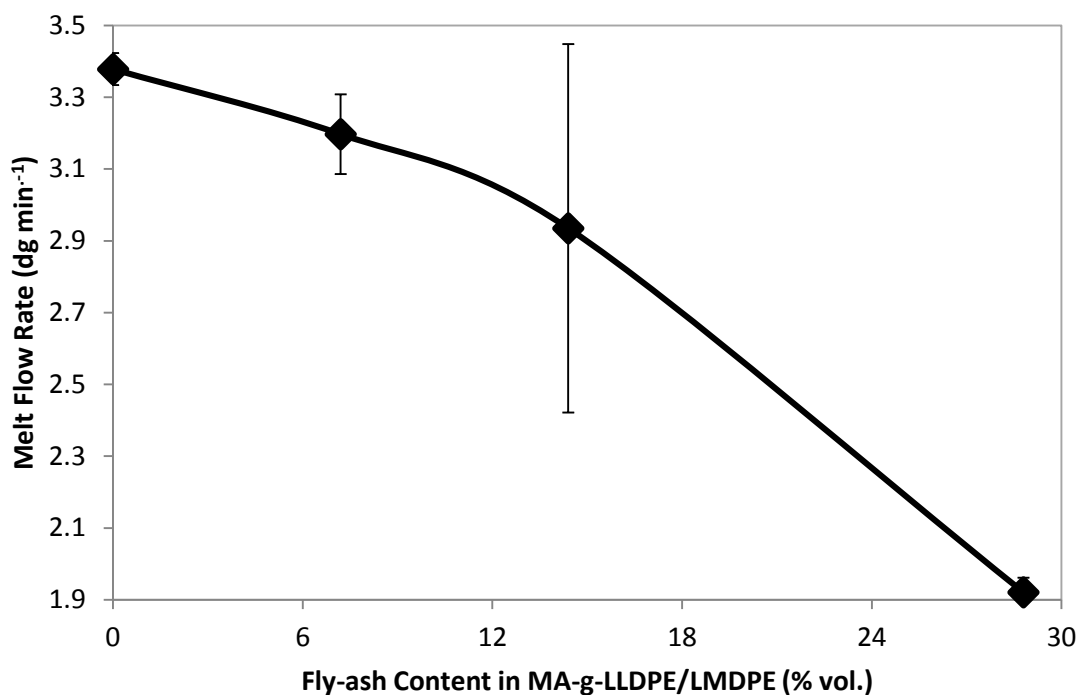


Figure 97. MFR of PE/fly-ash composites detailed in Table 18.

5.9.3 Key findings from the analysis of rotationally moulded small particle composites

The image analysis technique used to analyse pinholes on the surface of rotomoulded products forms another novel aspect of this research. For the purpose of clarity, the key findings of this investigation are summarised in the following bullet points:

- Upon visual inspection, small pinholes were seen on the both the internal (air side) and external (mould side) surfaces of the moulding, becoming greater in number with the increase in fly-ash content.
- The number and area fraction of the pinholes increase with the addition of fly-ash and decrease with rising MFR (ie. reduction in fly-ash addition). However, the average hole diameter progressively gets larger up to 28.8 % vol. fly-ash loading (50 % wt.) and then decreases at 31.7 and 34.6 % vol.
- With every level of fly-ash, the MFR of MA-g-LLDPE decreases. The latter observation confirms that the melt flow properties play a significant role in the overall quality of a rotomoulded part; high levels of filler particles can disrupt the rheology of the PE melt, decrease the MFR and thus produce mouldings with defects.

- In terms of tensile modulus (which increased with every fly-ash level investigated) the 14.4 and 28.8 % vol. fly-ash/PE composite material competed extremely well against the N307 tank grade and the M601 canoe/kayak grade, both of which have good stiffness for RM applications.
- The 14.4 % vol. fly-ash/PE composite performed consistently well in terms of tensile modulus and stress at yield. Moreover, the sharp jump in tensile stress at yield for both 7.2 and 14.4 % vol. fly-ash/PE composites suggests the MA-g-LLDPE coupling agent has good functionality with the surfaces of the spherical fly-ash particles, even with the zero-shear conditions encountered in rotomoulding.
- It is evident that the fly-ash content could be increased to some point between 14 and 28 % vol. in an effort to balance the increase in modulus with better impact properties.
- The increase in fly-ash content decreases the impact toughness of the composite; the sharp fall may be due to a change in fracture mechanism arising from the average distance between filler particles becoming too small for a crack pinning mechanism to operate (as seen at 7.2 % vol. fly-ash loading).
- The 14.4 and 28.8 % vol. fly-ash/PE safety steps undergo considerably less deflection of the loaded surface relative to the unfilled N307 HDPE and M601 HDPE safety steps under compression.
- The unfilled MA-g-LLDPE safety step is stiffer than the unfilled N250 LMDPE safety step. However, the overall stiffness of the PE/fly-ash steps increases with the increase in filler content; the superior stiffness of the PE/fly-ash composites showcases its great potential for rotomoulding applications.
- The viscosity of the PE/fly-ash composites in the melt state is high as a consequence of modification to the melt rheology by the fly-ash particles. Interestingly, this increase in melt viscosity may be promoting better distribution of the melt in the mould.

5.10 High Temperature Flexural Testing of Injection Moulded PE/Fly-ash Composites

The TSE compounded PE/fly-ash materials used to rotomould the safety steps in this report (Table 18) were injection moulded at MMU for ambient temperature (23 °C) and high temperature flexural three point bend tests (Experimental Section 4.6.3); it was appreciated that understanding the behaviour of the PE/fly-ash material at elevated temperatures was important, as this serves as another method of material characterisation. Figures 98 and 99 identify that the introduction of fly-ash particles to PE increases the flexural modulus and stress at 10 mm deflection regardless of temperature. However, the flexural performance of the PE/fly-ash composite becomes increasingly worse with the rise in temperature, particularly for the samples at 115 °C, whereby the flexural stress at 10 mm deflection is less than the unfilled matrix (Figure 99). At 85 °C, the amorphous regions (ductile regions) of PE are more easily affected by the heat, whereas the crystalline regions (stiffer regions) of PE will remain relatively more stable. Conversely, the crystalline structure of PE begins to breakdown when approaching its melting temperature, explaining the severe drop in flexural stress at 115 °C (Figure 99). The unfilled PE matrix at 115 °C performed so poorly a meaningful value of flexural modulus could not be determined (Figure 98).

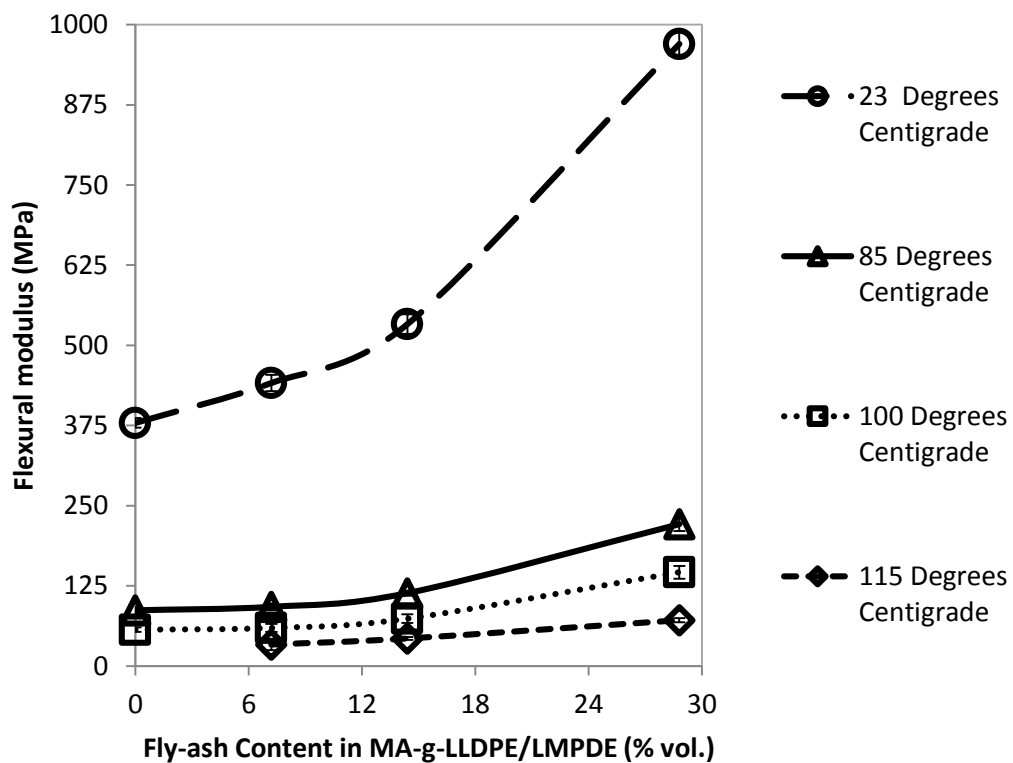


Figure 98. Flexural modulus of injection moulded PE/fly-ash composites at elevated temperatures.

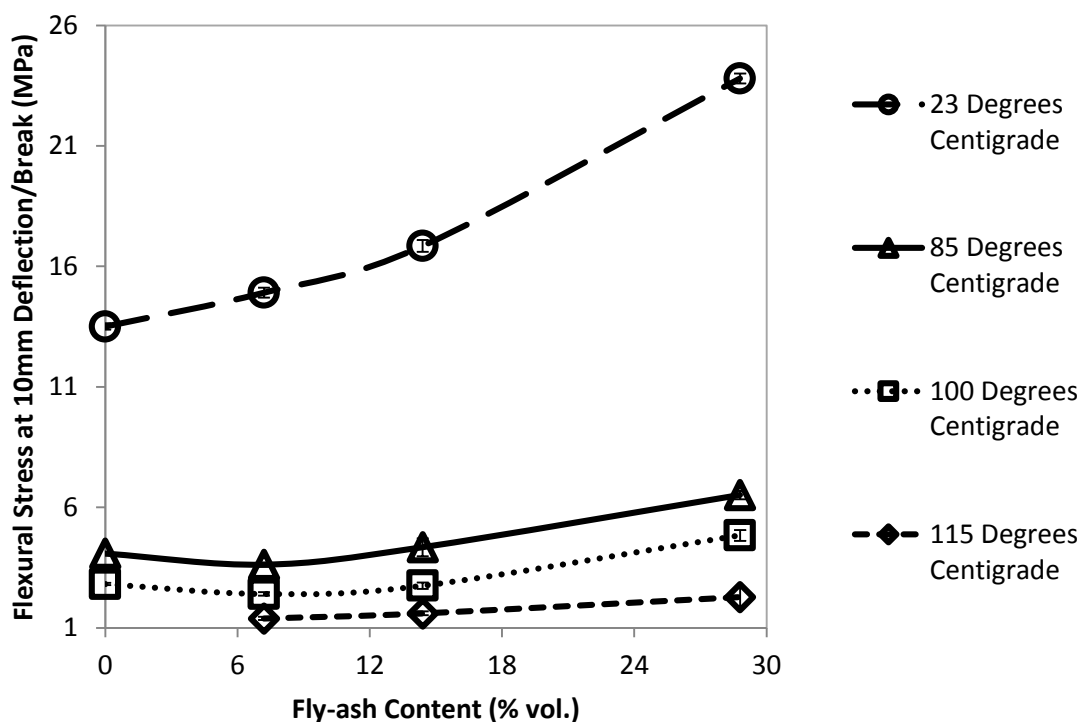


Figure 99. Flexural stress at 10 mm deflection for injection moulded PE/fly-ash composites at elevated temperatures.

5.11 Cost Benefit Analysis of the Small Particle Composites for Rotational Moulding

Arguably, the most attractive factor favouring use of PE for rotomoulding is the relatively low cost; PE is definitively the cheapest polymer in the context of RM. However, the modulus of PE is inherently low. Therefore, the wall thicknesses of rotomoulded products are increased to compensate for this low modulus. Increasing the wall thickness is a common tactic for larger load-bearing articles such as liquid storage tanks and silos, where manufacturers often over-thicken the walls to be confident in part strength. Although practically justified, increasing the wall thickness of RM products uses more material, slows production cycles and increases costs.

The PE/fly-ash composite at a filler loading of 50 % wt. (28.8 % vol.) was selected for an estimated cost comparison with the unfilled 25 % wt. MA-g-LLDPE/75 % wt. LMDPE formulation; with the latter formulation, the aim of doubling the modulus of the MA-g-LLDPE/LMDPE formulation was achieved with the addition of 28.8 % vol. fly-ash. The cost comparison is available in Tables 19 and 20 and discussed in the following paragraphs.

Table 19. Cost and modulus of the PE/fly-ash composite material.

PE/Fly-ash Composite			
Materials	MA-g-LLDPE	LMDPE	Fly-ash
Estimated Price (£ kg ⁻¹)	3	1.25	0.35
Amount (% wt.)	12.5	37.5	50
Price for Materials (£ kg ⁻¹)	0.38	0.47	0.35
Estimated Twin Screw Extrusion Price (£ kg ⁻¹)	0.25		
Estimated Pellet Grinding Price (£ kg ⁻¹)	0.15		
Total Cost (£ kg ⁻¹)	1.59		
Tensile Modulus	1847.30		
Tensile Modulus Standard Deviation	92.32		

Table 20. Cost and modulus of the unfilled MA-g-LLDPE/LMDPE material.

Unfilled PE		
Material	MA-g-LLDPE	LMDPE
Estimated Price (£ kg ⁻¹)	3	1.25
Amount (% wt.)	25	50
Price for Materials (£ kg ⁻¹)	0.75	0.94
Estimated Twin Screw Extrusion Price (£ kg ⁻¹)	0.25	
Estimated Pellet Grinding Price (£ kg ⁻¹)	0.15	
Total Cost (£ kg ⁻¹)	2.09	
Tensile Modulus	932.61	
Tensile Modulus Standard Deviation	124.56	

It is clear from Tables 19 and 20 that the PE/fly-ash composite (with 28.8 % vol. fly-ash) is approximately 24 % cheaper (at £1.59 per kg) than the unfilled MA-g-LLDPE/LMDPE at £2.09 per kg. Furthermore, the PE/fly-ash composite has double the tensile modulus of the unfilled MA-g-LLDPE/LMDPE matrix. However, a reduction in material cost was not the ultimate objective of this PhD study. The potential of down-gauging part thickness due to the high modulus of the PE/fly-ash composite has far more significance to rotomoulders; currently, many large rotomoulded PE products (such as liquid storage tanks or kayaks) have large wall thicknesses, which makes them tedious and impractical to mould. Therefore, it is crucial to gauge the effectiveness of the higher modulus PE/fly-ash composite material at reducing the wall thickness; the flexural deflection (δ) of a rectangular cross-section beam is inversely proportional to the modulus (E) and the thickness cubed (d^3), as seen in Equation 27.

$$\delta = \frac{FL}{4Ebd^3} \quad \text{Equation 27.}$$

Where:

F = Force (N)

L = Support Span Length (m)

E = Tensile Modulus (Pa)

b = Width (m)

d = Thickness (m)

Therefore, in order to reduce the wall thickness by half, a material with 8 times the modulus would be required. For rotomoulding, no such polymer with that high a modulus is available. Despite the latter, there is still potential to down-gauge part thickness with the selected PE/fly-ash composite material. It is clear from Table 21 that a potential 12.38 % reduction in wall thickness is possible with the higher modulus PE/fly-ash composite. Although the latter potential reduction in wall thickness is not particularly large, it would certainly be beneficial to rotomoulders as its modulus-to-price ratio is good (relative to PA or PC) and the possible reduction in wall thickness could help to rotomould more effectively.

Table 21. Wall thickness reduction potential of the PE/filler composite, relative to the unfilled MA-g-LLDPE/LMDPE matrix.

Material	Tensile Modulus (E)	Standard Deviation	$E_{(\text{Chosen Material})}/E_{(\text{MA-g-LLDPE/LMDPE})}$	Wall Thickness Reduction Potential (%)
MA-g-LLDPE/LMDPE	932.61	124.56	1	0
PE/Fly-ash	1847.30	92.32	1.98	12.38

5.12 Finite Element Analysis of Small Particle Composite Safety Step Sidewall Deflection

5.12.1 Specification of material properties for FE model development

It is clear that the PE/fly-ash composite material has a usefully high modulus relative to rotomoulding grade PE at the highest filler content investigated (28.8 % vol., Figure 90). Rotomoulders expected to use the new PE/fly-ash composite materials typically use FEA to verify the structural integrity of load-bearing designs before signing-off final revisions. The rotomoulded safety step was selected for FEA investigations due to its suitable size for compression testing, symmetrical geometry and relatively straightforward loading scenario. Parameters from direct physical test data such as the tensile modulus, Poisson's ratio, tensile yield stress and tensile

stress-strain curves for the PE/fly-ash materials (Table 18) were required for FEA of the safety steps sidewall deflection.

5.12.1.1 Tensile properties and Poisson's ratio

Table 22 displays the tensile properties derived from direct physical testing of the PE/fly-ash composites used for FE models of the PE/fly-ash safety steps. Figure 100 displays the tensile stress-strain curves of PE/fly-ash test pieces that were closest to the average tensile modulus and stress at yield. It is clear that the filled materials are stiffer relative to the unfilled PE matrix. The latter stress-strain curves were required for non-linear FEA only; linear and non-linear FEA are explained in the Literature Review Section 3.4.4).

Table 22. PE/Fly-ash material properties for FEA software input

PE (% wt.)	Fly-ash (% wt.)	Fly-ash (% vol.)	Tensile Modulus (MPa)	Standard Deviation	Yield Stress (MPa)	Standard Deviation
25 MA-g-LLDPE/75 LMDPE	0	0	932.61	124.56	17.04	1.22
25 MA-g-LLDPE/75 LMDPE	12.5	7.2	1069.88	75.80	18.99	0.51
25 MA-g-LLDPE/75 LMDPE	25	14.4	1190.96	179.81	18.74	0.64
25 MA-g-LLDPE/ 75 LMDPE	50	28.8	1847.30	92.32	17.41	0.76

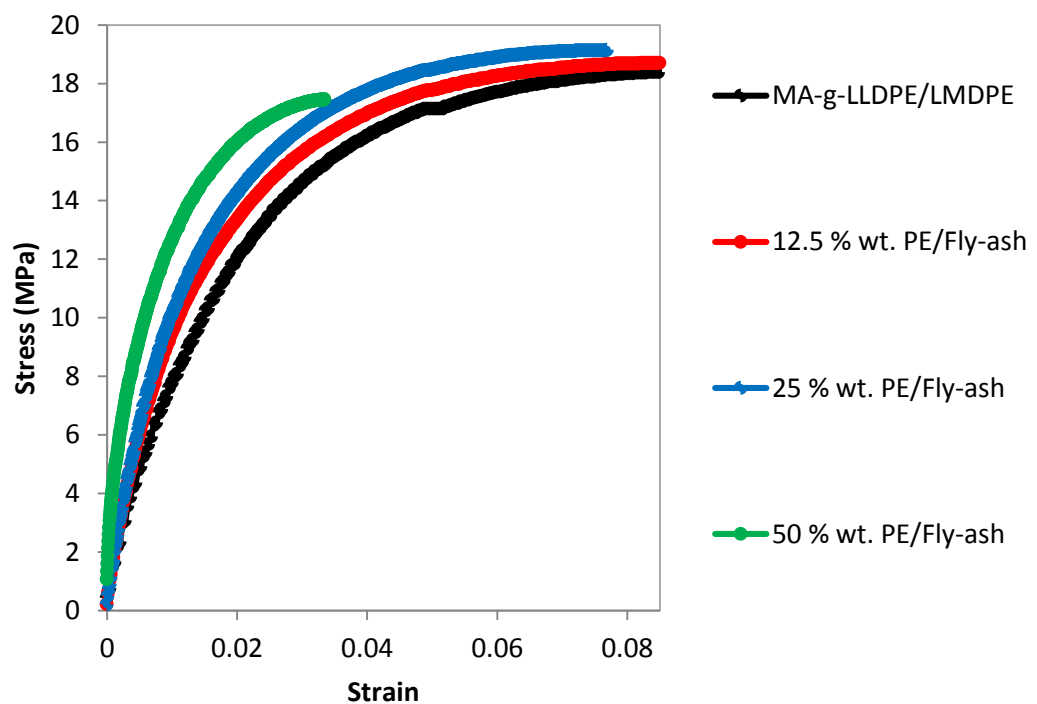


Figure 100. Tensile stress-strain to yield of rotomoulded PE/fly-ash composites for non-linear FE models.

Poisson's ratio values for the PE/fly-ash composite safety step materials detailed in Table 18 were also required for FEA; when a material is stretched, it usually deforms in a direction perpendicular to the stretching force, this is known as the Poisson's effect (Figure 101). Therefore, the Poisson's ratio is a fraction of transverse compressive strain divided by axial tensile strain. There is little available literature regarding the Poisson's ratio of PE; for the vast majority of materials such as metals, ceramics and some polymers (including PE), the Poisson's ratio is assumed to be between 0.3-0.5 [243]. However, the Poisson's ratio of an isotropic linear-elastic material can be any value between -1 and 0.5 [244]. Measuring the Poisson's ratio of PE is a challenge due to the non-linear behaviour of PE very low strains. Therefore, Poisson's ratio tests for non-linear materials typically require advanced equipment/instrumentation such as high resolution lasers and ultra-sound [245, 246, 247]. Consequently, Poisson's ratio determination of the PE/fly-ash composite safety step materials was carried out using the advanced video extensometer at the National Composites Certification and Evaluation Facility (NCCEF) within the University of Manchester. The resulting stress-strain curves were processed using MS Excel and the Poisson's ratio was calculated using Equation 20 in Experimental Section 4.6.4.

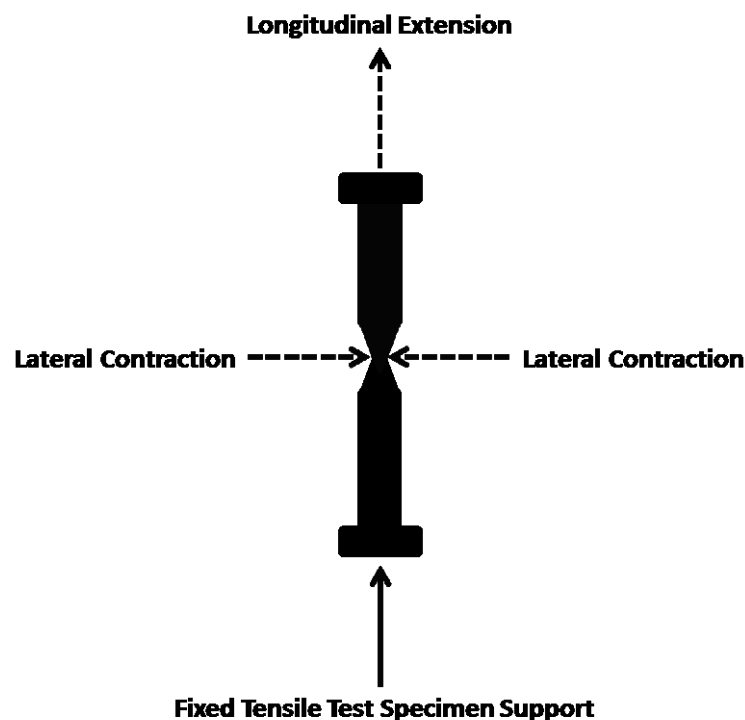


Figure 101. The lateral contraction of a material due to longitudinal extension; the latter phenomenon is known as the Poisson's effect.

Due to the non-linear behaviour of PE, it was found that calculating a consistent value of Poisson's ratio was not possible at the low to medium levels of strain. However, significantly more consistent values of Poisson's ratio were calculated at higher levels of strain (close to or at the

yield point). Therefore, the resulting values of Poisson's ratio were close to or at the yield point, rather than within the elastic region; Experimental Section 4.6.4.1 details the procedure applied to calculate Poisson's ratio. It can be seen from Figure 102 that the addition of fly-ash to MA-g-LLDPE had a relatively small effect on the Poisson's ratio.

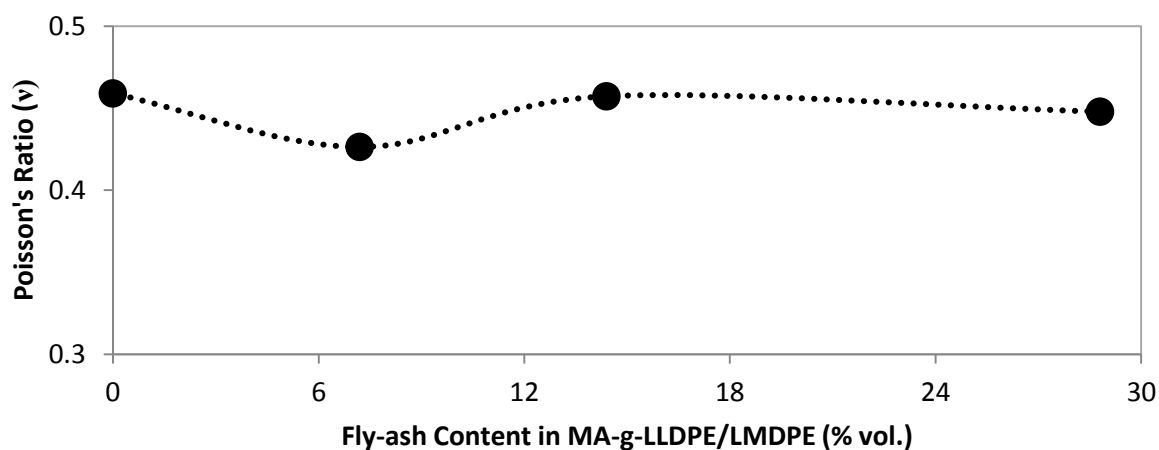


Figure 102. Poisson's ratio of MA-g-LLDPE/LMPDE with the addition of fly-ash.

Table 23. Poisson's ratio of PE/fly-ash composites for FEA of safety step sidewall deflection.

PE (wt.)	Fly-ash (% wt.)	Fly-ash (% vol.)	Poisson's Ratio	Standard Deviation
25 % MA-g-LLDPE/75 % LMDPE	0	0	0.46	0.00033
25 % MA-g-LLDPE/75 % LMDPE	12.5	7.2	0.43	0.00123
25 % MA-g-LLDPE/75 % LMDPE	25	14.4	0.46	0.00073
25 % MA-g-LLDPE/75 % LMDPE	50	28.8	0.45	0.00106

Consequently, the effect of varying the Poisson's ratio value on the outcome of FEA was explored; recently published work associated with this thesis concluded that reasonable values of Poisson's ratio between 0.3-0.5 had a minimal impact on FEA of the rotomoulded safety steps [248]. Therefore, the resulting values of Poisson's ratio at yield for the PE/fly-ash composite safety step materials (Table 23) were used for linear and non-linear FEA of the safety steps sidewall deflection.

5.12.2 Further compression testing of small particle composite safety steps

The PE/Fly-ash safety steps were further compression tested to a maximum of 5.5 kN for comparison of their sidewall deflection with FEA approximations (with the exception of the 28.8 % vol. fly-ash/PE safety step which fractured at 4.26 kN loading). Dial test indicators (DTI's) were installed on two opposing sidewalls of the safety step at predefined locations of maximum

deflection (predefined using SolidWorks Simulation 2013 FEA software, see Experimental Section 4.10). The load applied was well over the maximum required load of 2.6 kN (approximately 265 kg) defined by the British standard for the testing of safety stools, of which the original LMDPE safety step was compliant (BS EN 14183:2003). This purposefully high value of load was applied in an attempt to test the PE/fly-ash safety steps beyond their elastic region for comparison with non-linear FEA approximations.

It is clear from Figure 103 that the 25 % wt. and 50 % wt. (14.4 and 28.8 % vol.) fly-ash/PE safety steps underwent considerably less sidewall deflection relative to the unfilled and 12.5 % wt. (7.2 % vol.) fly-ash/PE safety steps. However, the 50 % wt. fly-ash/PE steps fractured at 4.26 kN; it is not surprising that this step developed a fracture on the load surface, considering the sharp drop in impact properties (brittle failure) at this fly-ash loading (Figure 92). Furthermore, the deviations in wall thickness of the PE/fly-ash safety steps decreased with the increase in fly-addition (Figure 96); the increase in melt viscosity of the PE/fly-ash composites may be promoting better wall thickness uniformity, which may also play a role in the geometric stiffness of the safety step. The resulting values of crosshead and sidewall deflection at maximum load from the PE/fly-ash safety step compression tests were tabulated for FEA investigations (Table 24).

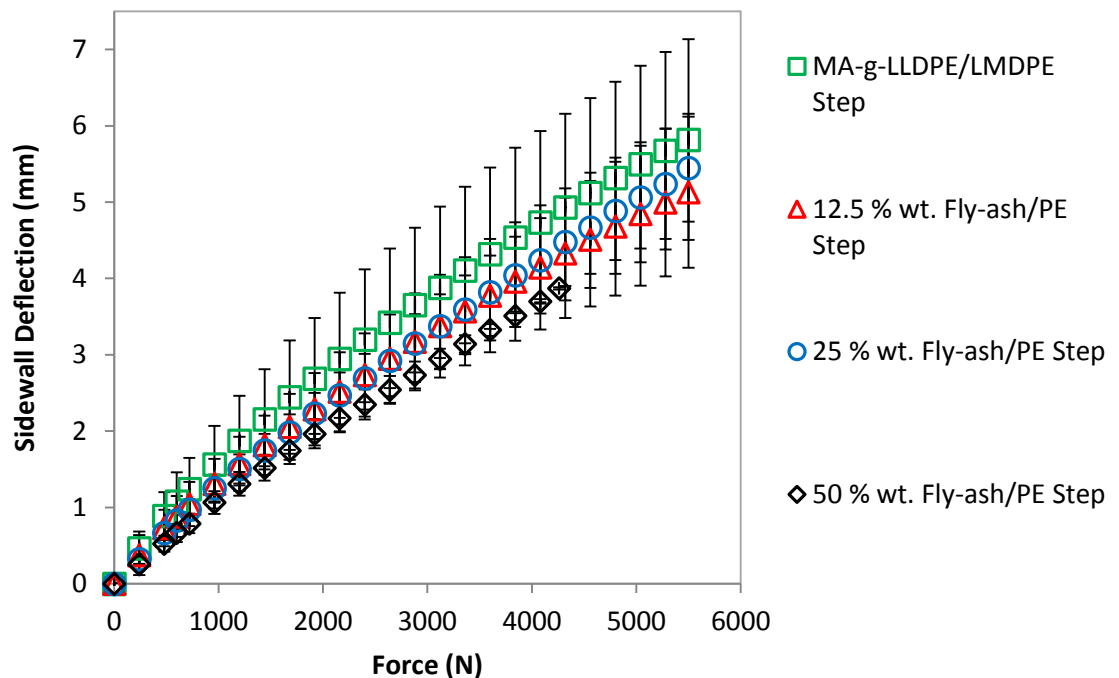


Figure 103. Force-deflection response of PE/fly-ash safety steps sidewalls.

Table 24. Maximum force, crosshead displacement and sidewall deflection of the PE/fly-ash safety steps.

PE (% wt.)	Fly-ash (% wt.)	Fly-ash (% vol.)	Total Force Applied (N)	Crosshead Displacement (mm)	Average Sidewall Deflection (mm)	Sidewall Deflection Standard Deviation
25 MA-g-LLDPE/75 LMDPE	0	0	5500	42	5.82	1.32
25 MA-g-LLDPE/75 LMDPE	12.5	7.2	5500	41	5.13	0.01
25 MA-g-LLDPE/75 LMDPE	25	14.4	5500	36	5.45	0.71
25 MA-g-LLDPE/75 LMDPE	50	28.8	4260	28	3.87	0.99

5.12.3 Comparison of small particle composite safety step sidewall deflection with FEA

Within SolidWorks Simulation 2013 FEA software, static linear-elastic and non-linear analyses were conducted to approximate the sidewall deflection of the PE/fly-ash safety steps during compression (Experimental Section 4.10). A force or crosshead displacement (corresponding to each PE/fly-ash safety step, Table 24) was applied to each linear-elastic and non-linear FE model to replicate the physical safety step compression test scenario (Experimental Section 4.6.6). The corresponding values of tensile yield stress, tensile modulus and Poisson's ratio taken directly from physical testing of the PE/fly-ash composite safety step materials were applied to all static linear-elastic FE models (Tables 22 and 23). H-adaptive (Figure 104) and P-adaptive mesh refinement (Literature Review Section 3.4.5) was also applied to all static linear-elastic FE models in order to gauge the effect of these techniques on FEA solutions. For non-linear FE models, the Poisson's ratio (Table 23) and full tensile stress-strain curves from direct physical testing of each PE/fly-ash composite material were applied (Figure 100) .

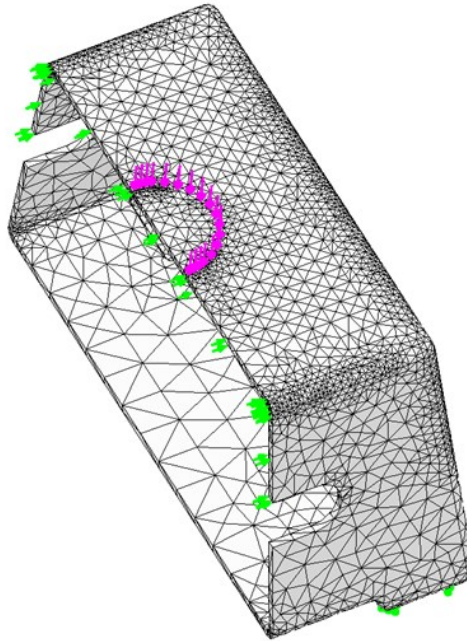


Figure 104. H-adaptive refined 3D safety step mesh. The corners and edges contain more elements than other areas of less stress concentration.

The accuracy of FEA is heavily dependent on the mesh size selected; an optimised mesh size can minimise error to a limiting value dependent upon the geometry of structure under analysis. On the other hand, a fine mesh increases the computational cost of the analysis in terms of simulation time and operating speed. H-adaptive mesh refinement subdivides the elements (therefore increasing the number of nodes) to increase the element count in areas of structural importance. However, H-adaptive mesh refinement does not affect the polynomial order of the equations that govern FEA. P-adaptive mesh refinement is simpler in mesh construction than H-adaptive as it maintains a fixed mesh but increases the polynomial order of the elements. P-adaptive mesh refinement is particularly useful for complex elements which deform due to both compression and tension, for example.

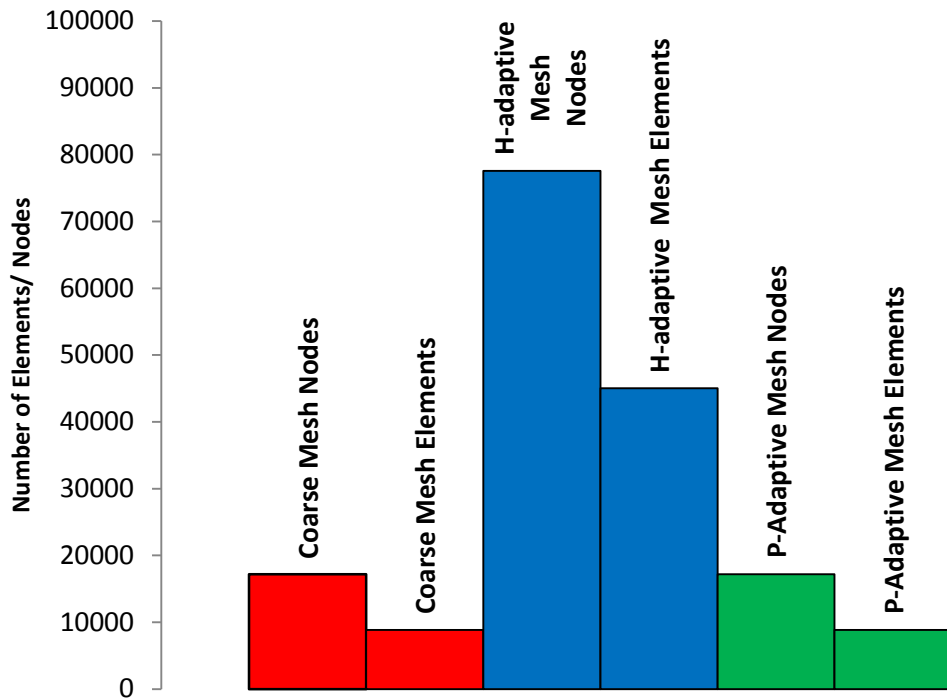


Figure 105. The resulting number of mesh elements and nodes of the 3D safety steps after applying standard coarse, H-adaptive, P-adaptive mesh refinement.

SolidWorks Simulation increases the number of elements in the corners and around the edges of the 3D safety step mesh as part of standard procedure (without the need to refine the mesh), these areas are effectively stress concentrators due to the geometry of the step; the increase in element count is to allow for better accuracy in such areas of structural importance. Figure 105 reveals the element and node count of the H-adaptive and P-adaptive refined FE meshes relative to the standard coarse mesh setting. It is clear that the H-adaptive mesh refinement technique significantly increases the number of nodes and therefore elements relative to the standard coarse mesh setting; the latter increase proves the H-adaptive mesh refinement technique is operating correctly. Furthermore, Figure 105 confirms the P-adaptive mesh refinement technique did not affect the element or node count relative to the coarse mesh setting, indicating it also operated correctly.

During non-linear FEA, the software uses iterative values of strain from a tensile stress-strain curve to calculate a nodal value of stress up to the maximum load specified, using a numerical time stepping procedure [249]. The latter procedure is complete when the solution converges to a limiting value (depending on the solution convergence option selected, Literature Review Section 3.4.4). Consequently, non-linear safety step FE models (applying a force or displacement, see Table 24) armed with tensile stress-strain data were expected to provide better accuracy at the expense of time (due to the large number of iterative calculations required). Equivalent static

linear-elastic FE models (H-adaptive and P-adaptive) of the safety step were expected to provide a quicker solution time at the expense of accuracy, due to the smaller amount of input data.

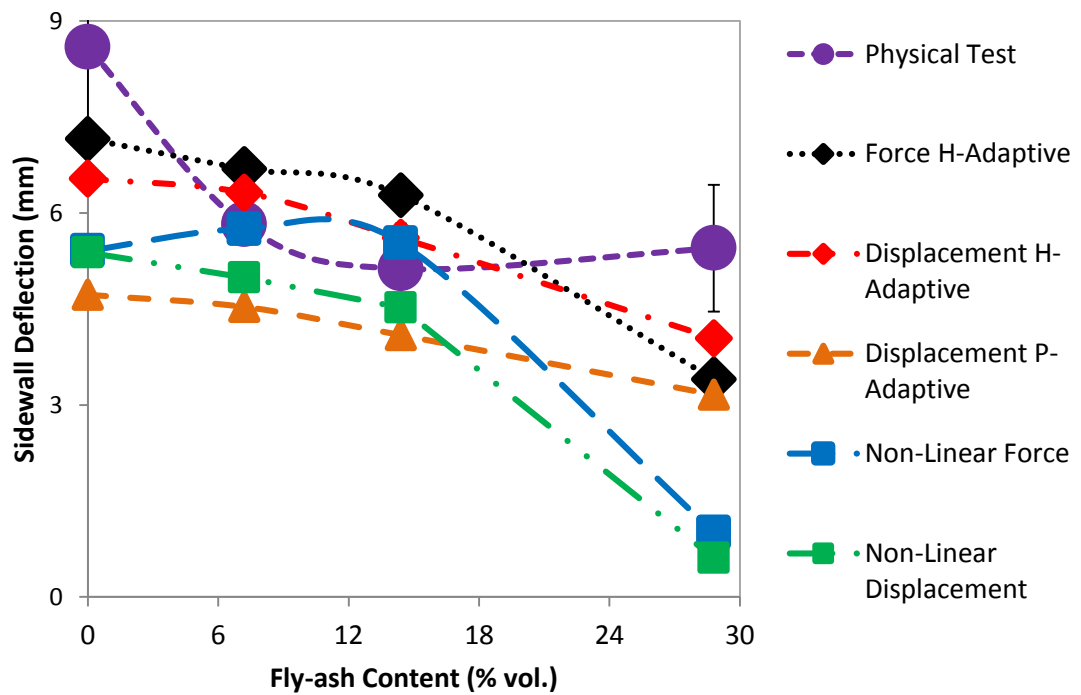


Figure 106. FEA approximations of sidewall deflection of PE/fly-ah safety steps from static linear-elastic H and P-adaptive, non-linear force and non-linear displacement models.

Figure 106 shows that FEA approximations of safety step sidewall deflection from the non-linear force, non-linear displacement, linear-elastic H-adaptive force and P-adaptive displacement FE models of the 12.5 and 25 % wt. fly-ash/PE safety steps corresponded reasonably well with physical measurements. The same is also true for the H-adaptive displacement FE models of the 12.5, 25 and 50 % wt. fly-ash/PE safety steps. The apparent correlation of sidewall deflection from the latter FE models with physical test measurements confirmed the practical value of the numerical material data obtained from direct physical testing; the static linear-elastic H and P-adaptive mesh refined FE models used the tensile and Poisson's ratio data detailed in Tables 22-23 and the non-linear FE models used the tensile stress-strain and Poisson's ratio data detailed in Figure 100 and Table 23. Furthermore, all static linear-elastic FE models had considerably shorter solution times in comparison to non-linear FE models and yet were surprisingly accurate in most cases. It is questionable whether (in this case) the non-linear models were necessary; for shorter solution times and reasonable accuracy, static-linear elastic solutions may suffice.

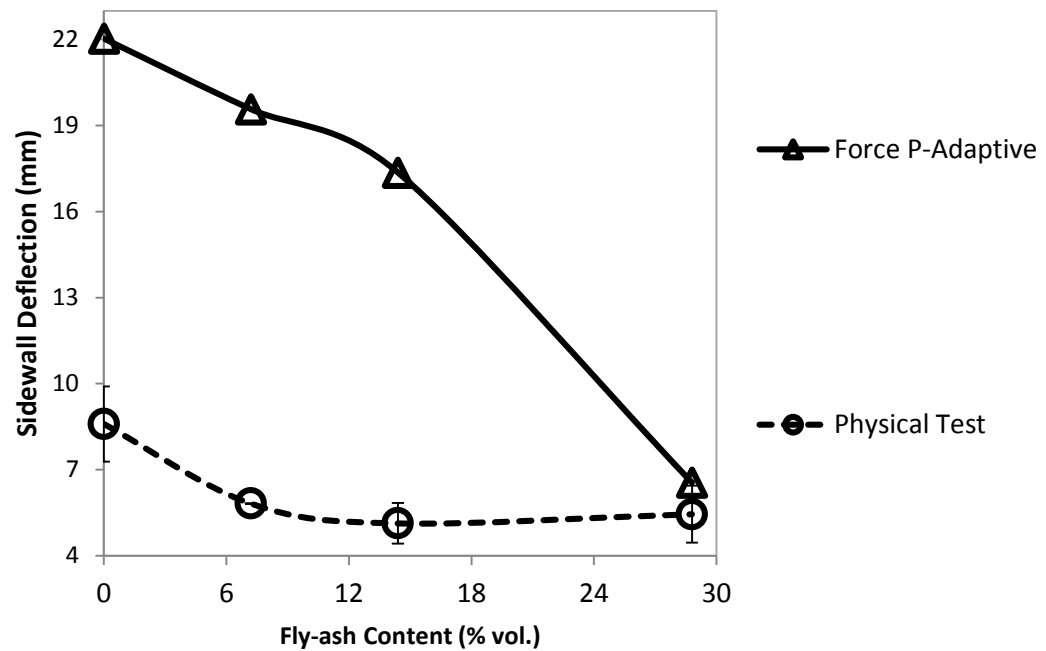


Figure 107. FEA approximation of PE/fly-ash safety step sidewall deflection vs. fly-ash content for P-adaptive force and displacement solution.

However, FEA approximations of sidewall deflection from all H-adaptive, P-adaptive and non-linear FE models of the 0 % fly-ash/PE (i.e. MA-g-LLDPE/LMDPE) and 50 % wt. fly-ash/PE safety steps (Figure 107) were significantly different to physical measurements (Figure 107). Static linear-elastic FEA over-estimated the stiffness of the 0 % fly-ash/PE safety step and the non-linear FEA under-estimated the stiffness of the 50 % wt. fly-ash/PE safety step (except the force P-adaptive FE model of the 50 % wt. fly-ash/PE safety step). The latter deviation from physical test results may be due to the accuracy of the numerical material property data; it is appreciated the mechanical response of both the unfilled and the highly filled 50 % wt. fly-ash/PE composite is non-linear, even at low strains. Therefore, a value of modulus for the latter materials is arguably an over-estimation. Furthermore, the MA-g-LLDPE/LMDPE and the 50 % wt. fly-ash/PE composite represent the unfilled and the highest filled PE material investigated; the behaviour of the latter materials are considerably different to the 12.5 and 25 % wt. fly-ash/PE composites, especially for the 50 % wt. fly-ash/PE composite which has nearly double the stiffness of the 25 % wt. fly-ash/PE composite. Modifying the tensile modulus values may help to accommodate for complex material properties within FEA; PE is viscoelastic, its mechanical response is a function of the magnitude of applied stress, the duration of applied stress and temperature. The latter generally explains why the tensile response of the PE/fly-ash composites are non-linear, even at low strains. Therefore, the generalised set of simple linear-elastic equations for FEA (such as equations 3 and 5 in Literature Review Section 3.4.3) are inappropriate to approximate the response of complex viscoelastic materials, as confirmed by Lai and Bakker ^[250]. Consequently, it was recognised that

non-linear materials such as PE require viscoelastic equations to approximate their mechanical response ^[249]; equations that approximate the non-linear behaviour of viscoelastic materials could produce a more representative value of modulus to enhance the accuracy of FEA. Furthermore, reducing the average strain energy difference between all the elements and nodes in the mesh may also help to improve the accuracy of FEA. The safety step FE models assume a constant wall thickness of 7 mm; geometrical differences between the 3D CAD models and the physical rotomoulded product (i.e. variations in wall thickness) may also have contributed to the differences between FEA approximations and the physical test result.

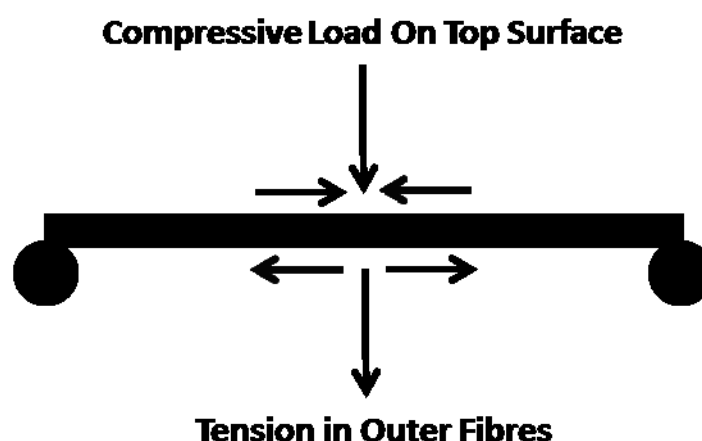


Figure 108. Tensile strain in the outer-fibres of a three point bend test piece.

Moreover, it was appreciated that only the outer-top surface of the PE/fly-ash safety steps (where the load was applied) was subjected to compressive stress whereas the inner-top surface was subjected tensile stress. Figure 108 demonstrates how this loading scenario was more complex than what was originally considered. The latter is another factor which may explain the differences between FEA and physical testing of the PE/fly-ash safety steps. Therefore, the compression response of the PE/fly-ash composite safety step materials was investigated.

5.12.4 *Formation of tensile-compression curve*

It was found that SolidWorks Simulation assumes the compressive stress-strain response of a material to be a reverse of the tensile response. The latter assumption may not be entirely true, especially for filled polymers. Therefore, it was sought to investigate the compressive properties of the 0 % and 50 % wt. fly-ash/PE composite safety step materials (Experimental Section 4.6.8). The height of the test specimens were varied; 15, 20, 25, 30, and 35 mm. Varying the height provided an opportunity to identify the optimum ratio of height to thickness for optimal results; if the ratio of height to thickness is too large, the test pieces could buckle prematurely during loading. For the purpose of the test, two specimens of each height were joined together using double-sided tape to support to each other in an upright position, this accommodated for both

pieces to be tested simultaneously and prevented premature buckling. The resulting compression curves were post-processed to include the machine compliance error (Experimental Section 4.6.8.1). It was found by experiment that the 35 mm height test pieces gave a reasonable result in this instance. Therefore, the compressive stress-strain response of the 35 mm height test piece was plotted on an x-y scatter graph with corresponding tensile data using MS Excel.

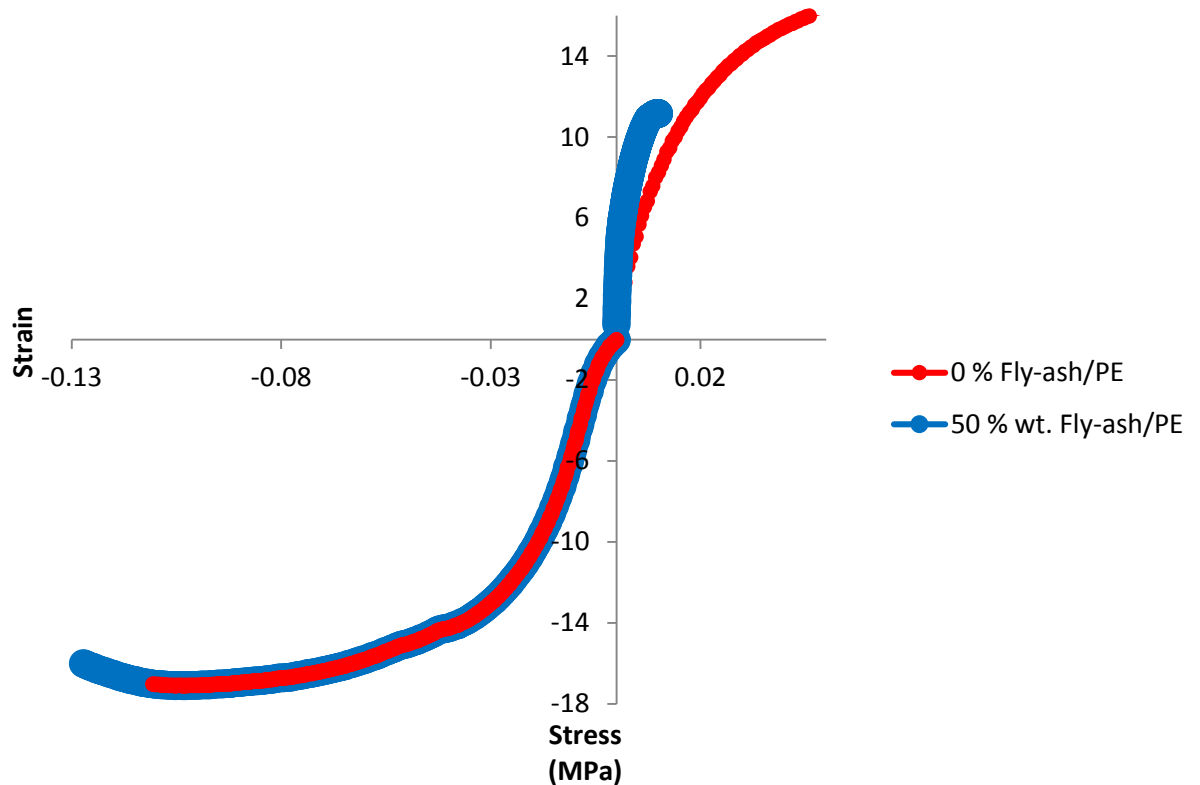


Figure 109. Tensile-compression curve of 0 % and 50 % wt. rotomoulded Fly-ash/PE.

It is evident from Figure 109 that the compression response of the 50 % wt. fly-ash/PE composites is similar to the compression response of the unfilled PE matrix. The unfilled PE matrix in compression is also somewhat similar to its tensile response. However, the 50 % wt. fly-ash/PE composite material is significantly stiffer in tension than compression. Preliminary trials were conducted using combined tensile and compressive stress-strain data for non-linear force and displacement FE models of the PE/fly-ash composite safety steps. However, it was found that accommodating for such data within the educational version of SolidWorks Simulation 2013 was more arduous than expected. Nevertheless, it was important to both understand the compressive response and provide numerical compression data of the new PE/fly-ash composite materials for future reference.

5.12.5 *Key findings from the finite element analysis of PE/fly-ash safety steps*

Investigating the FEM for the structural analysis of rotomoulded products made using a new particulate-filled PE composite is particularly novel in the field of rotomoulding. Furthermore, investigating the Poisson's ratio and compressive properties of particulate-filled polymer composites forms another novel aspect of this research. For the purpose of clarity, the key findings of this investigation are summarised in the following bullet points:

- The tensile yield stress, modulus and Poisson's ratio are required for static linear-elastic FE models. For non-linear FE models, the Poisson's ratio and full tensile stress-strain curves from direct physical testing of each PE/fly-ash composite material are required.
- Calculating a consistent value of Poisson's ratio was not possible at low to medium levels of strain. However, significantly more consistent values of Poisson's ratio were calculated at higher levels of strain (close to or at the yield point).
- The addition of fly-ash to MA-g-LLDPE had a relatively small effect on the Poisson's ratio.
- The 25 % wt. and 50 % wt. (14.4 and 28.8 % vol.) fly-ash/PE safety steps underwent considerably less sidewall deflection relative to the unfilled and 12.5 % wt. (7.2 % vol.) fly-ash/PE safety steps. However, the 50 % wt. fly-ash/PE steps fractured at 4.26 kN load.
- The H-adaptive mesh refinement technique significantly increased the number of nodes and therefore elements relative to the standard coarse mesh setting; the latter increase proves the H-adaptive mesh refinement technique is operating correctly.
- The P-adaptive mesh refinement technique did not affect the element or node count relative to the coarse mesh setting, indicating it also operated correctly.
- FEA approximations of safety step sidewall deflection from the non-linear force, non-linear displacement, linear-elastic H-adaptive force and P-adaptive displacement FE models of the 12.5 and 25 % wt. fly-ash/PE safety steps corresponded reasonably well with physical measurements. The same is also true for the H-adaptive displacement FE models of the 12.5, 25 and 50 % wt. fly-ash/PE safety steps.
- All static linear-elastic FE models had considerably shorter solution times in comparison to non-linear FE models and yet were surprisingly accurate in most cases. It is questionable

whether (in this case) the non-linear models were necessary; for shorter solution times and reasonable accuracy, static-linear elastic solutions may suffice.

- Static linear-elastic FEA over-estimated the stiffness of the 0 % fly-ash/PE safety step and the non-linear FEA under-estimated the stiffness of the 50 % wt. fly-ash/PE safety step (except the force P-adaptive FE model of the 50 % wt. fly-ash/PE safety step).
- The compression response of the 50 % wt. fly-ash/PE composites is similar to the compression response of the unfilled PE matrix. Moreover, the unfilled PE matrix in compression is also somewhat similar to its tensile response. However, the 50 % wt. fly-ash/PE composite material is significantly stiffer in tension than compression.

5.12.6 ***Key considerations for the finite element analysis of rotomoulded parts***

The combined effect of various complex factors on FEA such as FE model assumptions, the non-linear behaviour of PE and the variation in wall thickness of rotomoulded parts exemplified the importance of properly understanding FEA software; basic to intermediate users can create 3D structures, apply forces, constraints and material data with relatively little effort. Therefore, the following considerations should be made when using FEA software:

- Understand the boundary conditions (loads, constraints and material data). Ensure a simplified, representative loading scenario of the FE model for quicker solutions.
- Ensure the dimensions of the structure under analysis are accurately defined.
- Validate the FEA softwares calculations by hand (e.g. simple beam bending theory)
- Use FEA to identify areas of the structure beyond the yield stress of the material or maximum deflection required.
- Determine experimental error.

6. Conclusions

The investigations detailed in this thesis have resulted in several interesting conclusions regarding both the development of PE/filler composite materials for RM and the consequent application of FEA in order to numerically approximate the mechanical response of rotomoulded parts using such materials. These are summarised in the following paragraphs:

6.1 Mechanical Properties

In terms of the mechanical properties and processability of the proposed PE/filler composites, the original aims this study (Section 1.1) were to:

- Evaluate a selection of particulate fillers as reinforcement to RM grade PE in order to double its tensile modulus.
- Optimise the chosen composite system for performance and processability.

The aim of doubling the modulus of rotomoulding grade PE using a particulate filler was achieved at 28.8 % vol. fly-ash for composites based on a blend of 25 % wt. MA-g-LLDPE with 75 % wt. LMDPE (Figure 90, Results and Discussion Section 5.9.2); these observations verify the claimed coupling activity of the MA-g-LLDPE with the finer fly-ash particles. Furthermore, at 28.8 % vol. fly-ash loading, the tensile stress at yield (Figure 91) remains effectively the same as the unfilled matrix (when taking the data variation into account). However, the impact strength of the rotomoulded PE/fly-ash composites (Figure 92) decreased with every filler loading investigated; this was especially true for the 28.8 % vol. PE/fly-ash composites where the impact strength fell by approximately 88 %. The latter is unacceptable for rotomoulded applications such as underground water tanks or kayaks where the toughness and ductility of unfilled PE is essential. Therefore, future investigations to enhance the toughness of the PE/fly-ash composites are detailed in Section 7. Physical observations also confirmed that the PE/fly-ash composites were increasingly more brittle with the increase in fly-ash loading, relative to the ductile unfilled matrix.

Moreover, the MFR of the PE/fly-ash composites decreased with the addition of fly-ash. In terms of modulus enhancement (Figure 90) the optimum fly-ash loading of 28.8 % vol. corresponds to a 42 % loss in MFR relative to the unfilled matrix (Figure 88). Such a loss in MFR placed a question mark over the feasibility of the PE/fly-ash composites for rotomoulding applications. However, experimental data suggests an optimal balance between the tensile modulus (Figure 90), yield

stress (Figure 91) and MFR (Figure 88) of rotomoulded PE may be possible at fly-ash loadings between 14-28 % vol.; this should not be problematic to rotomould in powder form.

6.2 Filler-Matrix Blending Technique

Dry blending of coarse particle fillers (i.e. sand, garnet and cenospheres) with powdered LMDPE/MA-g-LLDPE blends followed by compression moulding generally gave composites with poor mechanical properties relative to equivalent composites where the filler particles were melt blended in to the same matrix using a two roll mill. Twin screw extrusion melt blending of composites based on the finer fillers (i.e. fly-ash) was also successful and produced compression mouldings with excellent mechanical properties. However, the improvements in tensile modulus and yield stress were accompanied by reduced impact toughness at high fly-ash loadings (50 % wt.) where the stiffness enhancement was more prominent. Furthermore, the addition of fly-ash impacts the melt flow behaviour of PE in a largely negative way.

6.3 Polyethylene, Filler and Coupling Agent

Compression moulded, melt blended MA-g-LLDPE/LMDPE blends with the addition of finer filler (i.e. fly-ash) had excellent mechanical properties. Remarkably, the TSE melt blended compression moulded highly-filled fly-ash/LMDPE (70 % wt.) composites displayed improvements in strength which showed signs of stabilising at 20-25 % MA-g-LLDPE. For equivalent HDPE composites, maximum stress was observed at 10 % wt. MA-g-LLDPE; the latter is probably due to poor compatibility between HDPE and MA-g-LLDPE due to the relatively high level of branching in MA-g-LLDPE. HDPE was initially selected for reinforcement with fly-ash particles due to its higher stiffness than LMDPE. However, better compatibility was observed between MA-g-LLDPE/LMDPE with the addition of fly-ash; these observations verify the claimed coupling activity of the MA-g-LLDPE with the finer fly-ash particles. Consequently, in the context of melt flow properties and cost, it was decided that the MA-g-LLDPE/LMDPE-fly-ash blends were more suitable for rotomoulding relative to the added expense and reduced melt flow properties of equivalent MA-g-LLDPE/HDPE composites. Therefore, MA-g-LLDPE/LMDPE-fly-ash blends were selected for rotational moulding. High temperature flexural tests revealed the addition of fly-ash to MA-g-LLDPE/LMDPE system improved the heat distortion behaviour of the resulting injection moulded composites relative to the unfilled matrix.

6.4 Fillers - Effect of Bimodal Particle Size Distribution

Maximum packing fraction determinations (using a modified oil absorption type test) confirmed that combinations of fly-ash and cenospheres could boost filler volume fraction in the composites. However, the mechanical response of these mixed filler composites was poor (in most cases poorer than with fly-ash alone). Bearing in mind the fact that the cenospheres form only a small fraction (ca. 2 %) of fuel ash from power stations and their relatively high cost, it was concluded that a filler system based on fly-ash/cenosphere combinations is not a viable option. During these preliminary melt blending trials, the small particle size fillers (i.e. fly-ash) performed best due to the fact that they do not act as large defects in the matrix and they provide sufficient interfacial area for the effective deployment of the MA-g-LLDPE coupling agent.

6.5 Small Particle Composites – Properties in the Context of Rotational Moulding

The objective of doubling the tensile modulus of MA-g-LLDPE/LMDPE based blends was achieved at fly ash volume fractions between 20-30 % for compression moulded samples; the latter fly-ash loading was not considered over problematic in the context of rotational moulding. It was found that rotomoulded safety steps made using the TSE melt blended maleanised PE/fly-ash composite materials offered stiffness comparable to that of higher density rotomoulding PE grades at the highest fly-ash loading investigated (28.8 % vol.). However, pinholes on the surface of rotomoulded PE increased with the addition of fly-ash; the addition fly-ash significantly decreases the MFR of the composite melt which complicates processability. The latter confirmed the challenge in using such highly filled PE composites for the zero-shear rotomoulding process. However, the variation in wall thickness of rotomoulded PE safety steps decreased with the addition of fly-ash; the loss in the MFR of the composite melt with the addition of fly-ash reduced the amount of bulk flow of the melt during rotomoulding, thus preventing material from gathering in the corners of the mould resulting in greater wall thickness uniformity.

The latter rotomoulded PE/fly-ash composite safety steps were compression tested and measured for sidewall deflection. Computer simulation of the rotomoulded PE/fly-ash safety steps sidewall deflection was conducted using FEA software. Poisson's ratio values for the PE/fly-ash composite safety step materials were required for FEA. Currently, there is little available literature regarding the Poisson's ratio of PE; for the vast majority of materials such as metals, ceramics and some polymers (including PE), the Poisson's ratio is assumed to be between 0.3-0.5 [243]. Measuring the Poisson's ratio of PE is a challenge due to the non-linear behaviour of PE very low strains; it was found that calculating a consistent value of Poisson's ratio was not possible at

the low to medium levels of strain. However, significantly more consistent values of Poisson's ratio were calculated at higher levels of strain (close to and at the yield point). Therefore, the resulting values of Poisson's ratio were close to or at the yield point, rather than within the elastic region (Experimental Section 4.6.4.1). However, it was observed the addition of fly-ash to MA-g-LLDPE had a relatively small effect on the Poisson's ratio. Recent published work associated with this thesis concluded that reasonable values of Poisson's ratio between 0.3-0.5 had a minimal impact on FEA of the rotomoulded safety steps ^[248].

6.6 Finite Element Analysis of Rotomoulded Small Particle Composites

The numerical material parameters required for FEA of the new high stiffness PE/fly-ash composite material was the tensile modulus, stress at yield, Poisson's ratio and full tensile stress-strain curves (for non-linear analyses). Measured values of sidewall deflection for the rotomoulded PE/fly-ash safety steps coincided reasonably well with FEA approximations from the static linear-elastic and non-linear FE models (depending on the mesh refinement type and material data applied to the FE model), confirming the practical value of the numerical material data. However, in some instances significant differences between FEA and the actual safety step were probably due to the effect of various complex factors such as the non-linear behaviour of PE and the variation in wall thickness of rotomoulded parts. These differences between the assumptions of the FE model and the physical rotomoulded part contribute to the accuracy of FEA, exemplifying the importance of verifying how FEA software calculates a solution. The following considerations should be taken into account when using FEA software for rotomoulded products:

- Understand the analysis type.
- Understand the boundary conditions (loads, constraints and material data). Ensure a simplified, representative loading scenario of the FE model for quicker solutions.
- Ensure the dimensions of the structure under analysis are accurately defined.
- Validate the FEA software's calculations by hand (e.g. simple beam bending theory)
- Use FEA to identify areas beyond the yield stress of the material or maximum deflection.
- Determine experimental error.

6.7 Overall Recommendations

A substantial variety of sample preparation and experimental methods were implemented to enhance the modulus of PE. Consequently, an optimum formulation for further investigation is suggested in the following paragraphs.

1. The fly-ash particles can double the tensile modulus of PE at levels that are acceptable to rotomould (ca. 30 % wt., even without the MA coupling agent). Furthermore, the small size and spherical shape of the fly-ash particles give sufficient interfacial area for the effective deployment of the MA-g-LLDPE coupling agent. Therefore, it is recommended to use the fly-ash particles for further investigation.
2. The MA coupling agent grafted LLDPE blended with LMDPE is a versatile matrix in terms of compatibility with the fly-ash particles; it is apparent that increasing the level MA-g-LLDPE in LMDPE increases the modulus at lower levels. Furthermore, the tensile yield stress of LMDPE/fly-ash composites increases with every level of MA-g-LLDPE (up to 25 % wt.). Due to the strong interaction of the MA-g-LLDPE/LMDPE blends with the fly-ash particles and the arguably more suitable MFR of the latter PE blends for rotomoulding (relative to alternative PE grades such as HDPE), it is recommended to remain with this particular blend of PE for further investigation.
3. The PE and fly-ash should be blended by TSE compounding prior to moulding, rather than dry blending or two roll mill blending. The TSE compounded composites had the best mechanical properties relative to two roll milled or dry blended equivalents; this is because the matrix and filler particles are blended under electro-mechanically controlled shear force and temperature, ensuring better dispersion of the filler particles in the matrix, homogeneity and reproducibility. Furthermore, TSE compounding improves the effectiveness of the MA-g-LLDPE coupling agent.
4. Tensile, flexural, Charpy impact and MFR tests are effective methods of gauging the modulus, strength, impact toughness and melt flow properties of the PE/fly-ash composites. However, it is suggested that zero-shear viscometry be conducted to gauge the MFR of the PE/fly-ash composites under the zero-shear conditions encountered in rotomoulding. Furthermore, one intended application of the PE/fly-ash composites is underground water tanks. Therefore, creep tests on actual rotomoulded tanks are essential at some point of the development phase.

5. The tensile modulus, stress at yield, Poisson's ratio and full tensile stress strain curves are required for FEA, (the latter is required for non-linear analyses). However, it should be appreciated that the moduli of non-linear materials are an over-estimation when calculated using a conventional method. Therefore, it is recommended that the moduli of the PE/fly-ash composites are re-calculated to a more representative value for the purpose of FEA; linear viscoelastic equations may be explored to accommodate for this. Moreover, it is crucial to understand the principles of FEA properly in order to represent the loading scenario accurately (e.g. the type of analysis selected and other application-specific factors such as the variation in wall thickness of rotomoulded products).

With further development, especially in terms of MFR and impact toughness, it is envisaged that the PE/fly-ash composite can provide the required modulus enhancement to PE whilst maintaining suitable impact and melt flow properties for rotomoulding. Upon achieving the latter objective, a numerical database of material properties can be compiled for comparative stress analysis studies (using FEA) of virgin PE tanks versus the new high stiffness PE/fly-ash composite tanks. Theoretically, the high modulus PE/fly-ash composite material can lower the wall thickness of load-bearing rotomoulded components whilst maintaining an acceptable factor of safety. If the latter is achieved, real tanks could be rotomoulded and physically tested for comparison with FEA to validate the material data and prove the effectiveness of the PE/fly-ash composite at lowering the wall thickness, due to its relatively high modulus.

7. Further Work

The PE/filler composites detailed in this thesis led to a number of different development formulations. However, it is apparent that fly-ash particles provide the best mechanical improvements to PE; the most viable composite system investigated thus far is that based on LMDPE and fly ash with an MA-g-LLDPE coupling agent. With the latter system, the objective of doubling the tensile modulus can be achieved at high fly ash volume fractions for rotomoulding applications (28 % vol.). Therefore, future investigations would still remain with optimising the PE/fly-ash blends for rotomoulding. However, the latter 28 % vol. fly-ash/PE composite had low MFR and impact properties, consequently leading to poor part surface quality. Investigations have suggested an optimal balance between the tensile modulus, strength and processability of rotomoulded PE may be possible at fly-ash loadings between 14-28 % vol.; this should not be problematic to rotomould in powder form. The following points summarise the future work suggested as a result of this study:

- **Development of thermo-oxidative stabilisation strategies for the PE/fly-ash composites with a view to maximising processability** - examining novel and sustained release stabilisation strategies for the MA-g-LLDPE/LMDPE blend with the addition of fly-ash is necessary for optimising the composite materials suitability for RM. Large rotomoulded parts such as underground water tanks or liquid storage silos take considerably long to manufacture (typically 8 hours duration at above 200 °C for a 10,000 litre PE tank). Therefore, it is crucial to investigate (and improve) the stability of the PE/fly-ash composite in such harsh processing conditions.
- **Assess the zero shear melt flow rate of PE fly-ash composites** - zero-shear viscometry is a more precise method of analysing the melt flow properties of the PE/fly-ash composites under conditions closer to those encountered in RM. The MFR of the rotomoulded MA-g-LLDPE/LMDPE blend is significantly reduced at the optimum fly-ash loading of 28.8 % in terms of modulus enhancement. Cryogenic grinding of the TSE compounded PE/fly-ash composite pellets to powder form and the addition of small amounts of powdered PE during rotomoulding may improve processability.
- **Improve the impact strength of the PE/fly-ash composites** - the addition of fly-ash particles to PE has a detrimental effect on the impact properties of the resulting composites. The latter can potentially be improved by incorporating an elastomeric

component in the composite to instil toughness. Furthermore, wetting agents such as Silanes can also be used to improve toughness via a reduction in the surface energy of the filler particles to better distribute them within the matrix. However, it is understood that increasing the toughness of the composite in this way will probably have a negative effect on the modulus and strength of the composite. Moreover, a multi-layer composite structure (sandwich laminate) could provide a good balance between the impact properties and tensile modulus of the PE/fly-ash composites. The industrial sponsor has extensive experience in utilising commercially established techniques for multi-layer laminate materials.

- **Development of creep data for the purpose of FEA** - numerical creep data from the PE/fly-ash composites will be required to create FE models of real RM products such as underground water tanks for creep analysis. A key mechanical parameter for design engineers is creep data; development of the latter can provide tailor made materials modelling tools for design engineers expected to model the new materials. Creep tests in three point bend mode are often at elevated temperature (typically 50 °C) for typically 1000 hours duration. Therefore, careful advance planning is required. The industrial sponsor constructed an in-house creep testing facility used to examine the creep behaviour of the new PE/fly-ash composite materials. Initial tests have indicated the material lifetime of the highly filled PE/fly-ash composite is considerably longer than unfilled LMDPE i.e. for a given lifetime the stress withstood by the latter composite is significantly greater than that of unfilled LMDPE.
- **FEA of industrial-scale rotomoulded PE/fly-ash load-bearing parts** - thus far, FEA has been applied to a relatively small (commercial-scale) rotomoulded safety step using numerical materials data from physical testing of the PE/fly-ash composite materials. The rotomoulded safety step had a relatively simple loading scenario and was practical for small-scale testing at MMU. However, it is appreciated that the effect of non-linear material behaviour and the variations in wall thickness of much larger rotomoulded parts (such as oil storage silos) presents a considerably more complex challenge for FEA, possibly requiring more advanced physical testing and FE modelling methods; it is envisaged that non-linear viscoelastic equations will be used to provide a more representative value of modulus (with respect to time, stress and temperature) for FEA.

8. References

1. Crawford, R.J. *Rotational Moulding of Plastics 2nd edition*, John Wiley and Sons Inc., May 1996.
2. Krohn, J.V. Hughes, B.J. Mcfaddin, D.C. Todd, W.G. *Higher Performance Polyethylene Powder*, Equistar Chemicals Ltd, Society of Plastics Engineers ANTEC Conference Proceedings, page 1, May 2005.
3. Sowa, M.W. *Rotational moulding of reinforced PE*, SPE Journal, 26, pp 31-34. July 1970.
4. European Plastics News Magazine. *Rotational process for GRP developed in Japan*, page 42. January 1975.
5. Mohr, J.G. *Rotational Moulding of Fibre Glass Reinforced Thermoplastics*, SPI Handbook of Technology and Engineering of Reinforced Plastics/Composites 2nd Edition, Chapter 6, 1981.
6. Plastics world Magazine. *Rotomoulded RP – Exciting route to new markets*, June 1970.
7. Ogasawara, Y. Tsuji, S. Yamamoto, R. *A New Continuous Rotational Moulding Process for RP Composition – CRM Process*, Polym. Plast. Technol. Eng, 24 (1), pp. 1-10. 1985.
8. Miller, D.L. *Fibre Glass Reinforced Plastic in Furniture*, Society of Plastics Engineers ANTEC (Annual Technical) Conference Proceedings, Section 16-C, pp. 1-4. 1975.
9. Kobe Steel Ltd. *Method of Rotational Moulding Reinforcer-Incorporated Plastics*, Japan, United States Patent No. 3,981,955, September 1976.
10. Rotoplas Ltd. *Method for the production of Reinforced Rotationally Moulded Thermoplastic Articles*, Jerusalem British Patent No. 1,381,863, January 1973.
11. Rotoplas Ltd. *Method for Producing a Layer of Fibre – Reinforced Rotationally Moulded Plastic Material*, Jerusalem, European Patent No. 0,022,165, January 1981.

12. Wisley, B.W. PhD Thesis, *Improving the Mechanical Properties of Rotomoulded Products*, Queens University Belfast, September 1994.
13. Murphy, M. MSc Thesis, *An Investigation into the effect of Incorporating Glass and Ceramic Microspheres in Rotationally Moulded Articles*, Queens University Belfast, September 1997.
14. Arnaud, R. Crawford R.J. *The effects of fillers on the properties of rotationally moulded Polyethylene*, Polymer Processing Research Centre, Queens University Belfast, Society of Plastics Engineers ANTEC Conference Proceedings, June 2002.
15. Hanna, P.R.W. McNally, T. Harkin-Jones, E. McMillan, P. *Mechanical Properties of Rotationally Moulded Nano-Composites*, Queens University Belfast, Society of Plastics Engineers ANTEC Conference Proceedings, May 2004.
16. Kanokboriboon, A. Sae-Chieng, W. *An Investigation on the Effects of Fine-Particulate Filler on the Properties of a Rotomoulding-Grade Polyethylene*, King Mongkut Institute of Technology North Bangkok and SCG Chemicals Co. Ltd. Thailand, Society of Plastics Engineers ANTEC Conference Proceedings, January 2007.
17. Chang, W. C. Harkin-Jones, E. Kearns, M. McCourt, M. *Glass Fibre-Reinforced PE Composites in Rotational Moulding*, Polymer Processing Research Centre, Queen's University Belfast, Society of Plastics Engineers ANTEC Conference Proceedings, May 2011.
18. Ward, J. Panigrahi, S. Tabil, L.G. Crerar, W.J. Powell, T. *Rotational Molding of Flax Fiber Reinforced Thermoplastic*, Department of Agricultural and Bioresource Engineering, University of Saskatchewan Canada. September 2002.
19. Butora, P. Náplava, A. Ridzon, M. Bílik, J. Tittel, V. *Particle Filled Polyethylene Composites Used in the Technology of Rotational Moulding*, Institute of Materials Science, Faculty of Materials Science and Technology, Slovak University of Technology, Slovakia. March 2012.
20. Lopez-Banuelos, R.H. Moscoso, F.J. Ortega-Gudino, P. Mendizabal, E. Rodrigue D. Gonzalez-Nunez R. *Rotational Molding of Polyethylene Composites Based on Agave*

Fibers, Department of Chemical Engineering University of Guadalajara, Mexico. December 2012.

21. Yan, W. Lin, R.J.T. Bhattacharyya, D. *Particulate reinforced rotationally moulded polyethylene composites – Mixing methods and mechanical properties*, Centre for Advanced Composite Materials, Department of Mechanical Engineering, The University of Auckland, New Zealand. December 2005
22. Mhike, W. MSc Dissertation, *Surface Resistivity, Mechanical and Thermal Properties of Rotationally Moulded Polyethylene/Graphite Composites*, Faculty of Engineering, Built Environment and Information Technology, University of Pretoria, South Africa. March 2012.
23. Milton, C. *Predicting Strength of Rotomoulded Parts*, Tennant Company, Minneapolis, USA. January 2006.
24. Crawford, R.J. Throne J.L. *Plastics Design Library. Rotational moulding technology*, William Andrew Publishing, page 295. December 2001.
25. D&M Plastics Inc. *A History of Rotational Moulding*. (no date). Available online: <http://www.rotationalmoulding.ca/history.htm>. Accessed: 11/10/12.
26. Ward, N.M. *History of Rotational Moulding*, *Plastiquarian*, Issue 19, page 3. December 1997
27. Kutz, M. *Plastics Design Library. Processing and Materials: Rotational Molding*, *Applied Plastics Engineering Handbook 1st Edition*, William Andrew Publishing, pp. 311–332. July 2011. Available online: <http://www.sciencedirect.com/science/article/pii/B9781437735147100182>. Accessed: 04/08/14.
28. Dragoi, M.V. *Advances in CAD/CAM Technologies, New Trends in Technologies*, *Devices, Computer, Communication and Industrial Systems*, Transylvania University of Braov, Romania, November 2010. Available online: <http://www.intechopen.com/books/new-trends-in-technologies--devices--computer--communication-and-industrial-systems/advances-in-cad-cam-technologies>. Accessed: 04/08/2014.

29. Drobny, J.G. *Plastics Design Library. Processing Methods Applicable to Thermoplastic Elastomers*, Handbook of Thermoplastic Elastomers, William Andrew Publishing. pp. 29-160 December 2008.
30. Webster, E.A. Weaver N. *Mechanical Properties of Rotationally Moulded Laminates of LLDPE and foamed LLDPE*, Pennsylvania College of Technology, Society of Plastics Engineers ANTEC (Annual Technical) Conference Proceedings, 2003.
31. Sekiguchi, H. et al. *Novel Foam Composite Having Thick Skin and Core Stiffening Dividers*, Furukawa Electric Company and Tokyo Medical and Dental University, Japan, Society of Plastics Engineers ANTEC (Annual Technical) Conference Proceedings, 2003.
32. Greco, A. Maffezzoli, A. Forleo, S. *Thermochimica Acta Volume 582, Sintering of PLLA powders for rotational molding*, Elsevier, pp. 59-67. March 2014.
33. Malpass, D. B. *Introduction to Industrial Polyethylene: Properties, Catalysts, and Processes*, John Wiley and Sons Inc., December 2010.
34. Hoffmann, F. Augustyn, F.J. Manning, M.J. *Dictionary of Toys and Games in American Popular Culture*, Routledge, page 11. October 2013.
35. Thompson, K. *Fruit and Vegetables: Harvesting, Handling and Storage*, John Wiley and Sons Inc., October 2014.
36. Rothon, R.N. *Particulate-Filled Polymer Composites 2nd edition*, Rapra Technology Ltd, p. 62. 2003.
37. Piringner, O.G. Baner, A.L. *Plastic packaging: interactions with food and pharmaceuticals 2nd Edition*, John Wiley and Sons Inc., June 2008.
38. Peacock, A. *Handbook of Polyethylene: Structures: Properties, and Applications*, CRC Press, page 1. January 2000.
39. Vasile, C. Pascu, M. *Practical Guide to Polyethylene*, iSmithers Rapra Publishing, page 1. January 2005.

40. Armstrong J. *General, Organic, and Biochemistry: An Applied Approach*, Cengage Learning, page 304. January 2014.
41. Taylor, P. Gagan, M. *Alkenes and Aromatics Volume 1*, Royal Society of Chemistry, page 11. January 2002.
42. Clements, A. Dunn, M. Firth, V. Hubbard, L. Lazonby, J. Waddington, D. *Ethene (Ethylene)*, Essential Chemicals Industry online, University of York, UK. January 2014. Available online: <http://www.essentialchemicalindustry.org/chemicals/ethene.html>. Accessed: 28/10/2014
43. Intratec Solutions Ltd. *Technology Economics: Ethylene Production via Ethanol Dehydration*, page 10. July 2013.
44. Osakada, K. *Organometallic Reactions and Polymerization*, Springer, page 1. 2014
45. Young, R. J. *Introduction to Polymers*, Chapman and Hall, 1987.
46. IUPAC Compendium of Chemical Terminology, *Chain Polymerization*, International Union of Pure and Applied Chemistry Gold Book, page 239. February 2014.
47. Clayden, J. Greeves, N. Warren, S. *Organic chemistry*, Oxford University Press, pp. 1450-1466. 2000.
48. Williams, J. *Ethylene: Properties and Uses*, Education Portal, (no date). Available online: <http://education-portal.com/academy/lesson/ethylene-properties-uses-quiz.html#lesson>. Accessed: 13/10/14.
49. Mathers, R.T. Meier, M.A.R. Green. *Polymerization Methods: Renewable Starting Materials, Catalysis and Waste Reduction*, John Wiley and Sons Inc., March 2011.
50. Vining, W. Day, R. Botch, B. *General Chemistry*, Cengage Learning, page 276. July 2014.
51. Rudin, A. Choi, P. *The Elements of Polymer Science and Engineering*, Academic Press, page 77. December 2012.

52. Ram, A. *Fundamentals of Polymer Engineering*, Springer Science and Business Media, page 36. December 1997.
53. Price, C.C. Vandenberg, E.J. *Coordination polymerization*, American Chemical Society, Plenum Press, 1983.
54. Ryan, L. Norris, R. *Cambridge International AS and A Level Chemistry Coursebook*, Cambridge University Press, page 21. July 2014.
55. Matyjaszewski, R. Davis, T.P. *Handbook of Radical Polymerization*, John Wiley and Sons Inc., page 1. April 2003.
56. Bagdasarian, K.S. *Theory of free-radical polymerization*, Israel Program for Scientific Translations, page 80. 1968.
57. Odian, G. *Principles of Polymerization* 4th edition, Wiley, 2004.
58. Wunderlich, B. *Thermal Analysis of Polymeric Materials*, Springer Science and Business Media, page 211. April 2005.
59. Salamone, J.C. *Polymeric Materials Encyclopaedia*, CRC Press, page 6807. July 1996.
60. Speight, J.G. *Handbook of Industrial Hydrocarbon Processes*, Gulf Professional Publishing, page 504. December 2010.
61. Alger, M.S.M. *Polymer Science Dictionary*, Springer Science and Business Media, page 26. 1997.
62. Feldman, D. *Synthetic Polymers: Technology, Properties, Applications*, Springer Science and Business Media, page 5. May 1996.
63. Hui, Y.H. *Handbook of Food Science, Technology, and Engineering Volume 2*, CRC Press, page 5. 2006.
64. Carraher, C.E. *Giant Molecules: Essential Materials for Everyday Living and Problem Solving*, John Wiley and Sons Inc., page 143. August 2003.

65. Boor, J. *Ziegler-Natta Catalysts Polymerizations*, Elsevier, page 1. December 2012.
66. Abdel-Bary, E. *Handbook of Plastic Films*, iSmithers Rapra Publishing, page 5. January 2003.
67. Ebewele, R.O. *Polymer science and technology*, CRC Press, March 2000.
68. Riegel, E.R. Kent, J.A. *Kent and Riegel's handbook of industrial chemistry and biotechnology Volume 1*, Springer Science and Business Media. May 2007.
69. Hoff, R. Mathers, R.T. *Handbook of Transition Metal Polymerization Catalysts*, John Wiley and Sons Inc., page 292. September 2010.
70. Whiteley, K.S. Heggs, T.G. Koch, H. Mawer, R.L. Immel, W. *Polyolefins; Ullmann's Encyclopedia of Industrial Chemistry 6th edition*, John Wiley and Sons Inc., page 1. 2003
71. Kaminsky, W. *Polyolefins: 50 years after Ziegler and Natta I: Polyethylene and Polypropylene*, Springer Berlin Heidelberg, page 1. January 2014.
72. Sinn, H. Kaminsky, W. *Advances in Organometallic Chemistry*, 18, Edited by Stone, F. G. A. West, R. Academic Press, New York, 1980.
73. Janiak, C. *Metallocene Catalysts*, Kirk-Othmer Encyclopedia of Chemical Technology 5th Edition, 16, John Wiley and Sons Inc., page 80. 2006
74. Zeus Industrial Products Inc., *Chemical Resistance of Fluoropolymers*, September 2006. Available online: <http://www.coleparmer.com/TechLibraryArticle/827>. Accessed: 13/10/14.
75. Saxena, A. Landes, J.D. Bassani, J.L. *Nonlinear Fracture Mechanics: Time-dependent fracture*, ASTM International, page 447. January 1988.
76. Mittal, V. *Optimization of Polymer Nanocomposite Properties*, John Wiley and Sons Inc., page 317. December 2009.

77. Doran, D. Cather, B. *Construction Materials Reference Book*, Routledge, page 230. July 2013.
78. Lupichev, L. N. Savin A.V. Kadantsev, V. N *Synergetics of Molecular Systems*, Springer, page 173. 2015.
79. Smallman, R. E. Bishop, R. J. *Modern Physical Metallurgy and Materials Engineering: Science, Process, Applications*, Butterworth-Heinemann, page 38. 1999.
80. Psaras, P.A. Dale Langford. *Advancing Materials Research*, National Academies Press, page 252. January 1987.
81. Seidel, A. *Characterization and Analysis of Polymers*, John Wiley and Sons Inc., page 282. February 2008.
82. Zhou, H. Wilkes, G.L. Comparison of lamellar thickness and its distribution determined from d.s.c., SAXS, TEM and AFM for high-density polyethylene films having a stacked lamellar morphology, *Polymer*, 38 (23), Elsevier, pp. 5735–5747. November 1997.
83. Brownstein, A.M. *US petrochemicals: technologies, markets, and economics*, Petroleum Publishing Company, page 275. June 1972.
84. Lappin, G. *Alpha Olefins Applications Handbook*, CRC Press, page 72. April 1989.
85. Walczak Z.K. *Processes of Fiber Formation*, Elsevier, page 178. 14 Feb 2002.
86. Benedikt, G.M. Goodall, B.L. *Metallocene Catalyzed Polymers: Materials, Processing and Markets*, Cambridge University Press, page 106. December 2008.
87. Bovey, F. *Chain Structure and Conformation of Macromolecules*, Elsevier, page 161. December 1982.
88. Eggers, R. *Industrial High Pressure Applications: Processes, Equipment and Safety*, John Wiley and Sons Inc., page 80. June 2012
89. Müller, W.W. *HDPE Geomembranes in Geotechnics*, Springer, page 12. November 2006.

90. Lappin, G. *Alpha Olefins Applications Handbook*, CRC Press, page 72. April 1989
91. Robertson, G.L. *Food Packaging: Principles and Practice 2nd Edition*, CRC Press, page 20. September 2005.
92. Black, B.C. *Crude Reality: Petroleum in World History*, Rowman and Littlefield, page 169. April 2014.
93. Schork, J. *Control of Polymerization Reactors*, CRC Press, page 97. March 1993.
94. Plastics News. *European Resin Demand for Rotational Moulding*. November 2012. Available online: <http://www.plasticsnews.com/article/20121116/FYI/311169976/european-resin-demand-for-rotational-molding-2012>. Accessed: 18/03/13.
95. Campbell, F.C. *Structural Composite Materials*, ASM International, 2010. Available online: http://sandiego.asminternational.org/content/ASM/StoreFiles/05287G_Frontmatter.pdf.
96. Sanadi, A.R. Caulfield D.F. Jacobson R.E. Rowell R.M. *Renewable Agricultural Fibers as Reinforcing Fillers in Plastics: Mechanical Properties of Kenaf Fiber–Polypropylene Composites*, *Ind. Eng. Chem. Res.*, 34 (5), pp. 1889–1896. May 1995.
97. Luthria, A. Sreekha, A. Hegde, J. Karale, R. Tyagi, S. Bhaskaran, S. *The reinforcement effect of polyethylene fibre and composite impregnated glass fibre on fracture resistance of endodontically treated teeth: An in vitro study*, *Journal of Conservative Dentistry*, 15, (4). pp. 372-376. October 2012.
98. Huang, R. Xu, X. Lee, S. Zhang, Y. Kim, Wu. *High Density Polyethylene Composites Reinforced with Hybrid Inorganic Fillers: Morphology, Mechanical and Thermal Expansion Performance*, *Materials* 2013, 6, (9). pp. 4122-4138. September 2013.
99. Li, G. Helms, J.E. Pang, S.S. Schultz, K. *Analytical Modelling of Tensile Strength of Particulate- Filled Composites*, *Polym. Compos*, 22, pp. 593–603. April 2004.

100. Brydson, J.A. *Plastics Materials 7th Edition*, Butterworth-Heinemann UK, p, 189. 1999. Available online: <http://www.scribd.com/doc/2491357/Brydson-Plastics-Materials-7th-Edition>. Accessed: 04/08/14.
101. Milewski, J.V. Katz H.S. *Handbook of Reinforcements for plastics*, Van Nostrand Reinhold Company New York, pp. 37-75. 1987.
102. Wypych, G. *Fillers*, ChemTec Publishing, pp. 175-251. 1993.
103. Sepe, M. *Use MFR Cautiously With Filled Materials*, *Plastics Technology Magazine Online*, August 2012. Available online: <http://www.ptonline.com/columns/use-mfr-cautiously-with-filled-materials>. Accessed: 4/08/14
104. Ahmed, S. Jones, F.R. *A review of particulate reinforcement theories for polymer composites*, *Journal of Materials Science*, 25 (12), pp 4933-4942. December 1990.
105. Liauw, C.M. PhD Thesis, *Influence of surface modification of aluminium hydroxide on the processing and mechanical properties of aluminium Hydroxide/polypropylene composites*, Manchester Metropolitan University, page 36. 1994.
106. Kerner, E.H. *The Elastic and Thermo-elastic Properties of Composite Media*, *Proc. Phys. Soc.* 69, page 808. 1956.
107. Goodier, J.N. *Transactions of the American Society of Mechanical Engineers*, 55 (39). 1933.
108. Nielsen, L.E. Lewis, E T.R. *Journal of Applied Polymer Science*, 1970, 14, 1449.
109. Stanford, J.L. Bentley, S.R. *Filpas '89*, (PRI, BPF, London, 1989).
110. Maiti, S.N. Lopez, B.H. *Journal of Applied Polymer Science*, 44, pp. 353-360. 1992.
111. Pukansky, B. Turczanyi B. Tudos, F. *Proceedings of the International Conference on Interfaces in Polymer Composites*, Cleveland Ohio, Elsevier, New York. 1988.

112. Pukansky, B. Turczanyi B. Tudos, F. *Journal of Material Science Letters*, 7, page 160-162. 1988.
113. Levita, G. Marchetti, A. Lazzeri, A. *Polym. Compos.* 10, page 39. 1989.
114. Danusso, F. Tieghi, G. *Polymer*, 27, page 1385. 1986.
115. Bascom, W.N. *The relationship between sand size and beach-face slope*, Transactions of the American Geophysical Union, 32 (6), University of California, USA, pp.866-874. December 1951.
116. Newsome, D. Ladd, P. *The use of quartz grain microtextures in the study of the origin of sand terrains in Western Australia*, CATENA, 35 (1), Pages 1–17. March 1999.
117. Lancaster, N. Baker, S. Bacon, S. McCarley-Holder, G. *Owens Lake dune fields: Composition, sources of sand, and transport pathways*, Desert Research Institute, Nevada, USA, page 7. January 2015.
118. Guven, O. Ozdemir, O. Karaagaclioglu, I.E. Çelik, M.S. *Surface morphologies and floatability of sand-blasted quartz particles*, Istanbul Technical University, Istanbul, Turkey, page 1. August 2014.
119. Novak, G. A. Gibbs, G. V. *The Crystal Chemistry of the Silicate Garnets*, the American Mineralogist, 56, page 791. June 1971.
120. Kolesov, B. A. Geiger, C. A. *Raman spectra of silicate garnets*, Physics and Chemistry of Minerals, 25 (2), pp 142-151. January 1998.
121. Zhang, L. Ahsbahs, H. Kutoglu, A. Geiger, C. A. *Single-crystal hydrostatic compression of synthetic pyrope, almandine, spessartine, grossular and andradite garnets at high pressures*, Physics and Chemistry of Minerals, 27 (1), pp 52-58. November 1999.
122. Ren, S. Song, C. Li, J. *Mineralogical Characteristics of Garnet in Garnet Mica Schist and Its Tectonic Significance in the Tongbai Section of the Shangdan Fault Zone*, Open Journal of Geology, 5 (1), pp 13-27, 2015.

123. Durdzińska, P. T. Dunanta, C. F. Hahab, M. B. Scrivenera, K.L. *A New quantification Method based on SEM-EDS to Assess Fly Ash Composition and Study the Reaction of its Individual Components in Hydrating Cement Paste*, Cement and Concrete Research, 73, pp. 111-122. July 2015.
124. Divya, V.C. Khan, M. A. Rao, B. N. Sailaja, R.R.N. *High-density Polyethylene/Cenosphere Composites Reinforced with Multi-Walled Carbon Nanotubes: Mechanical, Thermal and Fire Retardancy Studies*, Materials and Design Journal, 65, pp. 377-386. 2015.
125. Yao, Z.T. Ji, X.S. Sarker, P.K. Tang, J.H. Ge, L.Q. Xia, M.S. Xi, Y.Q. *A comprehensive review on the applications of coal fly ash*, Earth-Science Reviews, 141, pp. 105–121. 2015.
126. Feng, X. Clark, B. *Evaluation of the Physical and Chemical Properties of Fly Ash Products for Use in Portland Cement Concrete*, 2011 World of Coal Ash conference, Denver, CO, USA, page 6. May 2011.
127. Samuels, R.J. *Structured Polymer Properties*, Wiley, New York, 1974.
128. Gorrasi, G. Di Lieto, R. Patimo, G. De Pasquale, S. Sorrentino, A. *Structure property relationships on uniaxially oriented carbon nanotube/polyethylene composites*, Polymer, 52, pp. 1124-1132. 2011.
129. Bilotti, E. Fischer, H. Peijs, R.T. *Polymer Nanocomposites Based on Needle-like Sepiolite Clays: Effect of Functionalized Polymers on the Dispersion of Nano filler, Crystallinity, and Mechanical Properties*, Queen Mary University of London, Journal of applied polymer science 107 (2), pp. 1116-1123, January 2008.
130. Kendall, K. *Interface Science and Composites*, British Polymer Journal, 10, pp.35-38. 1978.
131. Wong, K. J. Yousif, B. F. Low, K. O. Ng, Y. Tan, S. L. *Effects of fillers on the fracture behaviour of particulate polyester composites*, The Journal of Strain Analysis for Engineering Design, 45 (1), pp. 67-78. January 2010.
132. Ribnikar, F. *Journal of Applied Polymer Science*, 42, pp. 2727-2732. 1991.
133. Kangoa, S. Kaliab, S. Celli, A. Njugunad, J. Habibie, Y. Kumara, R. *Surface modification of inorganic nanoparticles for development of organic–inorganic nanocomposites - A review*,

Jaypee University of Information Technology, India, Progress in Polymer Science Journal 38 (4), pp. 421. April 2013.

134. Arnaud, R. PhD Thesis, *An Investigation into the Effects of the Introduction of Fillers on the Properties of Rotationally Moulded Products*, Queens University Belfast, page 13. September 1998.
135. Fu, S. Feng, X. Lauke, B. Mai, Y. *Effects of particle size, particle/matrix interface adhesion and particle loading on mechanical properties of particulate-polymer composites*, Technical Institute of Physics and Chemistry, Beijing, China, Composites Journal, Part B: Engineering 39 (6), pp. 933–961. September 2008.
136. Schlumpf, H.P. *Kunststoffe*, 73, pp. 511-515. 1983.
137. Vu-Kahn, T. Fisa, B. *Polym. Compos*, 7, pp. 219-226. 1986.
138. Riley, A.M. Paynter, C.D. McGenity P.M. Adams J.M. *Factors affecting the impact properties of mineral filled polypropylene*, *Plast. Rubber Proc. Applic.* 14, pp. 85-93. 1990.
139. Trtignon, J.P. Verdu, J. De Bossard ,R. De Vallois, A. *Polypropylene-Mica Composites*, *Polym.Compos.*, Edited by Sedlacek B., Walter de Gruyter, Berlin, pp. 191-198. 1986.
140. Oey, T. Kumar, A. Bullard, J.W. Neithalath, N. Sant, G. The Filler Effect: The Influence of Filler Content and Surface Area on Cementitious Reaction Rates, *Journal of the American Ceramic Society*, 96 (6), pp. 1978-1990. June 2013.
141. Tanimoto, M. Yamagata, T. Miyata, K. Ando, S. Anisotropic Thermal Diffusivity of Hexagonal Boron Nitride-Filled Polyimide Films: Effects of Filler Particle Size, Aggregation, Orientation, and Polymer Chain Rigidity, *Applied Materials and Interfaces*, 5 (10), pp 4374–4382. 2013.
142. Liauw, C.M. Lees, G.C. Rathon, R.N. Voliotis, A. Wild, F. Sunderland, P. Schofield, J. Thetford, D. *Evolution of reactive unsaturated interfacial modifiers for polyolefin based composites*, *Composite Interfaces*, 13(8-9) p. 717-736. 2006.

143. Fernandes, E.M. Correlo, V.M. Mano, J. F. Reis, R. L. *Novel cork–polymer composites reinforced with short natural coconut fibres: Effect of fibre loading and coupling agent addition*, University of Minho, Portugal, *Composites Science and Technology Journal* 78, pp. 56–62. 2013.
144. Jaehyung, J. Morgan, R.J. *Interfacial Failure of Composites at Cryogenic and Elevated Temperatures*, Texas A&M University, NASA Glenn Research Centre Cleveland, USA, Society of Plastics Engineers ANTEC (Annual Technical) Conference Proceedings, page 1. 2006.
145. Vautarda, F. Fiouxa, P. Vidala, L. Schultza, J. Nardina, M. Defoort, B. *Influence of the carbon fiber surface properties on interfacial adhesion in carbon fiber–acrylate composites cured by electron beam*, *Composites Part A: Applied Science and Manufacturing*, 42 (7), pp. 859-867. July 2011.
146. Wang, H.W. Zhou, H.W Peng, R.D. Mishnaevsky, L. *Nanoreinforced polymer composites: 3D FEM modeling with effective interface concept*, *Composites Science and Technology*, 71 (7), pp. 980-988. May 2011.
147. Vollenberg, P.H.T. Heikens, D. *Polymer*, 30, pp.1656-1662. 1989.
148. Maiti, S.N. Mahapatro P.K. *Journal of Applied Polymer Science*, 42, pp. 3101-3110. 1991.
149. Yanjun, X. Callum, A.S. Hill. Zefang B.X. Militz. H. Carsten M. *Silane coupling agents used for natural fiber/polymer composites: A review*, Edinburgh Napier University, *Composites : Part A* (41), Journal, pp. 806–819. 2010.
150. Mahouche-Chergui, S. Gam-Derouich, S. Mangeney, C. Chehimi, M.M. *Aryl, diazonium salts: a new class of coupling agents for bonding polymers, biomacromolecules and nanoparticles to surfaces*, *Chemical Society Reviews*, 40, pp. 4143-4166. 2011.
151. Bluemmel, P. Setaro, A. Popeney, C.S. Haag, R. Reich, S. *Dispersion of carbon nanotubes using an azobenzene derivative*, *physica status solidi*, 247 (11-12), pp. 2891-2894, December 2010.

152. Liauw, C.M. Hurst S.J. Lees G.C. Rothon R.N. Dobson D.C. *The effect of filler surface modification on the mechanical properties of aluminium hydroxide filled polypropylene*. *Plastics Rubber and Composites Processing and Applications*, 24 (5), p. 249-260. 1995.
153. Pukánszky, B. *Influence of interface interaction on the ultimate tensile properties of polymer composites*, *Composites*, 21 (3), pp. 255–262. May 1990.
154. Brechet, Y. *Polymer Based Nanocomposites: Effect of Filler-Filler and Filler-Matrix Interactions*, *Advanced Engineering Materials*, 3 (8), 2001.
155. Bernada, A.C. *Fibre Glass Reinforced HDPE*, *SPE Journal*, 26, pp. 37-45. October 1970.
156. Kalia, S. Kaith B.S. Kaur I. *Pre-treatments of Natural Fibers and their Application as Reinforcing Material in Polymer Composites - A Review*, *Polymer Engineering and Science*, 49 (7), pp.1253-1272. March 2009.
157. Trivedi, B.C. Culbertso B.M. *Maleic anhydride*, Plenum Press, New York-London, pp. 459-462. 1981.
158. Marti, L.W. *Overview of Maleic Anhydride Grafted Polyolefin Coupling Agents – A Guide to Understanding their Uses, Benefits, Functions, Selections and Development*. ADDCOMP. (no date). Available online: http://www.speautomotive.com/SPEA_CD/SPEA2012/pdf/TP/TP9.pdf. Accessed: 01/04/2012.
159. Shih, R.H. *Introduction to Finite Element Analysis Using Creo Simulate 1.0*, SDC Publications, page 2. 2011.
160. Novak, M. Dolsak B. *Intelligent FEA-based design improvement*, *Engineering Applications of Artificial Intelligence*, 21. pp. 1239-1254. December 2008.
161. Haghghi, K. *Finite Element Method (FEM/FEA) Introduction*, University of Purdue, Indiana, USA, page 3. January 2001. Available online: <https://engineering.purdue.edu/~abe601/lecture/Introduction.pdf> Accessed: 25/06/14.

162. Burkhart, D. Hamann, B. Umlauf, G. *Finite Element Analysis for Linear Elastic Solids Based on Subdivision Schemes*, University of Kaiserslautern, Germany and University of California, USA. March 2010.
163. M.S. Gockenbach, *Understanding and implementing the finite element method*, Society for Industrial and Applied Mathematics (SIAM), January 1987.
164. Agarwal, R. B. *Introduction to Finite Element Analysis: An Overview of the Finite Element Analysis*, San Jose State University, August 2002.
165. Wang, W. Sadeghipour, K. Baran, G. *Finite element analysis of the effect of an interphase on toughening of a particle-reinforced polymer composite*, Composites: Part A, 39, (6). pp. 956–964. June 2008.
166. Pesaran, A.A. Kim, G.H. Smith, K. Santhanagopalan, S and Lee, K..J. *Computer-Aided Engineering for Electric Drive Vehicle Batteries*, Lee National Renewable Energy Laboratory, Colorado, USA. May 2011. Available online: <http://www.nrel.gov/vehiclesandfuels/energystorage/pdfs/50914.pdf>. Accessed: 05/08/14.
167. Draï, A. Aour, B. *Analysis of the temperature effect on the behaviour of high density polyethylene during high pressure torsion process*, 21ème Congrès Français de Mécanique proceedings, 26 August 2013.
168. Cailletaud, G. El Arem, S. *Introduction to Finite Element Method*, ParisTech Institute of Science and Technology Materials Centre. June 2010. Available online: http://mms2.ensmp.fr/tribo_paris/lectures/Introduction_FE.pdf Accessed: 4/08/14.
169. Kersale, E. *Analytic Solutions of Partial Differential Equations*, School of Mathematics, University of Leeds. September 2009. Available online: http://www1.maths.leeds.ac.uk/~kersale/Teach/M3414/Notes/m3414_1.pdf. Accessed: 09/06/14.
- 170.** Ames, W.F. *Numerical Methods for Partial Differential Equations*, Academic Press, page 1. June 2014.

171. Churchill, R. C. and Kovacic, J. J. *Introduction to Differential Galois Theory*, page 3. 2006. Available online: <http://www.sci.ccny.cuny.edu/~ksda/PostedPapers/intro.pdf> Accessed: 07/05/2015.
172. Maes, M. Huysse, L., *Reliability and Optimization of Structural Systems*, Proceedings of the 11th IFIP WG7.5 Working Conference, CRC Press, page 276. July 2004.
173. Cajori, F. *The Early History of Partial Differential Equations and of Partial Differentiation and Integration*, American Mathematical Monthly, 35 (9). November 1928.
174. Courant, R. Friedrichs, K. Lewy, H. *Partial Difference Equations of Mathematical Physics*, Mathematische Annalen, 100, (1). pp. 32-74. 1928.
175. Williamson, F. *Richard Courant and the Finite Element Method: A Further Look*, Historia Mathematica 7, (4). November 1980, pp. 369–378.
176. Courant, R. *Variational methods for the solution of problems of equilibrium and vibrations*, Bull. Amer. Math. Soc., 49. pp. 1-23. 1943
177. Hart, V. G. *The Hypercircle and J.L. Synge*, Mathematical Proceedings of the Royal Irish Academy, 107, (2). pp.153-161. January 2007.
178. Felippa, C. *The Origins of the Finite Element Method*. University of Colorado, USA August 2013. Available online: http://home.iitk.ac.in/~mohite/History_of_FEM.pdf Accessed: 05/08/14.
179. Heyman, J. *Structural Analysis: A Historical Approach*, Cambridge University Press, May 1998.
180. Turner, M. J. Clough, R. Martin, W. H. C. Topp, L. J. *Stiffness and Deflection of Complex Structures*, Journal of Aeronautical Sciences, 23, (9). pp. 805-824. September 1956.
181. Kurrer, K. *The History of the Theory of Structures: From Arch Analysis to Computational Mechanics*, John Wiley and Sons Inc., January 2012.
182. Ortiz M. *Computational micromechanics*, Computational Mechanics, 18, (5). pp. 321-338. September 1996.

183. A.F. Bower, *Applied Mechanics of Solids Chapter 8: Theory and Implementation of the finite element method*. Available online: http://solidmechanics.org/text/Chapter8_1/Chapter8_1.htm Accessed: 25/04/2015.
184. Boeraeve, P. *Introduction to the finite element method*, Gramme Institute, Angleur, Belgium, page 62. 2010. Available online: <http://www.gramme.be/unite9/FEM/Finite%20Element%20Method.pdf> Accessed: 29/04/2015.
185. Hibbit, H. D. Marcal, P. V. Rice, J. R. *A Finite Element Formulation for Problems of Large Strain and Large Displacement*, International Journal of Solid Structures, 6, Pergamon Press, pp. 1069 to 1086. 1970.
186. Huebner, K. H. *The Finite Element Method for Engineers*, John Wiley & Sons, page 668, September 2001.
187. Reddy, J. N. *An Introduction to Nonlinear Finite Element Analysis: with applications to heat transfer, fluid mechanics, and solid mechanics*, Oxford University Press, page 83. October 2014.
188. Farmaga, I. Shmigelskyi, P. Spiewak, P. Ciupinski, L. *Evaluation of Computational Complexity of Finite Element Analysis*, CAD Systems in Microelectronics (CADSM). pp.213-214. February 2011
189. Vicich, B. Ryan, C. Meredith, K. *Linear vs. Nonlinear Contact Analysis*, Samtec Inc., 2007. Available online: https://www.samtec.com/documents/webfiles/technical_library/reference/articles/linear_vs_%20non-linear_contact_analysis_082207.pdf. Accessed: 05/08/14.
190. Shahidi, Y.K. Article. *Key Assumptions in FEA for Design*, January 2010. Available online: <http://engineering-inventions.blogspot.co.uk/2010/01/key-assumptions-in-fea-for-design.html> Accessed: 26/06/14.
191. Ivančo, V. *Nonlinear Finite Element Analysis*, Faculty of Mechanical Engineering, Technical University of Košice, Slovakia. June 2011. Available online: <http://www.mb.hs->

- wismar.de/~heinze/subdir/FEA_of_Nonlinear_Problems_2011_Ivanco.pdf. Accessed: 05/08/14.
192. Felippa, C. *A Tour of Nonlinear Analysis*, August 2013. University of Colorado, USA, August 2013. Page 12 Available online: <http://www.colorado.edu/engineering/CAS/courses.d/NFEM.d/NFEM.Ch02.d/NFEM.Ch02.pdf>. Accessed: 05/08/14.
193. Prasad, N.P. *Introduction to Nonlinear Optical Effects in Molecules and Polymers*, Wiley and Sons. January 1991.
194. Dassault Systemes. *Understanding Nonlinear Analysis*, page 4. March 2010. Available online: http://files.solidworks.com/whitepapers/2010/Nonlinear_Analysis_2010_ENG_FINAL.pdf. Accessed: 05/08/14.
195. McHugh, P. *Non-Linear Finite Element Analysis: Finite Element Solution Schemes I and II*, Department of Mechanical and Biomedical Engineering, University of Ireland, 2007. Available online: <http://www.nuigalway.ie/micru/Non%20Linear%20Finite%20Element%20Methods.pdf>. Accessed: 05/08/14.
196. Bonet, J. Wood, D.R. *Nonlinear Continuum mechanics for Finite Element Analysis*, Cambridge University Press, 1997.
197. Dolšak, B. *Finite element mesh design expert system*, Knowledge-Based Systems 15, (5), pp. 315-322. July 2002.
198. Shengwei, M. Article. *Top 5 misunderstandings on (good) mesh*, October 2011. Available online: <http://caewatch.com/top-5-misunderstandings-on-good-mesh/>. Accessed: 05/08/14.
199. Behrens, J. Beisiegel, N. Pranowo, W. *Inundation modelling with adaptive triangular mesh refinement - state of the art numerical methods for accurate simulation*, University of Hamburg. September 2010. Available online:

http://www.loicz.org/imperia/md/content/loicz/stormsurges/posterd/p41_beispiel_et_al.pdf. Accessed: 05/08/14.

200. Babuvška I. Rheinboldt W. C. *Error Estimates for Adaptive Finite Element Computations*, SIAM Journal on Numerical Analysis, 15, (4). pp. 736-754. 1978
201. Li, Y. Premasathan, S. Jameson, A. *Comparison of h- and p- Adaptations for Spectral Difference Methods*, Aeronautics and Astronautics Department, Stanford University, California, USA. July 2010.
202. Babuska, M. S. *The P and H-P Versions of the Finite Element Method, Basic Principles and Properties*, SIAM Journal, 36, 4. pp. 578-632. December 1994.
203. Hodohara ,T. *Finite Element Mesh Using h-refinement Procedure*, Chuo University, Faculty of Science and Engineering, Tokyo, Japan. October 2002.
204. Fiedler, G. *Triangle subdivision*, (no date) Available online: <http://gafferongames.com/virtualgo/tessellating-the-go-stone/>. Accessed: 05/08/14.
205. Meschke, G. *Finite Element Methods In Linear Structural Mechanics: Short Presentation in Adaptive Finite Element*, Ruhr University, Germany. February 2009. Available online: http://www.sd.rub.de/downloads/Adaptive_Finite_Element_Methods. Accessed: 05/08/14.
206. Byfut, A. Schroder, A. *hp-Adaptive Extended Finite Element Method*, International Journal for Numerical Methods in Engineering, 89, 11, pp. 1392–1418. March 2012.
207. McRae, D. S. *r-Refinement grid adaptation algorithms and issues*, Department of Mechanical and Aerospace Engineering, North Carolina State University, USA. May 1999.
208. Kuo, Y.L. Cleghorn, W.L. Behdinan, K. Fenton, R.G. *The h-p-r-refinement finite element analysis of a planarhigh-speed four-bar mechanism*, Department of Mechanical and Industrial Engineering, University of Toronto, Ontario, Canada. September 2005.
209. Kuo, Y. L. Cleghorn W. L *The h-, p-, and r-refinements of Finite Element Analysis of Flexible Slider Crank Mechanism*, Journal of Vibration and Control, 13.pp. 415-435. April 2007.

210. Maddi, J.R. Vable, M. *An hpr-mesh refinement algorithm for BEM, Engineering Analysis with Boundary Elements*, 34. pp. 549-556. January 2010.
211. Maurer, D. Image. *P-Refinement of a Finite Element Mesh*. University of Landshut Applied Sciences, (no date). Available online: <https://people.fh-landshut.de/~maurer/femeth/node271.html>. Accessed: 05/08/14
212. *Kingspan vs Borealis County Court Judgement*. London Royal Courts of Justice. May 2012. Available online: http://www.7kbw.co.uk/media/uploaded_files/Kingspan_v_Borealis_Final.pdf. Accessed: 04/08/14.
213. Goldstein, J. Newbury, D.E. Joy, D.C. Lyman, C.E. Echlin, P. Lifshin, E. Sawyer, L. Michael, J.R. *Scanning Electron Microscopy and X-ray Microanalysis: Third Edition*, Springer Science & Business Media, page 1. December 2012.
214. Schroder, D.K. *Semiconductor Material and Device Characterization*, John Wiley & Sons, page 631. February 2006.
215. Goodhew, P.J. Humphreys, J. Beanland, R. *Electron Microscopy and Analysis Third Edition*, CRC Press, page 125. November 2000.
216. Khursheed, A. *Scanning Electron Microscope Optics and Spectrometers*, World Scientific, page 3. 2011.
217. Brundle, C. R. Baker, A.D. *Electron Spectroscopy Volume 3*, Academic Press, page 23. 1979.
218. Brundle, C. R. Evans, C.A. Wilson, S. *Encyclopedia of Materials Characterization: Surfaces, Interfaces, Thin Films*, Gulf Professional Publishing, page 122. 1992.
219. Lawson, G. *Chemical Analysis of Polymers*, iSmithers Rapra Publishing, page 18. December 1991.
220. Höhne, G. Hemminger, W. Flammersheim, H-J. *Differential Scanning Calorimetry*, Springer Science & Business Media, page 1. July 2003.

221. Sepe, M.P. *Thermal Analysis of Polymers*, iSmithers Rapra Publishing, page 3. January 1997.
222. Wunderlich, B. *Macromolecular Physics*, 1, Academic Press, New York, chapter 3. 1973.
223. Crompton, T.R. *Polymer Reference Book*, iSmithers Rapra Publishing, page 437. January 2006.
224. Wunderlich, B. Cormier, C. M. *Heat of fusion of polyethylene*, Journal of Polymer Science Part A-2: Polymer Physics, 5(5), John Wiley and Sons Inc., September 1967.
225. Studies and Information Services, Committee on Aeronautics Research and Technology for Vision 2050, Aeronautics and Space Engineering Board, Transportation Research Board, Division on Engineering and Physical Sciences, National Research Council. *Securing the Future of U.S. Air Transportation: A System in Peril*, National Academies Press, page 23. November 2003.
226. Potgieter, H. Liauw, C.M. Velado, D. *Effect of Fly Ash Washing Conditions on the Properties of Coupling Agent Modified Polypropylene/Fly Ash Composites*, Polymer Composites, 35 (4). April 2014.
227. Srivatsan, T. S. Bhatnagar, N. *Processing and Fabrication of Advanced Materials XVII Part 8*, Polymer-based composites and nano composites Volume Two, I. K. International Pvt Ltd., page 481. 2009.
228. Rothon, R. *Particulate-filled Polymer Composites*, iSmithers Rapra Publishing, page 19. January 2003.
229. Nurshamila, S.B. Ismail, H. Othman, N. *The effects of Rattan Filler Loading on the Properties of Rattan Powder-Filled Polypropylene Composites*. Bioresources Journal, 7(4), pp.5677-5690. 2012.
230. Deepthi, M.V. Sharma, M. Sailaja, R.R.N. Anantha, P. Sampathkumaran, P. Seetharamu, S. *Mechanical and thermal characteristics of high density polyethylene-fly ash Cenospheres composites*, Materials and Design, 31, pp.2051-2060. 2010.
231. Fanderlik, I. *Silica Glass and Its Application*, Elsevier, page 208. October 2013.

232. Whitney, D. L. Broz, M. Cook, R.F. *Hardness, toughness, and modulus of some common metamorphic minerals, American Mineralogist*, 92 (2), pp. 281-288. 2007.
233. Dong, M. Li, S. Xie, J. Han, J. *Experimental Studies on the Normal Impact of Fly Ash Particles with Planar Surfaces, Energies* 2013, 6(7), pp. 3245-3262. July 2013.
234. Okiyokota, M. *Fracture Behaviour of Fiber Reinforced PPS Injection Moulding, Society of Plastics Engineer ANTEC (Annual Technical) Conference Proceedings, CRC Press, page 3320. April 1997.*
235. Hosford, W. F. *Solid Mechanics, Cambridge University Press, page 7. March 2010.*
236. Yoo, Y. Spencer, M.W. Paul, D.R. *Morphology and mechanical properties of glass fiber reinforced Nylon 6 nanocomposites, Polymer*, 52, pp. 180-190. 2011.
237. Yoo, M. Masters Thesis, *Comparison of Interlaminar Fracture Toughening of Filament Wound Glass/Epoxy Composites by Using MWCNT's or Flexible Resin, The Pennsylvania State University Graduate School, Department of Aerospace Engineering, page 7. August 2009.*
238. Bashar, M. Sundararaj, U. Mertiny, P. *Study of matrix micro-cracking in nano clay and acrylic tri-block-copolymer modified epoxy/basalt fiber-reinforced pressure-retaining structures, eXPRESS Polymer Letters*, 5 (10), pp. 882–896. April 2011.
239. Friedrich, K. Fakirov, S. Zhang, Z. *Polymer Composites: From Nano- to Macro-Scale, Springer Science & Business Media, page 52. July 2005.*
240. Hassan, A. Abdul Rahman, N. Yahya, R. *Extrusion and Injection-Molding of Glass Fiber/MAPP/Polypropylene: Effect of Coupling Agent on DSC, DMA and Mechanical Properties, Journal of Reinforced Plastics and Composites, page 1. September 2011.*
241. Petchwattana, N. Covavisaruch, S. Chanakul, S. *Mechanical properties, thermal degradation and natural weathering of high density polyethylene/rice hull composites compatibilized with maleic anhydride grafted polyethylene, Journal of Polymer Research*, 19 (9921), page 4. June 2012.

242. Kord, B. *Influence of Maleic Anhydride on the Flexural, Tensile and Impact Characteristics of Sawdust Flour Reinforced Polypropylene Composite*, World Applied Sciences Journal, 12 (7), pp. 1014-1016, 2011.
243. Swallowe, G.M. *Mechanical Properties and Testing of Polymers: An A-Z Reference*, Springer Science & Business Media, page 134. November 1999.
244. Barbero, E.J. *Finite Element Analysis of Composite Materials Using ANSYS® 2nd Edition*, CRC Press, page 24. December 2013.
245. Fathi, J. Ashrafi, S. Movla, H. Sobhaian, S. *A novel method to determine Poisson's ratio by beta-ray absorption experiment*, Elsevier Ltd. January 2012.
246. Lee, J. Lee, S, Chang, J. Thompson, M.S. Kang, D. Park, S. *A Novel Method for the Accurate Evaluation of Poisson's Ratio of Soft Polymer Materials*, The Scientific World Journal (2013), published under the Creative Commons Attribution License. March 2013.
247. Priego-Capote, F. M.D. Luque-de-Castro, *Analytical Applications of Ultrasound*, Elsevier Ltd., page 354. February 2007.
248. Bhabha, H. Liauw, C.M. Henwood, N.G. Taylor, H. Condliffe, J. *Critical Factors Affecting the Use of Finite Element Analysis For Rotomoulded Parts*, Manchester Metropolitan University, Manchester, UK, Rotomotive Ltd., Northampton, UK, Society of Plastics Engineers ANTEC (Annual Technical) Conference Proceedings. April 2014.
249. Nicholson, D.W. *Finite Element Analysis: Thermomechanics of Solids 2nd Edition*, CRC Press, page 342. April 2008.
250. Lai, J. Bakker, A. *Polymer Engineering and Science*, 35 (17). pp. 1339-1347. 1995.

Appendix 1

A list of twin screw extrusion and two roll mill compounds is provided. The relevant Results and Discussion Sections and table numbers have been included for ease of reference to the thesis.

5.2 Characterisation of Materials for Composite Development

5.2.2 Dual polyethylene blends

5.2.2.2 Twin screw extrusion compounded formulations

Table 6. Combinations of MA-g-LLDPE with HDPE.

MA-g-LLDPE (% wt.)	HDPE (% wt.)
0	100
7.5	92.5
15	85
25	75
50	50
75	25
100	0

5.4 Comparison of Composite Formation Processes for Large Particle Composites (Dry Blending of Pre-Mix versus Two Roll Mill Melt Blending and Moulding)

Table 10. Blend details of two roll milled and dry blended composites.

MA-g-LLDPE/LMDPE (% wt.)	Filler (% wt.)
100	0
75	25
50	50
40	60
30	70
25	75
20	80
15	85

Appendix 1 (Continued)

Full list of two roll mill and TSE compounds

5.5 Use of Two Roll Mill Blending for Mixed Large/Small Particle Composites

Table 11. Combinations of fly-ash and cenospheres for addition to PE.

LMDPE/MA-g-LLDPE (% wt.)	Fly-ash (% wt.)	Cenospheres (% wt.)
100	0	0
75	6.25	18.75
50	12.5	37.5
40	15	45
30	17.5	52.5
25	18.75	56.25

Table 12. Ratio of fly-ash to cenospheres to maintain a volume of 50% filler.

LMDPE/MA-g-LLDPE (% vol.)	Fly-ash (of 50 % vol.)	Cenospheres (of 50 % vol.)
100	0	0
50	0	100
50	12.5	87.5
50	25	75
50	37.5	62.5
50	50	50
50	62.5	37.5
50	75	25
50	87.5	12.5
50	100	0

Appendix 1 (Continued)

5.6 Evaluation of Twin Screw Extrusion Compounding for Production of Small Particle Composites

Table 13. Fly-ash and maleanised PE combinations for twin screw extrusion compounding.

MA-g-LLDPE/LMDPE (% wt.)	Fly-ash (% wt.)
100	0
75	25
50	50
40	60
30	70
25	75

5.7 Verification of Maleic Anhydride Coupling Agent Effect on Small Particle Composites Produced by Twin Screw Extrusion Compounding

Table 14. Fly-ash analogue PE combinations investigated.

Analogue PE (% wt.)	Fly-ash. (% wt.)
100	0
75	25
50	50
40	60
30	70
25	75

Appendix 1 (Continued)

5.8 Comparison of Maleic Anhydride Coupling Agent Effect on HDPE and LMDPE Small Particle Composites Produced by Twin Screw Extrusion Compounding

Table 15. Blend details of HDPE or LMDPE with Fly-ash

MA-g-LLDPE (% wt.)	LMDPE or HDPE with and without 70 % wt. fly-ash (% wt.)
0	100
1	99
2.5	97.5
5	95
10	90
17.5	82.5
25	75

Appendix 1 (Continued)

5.9 Analysis of Rotationally Moulded Small Particle Composites

5.9.1 Rotomoulded rectangular box test mouldings

Table 16. Small Rectangular Box Mouldings

MA-g-LLDPE/LMDPE (% wt.)	Fly-ash. (% wt.)
100	0
75	25
50	50
40	60
30	70

5.9.2 Rotomoulded safety steps

Table 18. PE/fly-ash formulations for rotomoulded safety steps.

Target Wall Thickness (mm)	MA-g-LLDPE/LMDPE (% wt.)	Fly-ash (% vol.)	Fly-ash (% wt.)
7	50	28.8	50
7	75	14.4	25
7	87.5	7.2	12.5
7	100	0	0

Appendix 2

Tensile Testing (See Experimental Section 4.6.1 for full details of the test and sample dimensions)

Tensile testing to failure was carried out in accordance with ASTM D638 using a Hounsfield H10KS tensometer fitted with a 10 kN load cell. The gauge length was 50 mm. After collection of the data, the raw load - deflection data points were exported to MS Excel for further processing.

Example of Raw Load-Deflection Data

The raw load deflection data from the tensile tests was converted in to stress versus strain data using Equations 22 and 23 in Experimental Section 4.6.7 respectively. A typical example of this is provided in Table 25.

Table 25. An example of tensile load-deflection values alongside calculated stress-strain values.

Specimen 1			
6.41 mm Thickness - 13.06 mm Width			
Force (N)	Stress (MPa)	Deflection (mm)	Strain
112	1.34	0.00	0.0000
186	2.22	0.04	0.0008
284	3.39	0.08	0.0016
332	3.97	0.12	0.0024
400	4.78	0.16	0.0032
440	5.26	0.20	0.0040
504	6.02	0.24	0.0048

Example of Calculated Parameters

The tensile modulus was calculated by the Hounsfield Q-Mat software as part of the test routine selected. The latter was checked via linear regression of the raw data and values were found to be similar to those generated by the tensometer software. The latter can be seen in Figure 110 and Table 26.

Table 26. Tensile modulus and yield stress values calculated by the tensometer's software vs. manually calculated values.

Parameters	Tensometer Calculated Value	Manually Calculated Value
Tensile Modulus (MPa)	949.49	959.89
Yield Stress (MPa)	18.47	18.47

Appendix 2 (Continued)

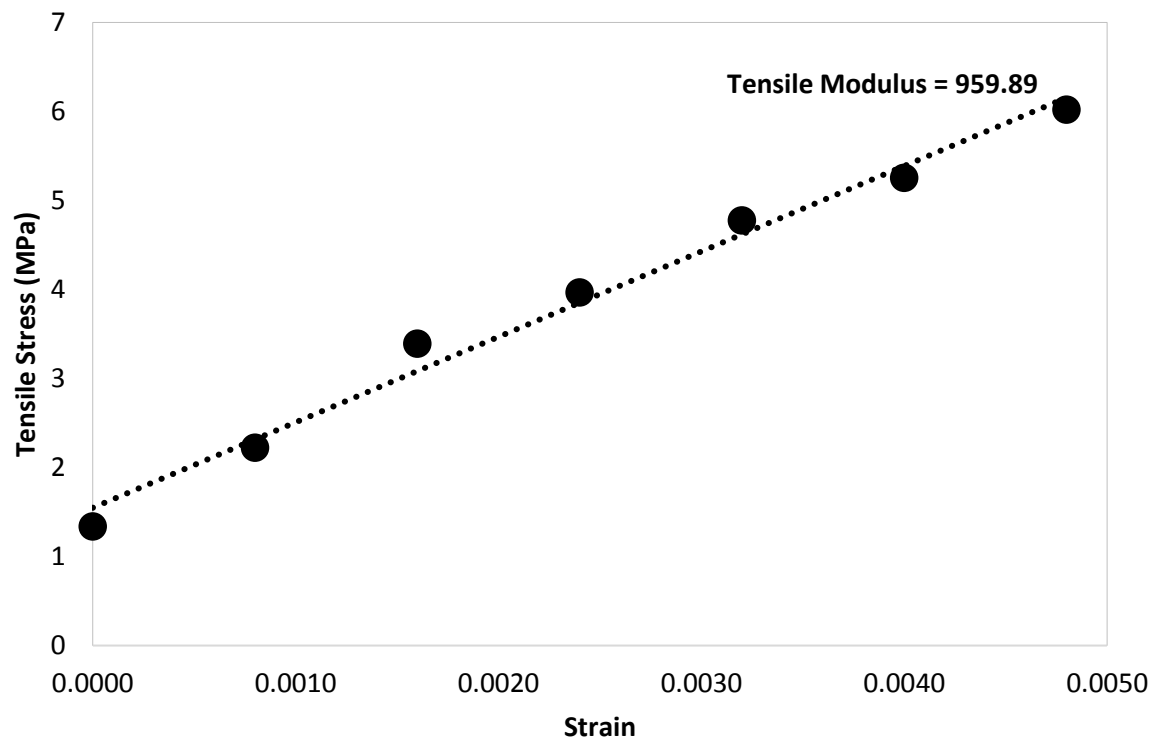


Figure 110. The tensile modulus of a PE specimen for comparison with computer generated values.

The tensile stress at yield values generated by the software were also checked by converting the load values at yield to stress (Table 27); it can also be seen from Table 26 that the manually calculated values of yield stress were the same as those values generated by the tensometers software.

Table 27. Yield force alongside its corresponding yield stress value.

Specimen 1	
6.41 mm Thickness - 13.06 mm Width	
Yield Force (N)	Yield Stress (MPa)
1546	18.47

Appendix 2 (Continued)

Flexural testing (See Experimental Section 4.6.2 for full details of the test and sample dimensions)

Flexural testing in three point bend mode was conducted according to ATSM D790 using a Hounsfield H10KS tensometer fitted with a 1 kN load cell. A 0.05 N pre-load was applied. Force and crosshead displacement were recorded and exported to MS Excel for further processing.

Example of Raw Load-Deflection Data

The raw load deflection data from the three point bend tests was first converted in to stress (in outer fibre) versus strain (in outer fibre) data using Equations 17 and 18 respectively. A typical example of this is provided in Table 28.

Table 28. An example of flexural load-deflection values alongside calculated stress-strain values

Specimen 1			
7.2 mm Thickness - 10.93 mm Width			
Force (N)	Stress (MPa)	Deflection (mm)	Strain
0.13	0.02	0.00	0.0000
0.25	0.04	0.01	0.0001
0.25	0.04	0.02	0.0002
0.38	0.06	0.03	0.0003
0.50	0.08	0.04	0.0004
0.63	0.11	0.05	0.0005
1.00	0.17	0.06	0.0006

Example of Calculated Parameters

The parameters determined from flexural stress-strain data were the flexural modulus (E_f), the secant modulus at 1 % strain ($E_{sf(1\%)}$) and the flexural stress at 10 mm deflection, yield or break (E_o).

Flexural modulus and stress at yield

The Flexural modulus was calculated from linear regression of the first 10 stress versus strain data points which showed the highest rate of change. The latter was checked by plotting the first 200 data points, identifying the region of maximum slope and selecting the first ten data points of that region for a modulus calculation (Figure 111). Flexural modulus values generated by the tensometer software were found to be an under-estimation (Table 29) due to inclusion of the excluded data points shown in Figure 111.

Appendix 2 (Continued)

The flexural stress at 10 mm deflection was calculated by Hounsfield's QMAT tensometer software and confirmed by manual calculation (Table 29 and 30).

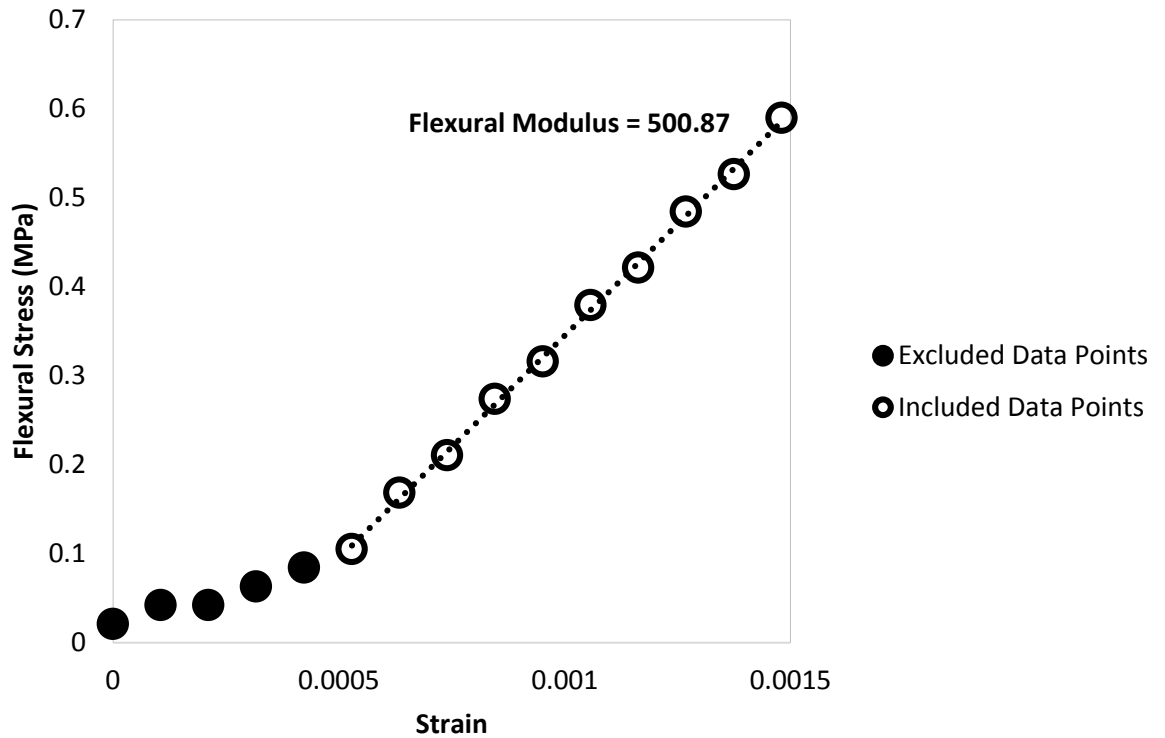


Figure 111. A graph to show which data points were used to manually calculate the flexural modulus of a PE specimen.

The flexural stress at 10mm deflection (or yield or break) values were calculated by converting the load values into stress. Tables 29 and 30 confirms that the manually calculated values of flexural stress were the same as those values calculated by the tensometers software.

Table 29. Flexural modulus and yield stress values calculated by the tensometer's software vs. equivalent manually calculated values

Parameters	Tensometer Calculated Value	Manually Calculated Value
Flexural Modulus (MPa)	403.66	500.87
Flexural Stress at 10 mm Deflection (MPa)	20.60	20.60

Appendix 2 (Continued)

Table 30. Force at 10mm deflection value alongside its corresponding stress value.

Specimen 1	
7.2 mm Thickness - 10.93 mm Width	
Force at 10 mm Deflection (N)	Flexural Stress at 10 mm Deflection (MPa)
122.25	20.60

Secant modulus at 1 % strain

The secant modulus at 1% strain was calculated using Equation 19. Table 30 displays the values required for input into equation 19 and the consequent value of secant modulus at 1 % strain obtained. Figure 112 shows the gradient of a flexural stress-strain response up to 1 % strain alongside the calculated value of secant modulus at 1 % strain.

Table 30. Secant modulus at 1 % strain calculation.

Secant Modulus at 1 % Strain Calculation		
Parameter	Value	Secant Modulus at 1 % Strain (MPa)
Stress Value after Toe (MPa)	0.11	454.88
Stress Value at 1 % Strain (MPa)	4.68	
Chosen Strain Value (%)	0.01	

Appendix 2 (Continued)

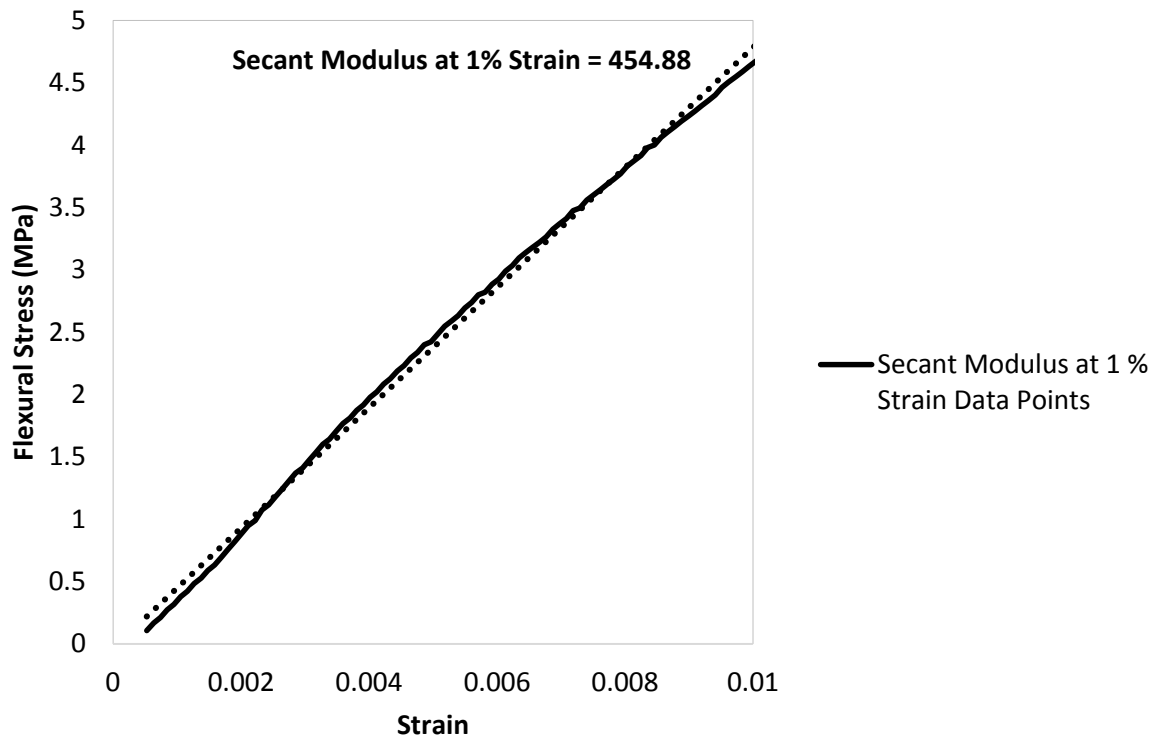


Figure 112. A graph to show the secant modulus calculation data points.

Poisson's ratio testing of PE/fly-ash composites (See Experimental Section 4.6.4 for full details of the test and sample dimensions)

Poisson's ratio tests (in tension) of the PE/fly-ash composite safety step materials were carried out in accordance with ASTM D638-10 using an Instron 5982 tensometer fitted with a 100 kN load cell. Axial and transverse strains were measured using an Instron AVE 2663-821 video extensometer at 10 samples per second. After collection of the data, the numerical axial and transverse strain data points (in % format) were exported to MS Excel for further processing.

Example of Raw Data and Calculated Parameters

Due to the strong consistency in behaviour between the tensile specimens of each PE/fly-ash composite material tested, it was decided to calculate an average axial and transverse % strain response up to the yield point for the latter materials. An average Poisson's ratio was then calculated with the first 100 average transverse and axial % strain values using Equation 20.

Appendix 2 (Continued)

Standard deviations were also calculated. The latter effectively resulted in a value of Poisson's ratio close to or at the yield point, rather than within the elastic region (see Figure 15 in Experimental Section 4.6.2). Table 31 shows how the raw data translated into Poisson's ratio values.

Table 31. Tensile test data and consequent calculation of Poisson's ratio.

Time (s)	Average Load (N)	Average Video Axial Strain (%)	Average Video Transverse Strain (%)	Average Poissons Ratio
0	3.95	0.0485	0.0012	0.0251
0.1	4.55	0.0560	0.0007	0.0117
0.2	12.47	0.1535	0.0090	0.0588
0.3	17.75	0.2184	0.0228	0.1043
0.4	22.63	0.2786	0.0347	0.1247
0.5	27.22	0.3351	0.0434	0.1295
0.6	31.92	0.3930	0.0539	0.1371
0.7	36.71	0.4519	0.0599	0.1325
0.8	41.39	0.5095	0.0714	0.1402
0.9	45.78	0.5635	0.0806	0.1431
1	49.94	0.6148	0.0890	0.1448

Safety Step Compression Testing

Full details of the compression test equipment, methods and sample dimensions are provided in Experimental Section 4.6.6 of this thesis for all safety steps. Both left and right sidewall deflections during the tests were measured and averaged at 20 N intervals using two Mitutoyo dial test indicators, standard deviation was also calculated; an example of this is in Table 32.

Appendix 2 (Continued)

Table 32. An example of the sidewall deflection measurements from safety steps during a compression test.

Step Sidewall Deflection				
Force (N)	Left (mm)	Right (mm)	Average (mm)	Standard Deviation (mm)
0	0.00	0.00	0.00	0.00
20	0.06	0.08	0.07	0.01
40	0.14	0.15	0.15	0.01
60	0.20	0.24	0.22	0.03
80	0.29	0.30	0.30	0.01
100	0.36	0.38	0.37	0.01
120	0.43	0.45	0.44	0.01
140	0.49	0.52	0.51	0.02
160	0.57	0.58	0.58	0.01
180	0.64	0.65	0.65	0.01
200	0.71	0.72	0.72	0.01

Charpy impact testing of PE/fly-ash composites (See Experimental Section 4.6.5 for full details of the test and sample dimensions)

8 Samples were tested using a Zwick model 5102 non-instrumented swinging pendulum type impact tester. The span between the sample supports was 40 mm and the samples were nominally 10 x 4 mm in cross section. The most appropriate tup (0.5 J, 1 J, 2 J or 4 J) was selected using a spare test piece. The average free swing energy (E_{free}) of the selected tup was calculated from 8 free swings.

Example of Raw Data and calculated parameters

The impact strength was calculated using Equation 21. An example of how the quoted parameters translated to an impact strength value (in kJ m^{-2}) using equation 21 is available in Table 33.

Appendix 2 (Continued)

Table 33. An example of Charpy impact specimen dimensions and calculated impact energy values.

Specimen	Sample Width (mm)	Sample Thickness (mm)	Cross-Sectional Area (m ²)	Free Swing Energy (J)	Tup (J)
1	10.10	3.75	0.000038	0.08	4
2	10.30	3.63	0.000037	0.08	4
3	10.21	3.69	0.000038	0.08	4
4	10.27	3.65	0.000037	0.08	4
5	10.50	3.70	0.000039	0.08	4
6	10.06	3.93	0.000040	0.08	4
7	10.17	3.80	0.000039	0.08	4
8	10.75	3.74	0.000040	0.08	4
Specimen	Impact Energy (J)	Energy Absorbed (kJ m ⁻²)	Failure Mode	Average Energy Absorbed (kJ m ⁻²)	Standard Deviation Energy Absorbed (kJ m ⁻²)
1	2.07	52.59	Brittle Fracture	52.36	1.53
2	2.06	53.06	Brittle Fracture		
3	2.05	52.24	Brittle Fracture		
4	2.02	51.65	Brittle Fracture		
5	2.12	52.51	Brittle Fracture		
6	2.16	52.61	Brittle Fracture		
7	2.20	54.86	Brittle Fracture		
8	2.06	49.35	Brittle Fracture		

Compression testing of safety step materials (See Experimental Section 4.6.8 for full details of the test and sample dimensions)

Specimens were compression tested using a Hounsfield HK10S tensometer fitted with a 10 kN load cell. Both circular compression platens were 75 mm \varnothing and 25 mm thick. A crosshead speed of 1 mm min⁻¹ was used. The test piece dimensions were 7 mm thick, 13 mm wide and 25 mm high. To ensure the samples remained upright during testing, two samples of the same height were stuck together using double-sided tape which joined the samples with little constraint.

Appendix 2 (Continued)

Example of Raw Data and calculated parameters

The resulting compressive load-deflection data was exported to MS Excel software by Hounsfield's QMAT tensometer software for conversion to stress-strain using Equations 22 and 23. The movement of internal components (such as the crosshead bearings) within the tensometer can constitute significant error during testing; in order to identify and remove this error for the small-scale compression tests (referred to as the machine compliance error) the procedure described in Experimental Section 4.6.8.1 was used. A typical example of the load-deflection data which has been modified to include the machine compliance error and subsequently converted to stress-strain is provided in Table 34.

Table 34. A typical example of load-deflection data from compression tests. The latter have been modified to include the machine compliance error for conversion to stress-strain.

Specimen 1					
13.36 mm Thickness - 18.32 mm Width - 24.55 mm Height					
Original Force-Deflection Curve		Machine Compliance Modified Force-Deflection Curve		Final Stress-Strain Curve	
Compression (mm)	Force (N)	Compression (mm)	Force (N)	Stress (MPa)	Strain
0.013	8	0.009	8	0.033	0.0003
0.025	16	0.017	16	0.065	0.0007
0.038	24	0.026	24	0.098	0.0010
0.050	32	0.034	32	0.131	0.0014
0.063	40	0.043	40	0.163	0.0017
0.075	64	0.043	64	0.261	0.0018
0.088	72	0.052	72	0.294	0.0021
0.100	80	0.060	80	0.327	0.0024
0.113	96	0.065	96	0.392	0.0026
0.125	128	0.061	128	0.523	0.0025

Appendix 3

Table 35. Tensile modulus and stress at yield of LMDPE with the addition of MA-g-LLDPE (dry blended).

MA-g-LLDPE (% wt.)	LMDPE (% wt.)	Tensile Modulus (MPa)	Standard Deviation	Tensile Stress at Yield (MPa)	Standard Deviation
0	100	644.62	24.55	15.37	0.12
7.5	92.5	628.29	23.20	15.19	0.3
15	85	582.81	26	14.53	0.18
25	75	570.9	21.03	14.3	0.09
50	50	485.42	6.56	12.52	0.11
75	25	385.81	12.36	11.74	0.05
100	0	365.59	25.94	10.29	0.25

Table 36. Tensile modulus and stress at yield of HDPE with the addition of MA-g-LLDPE (dry blended).

MA-g-LLDPE (% wt.)	HDPE (% wt.)	Tensile Modulus (MPa)	Standard Deviation	Tensile Stress at Yield (MPa)	Standard Deviation
0	100	1388.89	40.37	24.49	0.13
7.5	92.5	1202.78	27.27	23.35	0.3
15	85	1158.88	120.67	21.78	0.18
25	75	984.22	15.37	20.7	0.23
50	50	727.77	8.49	16.27	0.06
75	2	479.66	7.84	12.43	0.11
100	0	314.01	6.50	9.41	0.05

Table 37. Tensile modulus and stress at yield of HDPE with the addition of MA-g-LLDPE (TSE melt blended).

MA-g-LLDPE (% wt.)	HDPE (% wt.)	Tensile Modulus (MPa)	Standard Deviation	Tensile Stress at Yield (MPa)	Standard Deviation
0	100	1386.81	62.90	25.11	0.86
7.5	92.5	1183.89	32.84	23.19	0.37
15	85	1102.3	50	22.50	0.57
25	75	943.1	39.14	20.35	0.48
50	50	659.64	17.36	15.99	0.27
75	25	490.73	23.77	12.96	0.46
100	0	305.51	137.46	9.41	0.20

Appendix 3 (Continued)

Table 38. Tensile modulus and stress at yield of fly-ash-cenosphere PE composites (50 % vol.)

MA-g-LLDPE/LMDPE (% vol.)	Fly-ash (of 50 % vol.)	Cenospheres (of 50 % vol.)	Tensile Modulus (MPa)	Standard Deviation	Tensile Stress at Yield (MPa)	Standard Deviation
100	0	0	567.4	12.8	14.85	0.32
50	0	100	1902.43	23.51	10.23	0.04
50	12.50	87.50	2020.47	174.37	11.64	0.27
50	25	75	1924.69	196.25	12.85	0.25
50	37.50	62.50	1923.51	88.11	13.26	0.16
50	50	50	1922.51	85.51	14.17	0.13
50	62.50	37.50	2110.86	41.5	13.27	0.04
50	75	25	2175.38	174.06	13.84	0.44
50	87.50	12.50	2274.83	212.28	15.65	0.57
50	100%	0	2234.49	89.94	19.15	0.29

Table 39. Charpy impact test results for TSE melt blended maleanised PE/ fly-ash composites.

Maleanised PE (% wt.)	Fly-ash (% wt.)	Average Energy Absorbed (kJ m ⁻²)	Standard Deviation
100	0	57.8	1.46
75	25	64.76	1.82
50	50	74.3	8.24
40	60	40.39	3.86
30	70	24.66	1.42
25	75	15.18	1.02

Table 40. Charpy impact test results for TSE melt blended analogue PE/fly-ash composites

Analogue PE (% wt.)	Fly-ash (% wt.)	Average Energy Absorbed (kJ m ⁻²)	Standard Deviation
100	0	55.54	1.33
75	25	59.79	0.52
50	50	59.78	0.91
40	60	56.66	3.2
30	70	5.57	0.46
25	75	3.48	0.20

Appendix 4

Differential scanning calorimetry (*See Experimental Section 4.9 for full details of the analysis procedure*)

DSC was carried out on the particulate-filled PE and unfilled PE materials. Sample mass was typically between 4 and 10 mg. The crystalline content of unfilled PE materials was determined using Equation 26. For PE/filler composites, crystallinity content was also calculated using Equation 25. However, Equation 26 was used to calculate ΔH_f for input into Equation 25. The following heat – hold – cool – heat cycle was used:

- Heat from 20 °C to 240 °C at 20 °C min⁻¹
- Hold at 240 °C for 5 minutes
- Cool from 240 °C to 20 °C at 20 °C min⁻¹
- Hold at 20 °C for 2 minutes
- Heat from 20 °C to 240 °C at 20 °C min⁻¹

Samples were heated in a nitrogen atmosphere (flow rate 30 cm³ min⁻¹). The following parameters were recorded during DSC:

1st Heat

- Onset of melting temperature
- Peak melting temperature
- Melting temperature range
- Heat of fusion ΔH_f (for calculation of crystalline content. The samples were held at 240 °C for five minutes to ensure complete melting and total eradication of previous thermal history)

Cool from melt

- Onset of crystallisation temperature
- Crystallisation exotherm peak temperature
- Crystallisation temperature range
- Heat of crystallisation (for calculation of crystalline content obtained during controlled crystallisation)

2nd Heat

- The same parameters as recorded during the 1st heat were recorded

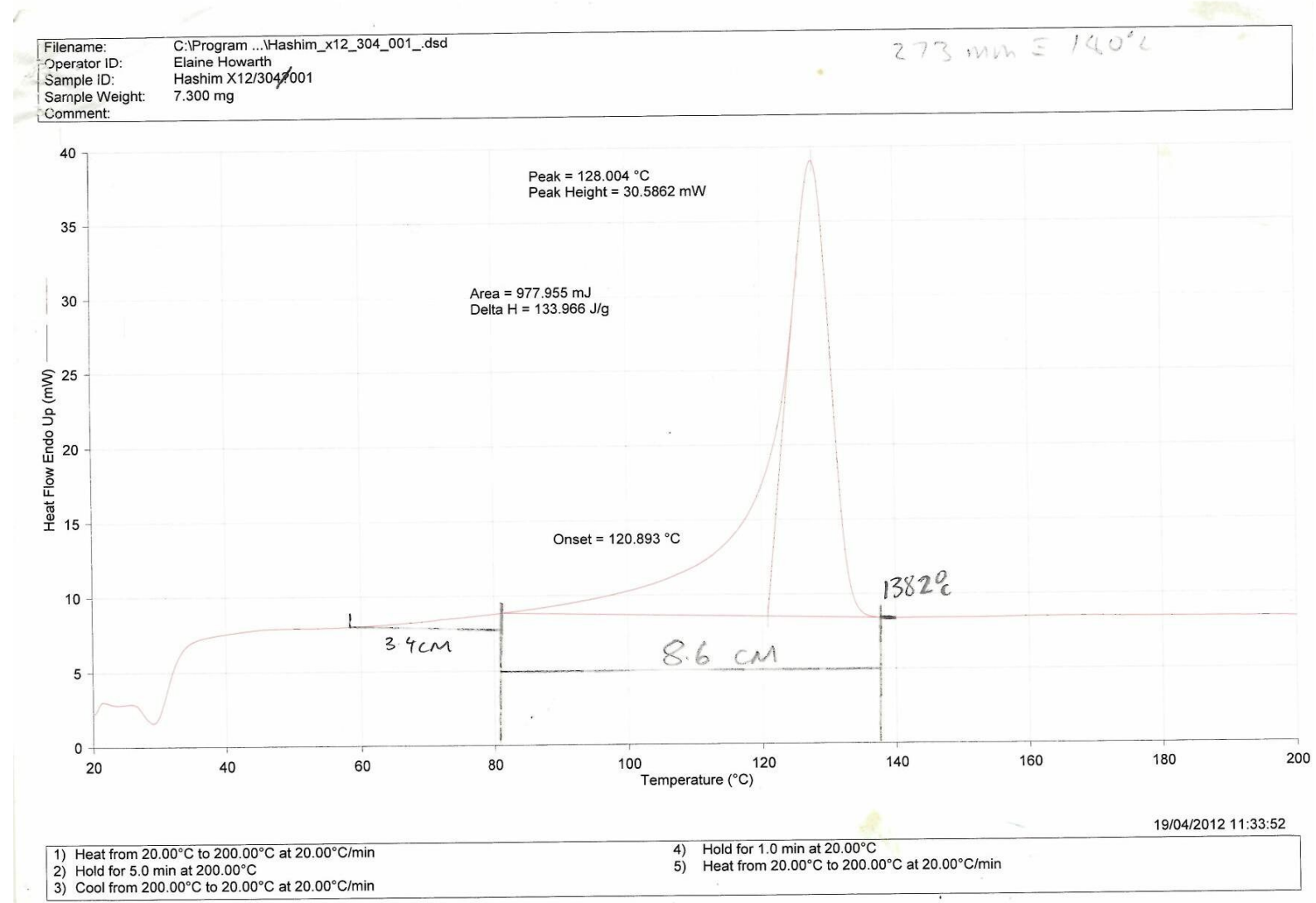


Figure 113. DSC Example Trace – First Heat (for determination of the specimens melting characteristics in its as-moulded component)

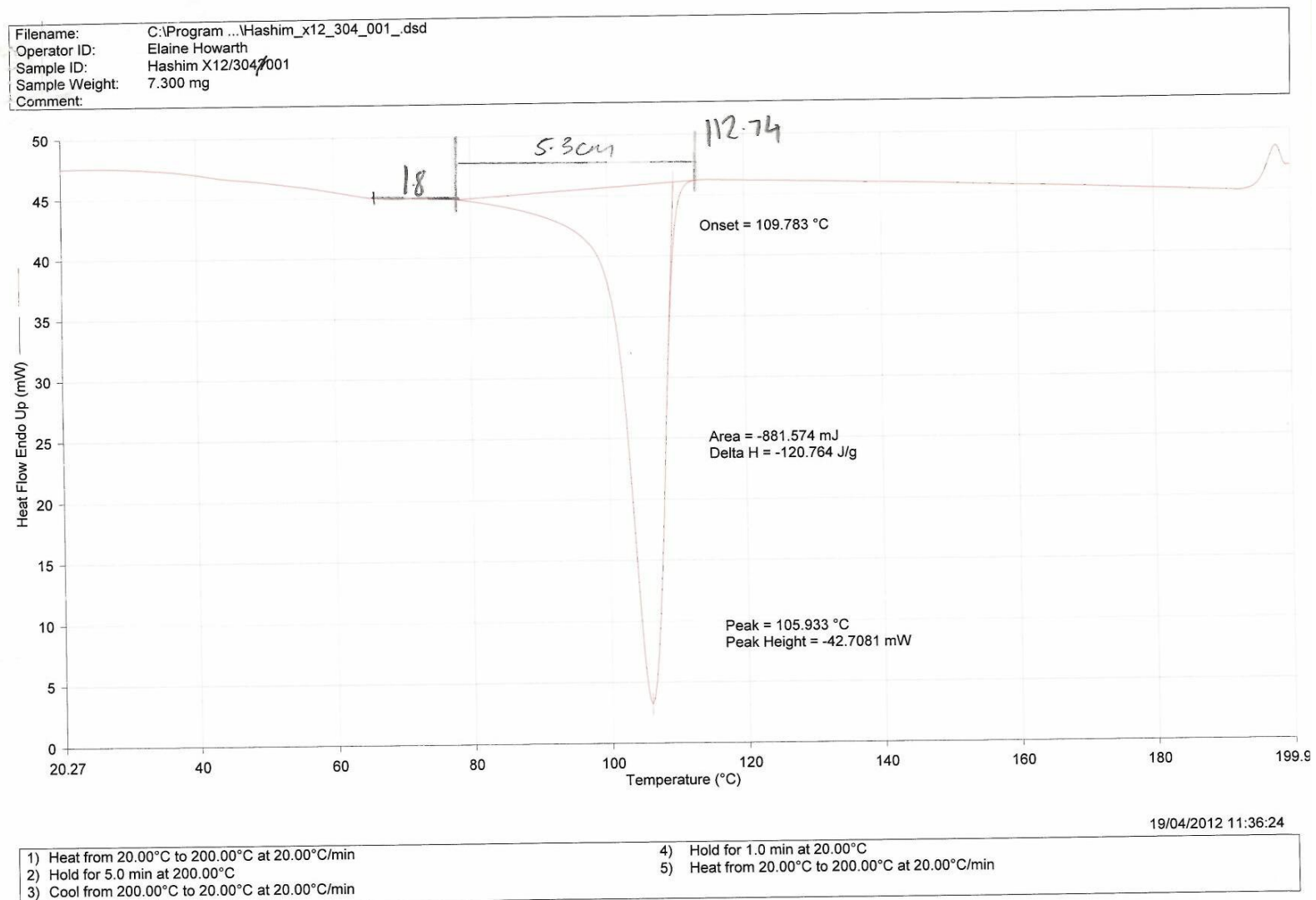


Figure 114. DSC Example Trace – Cool (to provide controlled crystallisation)

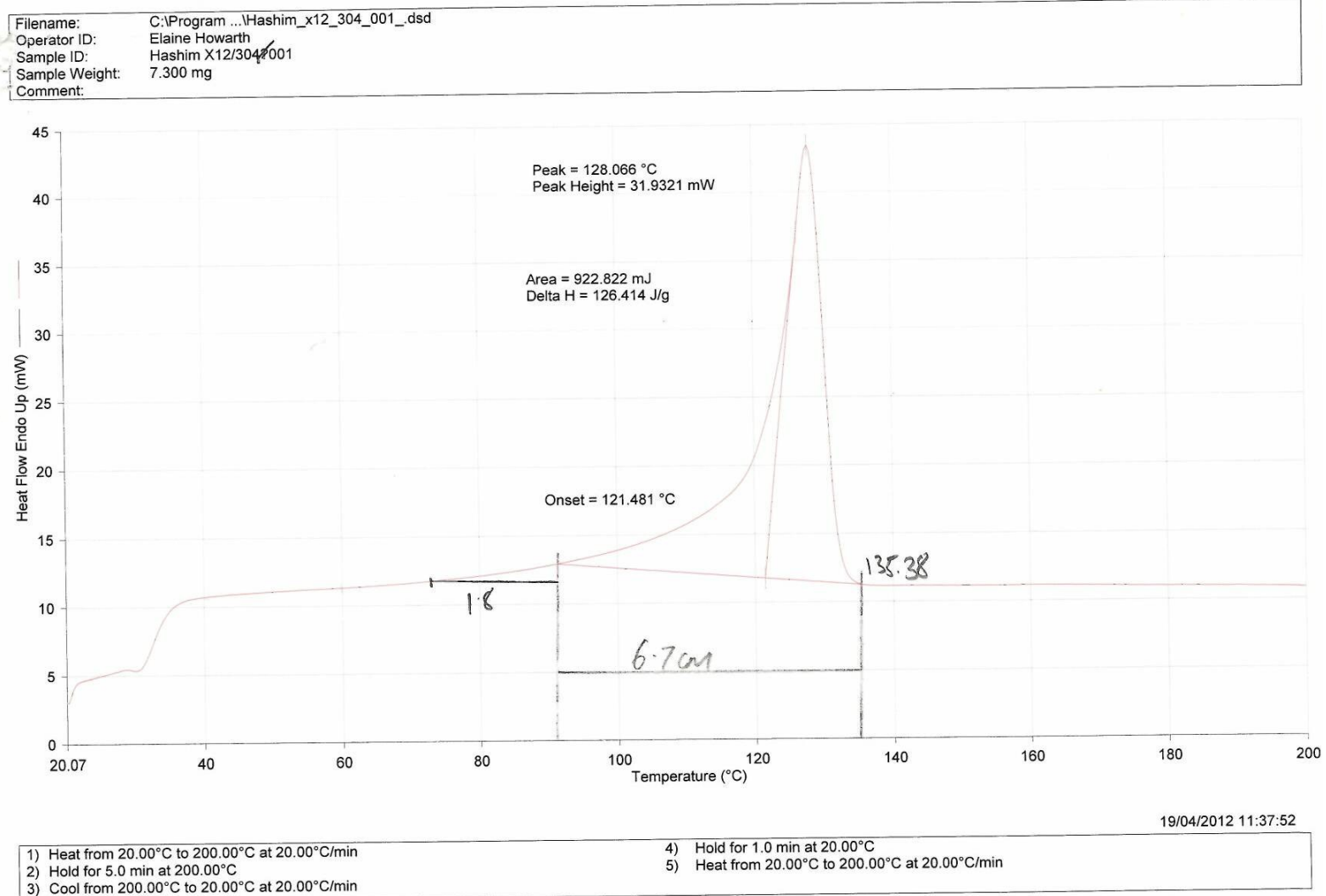


Figure 115. DSC Example Trace – Second Heat (to examine the melting of crystal structures formed because of controlled crystallisation)

Appendix 4 (Continued)

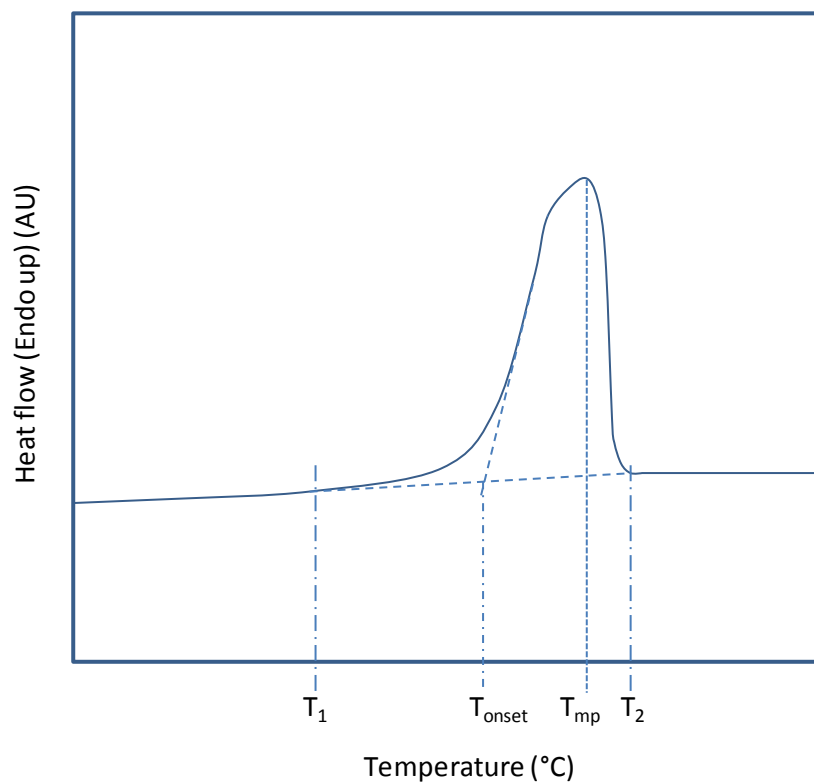


Figure 116. Schematic DSC trace showing key parameters obtained - heating data

- The heat of fusion (ΔH_f) is the area under the curve with integration limits and baseline defined by T_1 and T_2 .
- T_{mp} is the peak melting temperature
- T_{onset} is the onset of melting temperature
- Melting temperature range = $T_2 - T_1$

Appendix 4 (Continued)

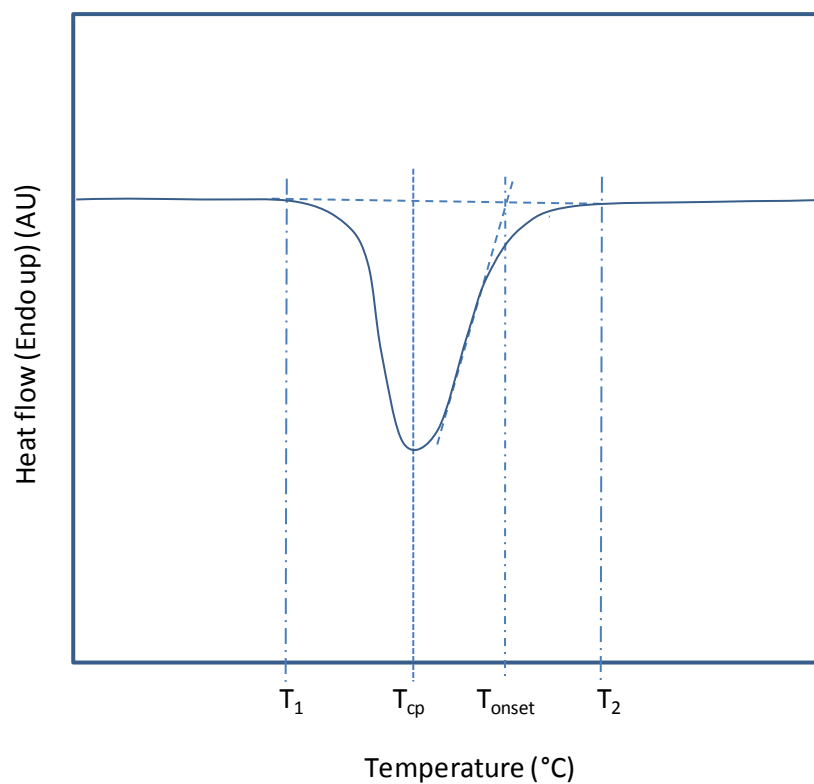


Figure 117. Schematic DSC trace showing key parameters obtained - cooling data

- The heat of crystallisation (ΔH_c) is the area under the curve with integration limits and baseline defined by T_1 and T_2 .
- T_{cp} is the peak crystallisation temperature
- T_{onset} is the onset of crystallisation temperature
- Crystallisation temperature range = $T_2 - T_1$

Appendix 4 (Continued)

DSC Data – 1st Heat

Table 41. Combinations of MA-g-LLDPE with LMDPE (dry blended).

Specimen	MA-g-LLDPE (% wt.)	LMDPE (% wt.)
1	0	100
2	7.5	92.5
3	15	85
4	25	75
5	50	50
6	75	25
7	100	0

Table 42. DSC data for the materials specified in Table 41 – first heat

Specimen	Heat of Fusion (J g ⁻¹)	% Crystallinity	Onset Temperature (°C)	Peak Melting Temperature (°C)	Melting Temperature Range (°C)
1	133.93	48.35	120.89	128.00	79.92
2	142.14	51.31	120.99	135.67	86.58
3	149.84	54.09	124.15	132.67	67.93
4	134.38	48.51	119.32	131.00	72.93
5	125.71	45.38	119.04	127.34	79.25
6	99.01	35.74	116.51	126.74	51.28
7	90.98	32.84	112.48	125.00	65.60

Appendix 4 (Continued)

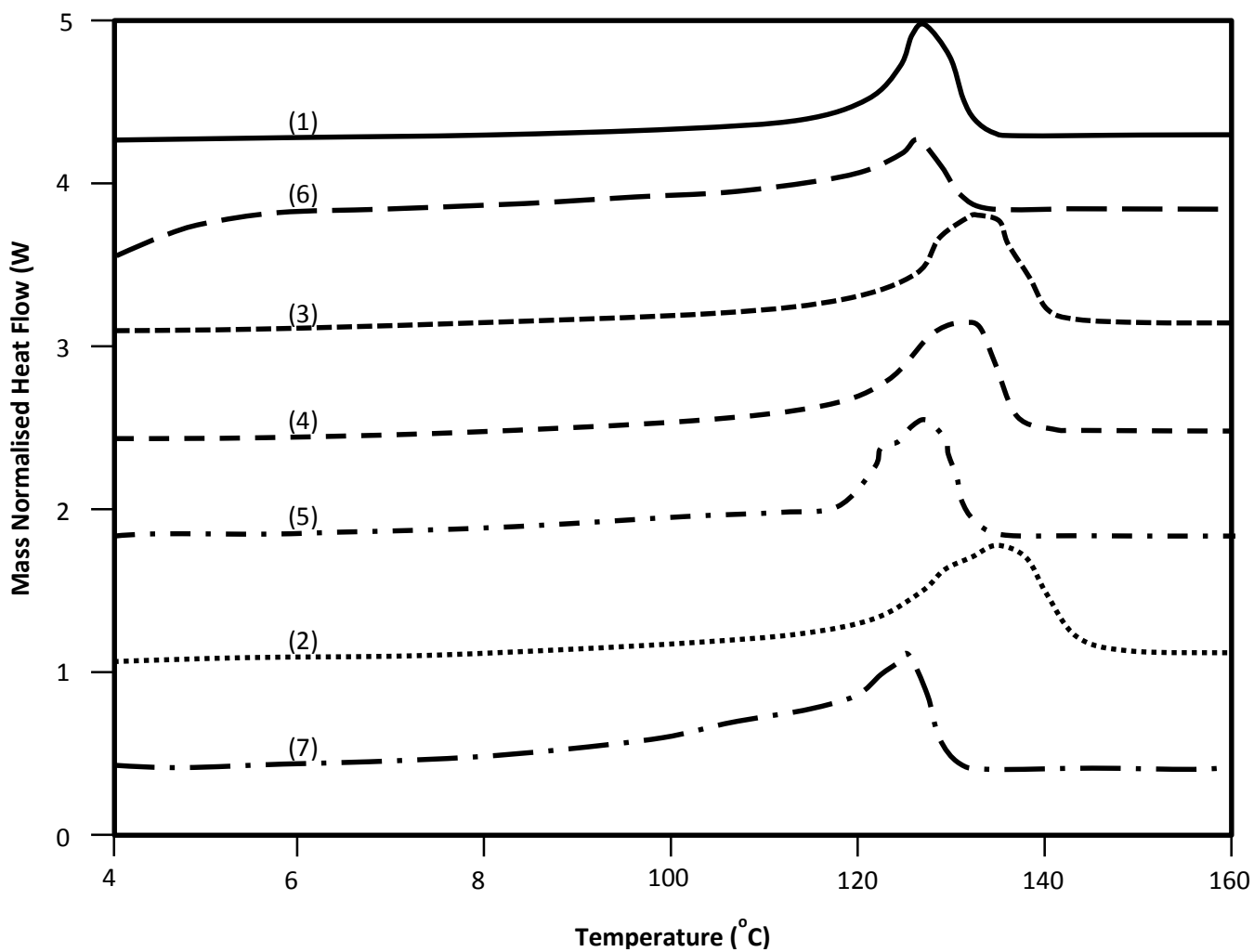


Figure 118. DSC thermogramme for materials and data specified in Table 41 and 42 – first heat

Appendix 4 (Continued)

Table 43. Combinations of MA-g-LLDPE with HDPE (dry blended).

Specimen	MA-g-LLDPE (% wt.)	HDPE (% wt.)
1	0	100
2	7.5	92.5
3	15	85
4	25	75
5	50	50
6	75	25
7	100	0

Table 44. DSC data for the materials specified in Table 43 – first heat

Specimen	Heat of Fusion (J g ⁻¹)	% Crystallinity	Onset Temperature (°C)	Peak Melting Temperature (°C)	Melting Temperature Range (°C)
1	185.52	66.98	125.86	135.67	55.94
2	170.31	61.48	126.57	132.67	51.28
3	166.08	59.96	125.36	133.00	59.94
4	153.39	55.37	125.26	133.33	65.27
5	155.61	56.18	121.87	129.33	77.26
6	135.94	49.07	119.87	128.00	81.25
7	115.72	41.77	117.39	128.00	84.58

Appendix 4 (Continued)

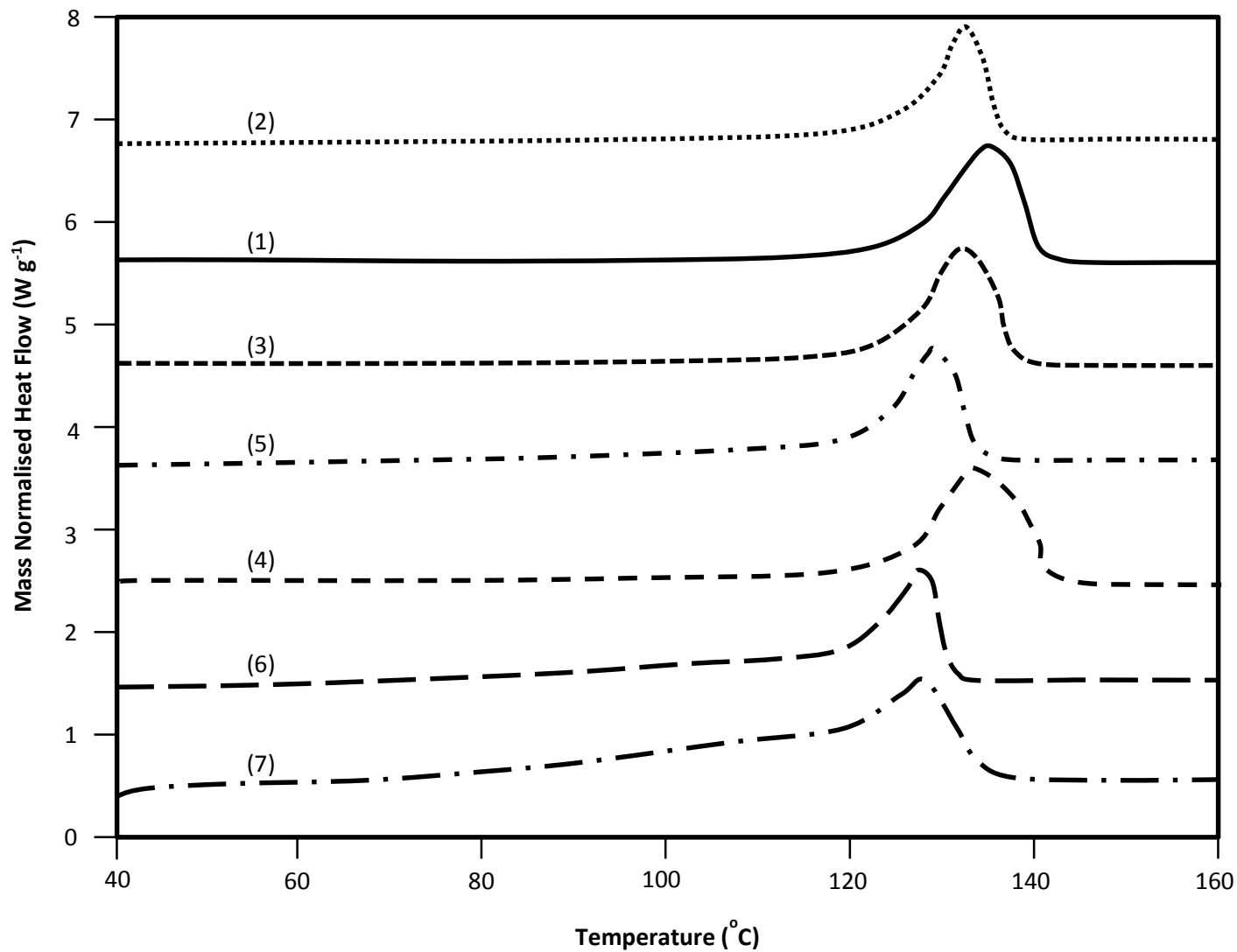


Figure 119. DSC thermogramme for materials and data specified in Table 43 and 44 – first heat

Appendix 4 (Continued)

Table 45. Combinations of MA-g-LLDPE with HDPE (TSE compounded).

Specimen	MA-g-LLDPE (% wt.)	HDPE (% wt.)
1	0	100
2	7.5	92.5
3	15	85
4	25	75
5	50	50
6	75	25
7	100	0

Table 46. DSC data for the materials specified in Table 45 – first heat

Specimen	Heat of Fusion (J g ⁻¹)	% Crystallinity	Onset Temperature (°C)	Peak Melting Temperature (°C)	Melting Temperature Range (°C)
1	182.93	66.04	130.24	149.00	59.27
2	185.60	67.00	126.83	137.67	89.24
3	177.98	64.25	125.48	134.00	77.92
4	164.75	59.48	126.08	135.67	51.28
5	116.42	42.03	123.22	132.34	56.28
6	113.53	40.99	120.63	132.00	65.93
7	83.75	30.23	113.50	124.34	67.27

Appendix 4 (Continued)

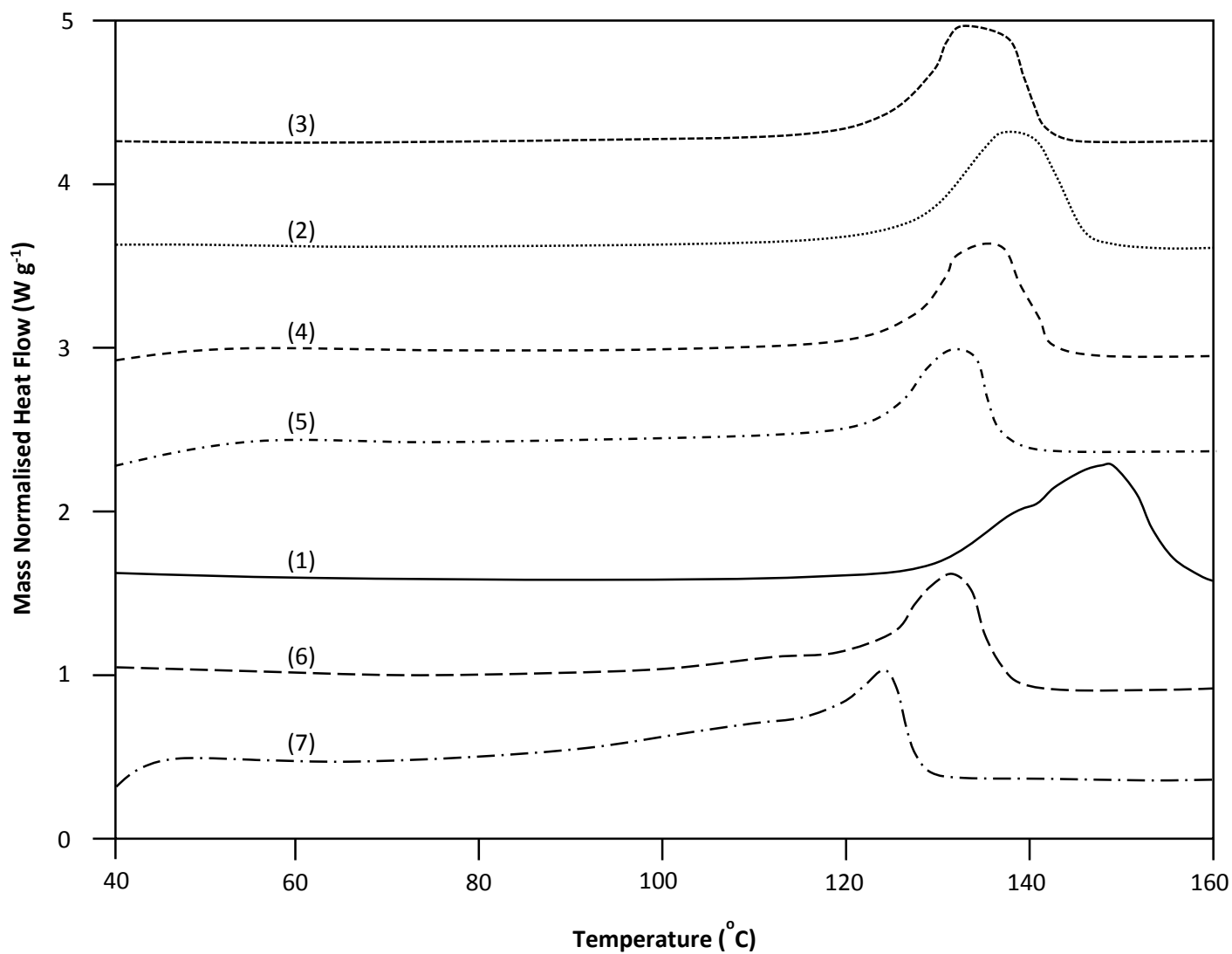


Figure 120. DSC thermogramme for materials and data specified in Table 45 and 46 – first heat

Appendix 4 (Continued)

Table 47. PE/fly-ash formulations.

Specimen	MA-g-LLDPE/LMDPE (% wt.)	Fly-ash (% vol.)	Fly-ash (% wt.)
1	50	28.8	50
2	75	14.4	25
3	87.5	7.2	12.5
4	100	0	0

Table 48. DSC data for the materials specified in Table 47 – first heat

Specimen	Heat of Fusion (J g ⁻¹)	% Crystallinity	Onset Temperature (°C)	Peak Melting Temperature (°C)	Melting Temperature Range (°C)
1	122.28	44.14	116.90	127.00	55.28
2	135.58	48.95	117.70	127.67	69.60
3	130.39	47.07	118.34	129.67	59.94
4	129.89	46.89	118.37	124.33	43.29

Appendix 4 (Continued)

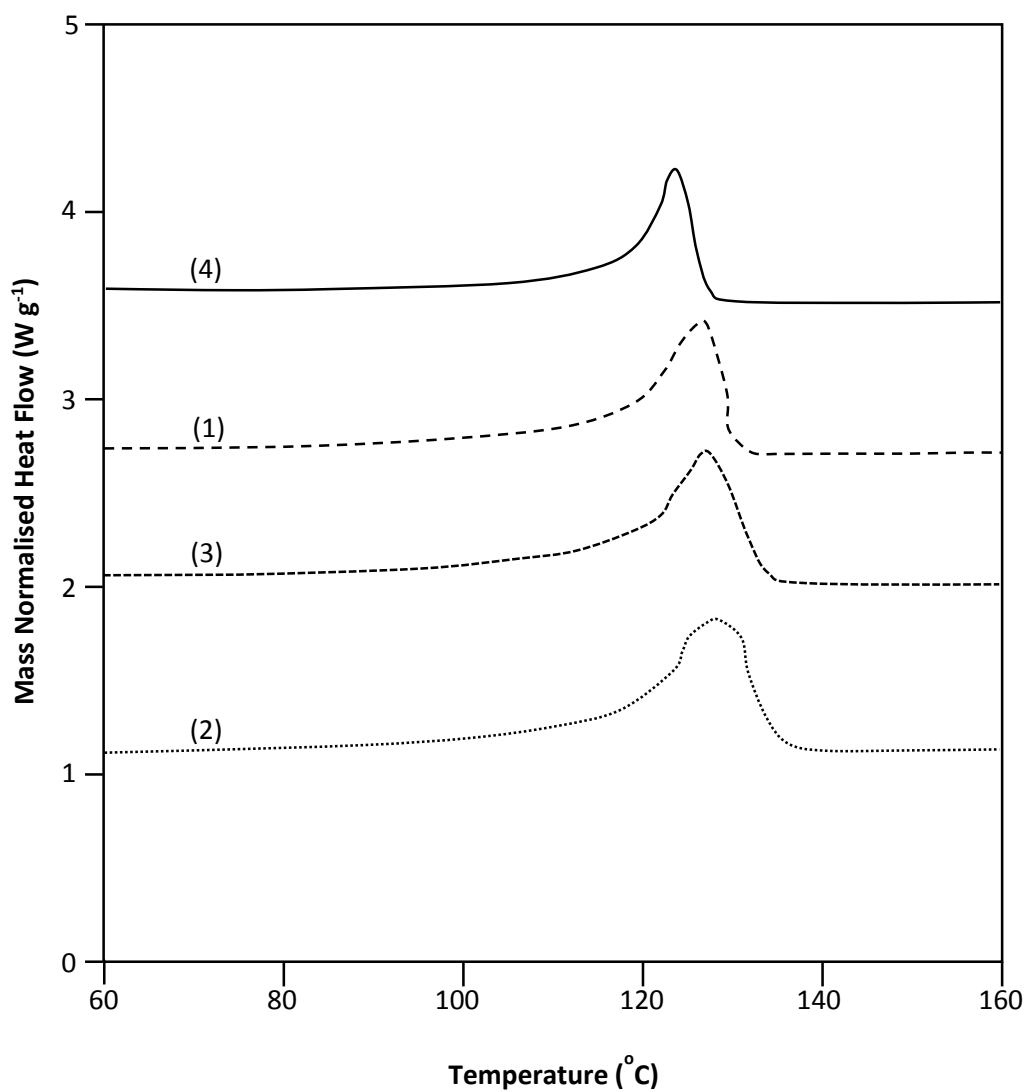


Figure 121. DSC thermogramme for materials and data specified in Table 47 and 48 – first heat.

Appendix 4 (Continued)

DSC Data – Cool from Melt

Table 49. DSC data for the materials specified in Table 41 – cool from melt

Specimen	Heat of Crystallisation (J g ⁻¹)	% Crystallinity	Onset Crystallisation Temperature (°C)	Crystallisation Exotherm Peak Temperature (°C)	Crystallisation Temperature Range (°C)
1	127.59	46.06	109.78	105.93	47.29
2	130.45	47.09	110.45	104.93	52.61
3	136.57	49.30	110.84	107.60	51.28
4	120.64	43.55	110.69	107.60	54.61
5	113.68	41.04	109.64	106.27	57.94
6	98.51	35.56	107.82	104.60	56.28
7	77.59	28.01	106.08	102.93	49.62

Appendix 4 (Continued)

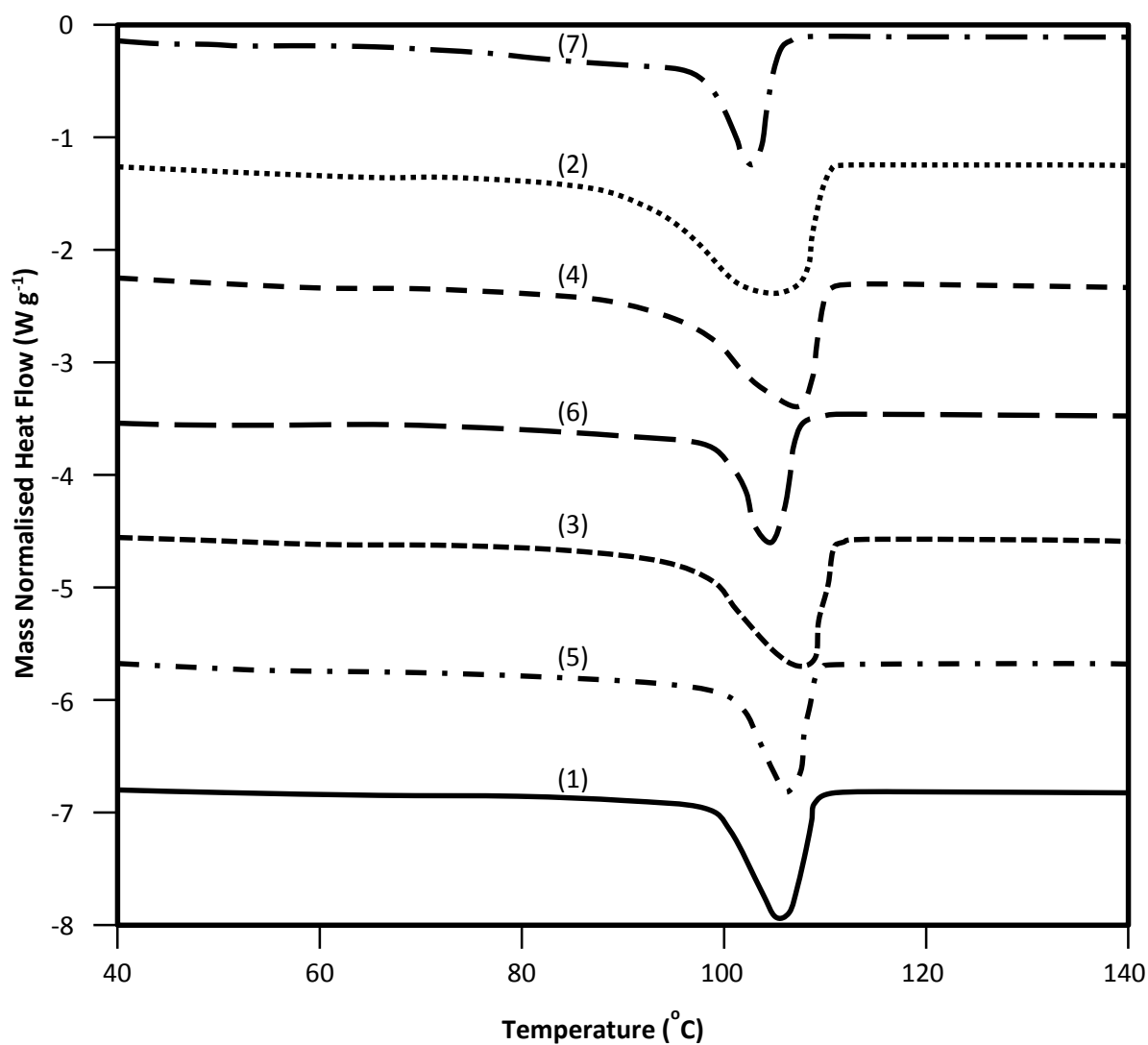


Figure 122. DSC thermogramme for materials and data specified in Table 41 and 49 – cool from melt

Appendix 4 (Continued)

Table 50. DSC data for the materials specified in Table 43 – cool from melt

Specimen	Heat of Crystallisation (J g⁻¹)	% Crystallinity	Onset Crystallisation Temperature (°C)	Crystallisation Exotherm Peak Temperature (°C)	Crystallisation Temperature Range (°C)
1	197.76	71.39	114.34	109.60	31.30
2	170.51	61.56	114.63	111.27	32.63
3	172.09	62.13	114.45	110.60	34.97
4	149.10	53.83	113.91	109.60	34.63
5	132.47	47.82	112.71	109.27	41.96
6	108.87	39.30	110.71	107.60	47.62
7	86.53	31.24	105.86	102.27	48.95

Appendix 4 (Continued)

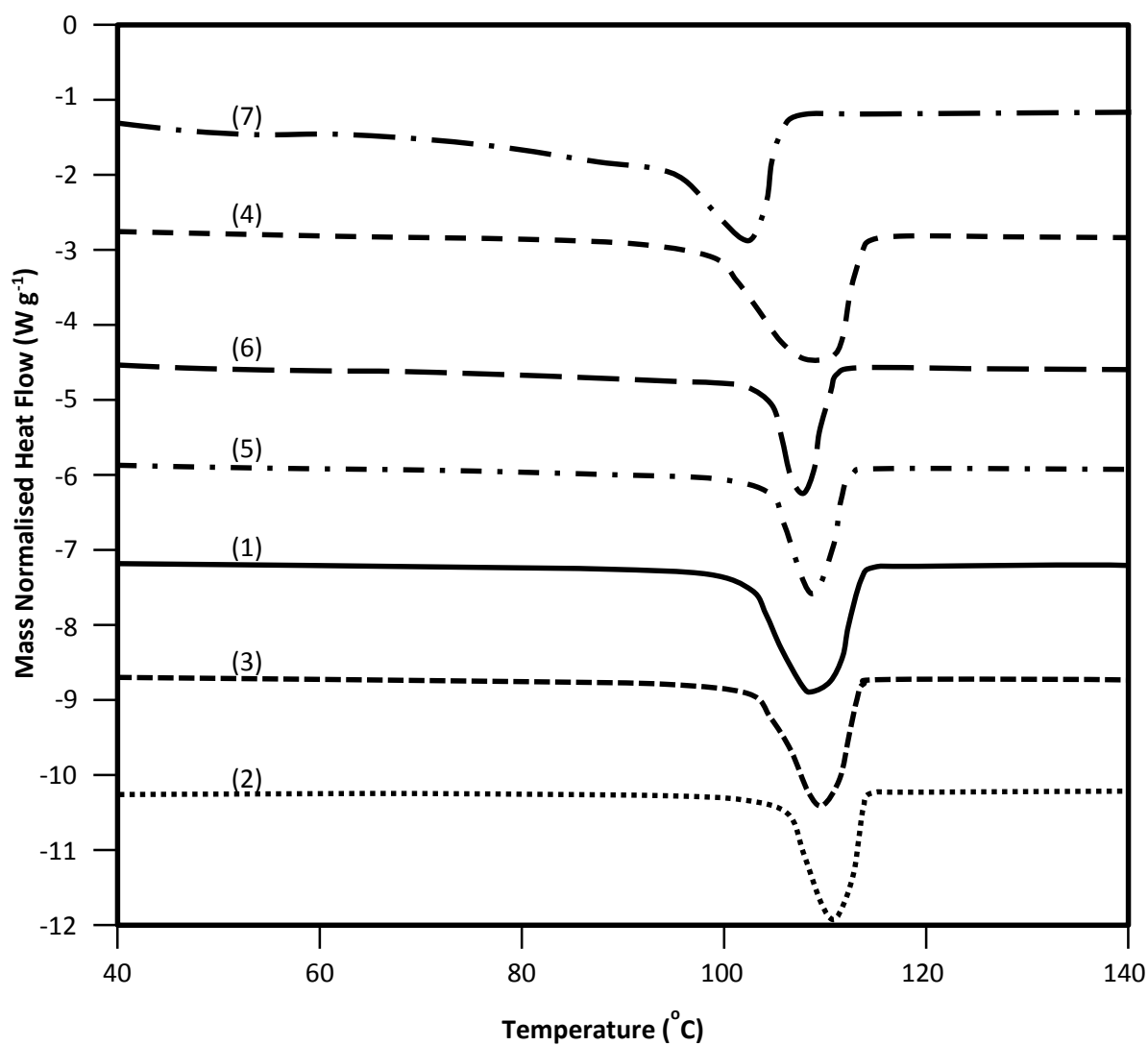


Figure 123. DSC thermogramme for materials and data specified in Table 43 and 50 – cool from melt

Appendix 4 (Continued)

Table 51. DSC data for the materials specified in Table 45 – cool from melt

Specimen	Heat of Crystallisation (J g⁻¹)	% Crystallinity	Onset Crystallisation Temperature (°C)	Crystallisation Exotherm Peak Temperature (°C)	Crystallisation Temperature Range (°C)
1	187.41	67.66	114.16	106.93	37.30
2	182.06	65.72	114.03	107.60	37.30
3	287.02	103.62	114.06	108.60	29.97
4	161.28	58.22	113.51	107.93	38.63
5	138.65	50.05	111.80	107.60	46.62
6	110.83	40.01	109.65	105.93	52.61
7	70.47	25.44	104.92	101.60	47.29

Appendix 4 (Continued)

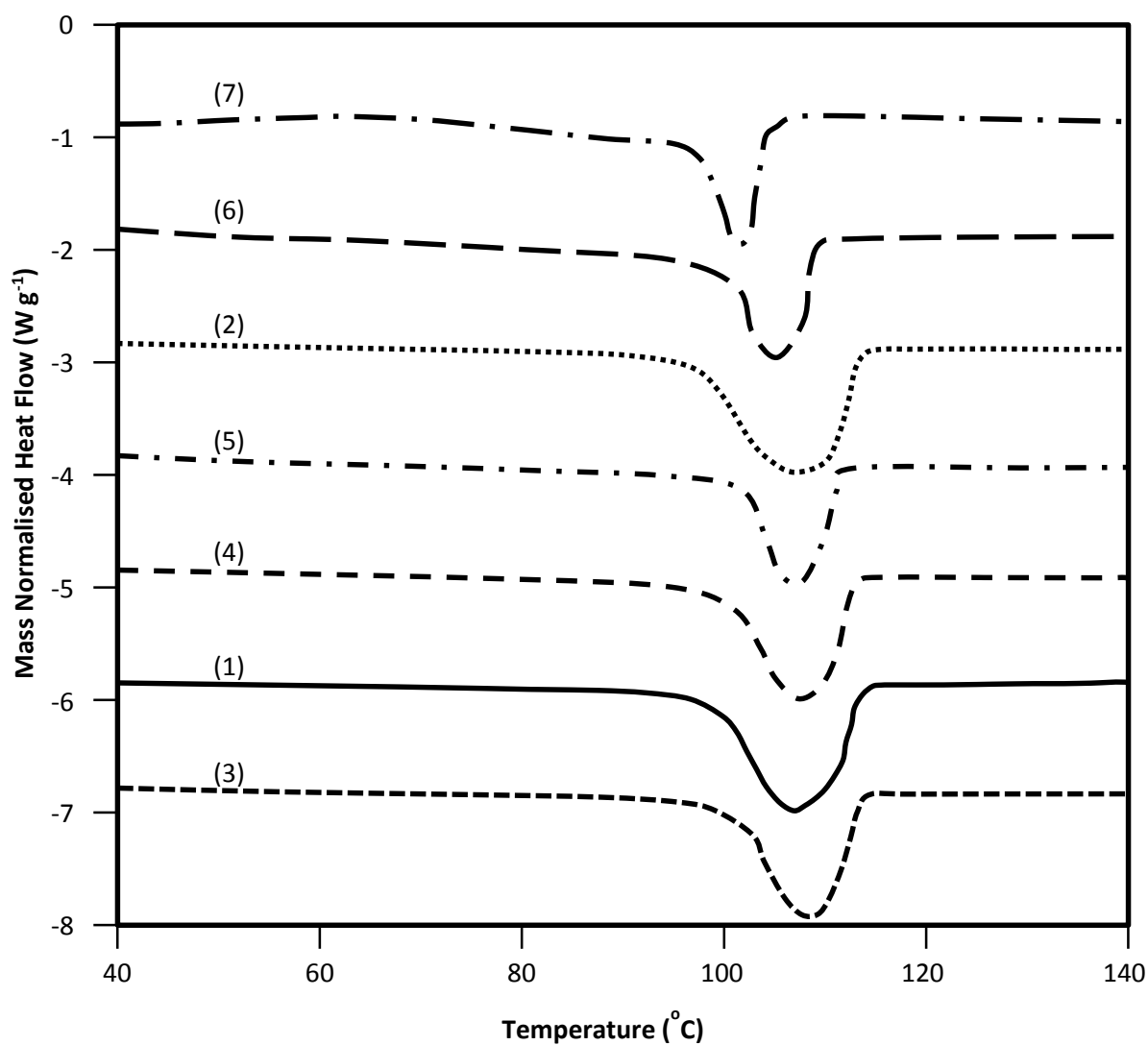


Figure 124. DSC thermogramme for materials and data specified in Table 45 and 51 – cool from melt

Appendix 4 (Continued)

Table 52. DSC data for the materials specified in Table 47 – cool from melt

Specimen	Heat of Crystallisation (J g⁻¹)	% Crystallinity	Onset Crystallisation Temperature (°C)	Crystallisation Exotherm Peak Temperature (°C)	Crystallisation Temperature Range (°C)
1	124.98	45.12	109.06	106.27	39.29
2	116.81	42.17	108.90	104.60	34.63
3	181.94	65.68	109.68	104.27	61.94
4	216.06	78.00	111.61	108.60	65.93

Appendix 4 (Continued)

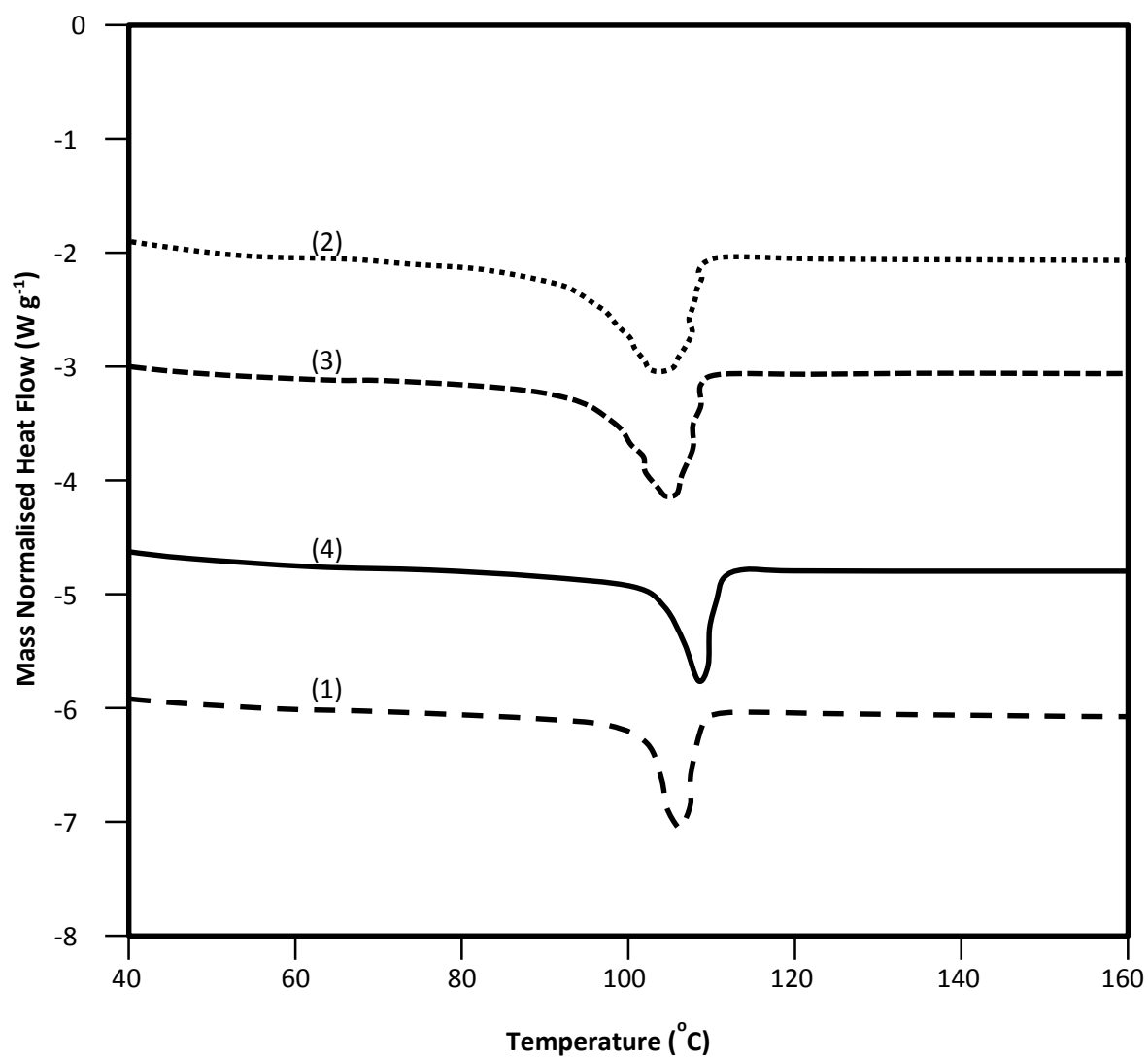


Figure 125. DSC thermogramme for materials and data specified in Table 47 and 52 – cool from melt

Appendix 4 (Continued)

DSC Data – 2nd Heat

Table 53. DSC data for the materials specified in Table 41 – second heat

Specimen	Heat of Fusion (J g⁻¹)	% Crystallinity	Onset Temperature (°C)	Peak Melting Temperature (°C)	Melting Temperature Range (°C)
1	141.26	51.00	121.48	128.07	56.61
2	141.36	51.03	118.76	131.73	74.26
3	155.85	56.26	118.84	127.73	76.92
4	128.57	46.42	119.64	129.07	68.27
5	128.73	46.47	119.98	126.73	68.93
6	103.49	37.36	120.83	126.40	61.61
7	82.17	29.66	117.25	125.07	64.27

Appendix 4 (Continued)

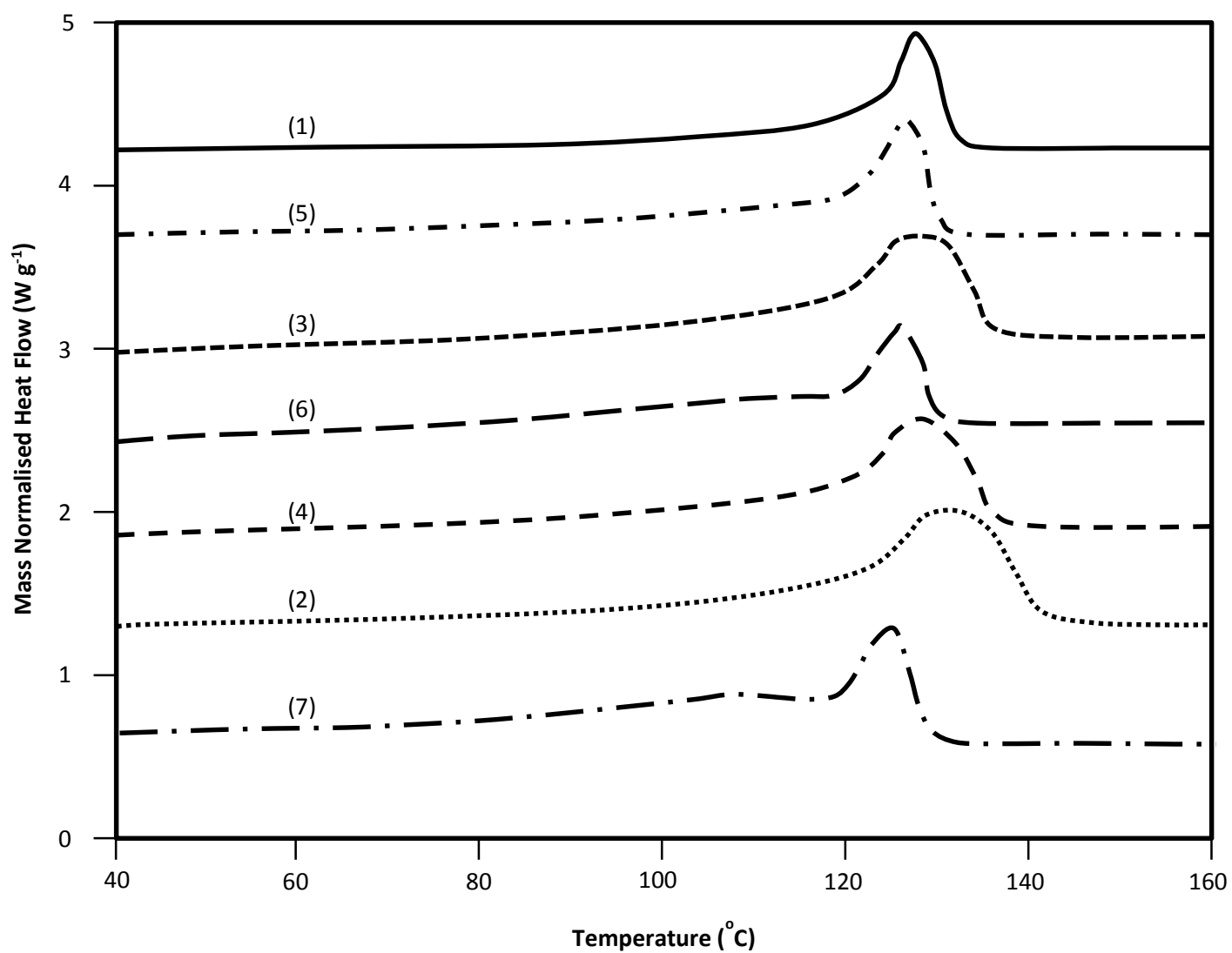


Figure 126. DSC thermogramme for materials and data specified in Table 41 and 53 – second heat

Appendix 4 (Continued)

Table 54. DSC data for the materials specified in Table 43 – second heat

Specimen	Heat of Fusion (J g⁻¹)	% Crystallinity	Onset Temperature (°C)	Peak Melting Temperature (°C)	Melting Temperature Range (°C)
1	202.65	73.16	126.66	136.73	59.94
2	187.88	67.83	125.95	133.07	52.28
3	190.91	68.92	125.60	134.40	71.60
4	170.53	61.56	123.82	134.40	78.59
5	159.79	57.69	123.48	130.07	77.26
6	131.33	47.41	121.69	127.73	74.59
7	114.25	41.25	114.95	126.40	81.92

Appendix 4 (Continued)

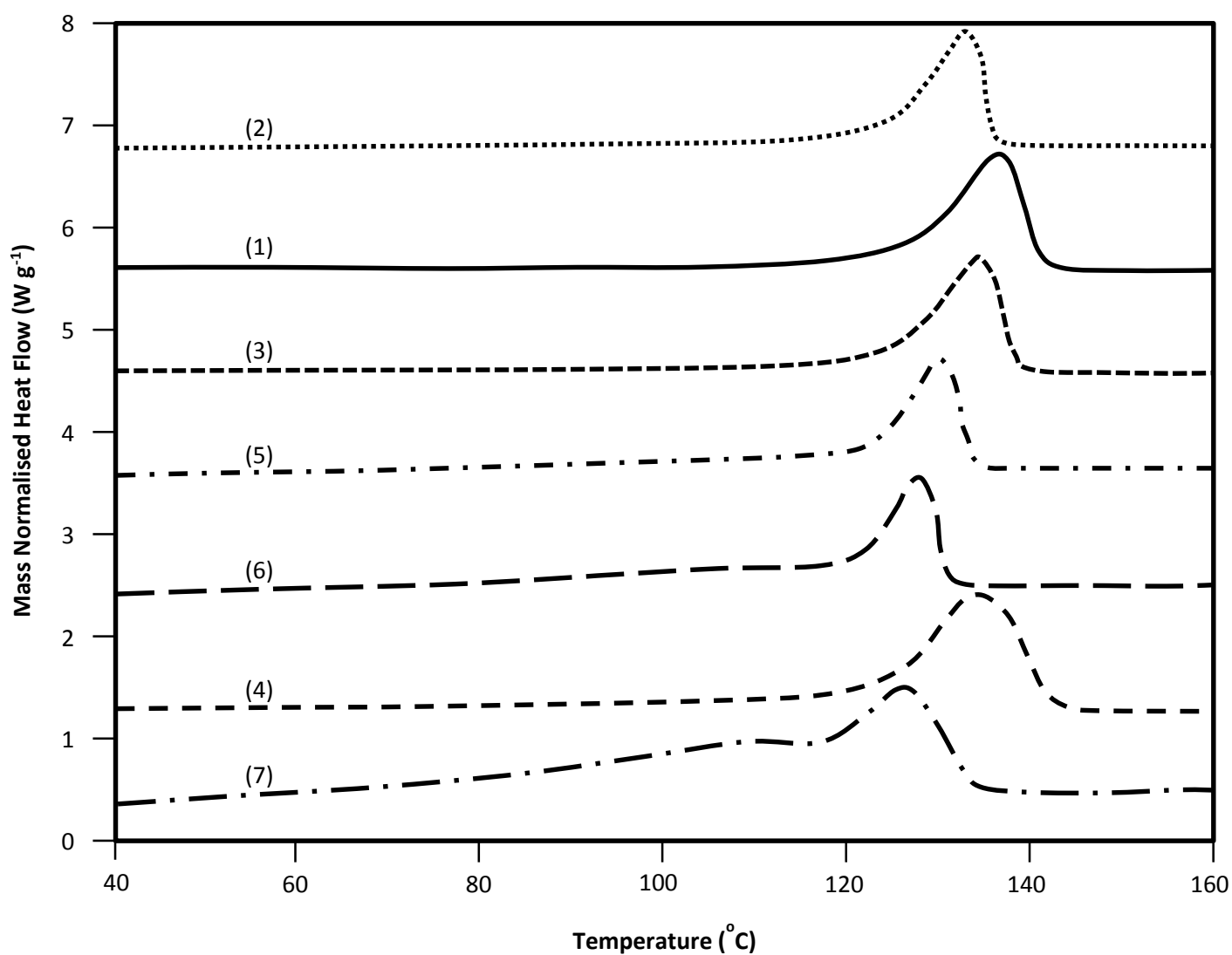


Figure 127. DSC thermogramme for materials and data specified in Table 43 and 54 – second heat

Appendix 4 (Continued)**Table 55.** DSC data for the materials specified in Table 45 – second heat

Specimen	Heat of Fusion (J g⁻¹)	% Crystallinity	Onset Temperature (°C)	Peak Melting Temperature (°C)	Melting Temperature Range (°C)
1	193.70	69.93	124.82	137.40	63.94
2	203.09	73.32	126.33	137.73	83.25
3	200.97	72.55	124.93	135.40	65.93
4	170.12	61.42	124.46	137.07	75.92
5	130.90	47.26	123.54	132.40	71.93
6	97.31	35.13	124.10	130.40	81.92
7	78.04	28.17	116.51	124.40	60.61

Appendix 4 (Continued)

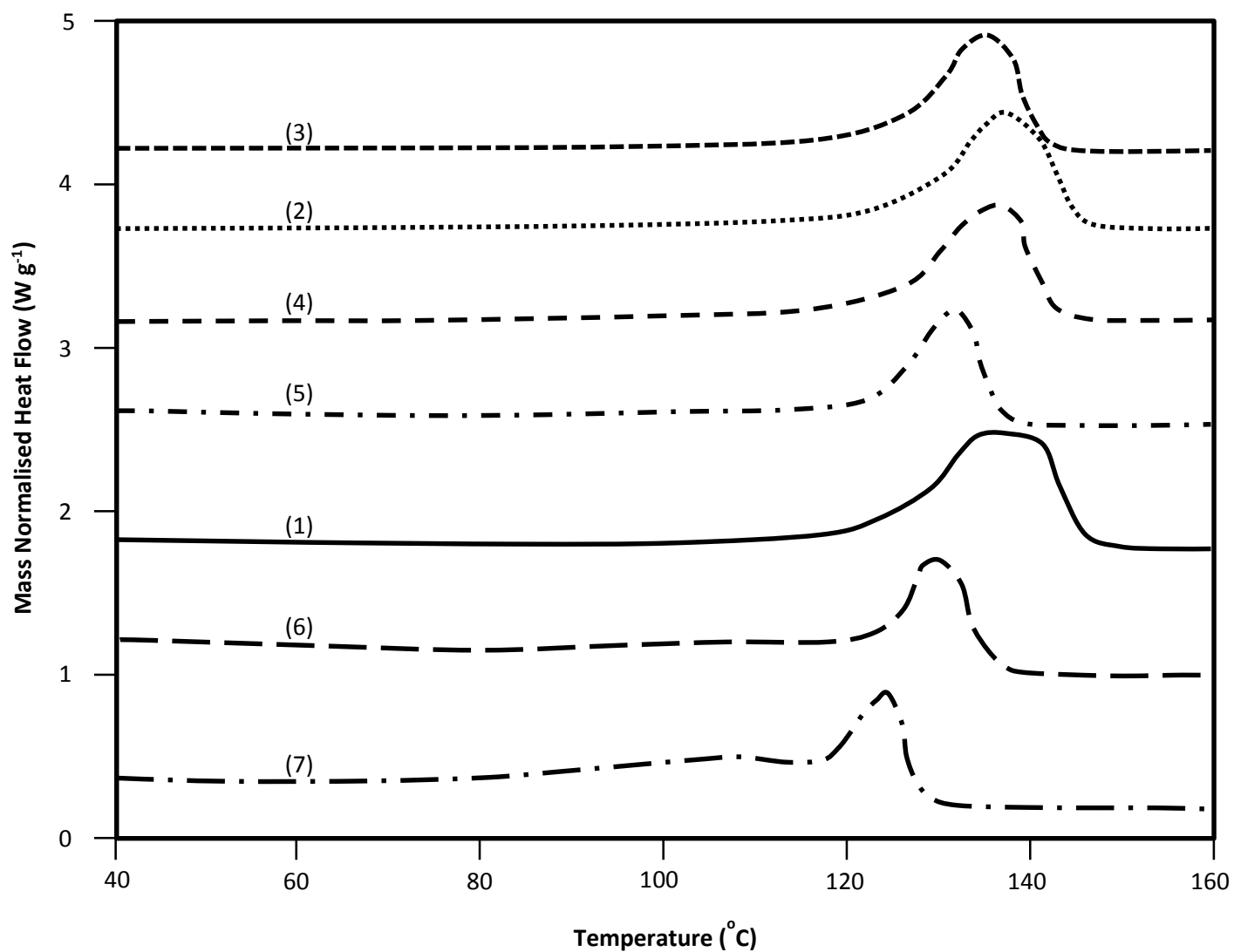


Figure 128. DSC thermogramme for materials and data specified in Table 45 and 55 – second heat

Appendix 4 (Continued)**Table 56.** DSC data for the materials specified in Table 47 – second heat

Specimen	Heat of Fusion (J g⁻¹)	% Crystallinity	Onset Temperature (°C)	Peak Melting Temperature (°C)	Melting Temperature Range (°C)
1	125.48	45.30	118.29	125.07	51.28
2	134.62	48.60	118.67	127.40	66.60
3	137.01	49.46	118.72	129.07	61.27
4	131.03	47.30	118.72	124.73	53.95

Appendix 4 (Continued)

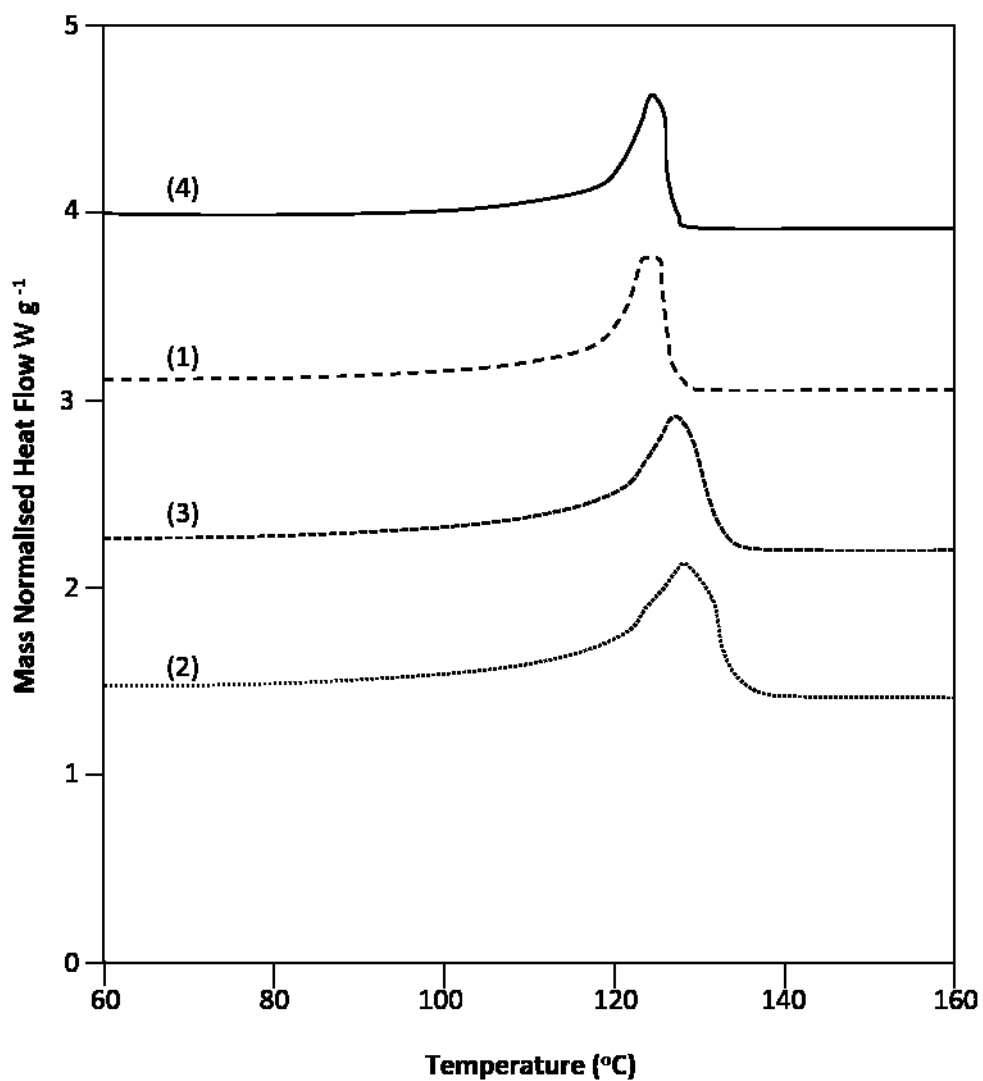


Figure 129. DSC thermogramme for materials and data specified in Table 47 and 56 – second heat

Appendix 5

Data sheets of the polymers used in this PhD study.

Issue number: 1
Issue Date: 28 March 2011



REVOLVE® N-211			
Rotational Moulding	Rotolining applications	M.F.I.	5.0
		Density	0.921

Description

Revolve N-211 is a rotational moulding modified octene polyethylene grade designed to provide metal bonding which makes ideal for rotolining applications.

Features & Benefits
Toughness
Good mouldability
Excellent impact strength
Good chemical resistance

Available as
Natural powder

Physical Properties**	Test Method	Value	Units
MFI	ISO 1133	5.0	g/10min
Density	ISO 1183	0.921	g/cm ³
Tensile Strength @ Yield (50 mm/min)	ISO 527	11	MPa
Flexural Modulus (1.3 mm/min)	ISO 178	450	MPa
HDT at 0.45 MPa	ISO 75-2	35	°C
ESCR at 100% Igepal	ASTM D1693	>1000	hr
ESCR at 10% Igepal	ASTM D1693	>350	hr
ARM Impact (-40 °C, 3 mm thickness)	ARM-I Standard	80	J

Notes

This information is to the best of our knowledge accurate. However, the circumstances and conditions in which it may be used are beyond our control and we do not accept liability for any loss or damage that may occur nor do we offer and warranty of immunity against patent infringement. The values indicated in the tables only describe typical properties. They do not constitute specification limits.

Consistently delivering value

22-20 Tenter Road, Moulton Park Industrial Estate, Northampton, NN3 6AX, United Kingdom.
Telephone: +44(0)1604 641640 Fax: +44(0)1604 641629 Email: info@matrixpolymers.com Website: www.matrixpolymers.com
© 2011 Matrix Polymers Ltd. All rights reserved.



Appendix 5 (Continued)

Issue number: 1
Issue Date: 16 March 2011



REVOLVE® N-250			
(4068)			
Rotational Moulding		M.F.I.	7.0
		Density	0.935

Description

Revolve N-250 is a rotational moulding polyethylene general purpose grade. It has been designed to provide wide processing window, excellent mouldability without compromising impact strength. The grade is UV8 stabilised and it is the base of all standard colours and mottle effects.

Features & Benefits

Superb natural colour
Good mouldability
Excellent impact strength
Suitable for complex articles

Available as

Natural pellets & powder
Black pellets & powder
Coloured powder

Physical Properties**	Test Method	Value	Units
MFI	ISO 1133	7.0	g/10min
Density	ISO 1183	0.935	g/cm ³
Tensile Strength @ Yield (50 mm/min)	ISO 527	16.8	MPa
Flexural Modulus (1.3 mm/min)	ISO 178	645	MPa
HDT at 0.45 MPa	ISO 75-2	47	°C
ESCR at 100% Igepal	ASTM D1693	1000	hr
ESCR at 10% Igepal	ASTM D1693	50	hr
ARM Impact (-40 °C, 3 mm thickness)	ARM-I Standard	101.6	J

Notes

All values tested on rotomoulded samples (except MFI and ESCR)

This information is to the best of our knowledge accurate. However, the circumstances and conditions in which it may be used are beyond our control and we do not accept liability for any loss or damage that may occur nor do we offer and warranty of immunity against patent infringement. The values indicated in the tables only describe typical properties. They do not constitute specification limits.

Consistently delivering value

22-40 Tenter Road, Moulton Park Industrial Estate, Northampton, NN3 6AX, United Kingdom
Telephone: +44(0)1604 641640 Fax: +44(0)1604 641659 Email: info@matrixpolymers.com Website: www.matrixpolymers.com
© 2011 Matrix Polymers Limited. All rights reserved.



Appendix 5 (Continued)



SABIC® HDPE M40060S

High density polyethylene for Injection moulding

Description.

SABIC® HDPE M40060S is an UV stabilized, high density polyethylene copolymer injection moulding grade with a narrow molecular weight distribution. It has improved mouldability. Articles produced from this grade exhibit excellent impact strength, low warpage, stress crack resistance (ESCR) and excellent gloss.

Typical applications.

SABIC® HDPE M40060S is recommended for the manufacture of injection moulded articles such as pails, shipping containers and industrial parts.

Processing conditions.

Typical moulding conditions for SABIC® HDPE M40060S are:

Melt temperature: 232 - 260 °C (450 - 500 °F)

Mould temperature: 20 - 40 °C (70 - 104 °F)

Injection pressure: 93 - 103 MPa (13500 - 15000)

Typical data.

Revision 20081029

Properties	Units SI	Values	Test methods
Polymer properties			
Melt flow rate (MFR) at 190 °C and 2.16 kg	g/10 min	4.0	ASTM D 1238
Density	kg/m ³	960	ASTM D 1505
Mechanical properties			
Tensile test			
stress at yield	MPa	33	ASTM D 638
stress at break	MPa	22	
strain at break	%	1200	
secant modulus at 1% elongation	MPa	1240	
Izod Impact notched at 23 °C	J/m	69	ASTM D 256
Hardness Shore D	-	69	ASTM D 2240
ESCR (100% Igepal), F50	h	6	ASTM D 1693B
Thermal properties			
Vicat softening temperature at 10 N (VST/A)	°C	128	ASTM D 1525
Brittleness temperature	°C	< -75	ASTM D 746

1) Test specimens are prepared from compression moulded sheet made according to ASTM D 1628 Procedure C.

Appendix 5 (Continued)

Issue Number: 1 Issue Date: 14/09/07



REVOLVE[®]			
Rotational Moulding	Revolve 5056	M.F.I	3.5
	N-307	Density	0.939
Description			
Revolve [®] N-307 is a high density, low melt index hexene polyethylene resin. It has excellent impact strength and is UV10 stabilised. This grade is especially suitable for large tanks. Additionally this grade carries WRC approval for potable water application.			
Features & Benefits		Available as	
<ul style="list-style-type: none"> * High stiffness and hardness * Good mouldability * Excellent impact strength * UV10 stabilised 		<ul style="list-style-type: none"> * Natural granules and powder * Black granules and powder * Coloured granules and powder * Turbo-Blend[™] 	
Physical Properties	Test Method	Value	Units
MFI	ISO 1133	3.5	g / 10 min
Density	ISO 1183	0.939	g / cm ³
Tensile Strength @ Yield (50 mm/ min)	ISO 527	17.7	MPa
Flexural Modulus (1.3 mm/ min)	ISO 178	790	MPa
Heat Distortion Temperature @ 1.8 MPa	ISO 75-2	48	°C
ESCR, 100% Igepal	ASTM D1693	>1000	hr
ESCR, 10% Igepal	ASTM D1693	400	hr
ARM Impact (3mm thick)	ARM standard	108	J

NotesREVOLVE[™] is a Trademark of Matrix Polymers Limited.Turbo-Blend[™] is a Trademark and Service Mark of Matrix Polymers Limited

This information is to the best of our knowledge accurate. However, the circumstances and conditions in which it may be used are beyond our control and we do not accept liability for any loss or damage that may occur nor do we offer a warranty of immunity against patent infringement.

The values indicated in the tables only describe typical properties. They do not constitute specification limits.

Consistently delivering value

22-40 Tanker Road, Moulton Park Industrial Estate, Northampton, NN5 6AX, United Kingdom.

Telephone: +44(0)1604 641640 Fax: +44(0)1604 641669 Email: info@matrixpolymers.com Website: www.matrixpolymers.com

Company registration No. 2669964 Registered Office as above



Appendix 5 (Continued)

Issue number: 1
Issue Date: 28 March 2011



REVOLVE® M-601

Rotational
Moulding

Super-Linear

M.F.I. 3.5
Density 0.949

Description

Revolve M-601 is a Super-Linear rotational moulding grade designed to provide high stiffness without compromising impact properties and toughness which makes the grade ideal for any leisure marine products like kayaks, canoes and boat. The grade is suitable for multi-layer application in combination with any Matrix foam.

Features & Benefits

Excellent impact properties
High toughness
Good mouldability
High stiffness

Available as

Natural powder
Black powder
Coloured powder

Physical Properties

Physical Properties	Test Method	Value	Units
MFI	ISO 1133	3.5	g/10min
Density	ISO 1183	0.949	g/cm ³
Tensile Strength @ Yield (50 mm/min)	ISO 527	21.4	MPa
Flexural Modulus (1.3 mm/min)	ISO 178	1304	MPa
HDT at 1.8 MPa	ISO 75-2	55	°C
ESCR at 100% Igepal	ASTM D1693	N/A*	hr
ESCR at 10% Igepal	ASTM D1693	N/A*	hr
ARM Impact (-40 °C, 3 mm thickness)	ARM-I Standard	118	J

Notes

* The grade is not suitable for ESCR applications

This information is to the best of our knowledge accurate. However, the circumstances and conditions in which it may be used are beyond our control and we do not accept liability for any loss or damage that may occur nor do we offer and warranty of immunity against patent infringement. The values indicated in the tables only describe typical properties. They do not constitute specification limits.

Consistently delivering value

22-20 Tenter Road, Moulton Park Industrial Estate, Northampton, NN3 6AX, United Kingdom
Telephone: +44(0)1604 641640 Fax: +44(0)1604 641659 Email: info@matrixpolymers.com Website: www.matrixpolymers.com
© 2011 Matrix Polymers Limited. All rights reserved.



Appendix 6

Data sheets of the filler particles used in this PhD study.



DESCRIPTION

Inert low density grey powder composed of hollow alumino – silicate glass spheres

Silicon	SiO ₂	50 - 63%
Aluminium	Al ₂ O ₃	24 - 38%
Ferric Oxide	Fe ₂ O ₃	1 - 5%
Calcium	CaO	0 - 2.0%
Magnesium	MgO	0 - 2.0%
Loss on ignition at 1000° C		< 2.0

Typical Chemical Analysis

Appearance	Light Grey Powder	Specific Gravity	< 0.60 / 0.70 g / cc
Particle Density	0.6 - 0.8 kg / litre	Compressive Strength	2500 - 5000 PSI
Shell thickness	3 - 7 % of diameter	CTE	8 x 10 ⁻⁶ °K
Thermal Conductivity	0.1 Wm ⁻¹ K ⁻¹	Oil Absorption	16 - 18g oil / 100g
Hardness (Moh's scale)	5	Sinkers	5 % max
Sintering temperature	1200 °C		
Moisture	0.5%		

Typical Physical Properties

B. S. Mesh	Microns	CENO 40 MBD	CENO 50 LBD	CENO 100 WPD
30	500	100	100	100
60	250	99	99	100
100	150	75	90	99
300	53	7	7	7
Loose bulk density	kg / litre	0.35 - 0.45		

Typical Sieve analysis - Cumulative percentage passing

Rodbourne Road - Fordingbridge - SP6 1RA - United Kingdom
 tel : +44 01425 654011 - fax : +44 01425 654141
 email : office@deantranter.co.uk - www.deantranter.co.uk

Appendix 6 (Continued)

MinTron 7™ Product Data Sheet

Data Sheet

MinTron 7™ is a mineral filler-extender intended for use in thermoplastic, thermoset, elastomer, vinyl and coating applications. Potential benefits include: 100% recycled product, spherical particle shape with improved flow characteristics and reduced stress distribution, lower particle density and improved physical properties.

Typical Product Properties

Typical Values	MinTron 7™
Sample Description	Alumino-silicate Spheres
Particle Shape	Predominantly Spherical
Moisture Content	<0.5%
Particle Specific Gravity	2.2 – 2.4g/cm ³
Bulk Density	~1.0g/cm ³
Mohs Hardness	5 – 6
Particle Size Distribution d90	20 – 35µm
Particle Size Distribution d50	5 – 9µm
Oil Absorption BS EN 787-5:1995	~35g oil/100g MinTron 7™
Hydrostatic Crush Strength	>200MPa (30,000psi)
Softening Point ASTM C24-01	1300 – 1317°C (cone 8-9)

Typical Product Analysis

SiO ₂	48–60%	Fe ₂ O ₃	3–7%
Al ₂ O ₃	20–30%	Alkali Oxides	5-9%

RockTron International Head Office:
Wessex House, Pixash Lane, Keynsham, Bristol, BS31 1TP, United Kingdom.

POWERFULLY GOOD FILL-MINERALS

Version Number: 01-07-11



RockTron

Appendix 6 (Continued)

Product Data Sheet

Waterjet Grade Product Range

typical weight % retained

	50 Mesh (600-200)	60 Mesh (400-200)	80 Mesh (300-150)	120Mesh (200-100)	
US Mesh microns					
35	500	2	-	-	-
40	425	14	0.2	-	-
45	355	45	10	2	-
50	300	85	45	20	-
60	250	96	78	50	0.01
70	212	95	96	85	25
80	180	99.9	99	95	70
90	150	-	99.8	99	93
115	125	-	-	-	99
150	106	-	-	-	99.9

Packaging:

- 80 x 25kg multilayer paper bags shrinkwrapped to 2 MT pallets, or
- 80 x 25kg multilayer paper bags packed into 2 MT bulk bags, or
- 2 MT top and bottom spouted bulk bags with internal PVC liner

Mineral Composition (Typical)

Garnet (Almandite).....	97-98 %
Ilmenite.....	1-2 %
Zircon.....	0.20 %
Quartz (free silica).....	<0.5 %
Others.....	0.25 %

Physical Characteristics (typical)

Bulk Density.....	2.3 T/m ³
Specific Gravity.....	4.1
Hardness (Moh).....	7.50 - 8.0
Melting Point.....	1250 °C
Shape of natural grains.....	sub-angular

Average Chemical Composition (Typical)

SiO ₂ *.....	36 %
Al ₂ O ₃	20 %
FeO.....	30%
Fe ₂ O ₃	2 %
TiO ₂	1 %
MnO.....	1 %
CaO.....	2 %
MgO.....	6 %

* refers to SiO₂ bound within the lattice of the homogenous garnet crystal (no free silica)

Other Characteristics (Typical)

Conductivity.....	10-15ms/m (max 25ms/m)
Radioactivity.....	Not detectable above background
Moisture Absorption.....	Non-hygroscopic, inert
Total Chlorides.....	10-15ppm (max 25ppm)
Ferrite (free iron).....	< 0.01 %*
Lead.....	< 0.002 %*
Copper.....	< 0.005 %*
Other Heavy Metals.....	< 0.01 %*
Sulphur.....	< 0.01 %*

* Generally below detectable levels.



Appendix 6 (Continued)



MOIST SAND

A Washed and graded, high quality silica sand

PRODUCT INFORMATION

ISSUE NO 3.03

TYPICAL GRADINGS	LEISURE SAND	MOIST 28	MOIST 40	MOIST 50	MOIST 60	MONEYSTONE
CLASSIFICATION	SIEVE SIZE MM	% RETAINED	% RETAINED	% RETAINED	% RETAINED	% RETAINED
VERY COARSE SAND	2.00 - 1.00	0.2	0.0	0.2	0.1	15.0
COARSE SAND	1.00 - 0.50	8.1	25.5	3.5	1.4	49.0
MEDIUM SAND	0.50 - 0.25	85.0	46.7	50.2	33.0	27.0
FINE SAND	0.25 - 0.125	5.9	22.0	45.4	59.1	8.0
VERY FINE SAND	0.125 - 0.063	0.8	5.9	0.7	5.8	TRACE
CLAY/ SILT	<0.063	TRACE	0.0	TRACE	0.6	TRACE
pH		5.5	7.1	7.1	7.1	6.1
FREE LIME CONTENT		NIL	NIL	NIL	NIL	TRACE
HYDRAULIC CONDUCTIVITY APPROXIMATE RANGE			500 mm/ hr	640 mm/ hr	450 mm/ hr	

Bathgate Silica Sand Limited

Ardid Quarry, Congleton Road, Sandbach, Cheshire. CW11 4SN

Telephone : 01270 762828 Fax : 01270 760557

www.bathgatesilica.co.uk

Silica sand is a natural raw material. All data is to be considered as indicative. Each customer is encouraged to determine the suitability of our product for their own application. Upon simple request we will be pleased to discuss tolerances on the above product data. Sales and supplies will always be according to our general sales conditions

All systems operate under the auspices of BS EN ISO 9001:2000 and the company is registered with the British Standards Institute as complying with these requirements



Certification No. FM 01596